Structure and Reactivity of Transition Metal Clusters

A thesis submitted for the degree of
— Doctor of Philosophy —

Alexander Christoph Hermes

Oxford,
August 2013

Structure and Reactivity of Transition Metal Clusters

Alexander Christoph Hermes
Magdalen College
A thesis submitteed for the degree of Doctor of Philosophy
Hilary Term, 2013

A range of computational and experimental techniques have been applied to the study of four metal cluster systems.

Decorated rhodium clusters $Rh_nO_m(N_2O)^+$ ($n = 4-8$, $m = 0-2$) have been investigated both experimentally by IR-MPD and computationally using DFT. The effect of cluster size as well as oxygen coverage on the spectroscopy of the N_2O bend are analyzed. The infrared-induced decomposition of N_2O on $Rh_nO_m^+$ is observed on all cluster sizes, with marked differences as a function of size and oxygen coverage, particularly in the case of $Rh_5(N_2O)^+$.

The oxidation of CO was studied on the surface of small platinum cluster cations $Pt_nO_m^+$ ($n = 3-7$, $m = 2,4$) by IR-MPD at $400 - 2100\,cm^{-1}$. Spectroscopically, oxygen is found to be bound both dissociatively and molecularly on the cluster surface, while the CO band is found to red shift in cluster size, and blue shift with oxygen coverage. Oxidation of CO proceeds on all cluster sizes, with a constant branching ratio of 40 % : 60 %. DFT calculations identified key stationary points and barriers on the $Pt_4O_2CO^+$ reaction pathway.

The one-colour Ta_2 photodissociation is studied by photoionization and VMI in the range $23\,500 - 24\,000\,cm^{-1}$, finding clear evidence of a fragmentation process producing Ta, which is interpreted as fragmentation of cationic Ta_2^+ at the two photon level. A majority of the observed channels produce either atomic ($Ta(^4F_{3/2})$) or cationic ($Ta^+(^5F_1)$) ground state. An improved value for the dissociation energy $D_0(Ta_2^+)$ is obtained, in agreement with computational predictions. The anisotropies observed show weak evidence of a perpendicular transition being involved in the photodissociation process.

Finally, the photodissociation dynamics of Cu_2 are studied by spectroscopy in the range $36\,000 - 38\,200\,cm^{-1}$ as well as VMI. Clear evidence for resonant photolysis of Cu_2 is obtained, as a result of both direct dissociation of the Cu_2^+ $^2\Pi$ ion state as well as dissociation of doubly excited Cu_2 states, which leads to a determination of dimer dissociation energies. Finally, the production of Cu_2^+ is interpreted as evidence of photolysis of Cu_3, from which a Cu_3 dissociation energy is derived.

Acknowledgements

It is a pleasant duty to thank all the people whose aid made this work possible. First and foremost, I extend the deepest gratitude to my supervisor Dr. Stuart Mackenzie, who in providing regular feedback and input helped guide me past many pitfalls and who inspired confidence even when things were not flowing as smoothly as they might have.

The impressive work ethic and unfailing enthusiasm for physical chemistry displayed by Dr. W. Scott Hopkins was a tremendous encouragement for my work both inside and outside the laboratory. I wish him well now that he has returned to his Canadian homeland.

Dr. Suzanne Hamilton was an invaluable resource, in particular in getting myself set up for the computational work as well as experiment programming in LabVIEW. She always found time to help even as she herself was finishing her DPhil thesis.

I have greatly enjoyed working with the the inimitable Dr. Aras Kartouzian, who contributed not only his great humour but also his unique and fresh insights into our work — I owe many a creative solution to him.

The electronic and metal workshops at Oxford proved, time and time again, to be a great help in the construction of equipment as well as in troubleshooting issues that arose. The computing facilities of the National service for computational chemistry (NSCCS) as well as the Oxford supercomputing centre (OSC) were invaluable in performing density functional theory calculations.

Finally, I thank my parents, Lucia and Christoph, for all their support and understanding.

Alexander Hermes
Oxford, August 2013

List of Publications

Parts of the work presented in this thesis have also appeared in the following publications:

[1] A. C. Hermes, S. M. Hamilton, G. A. Cooper, C. Kerpal, D. J. Harding, G. Meijer, A. Fielicke, and S. R. Mackenzie. "Infrared driven CO oxidation reactions on isolated platinum cluster oxides, $Pt_nO_m^+$". *Faraday Discussions*, **157**: 213–225, (2012).

[2] A. C. Hermes, S. M. Hamilton, W. S. Hopkins, D. J. Harding, C. Kerpal, G. Meijer, A. Fielicke, and S. R. Mackenzie. "Effects of Coadsorbed Oxygen on the Infrared Driven Decomposition of N_2O on Isolated Rh_5^+ Clusters". *Journal of Physical Chemistry Letters*, **2**: 3053–3057, (2011).

[3] C. Kerpal, D. J. Harding, A. C. Hermes, G. Meijer, S. R. Mackenzie, and A. Fielicke. "Structures of Platinum Oxide Clusters in the Gas Phase". *The Journal of Physical Chemistry A*, **117**: 1233–1239, (2013).

[4] I. S. Parry, A. C. Hermes, A. Kartouzian, and S. R. Mackenzie. "Imaging the photodissociation dynamics of neutral metal clusters: copper dimer, Cu_2 and copper oxide, CuO". *Physical Chemistry Chemical Physics*, Advance Article, (2013).

Contents

CHAPTER 1

Introduction

1.1 Motivation

Over the course of the last half century, the study of clusters has become a major area of research in the field of physical chemistry and molecular physics. Clusters, commonly defined as an aggregation of a countable number of independent moieties, are a form of matter that lies between the well understood atomic and bulk regimes. In contrast to what one might expect, physical and chemical properties such as dissociation energy, reactivity and magnetic moments do not smoothly vary from atom to bulk[1–7] — rather, a range of fascinating effects is often observed in the intermediate regime of clusters. In addition to the interest in understanding the size dependent phenomena of the clusters themselves (*e.g.* how big does a cluster have to be before it exhibits bulk-like behaviour), research in the area of cluster science is driven by three further considerations:

First, the notion that we can use small clusters as models for the heterogeneous catalysts commonly used throughout industrial processes, since many of these industrial catalysts involve highly dispersed metals and surface defect sites are often the active sites for surface chemistry.[8] One of the advantages of using isolated clusters as models, in contrast with bulk catalysts, is that the smaller scale of the clusters makes them much more amenable to detailed study by both experimen-

tation and computation, while still providing a road to the understanding of the bulk catalysts. A nice verification of this idea is the recent demonstration that coordinatively unsaturated ruthenium atoms act as catalytic sites for carbon monoxide oxidation on RuO_2.[9] A second, related factor is that clusters are sufficiently complex as to represent a good testing ground for theoretical and computational methods, and as a result work on clusters may be used as a vehicle to improve said methods. This is exemplified by the dramatic evolution that density functionals for use with (transition metal) clusters have undergone since DFT was first applied to such systems.[10] Finally, the clusters themselves may prove to be highly specific reagents in their own right, opening up new applications — for example, small copper complexes are used in the functionalization of alkanes[11] or selective oxidation reactions.[12]

This chapter will introduce the most important aspects of the field of *cluster science*, providing the context necessary to understand the work presented in the rest of the thesis.

1.2 Sources of isolated clusters

One of the major challenges in the study of atomic clusters is the generation of clusters in sufficient number densities as to be amenable to study. While rare gas and molecular clusters may be produced by the supersonic expansion of a high pressure of the gas through a small aperture into vacuum,[13] the formation of metallic clusters requires the vapourization of the metal.

Early methods of cluster generation involved heating the metal in question in an oven or boiler[14,15] and expanding the vapour formed through a nozzle to obtain a supersonic expansion cooling, which encourages clustering. However, this sort of method requires both a low boiling point metal ($< 1500\,\mathrm{K}$) and a substantial amount of sample, limiting its application. In particular, large clusters of high boiling point materials, such as transition metals, are difficult to form.

In independent developments in the 1980s, Smalley[16] and Bondybey[17] developed an alternative source based on the laser ablation of a metal target. The details of such sources have been the subject of a recent review by Duncan,[18] but the basic

principle of the source is simply explained: a laser pulse strikes a metal target (typically a rod or disc), locally heating the target and vapourizing the metal atoms. The resulting plasma is entrained within a gas pulse (typically helium), followed by supersonic expansion into vacuum. Such sources inherently produce a pulsed beam of clusters, and usually have a very high peak flux of clusters compared with other techniques, ideal for use with laser spectroscopy or mass spectroscopic measurements. This work employs just such a source, and it is described in detail in section 2.1.

Another method is *sputtering*: here, rare gas ions are accelerated towards a metal surface, ejecting metal atoms from the surface. The sputtering rare gas may be produced either *via* an ion gun[19] or a plasma trapped in a magnetic field.[20,21] Clusters formed in such sources cool primarily through evaporation, and as a result the size distribution reflects their relative stability.

A further way of generating clusters is the pulsed-arc cluster ion source (PACIS).[22] PACIS uses an arc discharge to vapourize the atoms and produces a more intense cluster beam than laser vapourization sources. It has the additional advantage of being applicable to liquid as well as solid metals. However, the arc discharge involved makes it more difficult to cool the clusters, due to the fact that the helium carrier gas also experiences the arc discharge and heats up.

1.3 Experimental investigation of Clusters

Traditional spectroscopy, based on direct adsorption according to the Beer-Lambert, law is not widely applicable on gas-phase clusters on account of several factors:

First, the cluster sources described in the previous section typically produce clusters in number densities far too low to be probed directly. For example a typical laser ablation source may produce on the order of 10^6 clusters (10^{-17} mole) per laser shot. Given a typical molar extinction coefficient of $1 \times 10^6\,\mathrm{cm}^2/\mathrm{mol}$,[23] a 1 cm cube containing these clusters would only give an absorbance of 10^{-11}. Second, a wide distribution of clusters is usually generated by such ablation sources, so any direct signal is necessarily a convolution of the signals of many different clusters.

Nevertheless, for di- and triatomics, some success was obtained by using trace detection techniques such as laser induced fluorescence or cavity ringdown spectroscopy.[17,24] However, even these techniques are not sensitive enough to probe the structure of larger clusters. In contrast, mass spectrometry is a technique which offers both a very high sensitivity, able to reliably detect even small numbers of clusters, as well as the possibility of isolating a particular cluster size of interest, so that size-dependent studies may be performed. These advantages have led to the development a large variety of techniques based on mass spectrometry either as a means of detection or mass-selection (or both).

1.3.1 Structure

The desire to understand the properties of clusters has fuelled great efforts to understand their structure, and thus gain insight into said properties.

Cluster size distribution

Some of the the first insights into the nature of cluster structure were provided by Knight *et al.*[25,26] Monitoring the abundance of sodium clusters by mass spectrometry (reproduced in fig. 1.1) they found marked maxima ("magic numbers") in the cluster distribution at cluster sizes $N = 8$, 20, 40, 58 and 92. These peaks in the abundance can be understood in the context of the spherical jellium model:[27] in this model the positive ions are treated as a positive background of uniform density, distributed over the volume of the cluster, treated as a sphere. Density functional theory is then used to self-consistently determine the electronic structure by solving the Kohn-Sham[28,29] equations in this background potential (which additionally requires an appropriate exchange-correlation functional to be chosen, see section 2.6). The model predicts an electronic shell structure with closed shells at 8, 20, 34, 40, 58 and 92 electrons. Recalling that alkali metals have only one valence electron this matches the peaks observed in fig. 1.1 — clusters with closed electronic shells are significantly more stable than clusters with one additional or one fewer atom, which results in an increased abundance.

Magic numbers were also observed in the size distribution of rare gas clusters,[13,30]

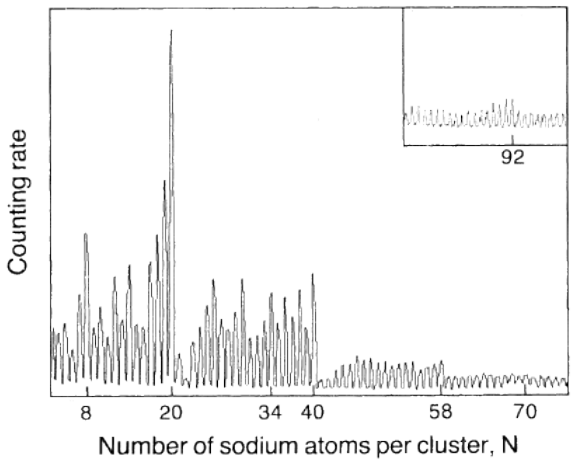

Figure 1.1 Mass spectrum of cationic sodium clusters, showing maxima at the "magic numbers" $N = 8$, 20, 40, 58 and 92. Adapted, with permission, from ref. [25]. Copyright (1984) by The American Physical Society.

corresponding to the number of atoms needed to complete the packing into Mackay icosahedra;[31] a family of closed icosahedral arrangements made up of concentric icosahedral shells. This experimental finding was supported by calculations showing that, for clusters with a potential made up of a short-range steeply repulsive term and a weakly attractive long-range term, such icosahedral clusters have the highest binding energy per atom.[32] This explains why rare gas clusters, whose interaction are well modelled by such a potential, show exactly such icosahedral growth patterns, whereas transition metal clusters follow the aforementioned pattern.

Cluster geometry

A somewhat more refined approach was developed by Riley *et al.*;[33] utilizing the adsorption of small molecules such as N_2 or NH_3 as a probe for structure: by using empirically determined binding rules for these small molecules, the number of apex and surface atoms in a cluster may be estimated. This led to the discovery of contrasting packing motifs in the structures of nickel and cobalt, with the former having packing characteristic of the bulk and the latter having pentagonal symmetry.[34]

Another way to study the geometric structure of clusters is provided by ion mobility measurements.[35] In these measurements, a mass selected ion drifts through a cell filled with buffer gas. The drift is affected by the drag a cluster feels in passing through the buffer gas, which in turn will depend on its geometric cross section. By comparing the cross section obtained experimentally to computational simulations, inferences on the structure can be made. These measurements have proven quite successful in the investigation of the geometric structure of gold cluster cations and anions,[36] finding planar structures for the gold anions[37] Au_n^- ($n \leq 12$) and cations[35] Au_n^+ ($n \leq 7$), whereas three-dimensional structures were found for the larger clusters. Furthermore, by heating and cooling of the buffer gas one may change the temperature of the clusters, and thus probe the temperature dependence of the cluster structures. This method was applied to the Au_9^+ cluster, finding a marked change in the drift time distribution of Au_9^+ at temperatures below 140 K, which was interpreted as the temperature dependent conversion between the two lowest lying isomers of Au_9^+. Ion mobility techniques have also been applied to clusters of Al and Si, indicating the co-existence of multiple isomeric forms over a range of cluster sizes.[38,39] A limiting factor for ion mobility measurements is that only structures with substantially differing crossections may be distinguished.

A further technique, pioneered by Parks *et al.* on C_{60}^+ molecules,[40] is trapped ion electron diffraction (TIED). As the name implies, this method involves the trapping of (mass-selected) ions in a rf trap, followed by exposure to an electron beam. The recorded diffraction pattern is sensitive to the geometric structure of the clusters, particularly to nearest neighbour distances. With the aid of theoretical predictions, structural information can thus be extracted from the diffraction patterns. Kappes and coworkers have applied this method to study the 2D to 3D transition in anionic gold clusters,[41] showing that Au_{12}^- is the first cluster to have a three-dimensional structure. The Au_{34}^- cluster was shown to adopt a chiral structure,[42] while weak Jahn-Teller distortions were found in Ag_{55}^- clusters compared to their cationic counterparts.[43]

A more recent development is the use of so-called *action* spectroscopy. These experiments proceed by monitoring a mass spectrometric signature of a photon-

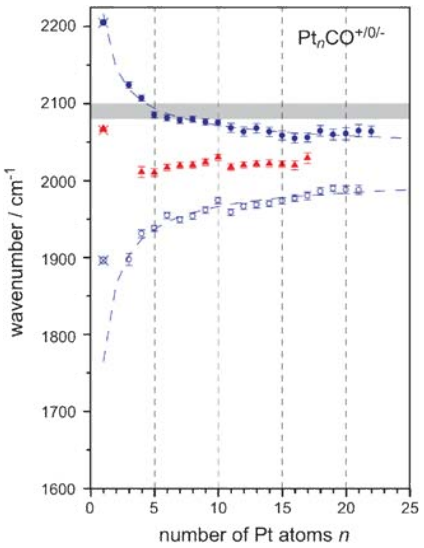

Figure 1.2 Frequency of the ν(CO) vibration in Pt_nCO cations(●), neutral species (▲) and anions(❍). The grey band marks the range of ν(CO) reported for CO adsorbed at μ_1 sites on platinum surfaces. Adapted from ref. [44] with permission from the PCCP Owner Societies.

induced event, *e.g.* a photodissociation, thereby exploiting the high sensitivity of mass spectrometry for wavelength dependent spectroscopy. Fielicke *et al.* have successfully applied this technique in the infrared to study the binding sites of CO on rhodium and platinum clusters (see fig. 1.2).[44,45] The scope of this experiment can be widened by weakly adsorbing rare gas atoms to the cluster of interest, which provides a mass spectrometric signature (through rare gas atom loss) even for clusters that would not rapidly fragment upon irradiation. This allows the technique to be used to probe the far-IR metal-metal modes of metal clusters, which encode a significant amount of structural information. Using Ar-tagging, the far-IR spectra of Nb clusters have been recorded,[46] which has led to the determination of their structure (by comparison with computational predictions.) The application of this method to the structure of cationic rhodium clusters[47,48] has led to the resolution of the long-standing question whether such clusters adopt cubic motifs or motifs based on icosahedral fragments: the far-IR spectra conclusively show that the structures of the Rh_n^+ ($n = 6-12$) clusters are based on octahedral and tetrahedral motifs. This work also employs this technique, called Infrared Multiple Photon Depletion (IR-MPD), and it is discussed in detail in section 2.3. Action spectroscopy techniques, in combination with rare gas tags, have also been used to measure the UV/vis spectra of metal clusters.[49]

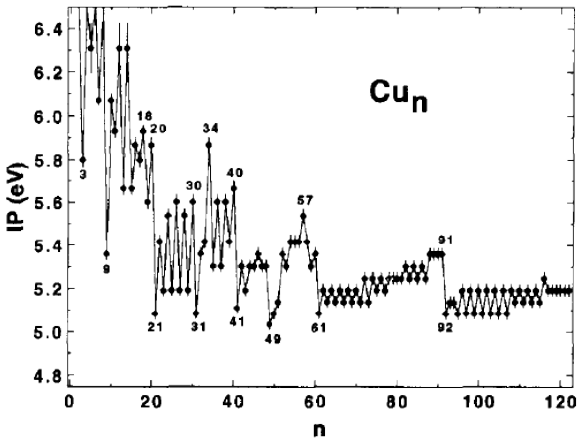

Figure 1.3 Vertical ionization potentials for copper clusters, showing features corresponding to electronic shell closings. Adapted, with permission, from ref. [52]. Copyright (1992) Elsevier.

Photoionisation

Understanding the electronic structure of clusters is another major goal of researchers in the quest for a complete understanding of the properties of clusters. Photonionisation, that is the use of typically visible or ultraviolet photons to ionise a species, was one of the first techniques brought to bear upon this issue. By measuring the yield of positive ions as a function of photoionisation wavelength one obtains a photoionization efficiency spectrum, from which the ionization potential may be obtained.[50] The size dependent variation in ionization potential of clusters can already reveal much information on the electronic structure, as in the case of alkali and coinage metal clusters, where distinct maxima in IP are correlated with the electronic shell closings mentioned above (for example, see fig. 1.3).[51,52] In contrast, the ionization potentials of other transition metals such as Nickel,[50] Iron and Cobalt[53] do not exhibit these discontinuities associated with shell closings. The ionization potentials of the different isomeric forms of Niobium clusters Nb_n ($n = 9 - 12$) showed that in all cases except $n = 10$ the less reactive form possessed higher ionization potential than the more reactive form.[54]

Ionisation studies measuring the wavelength dependent enhancement of ionization *via* a resonant state are a more advanced use of photoionisation and

are particularly useful for the smallest clusters (two to four atoms). Direct photoionization *via* resonance enhanced multi-photon ionisation (REMPI) has been used to measure the spectra of several metal dimers and trimers such as Ni_2,[55] Au_2[56] and Cu_3[57] and assign their electronic states. The zero electron kinetic energy (ZEKE) method uses a pulsed electric field to ionize clusters following their photoexcitation to high lying Rydberg states. It offers much improved resolution compared to REMPI and has expanded the range of clusters studied to include larger complexes such as Nb_3C_2.[58] Yang and Hackett have recently reviewed its application to metal clusters.[59] Instead of detecting the electrons produced in the ZEKE process, one may also use mass spectrometry to analyze the cations simultaneously produced. In this form the technique is known as mass analyzed threshold ionization (MATI), and provides substantially greater mass resolution and mass discrimination.[60]

Photoelectron spectroscopy (PES) probes the electrons ejected in an ionization or photodetachment process, and as such represents a direct probe of electronic structure. It has been used to study the electronic structure of metal dimers,[61] the uptake of N_2 on metal clusters[62] and has even allowed an understanding of how electronic structure correlates with reactivity.[63]

Other cluster properties

A variety of other properties of clusters have been measured in addition to the ones mentioned above. For example, by measuring the deflection of a molecular beam of clusters under the influence of an electric deflection field, it is possible to determine the electric dipole polarizabilities of the clusters.[64] This technique has been employed by Knickelbein to study the polarizabilities of nickel clusters,[64] finding anomalously large polarizabilities for particular cluster sizes corresponding to icosahedral structures with one missing atom, while minima are observed for structures that are spherical. Niobium clusters exhibit significant variation in their dipole moments as a function of temperature, with cold clusters having very large electric dipole moments, while the clusters at room temperature show normal metallic polarizabilities.[65,66] In a similar experiment measuring the polarizabilities of rhodium clusters, the Rh_7 clusters was found to have a

permanent dipole, unique in the size range studied ($n = 5 - 28$), while the Rh_{10} cluster exhibited paraelectric behaviour.[67]

In closely related approach, the magnetic moments of several clusters can measured in Stern-Gerlach-type experiments by measuring the beam deflection induced by a magnetic field.[68] In this way the magnetic moments of cobalt clusters were found to be substantially in excess of the bulk value, while the moments of gadolinium clusters are significantly below the bulk value.[68] One of the most striking results obtained by this method was the discovery that small clusters of rhodium exhibit giant magnetic moments, in contrast with the bulk material which is non-magnetic.[69,70] Furthermore, significant variations in the magnetic moments of adiacent cluster sizes were observed, contrasting the behavious of other transition metal clusters such as cobalt[68] and nickel.[71] These results have prompted a significant amount of theoretical investigation of the rhodium (see section 1.4).

1.3.2 Reactivity

As alluded to in the beginning, the reactivity of transition metal clusters has attracted a great deal of attention over the last 50 years. Consequently, significant amount of both experimental and computational work has been devoted to researching this aspect. This section shall give an overview of some of the most important techniques and results relevant to the work described in this thesis.

Experimental techniques

One of the most common approaches to studying reactivity is the use of a *trap* to confine cluster ions of interest, usually after mass selection has taken place. In an ion cyclotron resonance (ICR) cell ions can be contained in a stable cyclotron orbit for extended periods of time — up to several minutes are possible.[72,73] A controlled pressure of reactant gas can be admitted in this time, allowing reaction kinetics to be studied in detail. The technique is typically applied as fourier transform ICR (FT-ICR), where the mass spectrum of the ions is collected by a fourier transform of their transient time signal, which allows a very high mass

resolution to be attained.

In fast-flow reactors,[74,75] the cluster ions expand from their narrow clustering channel (typically 1 – 2 mm diameter) into a flow tube (*e.g.* 10 mm diameter, 10 cm length). A mixture of buffer and reactant gases is let into the flow tube, after which the products may be extracted. The technique permits both neutral and ionic clusters to be studied, but in general leaves no opportunity for mass selection prior to reaction. The Bernstein group have developed a similar design to study the reactions of neutral clusters: clusters are generated in a narrow clustering channel, generating a supersonic cluster beam. Ions in the beam are then deflected by an applied electrostatic field, after which the neutral clusters pass into a reaction/pickup cell filled with the reactant gas of choice.[76,77]

Collision cell experiments are conceptually similar to fast-flow reactors in that they also employ a cell filled with reactant gas.[78] However, this collision cell typically houses much lower gas pressures, and the nascent clusters are skimmed into a molecular beam before they pass into the cell. Both ionic and neutral clusters may be studied in this way, although ionic clusters offer additional control: using suitable extraction fields, ions may be mass-selected[79] and their kinetic energy regulated. This allows the study of both collision induced dissociation (CID)[80] and reactivity[79] as a function of kinetic energy.

Recently, members of this group, in collaboration with the Meijer group in Berlin, have developed another technique for the study of reactions of transition metal clusters. The technique is an adaptation of the IR-MPD method previously used to study the spectroscopy of transition metal clusters, and uses the resonant absorption of infrared photons to heat the clusters and trigger reactions (it is described in more detail in section 2.3.3). This method has been used to probe the activation of methane on platinum clusters,[7] as well as the reduction of N_2O on rhodium clusters[81,82] and the oxidation of CO on platinum clusters[83] (see also chapters 3 and 4).

Cluster reactivity results

The reaction rates observed on small metal clustes can differ drastically from those observed on corresponding metal surfaces,[84] and their reactivity is sensitive to a

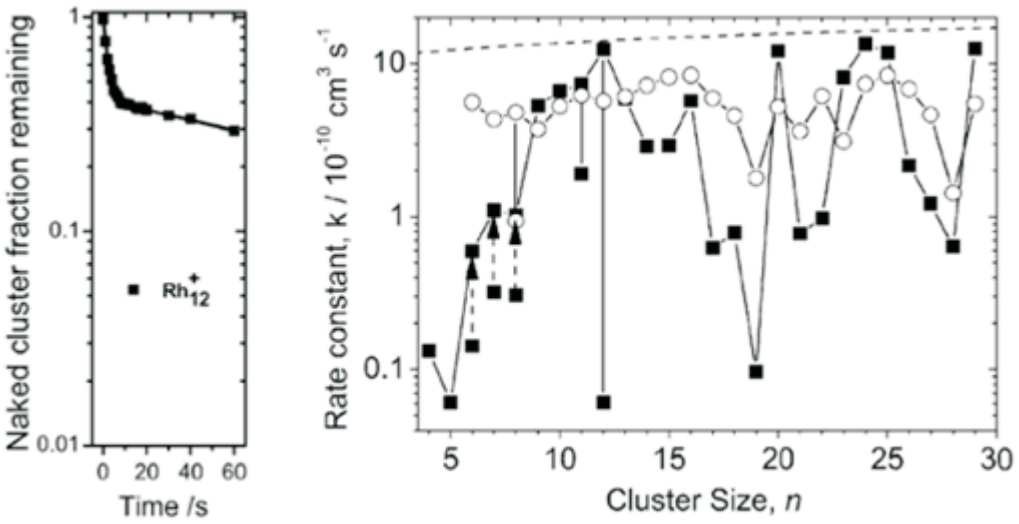

Figure 1.4 (Left) Biexponential kinetics in the reaction of Rh_{12}^+ with NO. (Right) Bimolecular rate constants for the reactions of rhodium cluster anions (○) and cations (■). Adapted from ref. [87] with permission from the PCCP Owner Societies.

number of factors. In one of the first FT-ICR reactivity studies on clusters, Smalley and coworkers studied the dissociative chemisorption of hydrogen on niobium clusters.[85,86] Their results showcase two important aspects of cluster reactivity: First, the strong size dependence of reactivity as a function of cluster size, with differences of up to five orders of magnitude in reaction rates for different sizes. Previous work by this group has observed similar, strong size dependence in the rates of reactions of rhodium anion and cation clusters with N_2O;[87] with certain cluster sizes being almost inert, while others are highly active (see right hand side of fig. 1.4). This effect has also been observed for a number of other reaction such as the dehydrogenation of methane on platinum clusters;[88] and methanol reactions on cobalt clusters.[89]

Our study of rhodium cluster reactivity also illustrates the the second typical aspect of cluster reactivity: for certain clusters sizes (*e.g.* Rh_{12}^+), the kinetics of the reaction are biexponential in nature (see left portion of fig. 1.4), which is interpreted as evidence for different structural isomers of differing reactivity being present in the experiment.

The presence of ligands also plays an important role in cluster reactivity,

exemplified by the dehydrogenation reaction of methane on rhodium clusters, which is found to increase when argon ligands are adsorbed to the cluster prior to the reaction.[90] In collision reactions, the complex formed by collision between a cluster and adsorbate is often stabilized by a redistribution of the interaction energy into internal cluster modes, which leads to an increase in the internal cluster temperature. This effect was studied by the Bondybey group using FT-ICR, finding that in general this temperature rise effect is lessened with increasing cluster size, on account of the increase in heat capacity.[91]

In searching for the origin of these effects it has become clear that reactivity is closely linked to both electronic and geometric structure. The reaction rate of tungsten clusters W_n experiences a sharp increase around $n = 15$, correlated with a structural transition from more closely packed to open structures.[92] The effect of charge and electronic structure on reactivity is not uniform: in coinage metals, electronic shell closings lead to odd-even alternation in reactivity with respect to oxygen[93,94] and Pt_4 clusters react very differently with CH_4 depending on charge.[95] However, the same coinage metal clusters show no such variation in the reaction with CO. Similarly, no effect of charge is observed for the attachment of CO to group 9 transition metal clusters or the reaction of H_2 with niobium.[86,96]

The reaction of copper clusters with O_2 and H_2O shows that in some cases there is a complex interplay of electronic and geometric effects: while cluster sizes associated with electronic shell closings turn out to be particularly unreactive, others associated with sizes one larger than icosahedrally closed structures are especially reactive.[97]

In conclusion, despite the effort directed at understanding the complex reactions of metal clusters, no coherent picture of their reactivity has emerged. There is hence still a significant scope for additional work to probe the various effects affecting cluster reactivity. Chapters 3 and 4 of this thesis are examples of such work.

1.4 Computational modelling

Common to many of the experimental techniques discussed above is the requirement for simulation either as part of data analysis or as a tool to aid in the understanding of trends and features observed in the results. As a consequence, there is a very active field of computational and theoretical investigation of transition metal clusters. This is also fuelled by the fact that transition metal clusters provide a challenging benchmark for computational methods and can thus help in the development or refinement of these methods.

Indeed, transition metal clusters are considered notoriously difficult on account of strong near-degeneracy correlation that results from partially filled *d*-shells. In general multireference techniques such as multi-reference configuration interaction (MRCI) or complete active space self-consistent field with second-order perturbation (CASPT2) are needed to obtain accurate wave functions in these cases. While these techniques have been successfully applied to a few (very small) model systems,[98,99] the dramatic scaling of computational cost with increasing cluster size n precludes their use for many problems of chemical interest. Hartree-Fock (HF) and Møller-Plesset (MP2) approaches scale more efficiently, but fail to correctly predict the ground states of many open shell transition metal atoms, which limits their use to special cases such as d^0 or d^{10} systems. Consequently, density functional theory (DFT) has become the *de facto* standard for computational chemistry on transition metal clusters. DFT is discussed in some detail in the next chapter (section 2.6), but the basic idea is to obtain from the total electron density the total electronic energy.

The prediction of metal cluster structure and other properties on the basis of DFT is a very expansive area of research covering a wide range of systems (see the review of Cramer and Truhlar[10]), but DFT has also been used as an auxiliary in the analysis of diffraction patterns,[43] ion mobility experiments,[35] infrared[100,101] and photoelectron spectra.[102] However, DFT provides additional information — for example, the spin multiplicities of the electronic ground states of rhodium clusters led to the prediction of superparmagnetism[103] which was later confirmed experimentally.[69] The large magnetic moments of small transition metal clusters

have remained at the centre of a large number of theoretical investigations into the cluster structure, in particular on the rhodium system. Reddy and coworkers were the first to provide a systematic theoretical investigation of rhodium clusters in the size range in which large magnetic moments were observed.[104] Their work linked the observed variation in magnetic moments to the calculated electronic structure, but overestimated the value of the magnetic moments. In view of the scarce experimental data on rhodium clusters (outside knowledge of their magnetic moment) work has therefore continued on this system, with a variety of electronic and geometric structures proposed by several authors to explain the phenomena.[104–107] Only recently has the measurement of vibrational spectra of transition metal clusters such as rhodium[47,48] and platinum[108] provided for a more stringent test of computational predictions, leading to more solidly grounded assignement of the geometric structures of the clusters.

The time dependent version of DFT (TD-DFT) is used for calculations involving excited electronic states, for example in the analysis of electronic photoabsorption spectra. Kappes and coworkers used this method to determine that the structural transition of gold clusters from two- to three-dimensional occurs between $n = 7$ and $n = 8$.[109] The effect of silver nanoparticles on the UV/vis spectra of thiols has been studied by Harb *et al.*, finding evidence of charge transfer reactions.[110]

A further application of DFT is in the search for saddle points on the potential energy landscape since saddle points connecting particular minima on the potential energy landscape represent the transition states for the transformation between those minima. This allowed Harding *et al.* to find the transition states for the reaction of NO with Rh_6^+, rationalizing the observed reaction rates.[111]

1.5 Thesis outline

The next chapter will introduce both experimental and computational methods and concepts employed throughout this work, summarising the salient aspects of each technique.

Chapters 3 and 4 present IR-MPD studies of small transition metal clusters *via* IR-MPD. In chapter 3, we show a study of the small cationic rhodium clusters Rh_n^+

($n = 4 - 8$) with coadsorbed nitrous oxide (N_2O) and oxygen in the region of the N_2O bending vibration ($505 - 685\,cm^{-1}$). The trends in the N_2O band with size and coadsorbates are analyzed. In addition, IR-MPD is utilized as a mechanism to heat clusters, driving the decomposition of N_2O on $Rh_nO_m^+$ ($n = 4 - 8$, $m = 0 - 2$), which reveals that both cluster size and presence of O have a significant impact on the reactivity of the clusters. The drastic effect of oxygen on the reactivity of the Rh_5^+ cluster is investigated by DFT calculations, which indicate that the cooperative binding of oxygen is key in enabling reactivity. The rhodium work has been published in the Journal of Physical Chemistry Letters.[82]

Chapter 4 shows a study of small platinum clusters $Pt_nO_m^+$ ($n = 3-7$, $m = 0, 2, 4$) decorated with oxygen and carbon monoxide. Ar-loss IR-MPD is employed to probe the structure of the clusters, finding evidence of both dissociatively and molecularly adsorbed oxygen on the cluster surface. In addition, the CO band is spectrally analysed, revealing wavelength shifts both as a function of cluster size and oxygen coverage. These results are interpreted in the context of a simple backbonding model. As a second step, IR-MPD is once more utilized as a probe of reaction to study the oxidation of CO on the platinum cluster surface. Efficient oxidation is observed for all clusters, demonstrating that this use of IR-MPD is a general tool to study a diverse range of reactions. The work has also been published in the Faraday Discussions.[83]

Chapters 5 and 6 present work done on our local VMI setup equipped with a laser ablation source for the purpose of studying the photolysis dynamics of small metal and metal-containing clusters. In chapter 5 we report on the photodissociation of Ta_2 in the visible range ($23\,500 - 24\,000\,cm^{-1}$). The images show that the photodissociation proceeds by a three-photon ionization followed by a two-photon photodissociation. A range of exit channels are observed, with channels correlating with ground state products being favoured. We obtain a significantly more tightly defined value for the dissociation energy of Ta_2^+ than has been previously observed, in good agreement with computational predictions.

In a similar vein, chapter 6 deals with the electronic spectroscopy and photodissociation dynamics of the copper dimer Cu_2 in the ultraviolet ($36\,000 - 38\,200\,cm^{-1}$). Resonant excitation of Cu_2 leads to significant fragmentation that

can be ascribed to a combination of direct dissociation of Cu_2^+ and the dissociation of doubly excited Cu_2^{**} states above the ionization threshold. Fits of the TKER spectra of Cu^+ to predicted dissociation thresholds determine values for the dissociation energies of both Cu_2 and Cu_2^+. In addition, the production of Cu_2^+ fragments with non-zero kinetic energy is interpreted as evidence for Cu_3 photodissociation and yields a new estimate for the trimer dissociation energy. The Cu study has been published in Physical Chemistry Chemical Physics.[112]

CHAPTER 2

Methods

This chapter will introduce the key concepts and techniques used in this work, some of which was carried out in Oxford and some at the FELIX facility (see section 2.3.4) in the Netherlands.

2.1 Oxford cluster source

As explained in section 1.2, several methods have been used over the years to generate metal clusters. We employ a Bondybey / Smalley type pulsed laser ablation source.[113,114] A schematic outline is shown in fig. 2.1.

To generate clusters, pulsed laser light at 532 nm, from a frequency doubled Nd:YAG laser (Litron NanoLite, typically 20 mJ per pulse), is focussed by a 30 cm focal length bi-convex lens onto the target. The target consists of a 1 cm diameter, 0.1 mm thick disc of the metal to be studied glued on a stainless steel mount using thermal silver adhesive. The mount is continuously rotated to avoid drilling a hole into the target. A second motor allows translation of the target along the direction of the molecular beam so that the whole surface of the disc can be used.

The incidence of the laser on the metal surface generates a plasma of metal ions which expand into the cluster channel. The laser pulse is synchronized with an intense pulse of gas generated by the pulsed valve (for Ta experiments: a

Parker-Hannifin General Valve, for Cu a pulsed supersonic valve by Jordan) which cools the plasma and carries it through the cluster channel. The cluster channel (18 mm length, 3 mm diameter) confines the gas expansion and promotes the three-body collisions required for cluster growth. The cluster atoms and ions thus formed travel downstream for approximately 60 mm where they pass through a 1 mm diameter skimmer (Beam Dynamics) and can studied by the techniques detailed in the rest of this chapter.

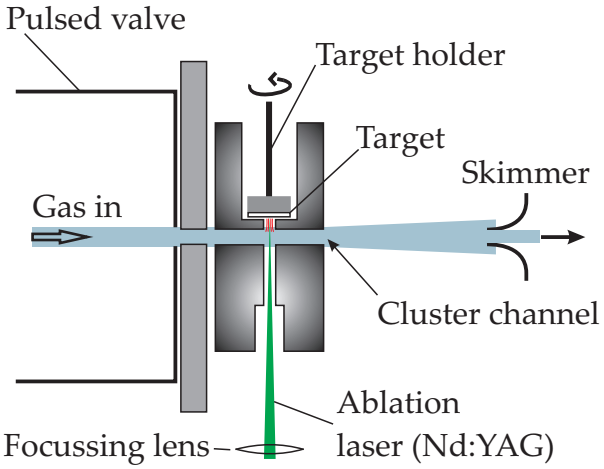

Figure 2.1 Schematic representation of the Oxford cluster source.

2.2 Time-of-flight mass spectrometry

Mass spectrometry is an essential tool in any cluster study, both for the characterization of the species produced by one's cluster source as well as for its use as a detection method in action spectroscopy.

Time-of-flight mass spectrometry (Tof-MS) is a widely used variant that has a number of distinct advantages for cluster work. In particular the speed at which one can collect Tof-MS spectra alleviates the stability issue that plagues even the best cluster sources. In combination with the fact that one collects all masses simultaneously this means that full Tof-MS spectra can be recorded at high repetition rates, an essential component in obtaining *e.g.* good quality action

spectra.

The principle employed by time-of-flight mass spectrometry is simple: ions of charge q are accelerated by an electric field $\mathbf{E}$ through a displacement $\mathbf{s}$, converting their potential energy into kinetic energy (KE) and thus

$$\begin{aligned} \mathrm{KE} &= q\mathbf{s}\cdot\mathbf{E} \\ \frac{1}{2}mv^2 &= q\mathbf{s}\cdot\mathbf{E} \\ v &= \sqrt{\frac{2q\mathbf{s}\cdot\mathbf{E}}{m}}\,, \end{aligned} \tag{2.1}$$

where v is the ion speed and m their mass. Particles with different mass to charge ratio $\frac{m}{q}$ will thus spread out in time as they travel towards the detector — in fact, it can be shown,[115] that the time of flight is proportional to the square root of this ratio. Hence, the time of flight can be used as a measure of an ions mass to charge ratio. In practice, therefore, the mass is calculated from the time of flight t by fitting to the expression

$$t = A\sqrt{m} + c\,, \tag{2.2}$$

where A and c are fit parameters.

In a real experiments ions are generated over a finite volume of space, *e.g.* the size of a molecular beam. Different spatial positions mean that the ions of the same $\frac{m}{q}$ will be accelerated for different amounts of time by the electric field — ions that were initially furthest from the detector spend the longest time in the electric field and thus have the largest velocities. At some point in space after the acceleration, called the *space focus*, the ions that initially started furthest from the detector will overtake the ions that initially started closer. If the detector is not placed at the space focus, the resulting time distribution will be broadened. However, in a simple acceleration optic with only two plates, this space focus is very close to the accelerating plates (twice the plate separation from the final plate). In their seminal paper Wiley and Mclaren found that a much improved resolution can be obtained by introducing a second electric field which allows the space focus position to be tuned.[115] The Wiley design has the added benefit

of requiring much lower pulsed voltages and being more widely tuneable. Both time-of-flight spectrometers used throughout this work are based on this design.

2.3 IR-MPD spectroscopy

2.3.1 Background

Several indirect or *action* spectroscopic techniques have been developed on the basis of mass spectrometry to address the issue of low number densities of clusters produced by typical sources such as the one described in section 2.1.[116–118] The infrared spectra in this work are collected using the variant known as infrared multiple photon depletion (IR-MPD) spectroscopy,[100] including, in some cases, using inert gas tagging.

2.3.2 Outline of the technique

In IR-MPD, a molecule absorbs several photons of a resonant wavelength until its internal energy lies above its dissociation threshold, so that it fragments. In the mass spectrum, this manifests as a decrease in its signal intensity, while the signal of any species produced in the fragmentation is boosted. This process is illustrated in figs. 2.2 and 2.3. Monitoring the difference between mass spectra recorded in the presence and absence of infrared radiation will thus produce a spectrum where the resonances of a species are marked by a depletion in its signal.

Given the large number of far-IR photons needed to dissociate even loosely bound species[119] it is clear that their absorption cannot solely consist in the resonant climbing of the vibrational potential — the anharmonicity of the potential means that any single photon wavelength can be resonant or near-resonant with only a very small number of transitions (see fig. 2.4a). The IR-MPD process can be described as an initial resonant absorption of IR photons which is followed by rapid internal vibrational redistribution of energy (IVR) to one of the many other vibrational modes.[118,120] The IVR completes prior to the absorption of subsequent photons, which means that the molecule is fully on resonance with each incident

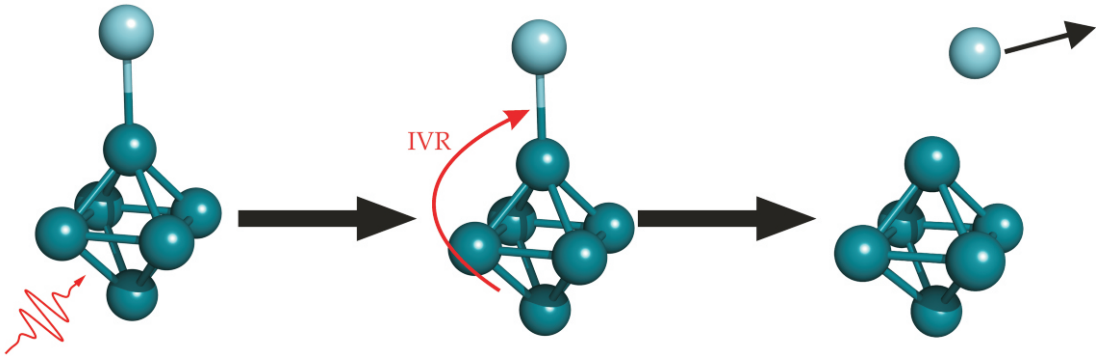

Figure 2.2 Illustration of the IR-MPD process using the example of Rh_6Ar. The Rh_6Ar cluster absorbs one or more infrared photons whose energy is rapidly redistributed by IVR. This process repeats until enough energy accumulates in the Rh_6–Ar bond to overcome the binding energy, resulting in desorption of Ar.

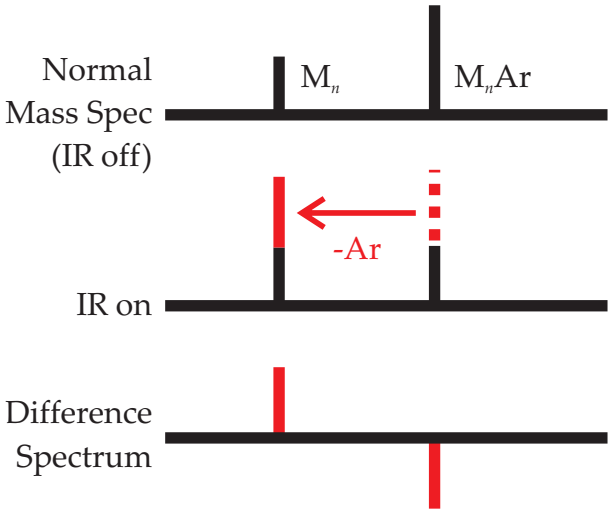

Figure 2.3 Illustration of the effect of IR-MPD on schematic mass spectra. The argon tagged cluster M_nAr dissociates upon irradiation with resonant IR light, decreasing the M_nAr intensity in favour of M_n.

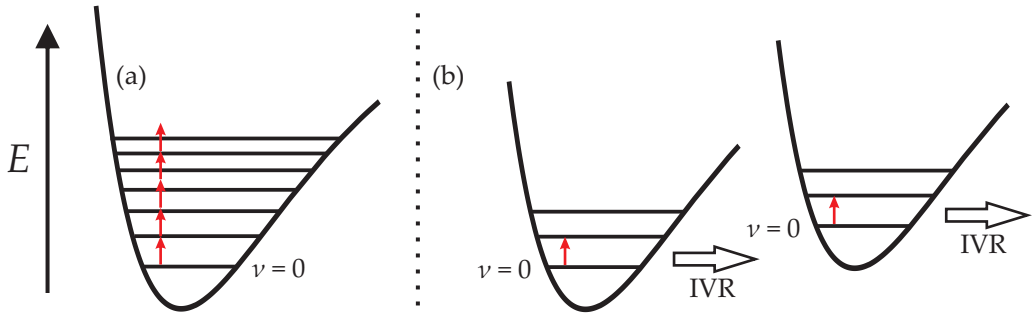

Figure 2.4 (a) Anharmonic quenching of multiple resonant absorption of photons. (b) Resonant absorption of photons followed by IVR redistributing the energy into the other cluster modes. The IVR completes before the incidence of the next photon, so that the the system is fully on resonance with subsequent photons.

photon (see fig. 2.4b), and this makes the IR-MPD a very efficient means of imparting energy to a cluster. The pulse structure of free electron lasers (see section 2.3.4), with several micro pulses in short succession, is ideally suited for this kind of process as the IVR completes in between each micro pulse of the FEL, so that each micro pulse is on resonance.

2.3.3 Infrared tags

Messenger technique

An implicit requirement of IR-MPD is that a system to be studied must contain at least one vibrational mode that has a large infrared crossection, so that the resonant step can occur efficiently. However, vibrational modes of bare metal clusters have very small infrared crossections, on account of their non polar nature. In addition, they usually lie in the far infrared ($50 - 500\,\mathrm{cm}^{-1}$), which means that a very large number of photons would be needed to cross typical metal cluster dissociation barriers (*e.g.* 2 – 4 eV for Cu_n clusters[121]).

As a result, the IR spectroscopy of bare clusters is usually done *via* the inert *messenger* technique,[122,123] which involves the coadsorption of a weakly bound *messenger* molecule such as Ar onto the target complex. The messenger molecule is bound sufficiently weakly as not to perturb the underlying structure and may

also provide for an increased infrared absorption crossection.[124] IR-MPD spectra of the metal cluster can then be obtained by monitoring the loss of the weakly bound species. The schematics of figs. 2.2 and 2.3 are examples of this.

Other tags

In some cases, a system to be studied already has both a sufficiently low dissociation energy and a strong chromophore. Such is the case for the CO complexes of transition metal clusters, *e.g.* $Pt_n(CO)$ clusters — CO strongly absorbs infra-red photons in the range 1900 – 2100 cm^{-1} and is typically bound sufficiently weakly (< 1 eV) to be dissociated with only a small number (≤ 5) of photons. Thus, the CO absorption region of such complexes is easily studied by monitoring the loss of CO.

Infra-red induced reactivity

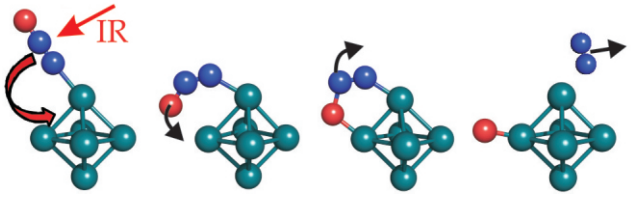

Figure 2.5 N_2O dissociation reaction triggered on the surface of a Rh_6^+ cluster by IR-MPD. The absorption of infrared light triggers the dissociation of N_2O, followed by desorption of N_2, which provides the mass spectroscopic signature for the reaction.

This group has developed the IR-MPD technique for the study of cluster surface chemistry, wherein the infra-red chromophore used on a cluster is a species that can undergo a reaction with a low enough reaction barrier (a few eV or less). In these cases the energy provided by the IR-MPD process can trigger the reaction directly on the surface of the cluster itself. If the reaction is accompanied by a mass change, *e.g.* as a result of one of the products desorbing from the cluster surface, then the reaction can be detected by IR-MPD. This application of IR-MPD has great potential for *e.g.* probing the size dependent reactivity of clusters,[7] and in this work, IR-MPD is mainly used in this fashion — see chapters 3 and 4.

An example is shown in fig. 2.5. In this case the N_2O molecule is the reactive chromophore, and absorption of infrared photons *via* any of the N_2O modes leads to the dissociation of N_2O to form N_2 and a cluster oxide. The subsequent desorption of N_2 provides the mass spectrometric signature needed to detect the reactivity.

2.3.4 Free electron lasers

In order to effectively trigger multiple photon processes such as IR-MPD, an intense source of infrared radiation is needed. Ordinary table-top laser systems typically do not provide sufficient photon fluence at the infrared wavelengths needed for cluster study, although the recently developed infrared optical parametric oscillators can compete in the mid infrared region.

Free electron lasers (FELs) on the other hand can provide very intense radiation over a wide range of wavelengths, particularly in the infrared. In addition, their macro-micro pulse structure is ideally suited for the IR-MPD technique (see section 2.3.2). The main drawbacks is that these require research facilities of a national scale, which are not always readily available.

The operation of FELs, as well as the particular FEL we used (the Free Electron Laser for Infrared eXperiments, FELIX), are described below.

Principle of Operation

In a free electron laser, electrons are generated by an electron gun at near-relativistic speeds and injected into a periodic magnetic structure called an undulator (see fig. 2.6). The alternating poles in the oscillator force the electrons to take a sinusoidal trajectory, and the accompanying acceleration leads to the spontaneous emission of synchrotron radiation.

This spontaneous radiation is incoherent and weak. To make use of this effect as a light source, the spontaneous radiation is captured in an optical cavity by means of enclosing mirrors. The field generated by the trapped radiation in the cavity causes further injected electrons to radiate coherently with the radiation already stored, resulting in a build up of power. A small fraction of the laser light

can then be coupled out of the cavity, *e.g.* by means of a centre hole in the output mirror.

The wavelength generated depends on the electron energy, the strength of the magnetic field and the spacing between the undulator magnets. In practice, short-range tuning is done *via* the undulator spacing, while the electron beam energy is adjusted only for larger changes in wavelength.

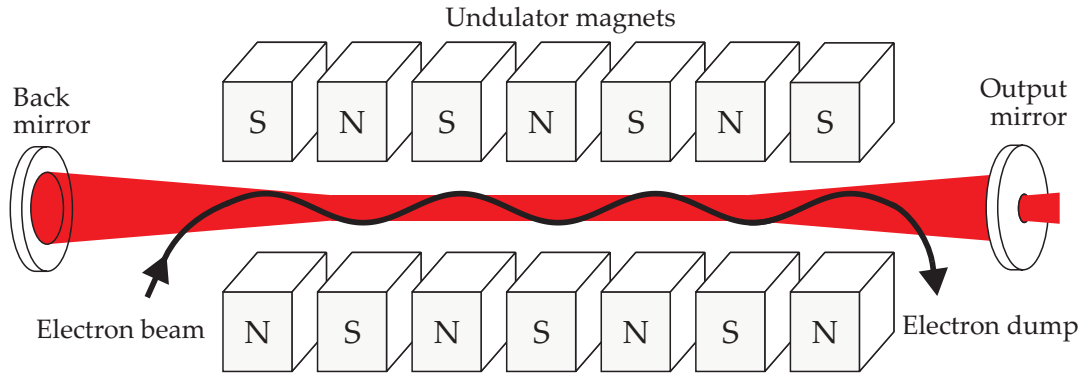

Figure 2.6 Schematic illustration of free electron laser light generation.

FELIX

The work using infrared radiation described in chapters 3 and 4 was carried out at the FELIX (Free Electron Laser for Infrared eXperiments) facility in The Netherlands.[125] The facility is currently being moved from its original location in Nieuwegein and being rebuilt at Nijmegen University. All of our work was carried out during experimental runs in December 2009 and January 2011 using the original incarnation, depicted in fig. 2.7 and described below.

At FELIX, 3.8 MeV electrons are generated by an electron gun and accelerated by two linear accelerators (linacs), which accelerate the electrons to 15 – 25 MeV and 25 – 45 MeV respectively. After each linac the electron beam can be bent towards one of two FELs, called FEL1 and FEL2, which provide radiation in the range 16 – 250 µm and 5 – 40 µm respectively.

The time-structure of the IR beam generated by FELIX is a reflection of the time structure of the electron beam. The rf-accelerator technology used means

that the IR beam is made up of 5 µs long *macro pulses*. These, in turn, consist of a train of *micro pulses* of width between 300 fs and a few ps, spaced by a few nanoseconds. Their width is the limiting factor in determining the bandwidth of the IR beam, which results in a spectral width of 0.3 – 1 % around the central wavelength.

For the experiments described herein, FELIX was used in a duty cycle of 5 Hz and with a macropulse energy of a few mJ.

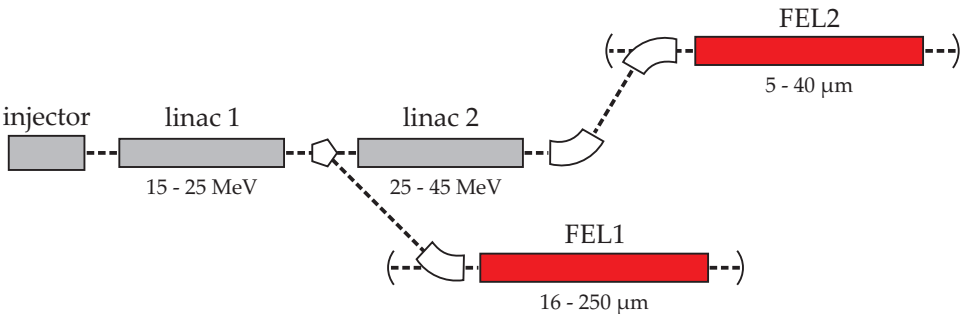

Figure 2.7 Schematic view of the Free Electron Laser for Infrared eXperiments FELIX, made after ref [118].

2.3.5 Apparatus and procedure

All of the IR-MPD work presented here was carried out in collaboration with the Meijer group (FHI Berlin) on their experimental apparatus on-site at FELIX, shown in fig. 2.8.

Clusters are generated *via* pulsed (10 Hz) laser ablation of a rotating metal rod by the frequency doubled (532 nm) output of a Nd:YAG laser. An intense gas pulse of pure helium entrains the resulting plasma. As the gas pulse travels down the length of the clustering channel (held at ambient temperature) neutral and ionic clusters are formed. The late-mixing valves seed the reactant gas(es) directly into the reaction channel, whose relative pressures are adjusted to produce the clusters of interest. For rare gas tagging, the cluster channel can be cooled with liquid nitrogen to enhance cluster-rare gas complex formation.

The resultant cluster distribution passes through a 2 mm diameter skimmer

and a 1 mm aperture into the extraction region of a reflectron time-of-flight spectrometer. The infrared FELIX beam is loosely focused on the aperture and synchronised with the gas pulse, ensuring good spatial and temporal overlap. In the work shown, the reflectron electrodes are poled positive, and we therefore extract only cationic species.

The experiment is run on a 10 Hz duty cycle, with the FELIX beam present on alternate shots. We thus obtain "on" and "off" mass spectra, and from these a difference mass spectrum is constructed. The difference between "on" and "off", tracked as a function of wavelength, yields the IR-MPD spectrum.

Before each experimental run, a calibration curve is recorded by measuring the putative FELIX wavelength against the value recorded by a spectral analyser. Our data is then corrected using this calibration.

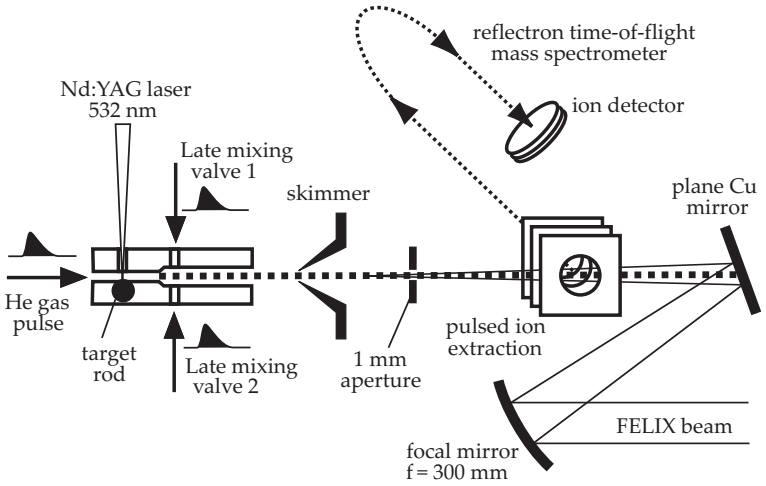

Figure 2.8 Experimental setup used for IR-MPD work at FELIX.

2.4 ToF action spectroscopy

The use of mass spectrometry as a sensitive detection method to measure the spectra of metal clusters is, of course, not limited to the infrared region. The availability of bench-top visible and ultraviolet laser sources mean that UV and visible spectroscopy of a kind similar to the one described in section 2.3 can be

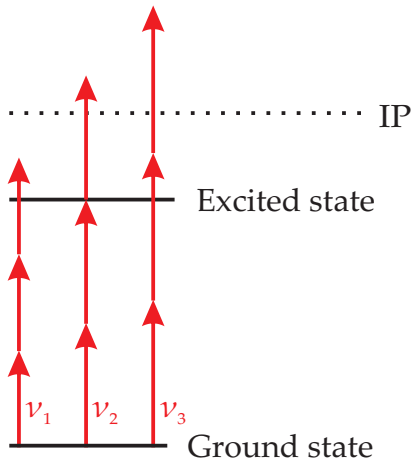

Figure 2.9 Exemplary REMPI scheme. Only photons of wavelength ν_2 have the correct energy to resonance enhance the ionization process.

carried out in research laboratories, without the need for a national facility like FELIX.

It is worth noting that the higher photon energies of ultraviolet and visible photons mean that only a few photons need generally be absorbed to trigger a process which leads to a change in the observed signal intensity, and thus a spectrum. As a result, these processes can generally occur coherently, in contrast with IR-MPD.

This section describes the apparatus employed, as well as the types of processes that can be studied with it.

2.4.1 Background

Resonant Multi-Photon Ionization

Perhaps the most straightforward process that can lead to an enhancement in the intensity of the a mass peak is an increase in its ionization efficiency by a resonantly enhanced multi-photon ionization (REMPI). Spectroscopy *via* REMPI has a long tradition,[126] so we will limit ourself to a brief description that captures the essence of what is needed to understand the data.

REMPI spectroscopy makes use of the fact that probability of a multi-photon

excitation can be greatly enhanced if there is a real excited state of the neutral molecule resonant at the energy of one or several absorbed photons.

An idealized example of this is shown in fig. 2.9. Here, the system is resonant with photons of wavelength ν_2 at the 2-photon level. If this transition has a non-zero transition probability and the intermediate state is sufficiently long-lived then the subsequent (one-photon) ionization step has a greatly increased probability compared to wavelengths ν_1 and ν_3, which are not resonant.

As a result, the yield of ions is greatly increased at wavelength ν_2, which manifests in the mass spectrum, and thus the action spectrum.

Fragmentation

The fragmentation of a species as a result of irradiation may lead to both enhancement in fragment signal and a depletion of the parent signal in exactly the same way as described for the IR-MPD technique in section 2.3.2. In contrast with IR-MPD however, the higher photon energies employed here mean that generally only a few photons are required to overcome typical dissociation barriers of dimers and clusters, and hence the processes may be of coherent nature.

2.4.2 Apparatus and procedure

The experimental setup used for time-of-flight mass spectroscopy and action spectroscopy is depicted in fig. 2.10.

The electrode arrangement used is optimized for Velocity Map Imaging(see section 2.5), not time-of-flight mass spectroscopy. However, the same electrodes can also be used for time-of-flight measurements: by choosing appropriate voltages the ions are sufficiently space focussed to achieve a mass resolution of $\frac{m}{\Delta m} > 350$, which is more than acceptable for our purposes.

For detection, the current of an anode coupled to a chevron arrangement of MCPs (Photonis) is measured *via* a digital oscilloscope (Lecroy) and read out using custom built LabVIEW software.

To record a time-of-flight mass spectrum, clusters are first generated by the ablation source described in section 2.1. The beam of clusters is then skimmed

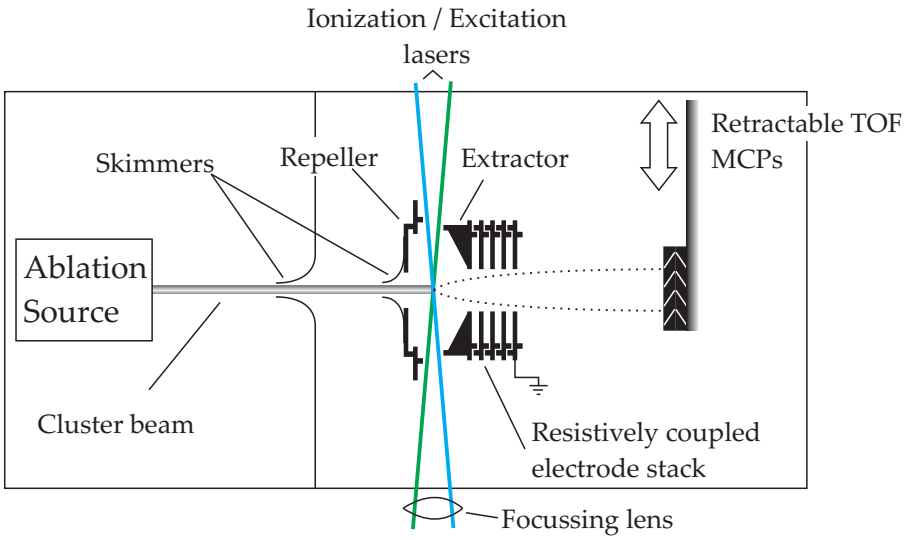

Figure 2.10 Schematic representation of the apparatus used for time-of-flight / action spectroscopy. Turbomolecular pumps maintain vacuum, but are omitted in this schematic for clarity.

(Beam Dynamic skimmer, 1 mm) and enters the interaction region, where the clusters pass a secondary skimmer (4 mm diameter) and are ionized. The ions formed are accelerated towards the detector by the ion optics.

Action spectra are recorded by introducing a second laser into the interaction region which provides excitation of the cationic clusters. The spectrum of each species is then obtained by monitoring the ion signal in the time-of-flight mass spectrum as a function of the wavelength of the excitation laser. Our arrangement allows for the recording of the full mass spectrum at each wavelength, thereby recording the action spectra of all mass channels simultaneously. This task is performed by custom written LabVIEW code.

2.5 Velocity map imaging

2.5.1 Introduction

In the study of photodissociation, the measurement of product velocity distributions, and thus their kinetic energies, is of central importance. To measure the recoil velocity, both shifts in time of flight[127] as well as (Doppler) shifts in absorption frequency[128] have been successfully employed. More recently, imaging methods have come to the forefront for these sorts of studies, on account of their versatility and power, as showcased in a recent review.[129] In these methods, the three-dimensional fragment spheres are mapped onto a two-dimensional image. Both the recoil velocity and angular distribution can then be recovered directly from the spatial distribution of intensity of the images, without the need to analyze time of flight profiles or Doppler shifts.

Chandler *et al.*[130] were the first to demonstrate the power of such techniques. In their ion imaging study of the photodissociation of the CH_3I molecule, they were able to distinguish between two possible product states of iodine by inspecting the image radii, which are directly related to the velocities of the fragments, and thus to the kinetic energies of the fragments.

The technique has since been improved considerably, *e.g.* by moving from a grid electrode to a three-plate setup.[131] This form of the method became known as *velocity map imaging*, and the significant improvement in resolution brought by this widened the applicability of the technique considerably. In addition, much work has gone into refining the analysis and processing of the 2D projections.[132]

Imaging photodissociation

Let us consider a general photodissociation experiment producing a fragment to be studied F and its cofragment C. Each combination of quantum states that F and C are produced in will result in F and C being produced with different recoil velocities (fig. 2.11). Thus, starting from the point at which they dissociate, the fragments will expand in a series of nested spheres, called Newton spheres. In an imaging experiment, we observe the 2D projection of the spheres of F

on our detector. One of the difficulties with this lies in the fact that in most photodissociation experiments F and C are created over a volume that is large compared to the size of most 2D detectors, which results in significant blurring of the images.

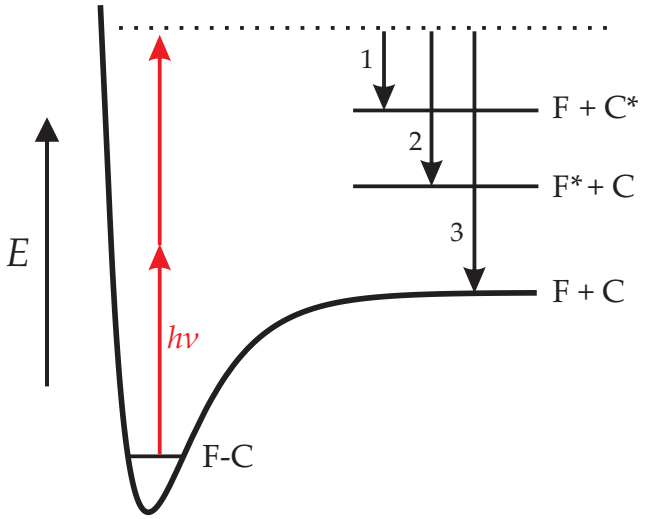

Figure 2.11 Schematic representation of a general photodissociation of a species F-C into a fragment F and its cofragment C. Different combinations of product quantum states lead to different product kinetic energies (1-3) and thus different recoil velocities.

Fortunately, this problem was addressed by the advent of ionic Velocity Map Imaging (VMI).[131] Using a set of electrodes with suitably chosen voltages, ions with the same initial *velocity* vector but different source positions can be mapped to the same point in the focal plane. The method can be directly applied to ions, whereas neutral fragments must be ionised first.

With this mapping in place, the next question that arises is how to go from the 2D image that is recorded to the 3D distribution that contains the desired information. Some experimental setups involving electrostatic "slicing" of the fragment distribution[133–135] obviate the need for this processing, as the central slice through the Newton sphere can be directly used to obtain the 3D distribution. However, this method carries a significant penalty in signal intensity as only a small fraction of the full sphere of photofragments is retained. If the signal intensity is not sufficient, as is the case for transition metal clusters, the full

Newton sphere is flattened onto the detector, and must be deconvoluted.

Image deconvolution

The deconvolution of the image and reconstruction of the 3D distribution can be performed analytically in the case of systems that have cylindrical symmetry using the Abel transform.[136] Careful alignment of pump and probe laser allows the Abel method to also be used in other cases,[137] but this is not always practical. Several forward projection techniques, based on a comparison between a convoluted trial distribution and the experimental image, have been developed as a result.[132]

One of the most popular approaches, BASEX, involves the projection of several ideal gaussian functions, which are linearly combined to fit the experimental image.[138] The 3D distribution can hence be regenerated from the superposition of the gaussian functions. It has been extended[139] to use polar basis functions which allows the reconstruction of the angular distribution and limits the line noise generated in most other methods to the centre of the image.

Another successful method is the so-called onion-peeling method[140]: here, the virtual slice is recovered by progressively removing contributions from the outside of the slice plane starting from the outermost radius. Once again, error accumulation can be mitigated by employing polar coordinates.[141] This work employs the most recent formulation[142] of polar onion peeling (POP), which incorporates the basis set concepts of BASEX to accelerate POP.

2.5.2 Theoretical basis

The principle of Polar Onion Peeling

Consider a 3D radial distribution $F(r,\theta,\phi)$ that is cylindrically symmetric about the z-axis, with a 2D projection $G(R,\alpha)$ (see fig. 2.12). The total projection $G(R,\alpha)$ can be written as a sum

$$\int_0^{r_{\max}} g(r;R,\alpha)\,dr$$

where $g(r;R,\alpha)$ is the portion of the $F(r,\theta,\phi)$ projection at one particular radius r only ($R \leq r$).

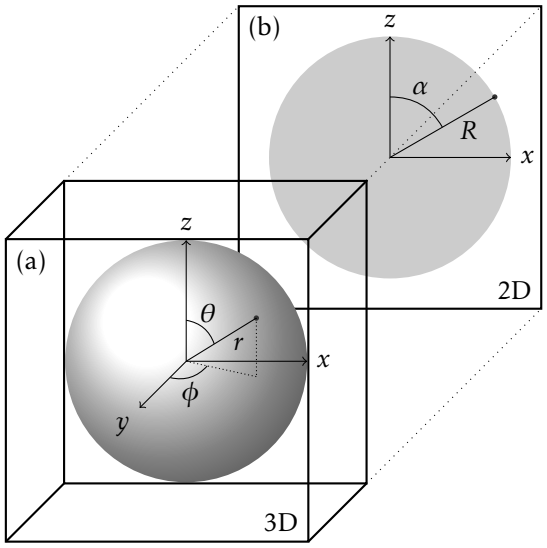

Figure 2.12 (a) 3D Newton sphere of photofragments $F(r,\theta,\phi)$, exhibiting cylindrical symmetry about the laser polarization axis (z-axis). (b) Measured 2D distribution $G(R,\alpha)$ generated by mapping $F(r,\theta,\phi)$ onto the 2D xz-plane, parallel to the z-axis. Made after ref. [142].

If we assume that there is no signal at radii larger than our detector, then at the outermost radius $R = r_{\max}$ our projected image $G(R,\alpha)$ only has a contribution from the central slice through the full distribution, *i.e.* $F(r_{\max},\theta,\phi = 90)$. Labelling this slice as $h(r_{\max},\theta)$, we can then make the identification

$$h(r_{\max},\theta) = g(r_{\max};R,\alpha)\,,$$

for $R = r_{\max}$.

The next step in the procedure is to perform a linear fit to the well known angular distribution[143,144] for photofragments

$$h(r_{\max},\theta) = I(r_{\max})\sum_n \beta_n(r_{\max})P_n[\cos(\theta)] \quad (n \text{ even}) \tag{2.3}$$

where P_n is the legendre polynomial of order n, I the intensity factor and β_n are the anisotropy parameters. The integer n is determined by the physics of the process.

With these parameters we now simulate a new 3D distribution at $r = r_{\max}$. We

can then subtract the projection of this simulation, $g_{\text{fit}}(r_{\text{max}}; R, \alpha)$, from our full image

$$G'(R, \alpha) = G(R, \alpha) - g_{\text{fit}}(r_{\text{max}}; R, \alpha)$$

at each radius R. Thus $G'(R, \alpha)$ is now a modified image that has had the effect of the outermost part of the Newton sphere "peeled off".

The above process is then repeated, using $G'(R, \alpha)$ in place of $G(R, \alpha)$, for $r = r_{\text{max}} - dr$ until $r = 0$ is reached. At this point $G'(R, \alpha)$ contains the residuals of the fits in eq. (2.3), while the the sum of the $h(r, \theta)$ at each radius r gives the desired reconstructed 2D slice.

In the implementation here employed,[142] the construction of the projection $g_{\text{fit}}(r_{\text{max}}; R, \alpha)$ from the fit parameters I and β_n is accelerated by the use of a series of basis functions, but the principle of the procedure remains the same. An example of image deconvolution with the POP method is given in fig. 2.13.

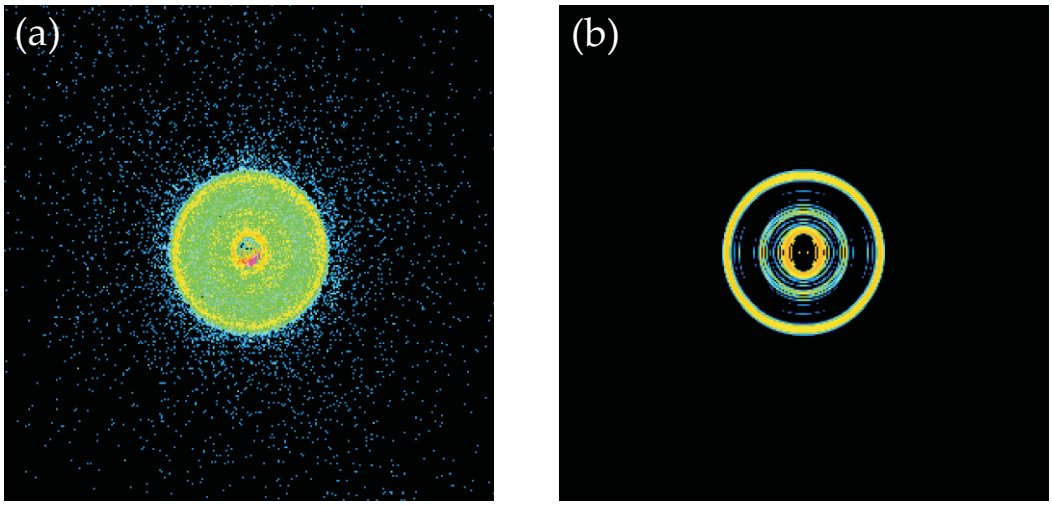

Figure 2.13 (a) Raw velocity map image of Ta^+ ions produced by photodissociation of Ta_2^+. (b) Deconvolution of image (a) by the polar onion peeling method. Three distinct rings become apparent, indicating the production of Ta^+ with three distinct kinetic energies.

2.5.3 Application

From image to internal energies

Having reconstructed a central slice through the real 3D distribution we are now in a position to recover the desired information. A series of particles with transverse speed v (parallel to the image plane) will produce a ring feature in our reconstructed slice. The radius r of this ring determines the speed *via*

$$v = \frac{r}{N \times t}$$

where t is the time of flight. N is an instrument specific *magnification factor* that accounts for the electrostatic lensing of the electrode setup. It is readily determined by simulation or measurement on a known system.

In a molecular beam experiment, the transverse speed of the particles in the molecular beam is negligible. Therefore, the transverse velocity that we measure can be solely ascribed to energy gained as a result of the photodissociation. Thus, if we consider the dissociation of a system F–C into fragments F and C, the kinetic energy released (KER) for each fragment is equal to the transverse kinetic energy we measure. Hence, if we observe particle F with transverse speed v_F and mass m_F, its KER is

$$\mathrm{KER}_\mathrm{F} = \frac{1}{2} m_\mathrm{F} v_\mathrm{F}^2 \,. \tag{2.4}$$

However, of interest is the total kinetic energy released (TKER) in the photodissociation, *i.e.* the sum of KER_F and KER_C. As we cannot detect the KER of the C particles that are formed in coincidence with F we cannot obtain their KER in the same way. But momentum must be conserved, and, since the initial transverse momentum is negligible, we have, for fragments C and F travelling in opposite directions,

$$\begin{aligned} m_\mathrm{C} v_\mathrm{C} &= m_\mathrm{F} v_\mathrm{F} \\ \Leftrightarrow v_\mathrm{C} &= \frac{m_\mathrm{F} v_\mathrm{F}}{m_\mathrm{C}} \,. \end{aligned} \tag{2.5}$$

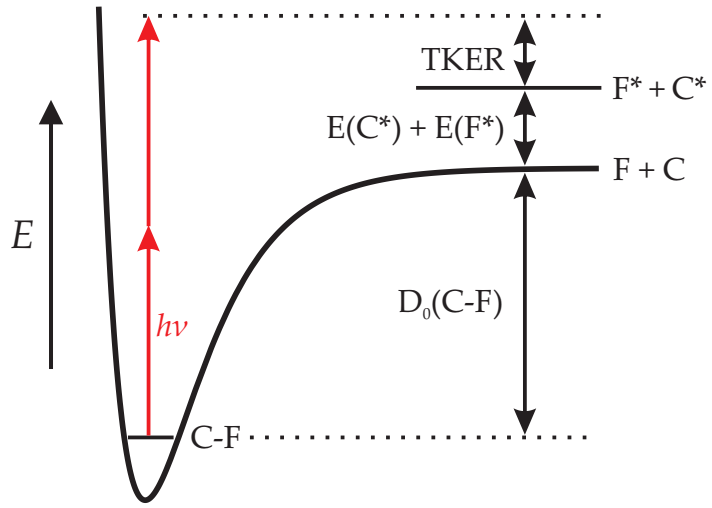

Figure 2.14 Schematic photodissociation of a species F–C at the two-photon level, forming excited state products F* and C*.

where m_C and v_C refer to C's mass and speed, respectively. Using eq. (2.5) we can calculate the TKER from known quantities:

$$\begin{aligned} \mathrm{TKER} &= \mathrm{KER_C} + \mathrm{KER_F} \\ &= \frac{1}{2} m_C v_C^2 + \frac{1}{2} m_F v_F^2 \\ &= \frac{1}{2}\left(m_C \frac{m_F v_F^2}{m_C^2} + m_F v_F^2 \right) \\ &= \mathrm{KER_F}\left(1 + \frac{m_F}{m_C} \right). \end{aligned} \tag{2.6}$$

The photodissociation of C–F by n photons of energy $h\nu$ (h is Planck's constant) into fragments C and F can be written as

$$\mathrm{C{-}F} + n \times h\nu \longrightarrow \mathrm{C^*} + \mathrm{F^*}\,. \tag{2.7}$$

where C* and F* are electronic states of the products C and F which will in general not be the ground states.

Balancing the energies on each side of this equation yields (see fig. 2.14)

$$n \times h\nu = \mathrm{TKER} + E(\mathrm{C}^*) + E(\mathrm{F}^*) - D_0(\mathrm{C–F})\,, \tag{2.8}$$

where $E(\mathrm{C}^*)$ and $E(\mathrm{F}^*)$ mark the internal energies of the fragments and $D_0(\mathrm{C–F})$ the dissociation energy of C–F.

As we measure the TKER and know the photon energy $n \times h\nu$, the only unknown quantities are the internal energies $E(\mathrm{C}^*)$ and $E(\mathrm{F}^*)$ as well as the dissociation energy of our compound, $D_0(\mathrm{C–F})$. Hence, if the dissociation energy $D_0(\mathrm{C–F})$ has been independently established, we may use eq. (2.8) to determine the internal energies of the fragments produced in the photodissociation and thus learn something about the electronic structure of the products. Conversely, if the internal energies of the products can be deduced, *e.g.* by resonant ionization of particular product states, then eq. (2.8) determines the dissociation energy of C–F.

In a real photodissociation experiment, more than one single set of excited states C^* and F^* will typically be formed. These different sets result in different total internal energies and thus yield different TKER for a given wavelength. These different combinations are referred to as dissociation "channels" and lead to the observation of multiple rings.

Branching ratio

While the radius of a ring feature leads to the TKER in a process, its intensity (easily computed by radial integration) can also represent useful information — it is a measure of the relative likelihood for a fragment with that particular velocity to be formed. Once we have identified what internal energies that velocity corresponds to (see above) we can use the ratio in the intensities (or *branching ratio*) of different channels to obtain the relative likelihood of producing the particular internal states associated with each channel.

Anisotropy

So far, we have only considered the kinetic energy of our fragments, *i.e.* the speed at which they emerge from the photodissociation process, which manifests in rings

of different sizes in the images. However the images also contain information on the distribution of directions that the fragments take after photodissociation.

As alluded to in the discussion of the fit earlier, the angular distribution of fragments emerging from a N-photon photodissociation process takes the general form[143–145]

$$P(\theta) = \sum_n \beta_n P_n[\cos(\theta)] \quad n \leq 2N, n \text{ even} .$$

It can be shown[145] that for linearly polarized light the recoil anisotropy encoded in the β_n parameters is a signature for the molecular symmetry of the states involved in the photodissociation.

In particular, for a one-photon process there is only a single anisotropy parameter β_2: this takes the value $\beta_2 = -1$ for a perpendicular transition (*i.e.* one for which $\Delta\Omega = \pm 1$), leading to a $\cos^2(\theta)$ angular distribution. Parallel transitions ($\Delta\Omega = 0$) correspond to a value of $\beta_2 = +2$, resulting in a $\sin^2(\theta)$ angular distribution.

The above discussion strictly only holds in cases of very rapid dissociation without rotation. In practice, pre-dissociation, rotation of the intermediate state or dissociation *via* a diffuse intermediate state[145] can mean that the signature for anisotropy is lost and an isotropic image results, in which $\beta_n = 0 \,\forall\, n$.

2.5.4 Apparatus and procedure

The VMI experiment in Oxford is carried out using the apparatus shown in fig. 2.15. It is largely the same setup as used for action spectroscopy (*cf.* fig. 2.10). The advantage of this is that we are able to switch between the two different types easily and can quickly *e.g.* image a peak observed in an action spectrum to determine if it is a result of dissociation, *etc*.

The ion optics responsible for the velocity mapping are made up of a circular repeller and a conically shaped extractor which is connected to a series of resistively coupled electrodes which step the extractor potential down to ground.[146] This design was implemented as a result of extensive modelling with the Simion[147] program, and has improved VMI characteristics over a simple three electrode

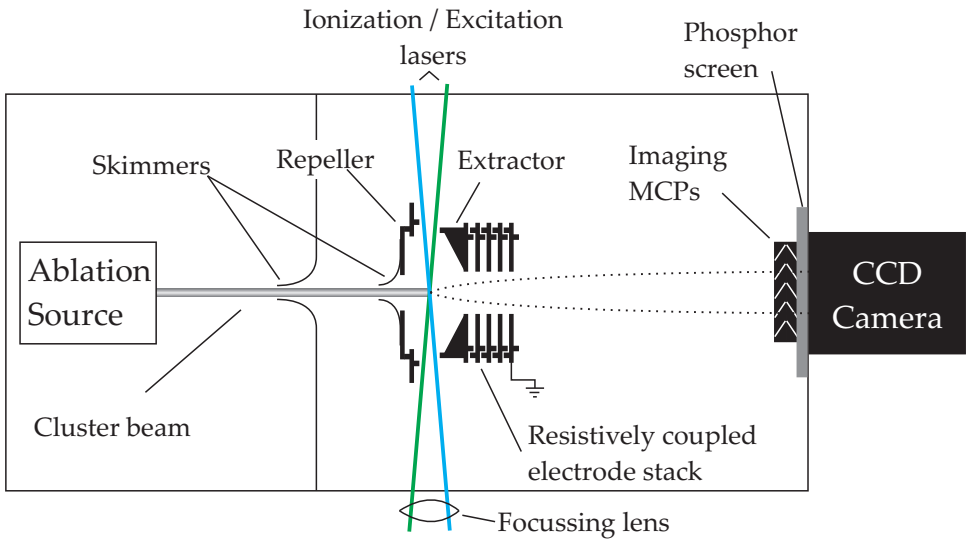

Figure 2.15 Schematic top-down view of the VMI setup. Turbomolecular pumps maintain vacuum, but are omitted in this schematic for clarity.

setup.[148] In particular, it has been very recently shown that ion optics of this type lead to velocity mapping of a considerably larger source volume than a simple three electrode design.[149]

The photofragments are detected by a commercial ion imaging arrangement (Photek), which employs a chevron arrangement of imaging quality MCPs that are gated to only record fragments arriving within a specific time-of-flight window. While the time-of-flight resolution obtained with velocity map conditions is not as high as when space focussing conditions are employed, this gating still allows us to select fragments to within 1 amu, sufficient for our purposes.

The electron cascade triggered by the fragment's arrival on the MCP plates impinges on a phosphorescent screen. A CCD camera (776×586 pixels) records the phosphorescence events, thereby recording the positions of the arriving fragments. The images are accumulated over time (typically 15 – 30 min) and read out on a PC.

The experimental procedure for VMI on this setup is as follows: A molecular beam of the desired clusters is generated by the ablation source previously discussed (see section 2.1). The beam passes through a 1 mm diameter skimmer

(Beam Dynamics) into the differentially pumped VMI region where they pass a secondary skimmer. Here, clusters are dissociated and ionized by one or more lasers crossing orthogonally to the molecular beam. Finally, the ion optics velocity map the cloud of resultant ions onto the detector.

2.6 Density functional theory

2.6.1 Introduction

The work presented herein necessitated a wide range of calculations on small clusters of transition metals. One of the fundamental issues encountered in attempting these sorts of calculations is the large computational cost associated with calculating a large range of structures made up of atoms with a large number of valence electrons. Of the methods that are computationally viable, Density Functional Theory (DFT) has become the preferred method to calculate the structure and properties of anything but the simplest transition metal systems.[10]

Density functional theory is based on the proof, by Hohenberg and Kohn,[28] that every observable of a stationary quantum mechanical system (energy included) can be determined, in principle, from the ground state electron density ρ alone. In addition, Hohenberg and Kohm showed that the variational principle applies to ρ, meaning that the ground state density may be found by minimising the energy. The basis for the use of the DFT method in computational chemistry is the introduction of orbitals, as suggested by Kohn and Sham.[29] In this *Kohn-Sham* formalism, the total electron density is defined as

$$\rho(\mathbf{r}) = \sum_{i=1}^{N} |\psi_i(\mathbf{r})| \,, \tag{2.9}$$

where N is the total number of electrons and $\psi_i(\mathbf{r})$ are the molecular orbitals. The molecular orbitals are typically approximated using a set of basis functions comprising of a gaussian radial component, a spherical harmonic function as well as set of polarization functions. The total energy can be written as a sum of

functionals

$$E[\rho] = T_S[\rho] + E_{ne}[\rho] + J[\rho] + E_{xc}[\rho]\,. \tag{2.10}$$

T_S is the kinetic energy functional for non-interacting electrons, $J[\rho]$ contains the coulomb repulsion portion of electron-electron interaction and E_{ne} the attraction between nuclei and electrons. The functional E_{xc} is the *exchange-correlation* functional, and includes the electron exchange and correlation energies as well as a correction to account for the fact that a non-interacting kinetic energy term is used. This functional is the crux of the method, and, were it to be known exactly, the method could be used to obtain exact solutions to the Schrödinger equation for any system. Alas, this is not the case, and a number of approaches have have been used over the years in an attempt to approximate the true functional. They are often thought of in terms of a *ladder* of functionals, with higher rungs corresponding to functionals including more information from the system.[150,151]

The lowest rung of this ladder is the *local density approximation* (LDA), in which it is assumed that the density can be locally treated as a uniform electron gas. In practice, a more general version of this approximation is used, the *local spin density approximation* (LSDA), where the the densities of the different electron spins are treated separately. Although LSDA functionals have found extensive use in describing extended systems, they perform poorly on molecular systems, overestimating bond strengths considerably (up to $100\,\mathrm{kJ\,mol^{-1}}$) and overestimating electron correlation by up to a factor of two.[152]

One of the first improvements made to the LSDA approach was to introduce the derivatives of the electron density as additional variables in determining the exchange and correlation energies. This is termed the *generalized gradient approximation* (GGA) and several GGA functionals such as PBE[153] and BLYP[154,155] have been successfully applied to chemical systems.

The logical extension of the GGA approach is to include higher derivatives of the electron density in the determination of exchange and correlation energies. Functionals that use the second-order term of the density (the Laplacian), or, equivalently, include the orbital kinetic energy, are called *meta*-GGA functionals. Popular examples of this include the nonempirical TPSS functional by Tao and

coworkers,[156] and the τ-HCTH functional by Handy *et al*.[157]

In a further development corresponding to the "fourth rung" in the ladder of density functionals, a portion of Hartree-Fock exchange is used in place of the exchange energy of the LSDA or GGA functionals. Functionals formed in this way are known as *hybrid* functionals, and may be formed on the basis of both LSDA and GGA functionals. The amount of exact exchange added, as well as its parametrization, vary from case to case, and are generally determined by fitting to experimental data. Despite the added computational cost of including a portion of HF exchange, functionals in this category have seen significant success, with *e.g.* the B3LYP[158] functional being employed for the vast majority of calculations in organic chemistry. The aforementioned PBE and TPSS functionals also have hybrid counterparts: PBE1,[153,159] where the 25 % of exact is added on the basis of perturbation arguments and TPSSh[160] which contains 10 % of exact HF exchange (empirically determined from fits to experimental data.)

The choice of functional for the transition metal systems discussed in this work is not obvious, with no single functional performing well across the range of metals — thus, the functionals used in this work are discussed in the context of the system they are used in (see for example section 3.3.1).

2.6.2 Implementation in Turbomole

A veritable zoo of implementations of the DFT method exist, but we chose Turbomole,[161] a package which combines computational speed with access to advanced functionals and basis sets.

Geometry optimization

In Turbomole, geometry optimization of a given trial structure is carried out by cycling three steps:

1. Calculate, using a self consistent field (SCF) method, the energy and molecular orbitals of the trial structure.

2. Calculate first and second derivatives of the potential energy surface.

3. Force relaxation, *i.e.* step the coordinates of the trial structure according to the gradient in an attempt to bring it toward a (local) minimum.

The SCF step is performed using an improved, direct version of SCF developed by Häser *et al*.[162] Gradients of the potential energy surface as well as the Hessian matrix are calculated using Turbomole's `statpt` module. This determines the stationary points on the potential energy surface, as well as their nature. The procedure used by `statpt` is based on a quasi-Newton-Raphson method.[152]

Force relaxation is carried out by the appropriately named `relax`[163] module of Turbomole. The coordinate update is computed using the calculated Hessian and gradients. As a full recalculation of the Hessian matrix at every step is expensive, the program uses a variety of methods[164] to update it as the calculation proceeds.

These steps are repeated until the convergence criteria are met. For all the calculations reported here, the key convergence criteria consisted in a maximum change in the energy between cycles of $1 \times 10^{-6}\, E_\mathrm{h}$, and maximum changes in the gradient and coordinates of 1×10^{-3} atomic units. These values are a result of experience and have been proven to provide good results previously.[165,166]

Normal mode analysis

Knowledge of the Hessian matrix enables us to calculate, within the harmonic approximation, vibrational normal modes and frequencies. Turbomole employs standard methods[167] to calculate both vibrational frequencies and approximate intensities of all the vibrational modes of a molecule.

It is worth noting that the normal mode analysis provides an easy way of identifying minima: at a (local) minimum, the energy will increase in all directions of the potential energy landscape, and thus all the vibrational frequencies will be real. Conversely, imaginary vibrational frequencies indicate that the energy is not yet minimized with respect to all directions.

Reaction profiles

While locating minima is (relatively) straightforward, the optimization of transition states is considerably harder. In general, in order to successfully optimize

towards a transition state, it is necessary to start with a trial structure that is already quite close to the final transition state. In addition, the structure must contain a Hessian eigenvector along which the energy increases, *i.e.* that has a negative eigenvalue. This is generally called the "transition vector" and as the eigenvalue is negative, the associated frequency is imaginary. Finally, the inital search often yields a structure that is not a true transition state, having multiple imaginary modes, and must thus be further optimized.

Once a satisfactory trial structure has been obtained, Turbomole employs the Trust Radius Image Minimization (TRIM)[168] method to optimize the structure. Essentially the method involves an "image" of the true structure, with the same gradient and Hessian, but with opposite signs for the eigenvalue of the transition vector. Minima of the image thus correspond to transition states of the real structure, and an optimization of minima of the image leads to transition state of the real structure.

To construct a reaction profile, the transition states are distorted in both directions along the the transition vector, and the resultant structures are optimized using eigenvector following. Connecting together all of the transition states and minima then yields a reaction pathway.

CHAPTER 3

Reactivity of small rhodium clusters with N_2O*

Charged rhodium clusters and their oxides, $Rh_nO_m^+$ ($n = 4-8$, $m = 0-2$), decorated with nitrous oxide, N_2O, have been investigated both experimentally (by IR-MPD in the spectral region corresponding to the N_2O bend, 505 – 685 cm^{-1}), and computationally using density functional theory.

The N_2O bend of N_2O adsorbed on $Rh_nO_m^+$ shifts towards lower frequency as the size of the supporting cluster (n) increases. Increased N_2O coverage on a particular cluster size n has a similar red-shifting effect, which is most prominent on the smallest clusters.

Clear evidence for the infrared-induced decomposition of N_2O on $Rh_nO_m^+$ is obtained for most cluster sizes and oxygen coverages:

$$Rh_nO_m(N_2O)^+ \xrightarrow{IR} Rh_nO_{(m+1)}^+ + N_2 \,.$$

On the whole, the coadsorption of oxygen on the parent cluster is seen to promote the decomposition channel over simple N_2O loss. In the most extreme case,

*Published, in adapted form, as A. C. Hermes et al. "Effects of Coadsorbed Oxygen on the Infrared Driven Decomposition of N_2O on Isolated Rh_5^+ Clusters". *Journal of Physical Chemistry Letters*, 2: 3053–3057, (2011).

$Rh_5(N_2O)^+$ does not undergo the above reaction at all, but primarily exhibits simple N_2O loss. By contrast, irradiation of the corresponding oxide cluster $Rh_5O(N_2O)^+$ predominantly leads to N_2O reduction to form $Rh_5O_2^+$ and N_2.

DFT calculations reveal that this difference in reactivity arises from a significantly increased N_2O binding energy on Rh_5O^+ as compared to Rh_5^+, while the barrier to reaction remains mostly unchanged.[82]

3.1 Context

Rhodium plays an important role as a catalyst for heterogeneous reactions. The best-known example is certainly the automobile three-way catalytic converter, in which rhodiumm, supported on a metal oxide surface, is an essential component.[169] The chief reason for this is its unique efficiency in catalysing the selective reduction of NO to N_2 with minimal amount of NH_3 by-product, an effect that has been linked to its ability to easily dissociate NO.[170] Coupled with the ability to withstand the harsh conditions in the converter this has meant that attempts to replace rhodium as an active component have only started to bear fruit in recent years.[171] Rhodium is also widely used as a catalyst for the oxidation of CH_4,[172,173] reforming processes[174] and the conversion of noxious NO_x species.[175]

3.1.1 Rhodium clusters

Small clusters of rhodium, as models for these systems which are experimentally and computationally viable for study,[1,176] have attracted significant interest both experimental and computational: the propensity of various rhodium cluster sizes towards chemisorption of D_2, N_2 and CH_4 were investigated as early as 1988,[177] and the sharp increase in reactivity around $n = 4-5$ was correlated with a decrease in ionization potential. Early calculations predicted that although bulk rhodium is non-magnetic, certain cluster sizes should exhibit large magnetic moments.[103] This was confirmed experimentally by Cox *et al.*[70] who studied bare rhodium clusters and found that while overall the magnetic moment decreases monotonically from the smallest cluster to the bulk nonmagnetic state, several cluster

sizes exhibit anomalously high magnetic moments. This sparked several further theoretical works aimed at explaining the detail of these findings[104–106] and to this day rhodium remains a popular target for investigation.[178] The static dipole polarizabilities have also been measured,[67] finding evidence for a permanent dipole on Rh_7, which indicates that the structure of Rh_7 cannot possess multiple C_n axes, ruling out the pentagonal bipyramid structure that had been previously proposed.[104] Rh_{10} exhibited temperature dependent polarizability, which was attributed to the fluxionality of the structure.

One of the most attractive aspects of rhodium clusters, owing to their catalytic nature, is their reactivity. Gas-phase rhodium clusters can be used to dehydrogenate alkanes with cluster size dependent differences both in rate of reaction[179] and regioselectivity.[180] In the reaction with benzene, the extent of hydrocarbon activation was found to be strongly dependent on the charge state of the cluster,[181] which is also evident in a similar reaction with azidoacetonitrile.[182] More recently, the role of rhodium in the oxidation of NO was studied on charged rhodium clusters isolated in an ICR cell.[4,183] Kinetic measurements showed that the reaction involves the dissociative adsorption of NO, generating N_2 and even oxides for $n = 7-12$ and $14-16$. Once again, one cluster size, $n = 13$, was found to be atypical — sequential adsorption of NO was the only process observed, which was linked to the proposed icosahedral structure of Rh_{13}^+.

These examples illustrate how the complex interplay of electronic and geometric structure leads to very diverse and size-specific effects. In an attempt to understand this interplay, several studies have concentrated on elucidating the structures of the rhodium clusters. Until recently, knowledge was limited to the stretching frequency[184] and bond dissociation energy[185] of the dimer. In addition, electron spin resonance established that the trimer must possess D_{3h} symmetry, *i.e.* it is an equilateral triangle.[186]

In computational modelling using density functional theory (DFT) structures based upon both polytetrahedral (or octahedral) as well as cubic motifs have been predicted (dependent on the nature of the functional utilized), but no clear indication as to the real structures could be obtained.[104,106] However, recent work by this group[47,48] provided significant new insights into the structure of rhodium clusters:

using a combination of far infra-red multiple-photon dissociation spectroscopy and DFT, the structures of Rh_n^+ ($n = 6 - 12$) were investigated. Tetrahedral and octahedral structure motifs were found to be prevalent in this size range, while no evidence for cubic motifs was found. The work highlighted the deficiencies of DFT in dealing with high spin states, as a good match of computed and experimental spectra required the use of a functional including a portion of exact Hartree-Fock exchange (see also section 3.3.1).

3.1.2 The interaction of rhodium and N_2O

The interaction between rhodium and N_2O has garnered much attention, as N_2O is the main by-product of the catalytic reduction of NO_x in the automobile three-way catalytic converter;[175] yet it is a remarkable greenhouse gas. It has known been since the 70s that bulk rhodium readily absorbs N_2O, leading to the decomposition of the N_2O upon heating.[187] While a small amount of N_2O desorption does occur, decomposition is the main pathway at temperatures above 60 K.[188,189] The different crystal faces show noticeably different activity toward N_2O decomposition, with the (110) face being significantly more reactive than the (111) face[190] — although some reaction was later observed on the (111) face;[191] the extent is much less.

This provides good evidence that the the detail of the crystal surface plays an important role in determining the rate of reaction. Indeed, it has been suggested that the promotion of N_2O decomposition by oxygen preadsorbed on the surface is due to the fact that oxygen acts as a guide to the N_2O adsorbant, allowing it to find a reaction site with increased likelihood.[191] Further evidence of the effect of oxygen was provided by Liu *et al.*;[192] who showed that a rhodium surface annealed with oxygen modifies both the temperature required for the reaction as well as the angular distribution of the resultant N_2 evolved. On the other hand, the reaction was almost completely suppressed when the oxygen was not annealed prior to N_2O exposure.

The nature of the N_2O adsorption[193] and the mechanism for reaction[194,195] have also been investigated computationally. The studies indicate that N_2O is

bound *via* the terminal N atom, and in the first step forms a bridging intermediate, followed by N–O bond cleavage and N_2 desorption.

3.1.3 Previous work in this group

Previous work by this group has extended the study of the interaction of rhodium clusters with N_2O to the gas phase, and these are found to react in a consistent fashion: N_2O undergoes dissociative chemisorption on both cationic and anionic rhodium clusters $Rh_n^{\pm}$ ($n < 30$).[87] The rates of reaction are highly size-dependent, particularly for the cationic clusters, with variations of up to two orders of magnitude in the rate constant as a function of cluster size. In addition, for several cluster sizes, evidence was observed for the coexistence of multiple isomeric forms, and the relative ratio of each isomeric form had a significant effect on the reaction kinetics, once again highlighting the importance of both electronic and geometric cluster stucture in this context.

This interaction of N_2O with cationic rhodium clusters has also been probed using far-infrared radiation, in IR-MPD experiments performed in collaboration with the group of Gerard Meijer, experiments in which the author was involved.[81,166] The results confirm that, under the co-expansion conditions employed in the study, N_2O is molecularly absorbed on $Rh_n^{\pm}$ ($n = 4-8$) and that it is preferentially bound through the terminal nitrogen atom. It was also shown that, for most cluster sizes ($n = 4-6, 8$), the decomposition of N_2O on the cluster surface is a significant N_2O loss channel alongside N_2O desorption. The reaction can be triggered both by infra-red radiation resonant with a N_2O vibrational mode as well as by radiation resonant with the metal-metal modes of the supporting rhodium cluster. This supports the idea that the reaction is fundamentally thermal in nature. In marked contrast, $Rh_5(N_2O)^+$ does not exhibit this same behaviour, being inert with respect to N_2O decomposition, with the only observed process being the desorption of N_2O from the cluster surface.

This work extends the analysis to the reactivity of the oxides of the rhodium clusters $Rh_nO_m^+$ ($n = 4-8$, $m = 0-2$) with N_2O. In addition, we present a computational investigation into the anomalous reactivity of $Rh_5(N_2O)^+$.

3.2 Experimental method

This work is an example of the IR-MPD technique detailed in section 2.3 and used the arrangement described therein. For these experiments, the target consisted of a rhodium rod (provided by David M Rayner, NRC, to whom we are very grateful), while N_2O was seeded by a late mixing valve. FELIX was used in the range 505 – 685 cm^{-1} at full power in order to maximize the chance of initiating surface reactions.

The mass spectroscopic tag used to obtain the IR-MPD spectra is the N_2O molecule itself — if the cluster is resonant at a given wavelength, the N_2O molecule will be lost either by desorption or by decomposition followed by N_2 desorption. Thus, for a given $Rh_nN_2O_l^+$ cluster, the loss of intensity in the parent ion mass channel is a signature for resonance.

IR-MPD spectra were collected using 0.05 µm ($\approx 1\,cm^{-1}$) steps and averaged over several runs.

3.2.1 Data processing

The IR-MPD spectra presented herein are an average over several runs, to boost signal-to-noise ratio. In each case, a region of the mass spectrum with no features (the first 500 points) was used as a background and subtracted, to minimize any systematic error in the baseline. Each IR-MPD spectrum reported shows the raw data (black dots •) and a four point adjacent average (red line —), used to account for the bandwidth of the FELIX beam. The identities of the N_2O bend and Rh–O stretch modes, determined on the basis of calculations as well as the work on bare rhodium clusters,[196] are indicated by ν_{bend} and $\nu_{\text{Rh-O}}$, respectively.

3.3 Computational method

The calculations performed here employ the methods detailed in section 2.6 for structure and transition state searches, combining them to determine reaction profiles.

For a given rhodium cluster decorated with oxygen and N_2O ligands, a large number of possible geometries can be achieved by combining all possible structures of the underlying cluster, potential ligand binding sites and ligand binding modes. It is, therefore, not practical to simulate all the clusters that were observed experimentally. Instead, attention was focussed on the $Rh_5O(N_2O)^+$ cluster, as well as species related to it by reaction or desorption, *e.g.* $Rh_5O_2^+$. This system was chosen due to the unique reactivity it exhibits (see section 3.4.4).

To obtain initial guesses for the transition state structures, a series of intermediate structures between reactants and products were generated. The structure with the highest energy and appropriate imaginary mode was then chosen as a starting point for a transition state search.

3.3.1 Functional and basis sets

Much of the challenge in the calculation of structure and properties of transition metal clusters with DFT stems from the difficulty in identifying a suitable exchange-correlation functional. While a very large number of functionals are readily available for use in DFT calculations, the vast majority of functionals have been developed and parametrised for metal atoms with main group ligands or bulk metals.[10] However, transition metals have a markedly different nature and functionals that are successful in predicting main group chemistry typically predict the properties of transition metal clusters poorly.[197] In particular, such functionals deal poorly with high multiplicity electronic states, as evidenced by the work on the structure of rhodium clusters discussed in section 3.1.1. As of yet, the transition metal cluster world has no equivalent to the B3LYP functional[158] that is universally applied in organic chemistry.[198]

Nevertheless, several functionals exist that have, under certain circumstances, shown good performance for certain properties. In particular, the hybrid generalized gradient approximation (GGA) functional PBE1 (also known as PBE0)[153,159] has been shown to provide a good description of the structure of naked rhodium clusters.[48] Further IR-MPD work on rhodium clusters,[81] however, showed that while PBE1 accurately predicts the IR spectrum of the clusters, the reactions

barriers are not well modelled. On the other hand, the same work showed that the TPSSh[156,160] functional (with 25 % exact Hartree-Fock exchange) represents a good compromise for calculations that aim to use a consistent functional for both structure search and reaction pathway computation. Hence, we employed the TPSSh functional for all the calculations presented here.

The calculations were all carried out in Turbomole 6.0 and 6.1.[161] We employed the triple-ζ valence def2-TZVP basis sets[199] as well as an auxiliary basis.[200] The auxiliary basis allows the use of the multipole accelerated resolution of identity approximation (MARI-J),[201] which can reduce the computation time required by up to two orders of magnitude without significant loss of accuracy. For the rhodium atoms, the TZVP basis contains an effective core potential (ecp) which replaces the 28 core electrons of rhodium with a single potential and includes some corrections for relativistic effects.

3.4 Experimental Results

3.4.1 Cluster generation

The experimental setup as described above produces a wide array of rhodium clusters, complexed with both oxygen and N_2O. The source parameters (relative timing of gas and laser pulses, N_2O pressure, *etc.*) were optimized so as to produce a distribution of rhodium clusters Rh_n^+ peaked around $n = 6$ with appreciable N_2O coverage, while minimizing species with multiple N_2O as much as possible (see fig. 3.1a). As a result, the mass spectrum virtually separates into different portions, each containing almost exclusively clusters with one particular n.

An example of one such section of the full mass spectrum is shown in fig. 3.1b for Rh_5^+. Aside from the bare ion, the major species in the spectrum are based on oxygen and N_2O, or a combination of the two. The presence of oxide species in the cluster beam shows that a portion of the Rh_n^+ formed in the incipient cluster beam immediately react with the seeded N_2O gas to produce oxides. The mass spectrum shown in fig. 3.1b is representative for all cluster sizes studied, although the adsorption of multiple N_2O molecules becomes more favoured on larger clusters,

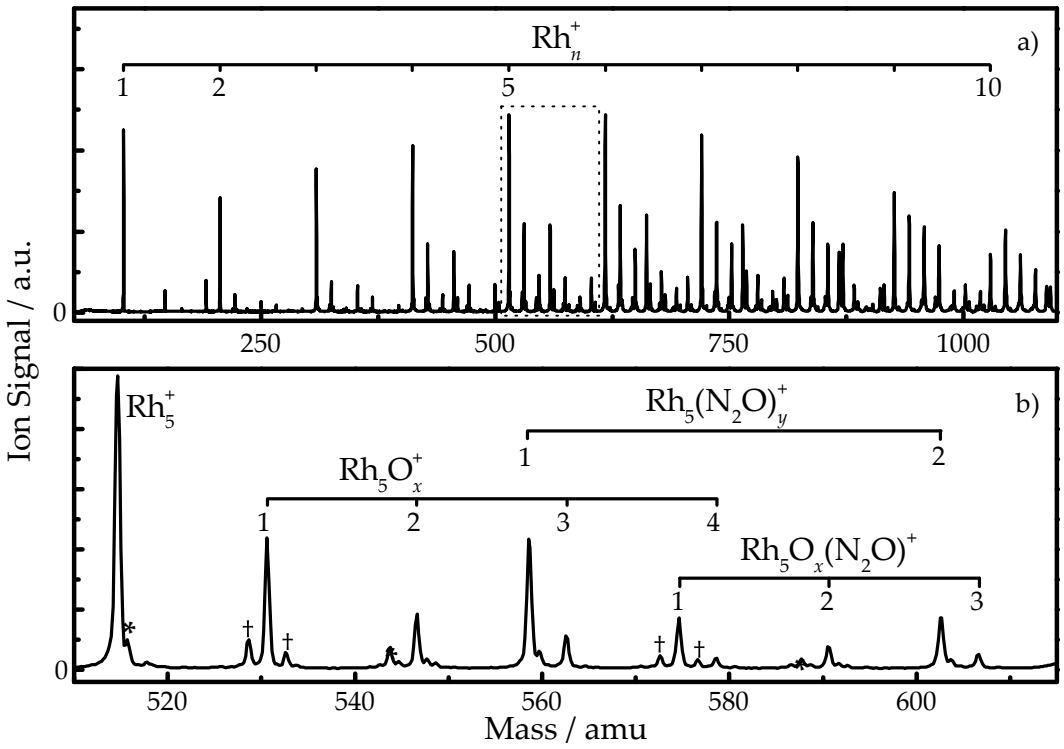

Figure 3.1 Mass spectra recorded in the absence of infrared irradiation. a) Full mass spectrum of the Rh_n^+ that have been investigated. b) Expanded view of the mass spectrum corresponding to Rh_5^+ clusters. (*) Species based on Rh_4^+, (†) minor background Rh_5^+ species (Rh_5N^+, $Rh_5H_2O^+$, etc).

as might be expected given the greater number of possible adsorption sites as the clusters grow.

3.4.2 Spectroscopy of the N_2O band

While a large portion of the spectroscopic detail exhibited by these clusters has already been covered elsewhere,[165] there are a number of noteworthy features of the N_2O band which were not discussed previously.

Figure 3.2 shows the IR-MPD spectra for $Rh_n(N_2O)^+$ in the N_2O bend region. The dips in intensity represent a depletion in the mass channel of the associated cluster in the presence of the IR beam (in the spectra shown, up to *ca.* 25 % of the mass channel is depleted). The depletion shows that a dissociation or loss

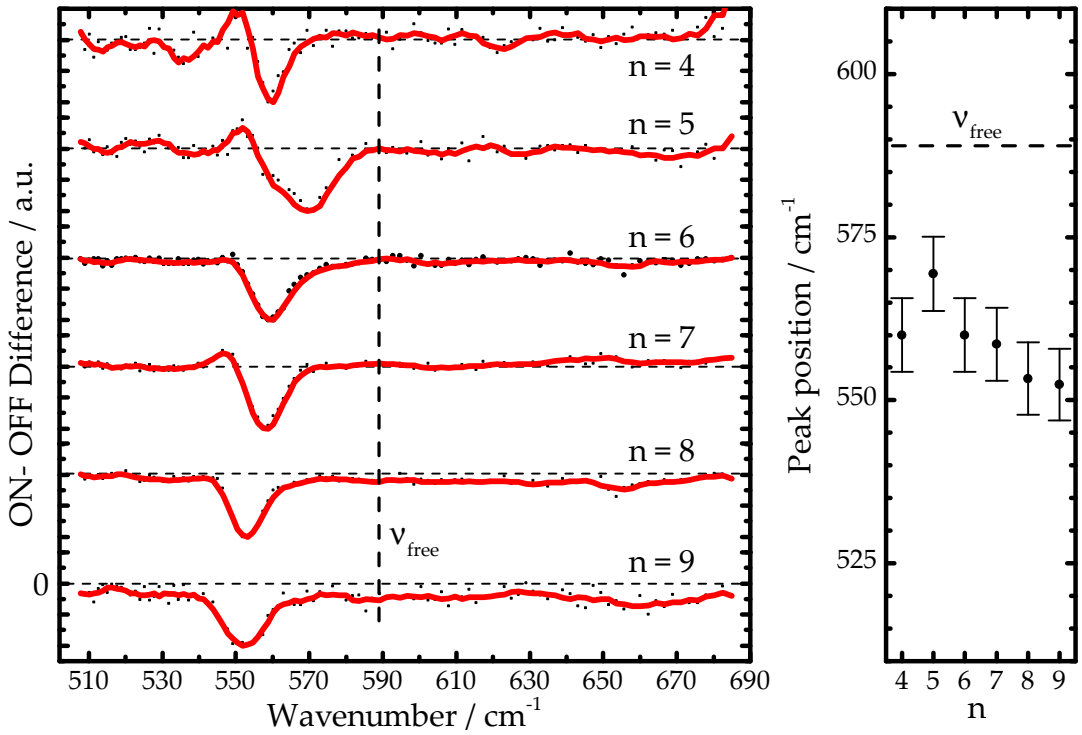

Figure 3.2 (Left) IR-MPD spectra of the N_2O bend on $Rh_n(N_2O)^+$ for $n = 4-9$. The black dots show the raw data while the red line is a 4 point adjacent average. The spectra are normalized such that the largest amplitude in each spectrum corresponds to unity. The dotted line labelled ν_{free} indicates the band position of the free N_2O molecule. (Right) Positions of the N_2O peak as a function of cluster size n, extracted by gaussian line fits. The uncertainties show the bandwidth of the FELIX beam, which is the dominant error.

process occurs in the presence of the IR beam at a given wavelength, indicating that the cluster is resonant at that wavelength. For all clusters, the resonance of the N_2O bend is shifted toward lower frequency compared to the free N_2O molecule ($\nu_{free} = 589\,cm^{-1}$).[202] Moreover, for $n = 5-9$ the shift increases with increasing cluster size, from about $20\,cm^{-1}$ for $Rh_5(N_2O)^+$ to almost $40\,cm^{-1}$ for $Rh_9(N_2O)^+$. Unlike the CO band on CO decorated rhodium clusters,[45] the N_2O bend frequency shows no clear signs of convergence towards an asymptotic value. The red-shift of the N_2O bend frequency has previously been noted on extended surfaces.[203,204]

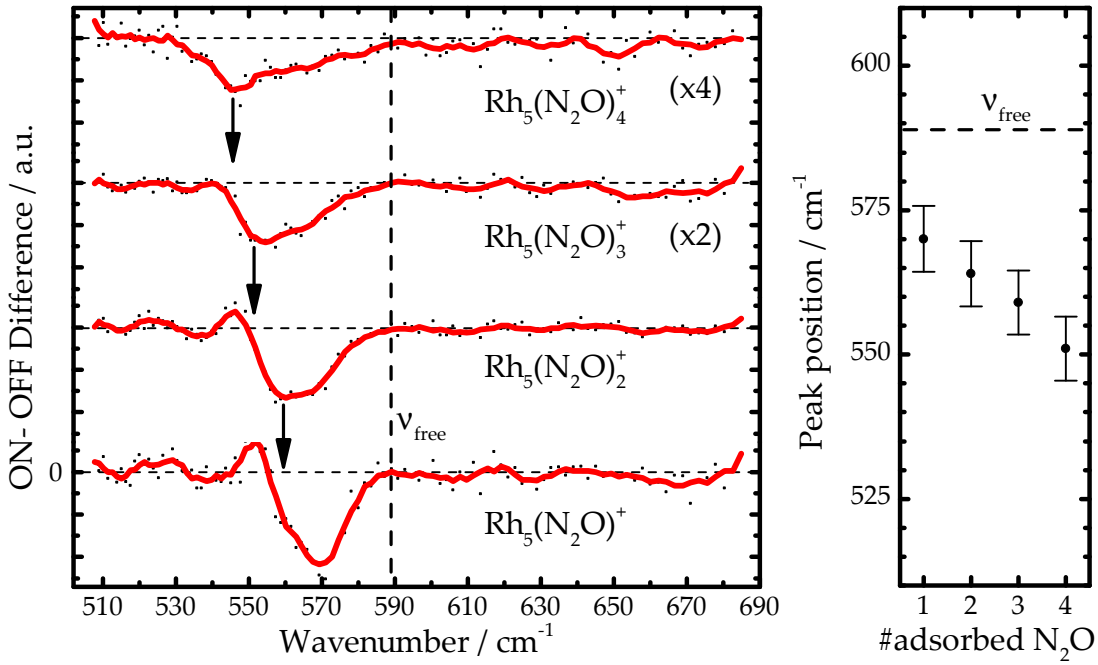

Figure 3.3 (Left) IR-MPD spectra of $Rh_5(N_2O)_l^+$ for $l = 1-4$, each showing the depletion due to the N_2O bending mode. The vertical scales are the same for each spectrum, with the spectra for $Rh_5(N_2O)_4^+$ and $Rh_5(N_2O)_3^+$ being scaled up by a factor 4 and 2 respectively. (Right) Positions of the N_2O bend feature extracted by gaussian line fits. The dotted line labelled ν_{free} indicates the band position of the free N_2O molecule. The uncertainties show the bandwidth of the FELIX beam, which is the dominant error.

Multiple adsorbed N_2O

Another feature exhibited by the spectra in fig. 3.2 are the enhanced "shoulders" on the low frequency side of the spectra. This is particularly evident for the smaller cluster sizes. This means that the $Rh_n(N_2O)^+$ clusters, as well as undergoing a loss process, are also being produced by a resonant process. A likely source of this production are clusters with multiple adsorbed N_2O molecules: resonant radiation triggers the desorption of an N_2O molecule from $Rh_n(N_2O)_l^+$, forming $Rh_n(N_2O)_{l-1}^+$.

Figure 3.3 shows the spectra of all the $Rh_5(N_2O)_l^+$ species with significant abundance in the cluster beam ($l = 1-4$). The addition of N_2O molecules beyond the first shifts the resonance of the cluster further toward lower frequency. This

effect is strongest on the smaller clusters ($n = 4, 5$), as might be intuitive given that the relative impact of an individual N_2O decreases with increasing cluster size. The band centre in the daughter species $Rh_n(N_2O)^+_{l-1}$ formed by desorption of N_2O from a parent cluster $Rh_n(N_2O)^+_l$ is blue-shifted compared to the parent. Therefore, the enhancement due to desorption from the parent and the depletion of the species itself do not fully overlap, leading to the asymmetric shape of the peaks in fig. 3.2. The fact that this asymmetric shape is clearest on the $n = 4$ and $n = 5$ clusters may be explained by the fact that since the frequency shift induced by additional N_2O molecules is reduced on the larger clusters, the aforementioned enhancement and depletion line up more closely, and a less asymmetric peak shape results.

It is possible to correct for this effect to an extent, and recover an unblended spectrum for a given $Rh_n(N_2O)^+$, by adding a portion of the $Rh_n(N_2O)^+_l$ ($l > 1$) spectra to the $Rh_n(N_2O)^+$ spectrum, effectively balancing out the enhancement shoulders. This clearly requires knowledge — or assumption — about the fraction of the depletion in each $Rh_n(N_2O)^+_l$ ($l > 1$) which ends up enhancing the $Rh_n(N_2O)^+$ channel. As we generally do not have this knowledge, the $Rh_n(N_2O)^+$ spectra which are presented in the next section are corrected only when they present obvious shoulders, where one can deduce the appropriate fraction by the asymmetry of the depletion peak. Figure 3.4 shows the result of this procedure for $Rh_5(N_2O)^+$. We can clearly see that the enhancement shoulder has been removed, leading to a more symmetric peak.

3.4.3 Metal-oxygen modes

As will be shown in the next section (see also figs. 3.6 to 3.10) there are a number of features in the spectral region studied which cannot be attributed to transitions involving the N_2O bend. IR-MPD studies of rhodium cluster oxides performed in parallel[196,205] show that several rhodium-oxygen bands fall in the range studied here, and, where applicable, they are identified in the spectra that follow.

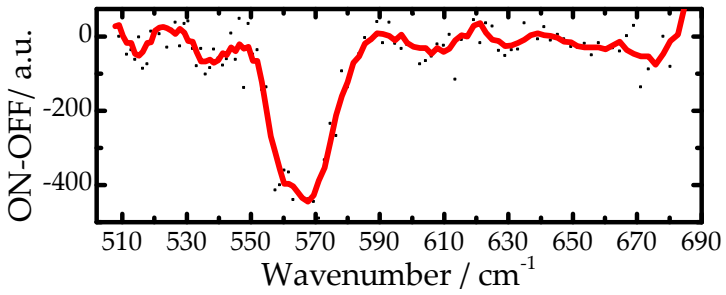

Figure 3.4 IR-MPD spectrum of $Rh_5(N_2O)^+$, corrected for enhancement due to desorption of N_2O from $Rh_n(N_2O)_l^+$ ($l > 1$) as detailed in section 3.4.2. Compare this with the raw $Rh_5(N_2O)^+$ spectrum shown, *e.g.* at the bottom of fig. 3.3.

3.4.4 Reactivity triggered on clusters

The following sections describe the IR-induced reactivity of rhodium clusters (and their oxides) with adsorbed N_2O. The reactivity of the bare clusters ($m = 0$) has been noted before,[166] but the spectra and reactivity of the oxides were not discussed and are presented here for the first time.

In general terms, the absorption of multiple IR photons either leads to a N_2O *reduction reaction*

$$Rh_nO_m(N_2O)^+ \xrightarrow{IR} Rh_nO^+_{(m+1)} + N_2 \tag{3.1}$$

or N_2O *desorption*

$$Rh_nO_m(N_2O)^+ \xrightarrow{IR} Rh_nO^+_m + N_2O\,. \tag{3.2}$$

As a visual aid to understanding this, a schematic outline of the N_2O reduction on Rh_6^+ is shown in fig. 3.5.

The branching ratio of reaction to desorption can be determined by careful examination of the IR-MPD spectra of the N_2O decorated species and their products ($Rh_nO^+_{(m+1)}$ and $Rh_nO^+_m$). The following sections describe this analysis in detail for each cluster size, and attempt to identify the major loss channels for each species. This determination can only be made qualitatively in most cases: the technique is

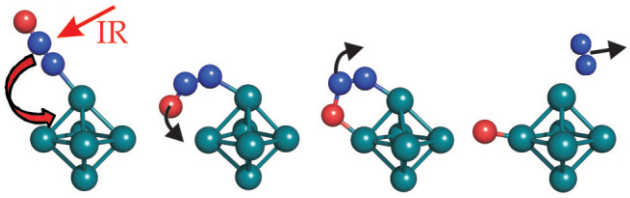

Figure 3.5 N_2O reduction triggered on the surface of a Rh_6^+ cluster by IR-MPD.

inherently sensitive only to species that are maintained within the cluster beam and hence depletions and enhancements do not balance perfecly across all the species of a given cluster size in general. This, combined with experimental uncertainty, means that we are limited to a range of plausible branching ratios for each process, and we hence restrict ourselves to qualitative or semi-quantitative observations.

Rh_4^+ clusters

The smallest cluster for which there is appreciable evidence of the reactive channel is Rh_4^+. Figure 3.6 shows IR-MPD spectra recorded simultaneously in the mass channels correlating to $Rh_4(N_2O)^+$ and $Rh_4O(N_2O)^+$ and the potential products of the processes (3.2) and (3.1). The spectra present several interesting features, which will be addressed in turn.

The first point to note is the strong depletion in $Rh_4(N_2O)^+$ signal at the N_2O bend frequency (*ca.* 559 cm^{-1}): the putative desorption product, bare Rh_4^+, shows an enhancement, but this does not match the frequency of the depletion. We conclude, therefore, that Rh_4^+ is *not* produced by IR-induced loss of N_2O from $Rh_4(N_2O)^+$. On the other hand, there is a matching enhancement in the Rh_4O^+ spectrum. It is therefore tempting to suggest that this is evidence for the reduction reaction (3.1) taking place on the cluster surface. However, to decide if this this assignment is correct it is necessary to consider the other likely source of Rh_4O^+, that is to say the oxide cluster $Rh_4O(N_2O)^+$.

The spectrum of $Rh_4O(N_2O)^+$ shows two depletions which can be readily identified as the the N_2O bend (*ca.* 559 cm^{-1}) and the Rh–O stretch (*ca.* 599 cm^{-1}). These two features correspond to two features seen in both the Rh_4O^+ and $Rh_4O_2^+$

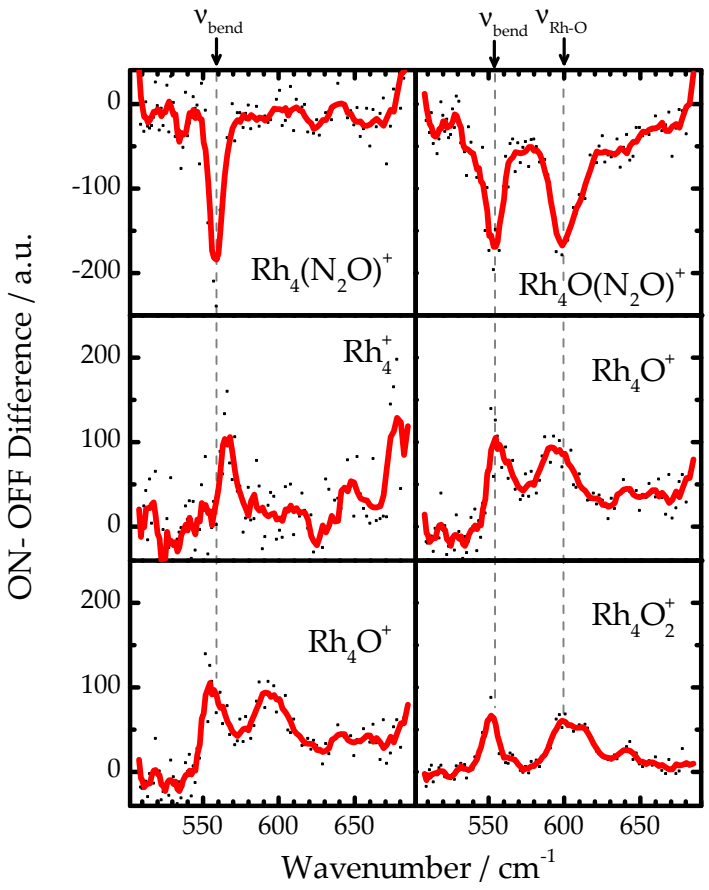

Figure 3.6 IR-MPD spectra of Rh_4^+ based clusters decorated with oxygen and N_2O. Each column shows the spectrum of a N_2O decorated reactive species (top row), the spectrum for the species that would be produced by N_2O desorption (centre row) and the spectrum produced by N_2O reduction (bottom row).

spectra, each an enhancement roughly half the size of the depletion seen in the $Rh_4O(N_2O)^+$ spectrum. Note that $Rh_4O_2(N_2O)^+$ was not present to any significant extent in the cluster beam, and can therefore be excluded as a possible source of $Rh_4O_2^+$.

These data together strongly indicate that approximately half of the depletion observed in $Rh_4O(N_2O)^+$ is a result of reduction of N_2O (eq. (3.1)) following pumping of either N_2O or Rh–O bands, highlighting the equivalence of vibrational bands as sources of energy for the reactive process. The other half of the depletion

can be accounted for by N_2O loss (eq. (3.2)). This assignment accounts for a large (> 80 %) portion of the enhancement in the Rh_4O^+ and $Rh_4O_2^+$ channels, therefore N_2O reduction cannot be a major $Rh_4(N_2O)^+$ loss process.

The enhancement in bare Rh_4^+ and the depletion in $Rh_4(N_2O)^+$ cannot be explained by the reactions eqs. (3.1) and (3.2), and indicate that a different kind of process is occurring. One possible explanation for the depletion in $Rh_4(N_2O)^+$ would be the fragmentation of the underlying rhodium cluster to produce several (decorated) rhodium fragments. However, the IR-MPD spectra of likely products of such a fragmentation (Rh_3^+, $Rh(N_2O)^+$, Rh_2^+, *etc.*) show no evidence of enhancements matching the $Rh_4(N_2O)^+$ depletion, preventing an unambiguous assignment. The enhancement in Rh_4^+ could be the result of $Rh_5(N_2O)^+$ fragmentation, as it matches spectrally, but without additional data such an assignment is somewhat speculative.

Rh_5^+

As alluded to in the introduction, the $n = 5$ cluster appears to be unique in this size range in supporting very little to no reaction on the bare $Rh_5(N_2O)^+$. This is illustrated in fig. 3.7: the depletion in the $Rh_5(N_2O)^+$ signal is accompanied by a significant enhancement in the bare Rh_5^+ signal. By contrast only a minimal enhancement above noise level is observed for Rh_5O^+. This is consistent with the dominant $Rh_5(N_2O)^+$ loss channel being simple N_2O desorption.

This ratio is completely reversed for the $Rh_5O(N_2O)^+$ cluster. Its spectrum shows a depletion feature at 529 – 568 cm^{-1}, which can be assigned to overlapping Rh–O stretch and N_2O bend modes. In this case, the minimal enhancement in Rh_5O^+ indicates that the desorption channel is insignificant. In contrast, the marked enhancement in $Rh_5O_2^+$ shows that the reaction channel is predominant.

The deduction is less clear-cut in the case of $Rh_5O_2(N_2O)^+$, as both the desorption product, $Rh_5O_2^+$, and the reaction product, $Rh_5O_3^+$, exhibit enhancements. The shape, position and magnitude of the depletion in $Rh_5O_2(N_2O)^+$ is well mirrored by the enhancement spectrum of $Rh_5O_3^+$, while the match with the spectrum of $Rh_5O_2^+$ is much poorer. We deduce that the desorption channel can at most be a minor route, and that N_2O reduction is the main loss pathway. This also fits the

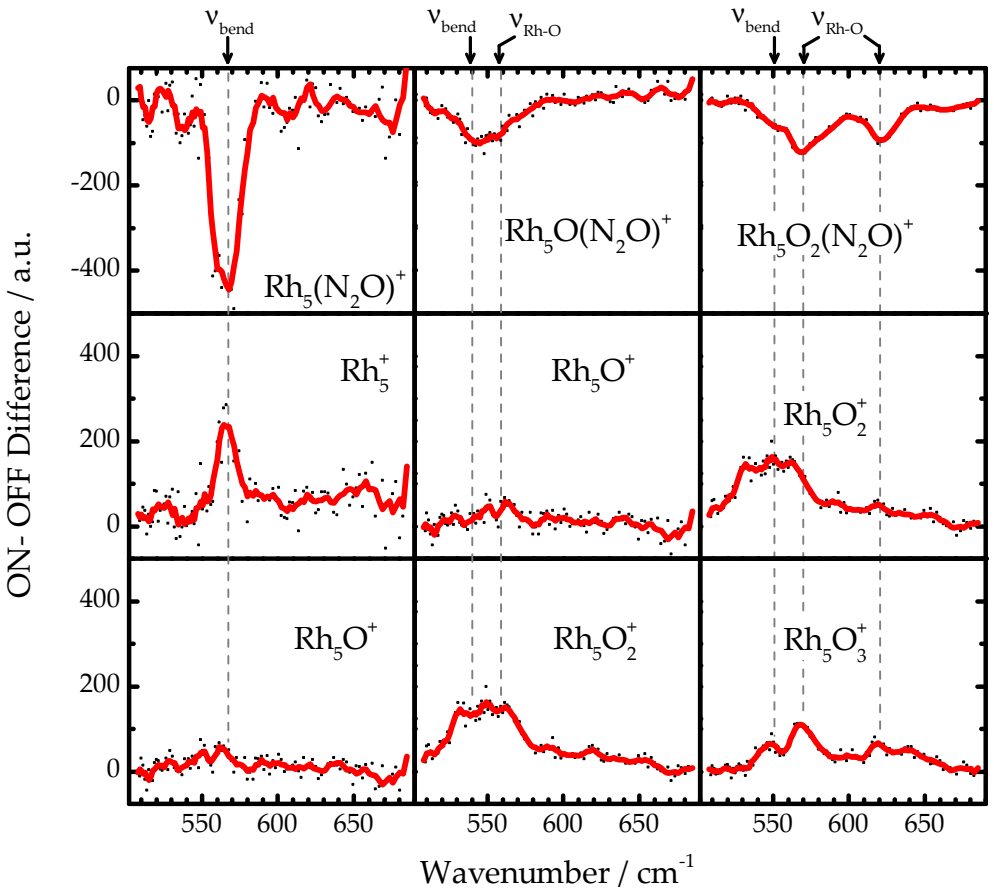

Figure 3.7 IR-MPD spectra of Rh_5^+ based clusters decorated with oxygen and N_2O. Each column shows the spectrum of a N_2O decorated reactive species (top row), the spectrum for the species that would be produced by N_2O desorption (centre row) and the spectrum produced by N_2O reduction (bottom row).

above interpretation, since most of the the $Rh_5O_2^+$ enhancement can already be accounted for by N_2O reduction on $Rh_5O(N_2O)^+$.

Rh_6^+ clusters

Several Rh_6^+ based oxide species are observed in appreciable amounts during our measurements, all with characteristic spectral features. The IR-MPD spectra of bare and oxide species, decorated with N_2O, are shown in fig. 3.8.

The complex interplay of reaction *vs.* desorption is perhaps best understood

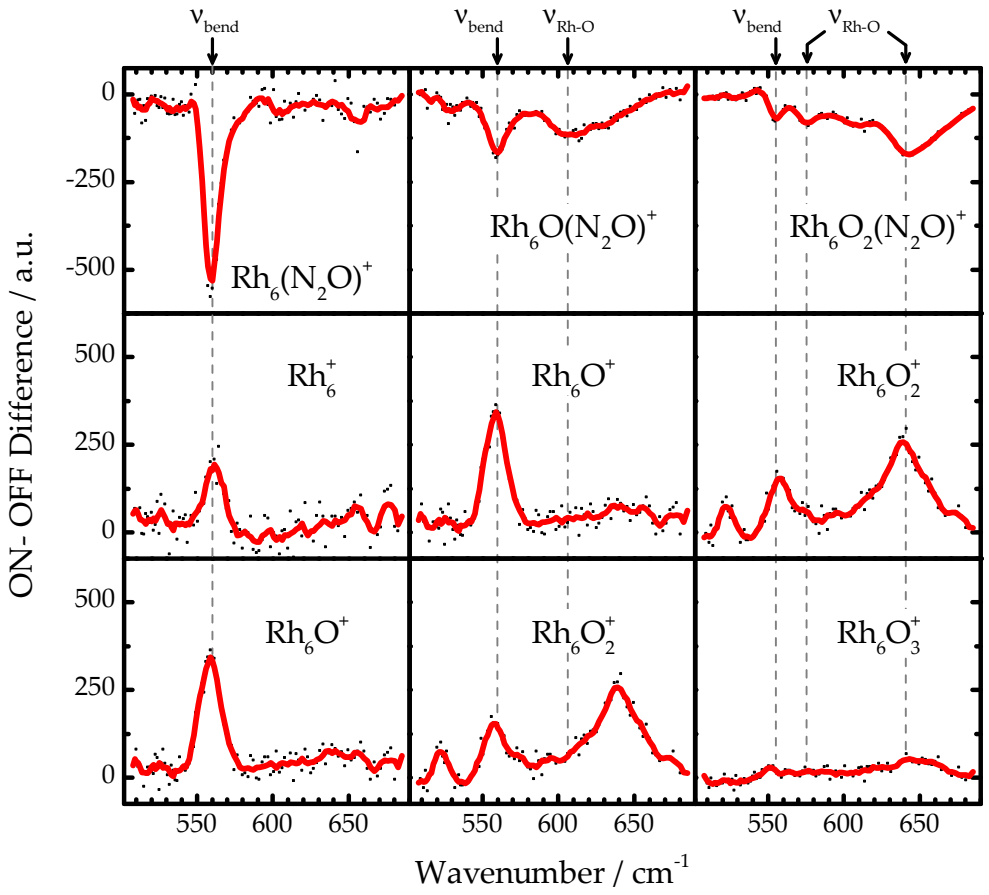

Figure 3.8 IR-MPD spectra of Rh_6^+ based clusters decorated with oxygen and N_2O. Each column shows the spectrum of a N_2O decorated reactive species (top row), the spectrum for the species that would be produced by N_2O desorption (centre row) and the spectrum produced by N_2O reduction (bottom row).

by first considering the spectrum of the species with the most oxygen coverage, $Rh_6O_2(N_2O)^+$. It exhibits a relatively weak N_2O bend feature (556 cm^{-1}) and three features of varying intensity assignable as rhodium-oxygen interactions (576, 608 and 643 cm^{-1}). Comparing with the potential products, we immediately notice that there is only a very weak enhancement signature in the $Rh_6O_3^+$ spectrum corresponding with the depletion in $Rh_6O_2(N_2O)^+$. By contrast, the $Rh_6O_2^+$ spectrum shows enhancements matching all of the spectral features described above. Comparing the intensities suggests that the major loss channel for $Rh_6O_2(N_2O)^+$

is N_2O desorption, with at most 20 % being due to reaction.

This assignment permits the deduction of the branching of $Rh_6O(N_2O)^+$. Its spectrum shows the N_2O bend (559 cm^{-1}), a weak rhodium-oxygen feature at 528 cm^{-1} and a broader more intense feature centered at approximately 620 cm^{-1}. Comparing these intensities with the proportion of the enhancement in $Rh_6O_2^+$ that is not explained by the N_2O desorption from $Rh_6O_2(N_2O)^+$ (see above) suggests that most of $Rh_6O(N_2O)^+$ is lost by reaction, with N_2O desorption being a minor channel.

With this in mind, the analysis of the $Rh_6(N_2O)^+$ loss processes is fairly straightforward: the depletion at the N_2O bend (560 cm^{-1}) is matched by concomitant enhancements in Rh_6^+ and Rh_6O^+. Their relative intensities indicate that $Rh_6(N_2O)^+$ loss partitions into reaction and desorption in approximately a 2:1 ratio.

Rh_7^+ clusters

Rh_7^+ clusters are also abundantly present in the mass spectrum, and the IR-MPD spectra show correspondingly good signal-to-noise (fig. 3.9).

The $Rh_7O_2(N_2O)^+$ spectrum shows two strong depletion features due to N_2O bend (559 cm^{-1}) and a double peak corresponding to the Rh–O stretch (643 and 663 cm^{-1}). The enhancements in the $Rh_7O_3^+$ spectrum match these features very well. Note that the $Rh_7O_3^+$ enhancement at 557 cm^{-1} owes approximately half of its intensity to N_2O desorption from $Rh_7O_3(N_2O)^+$ (not shown). The enhancements in the $Rh_7O_2^+$ spectrum do not match the $Rh_7O_2(N_2O)^+$ spectrum as exactly, but there is a small shoulder at 561 cm^{-1} in the $Rh_7O_2^+$ spectrum, as well as a broad feature 597 – 662 cm^{-1}. Taken together we deduce that while the major $Rh_7O_2(N_2O)^+$ loss channel is N_2O reduction on the cluster surface, a significant minor channel is represented by N_2O desorption.

The monoxide cluster $Rh_7O(N_2O)^+$ also shows the now-familiar N_2O bend (543 cm^{-1}) and Rh–O stretch (611 cm^{-1}) peaks. The match between these and the putative desorption product Rh_7O^+ is poor — in particular, there is no appreciable feature at around 611 cm^{-1} in the Rh_7O^+ spectrum. This indicates that the major loss channel is the reaction to produce $Rh_7O_2^+$, and indeed the matching

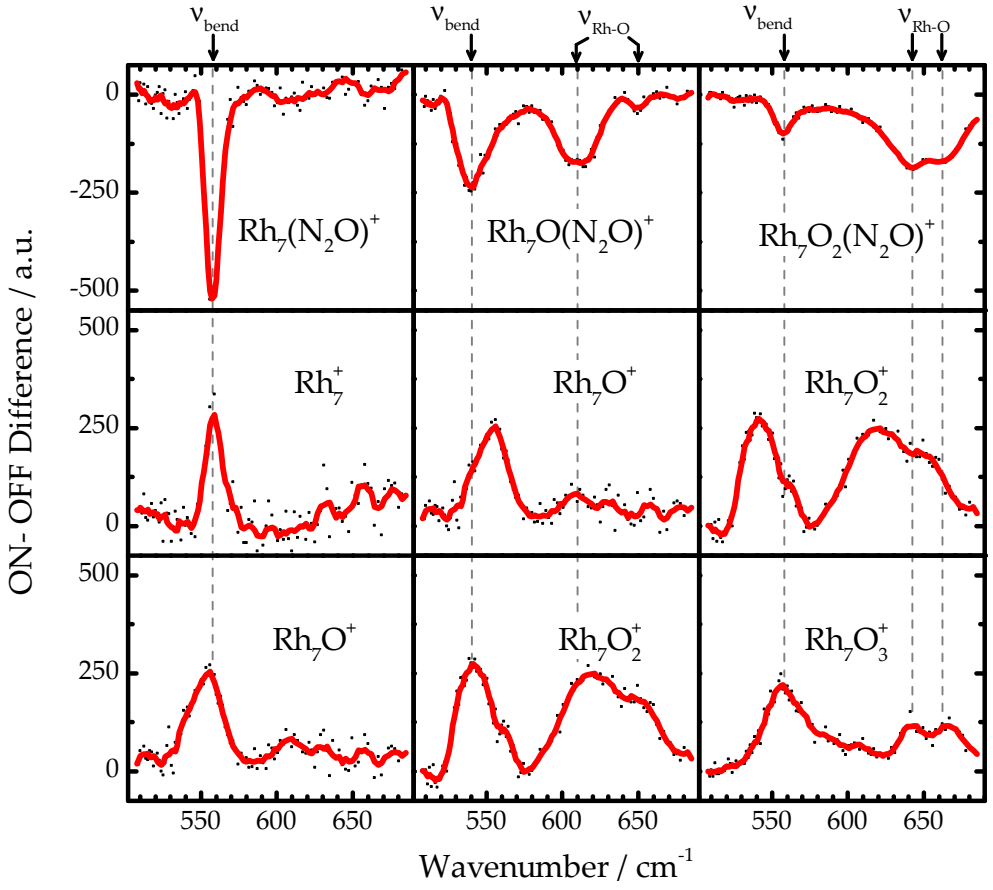

Figure 3.9 IR-MPD spectra of Rh_7^+ based clusters decorated with oxygen and N_2O. Each column shows the spectrum of a N_2O decorated reactive species (top row), the spectrum for the species that would be produced by N_2O desorption (centre row) and the spectrum produced by N_2O reduction (bottom row).

enhancements in the the $Rh_7O_2^+$ confirm this hypothesis.

Finally, the depletion of $Rh_7(N_2O)^+$ is matched by corresponding enhancements in both Rh_7O^+ and Rh_7^+, of approximately equal intensity, suggesting that the desorption and reaction channels are of equal significance for $Rh_7(N_2O)^+$ loss.

Rh_8^+ clusters

For the Rh_8^+ cluster, the spectrum of the decorated dioxide cluster, $Rh_8O_2(N_2O)^+$, spectrum could not be obtained due to its very low abundance in the mass

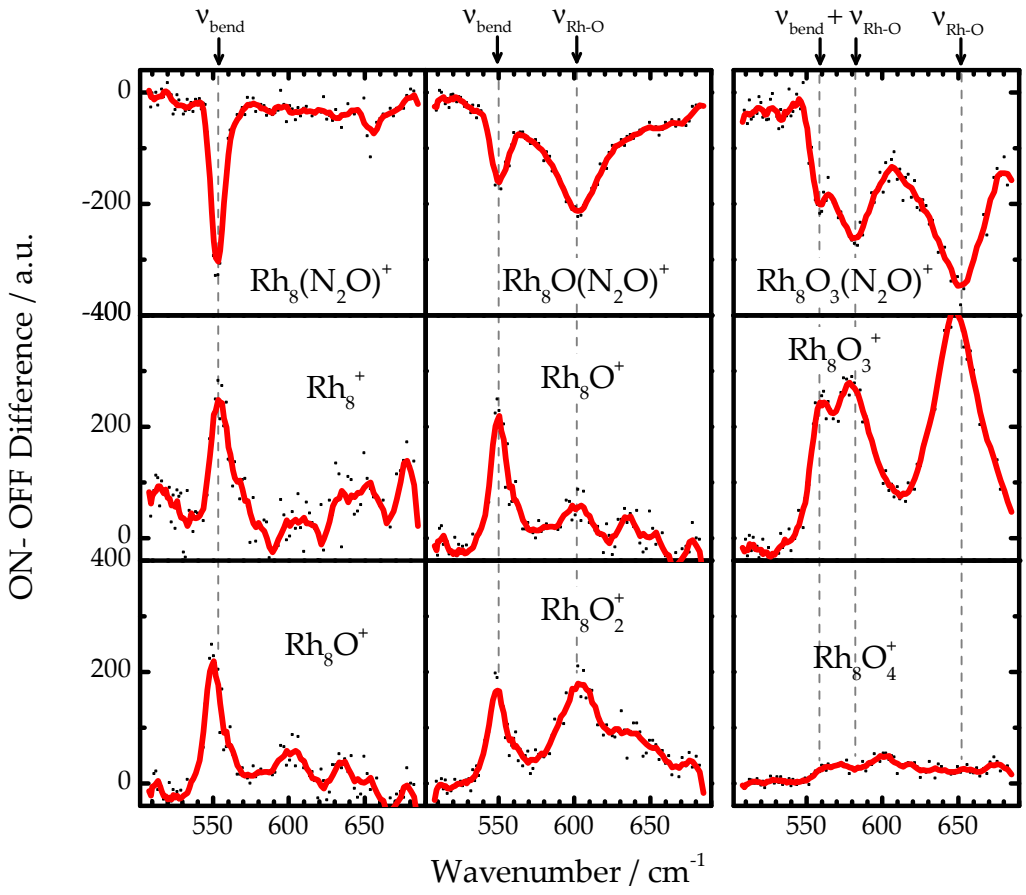

Figure 3.10 IR-MPD spectra of Rh_8^+ based clusters decorated with oxygen and N_2O. Each column shows the spectrum of a N_2O decorated reactive species (top row), the spectrum for the species that would be produced by N_2O desorption (centre row) and the spectrum produced by N_2O reduction (bottom row).

spectrum. In contrast, the next higher oxide $Rh_8O_3(N_2O)^+$, was sufficiently abundant to produce an IR-MPD spectrum and its spectrum is presented alongside those of the decorated bare and monoxide clusters in fig. 3.10. The anomalously low abundance of $Rh_8O_2(N_2O)^+$ suggests that it may be particularly reactive towards one of the loss processes (eqs. (3.1) and (3.2)).

$Rh_8O_3(N_2O)^+$ is the easiest to analyze: The depletions at 555 – 590 cm^{-1} (likely a merged N_2O bend and rhodium-oxygen feature) and 649 cm^{-1} (Rh–O stretch) correspond to equal and opposite features in the $Rh_8O_3^+$ spectrum, while the

enhancement in $Rh_8O_4^+$ is very minimal. We can thus confidently assert that the dominant $Rh_8O_3(N_2O)^+$ loss process is the desorption of N_2O, with only a small fraction undergoing N_2O reaction.

As for all previous cluster sizes both N_2O bend (551 cm^{-1}) and Rh–O stretch (604 cm^{-1}) are observed in the $Rh_8O(N_2O)^+$ spectrum. The Rh–O stretch in particular is diagnostic: The $Rh_8O_2^+$ spectrum has a coincident enhancement of similar magnitude, whereas the enhancement in Rh_8O^+ is minimal. It follows that the major $Rh_8O(N_2O)^+$ loss channel must be the N_2O reduction reaction, with N_2O desorption representing a minor process.

Finally, on the bare cluster, $Rh_8(N_2O)^+$, both reaction and desorption products (Rh_8O^+ and Rh_8 respectively) exhibit an enhancement matching the depletion at the N_2O bend frequency observed for $Rh_8(N_2O)^+$. The two enhancements are approximately the same in magnitude, and we conclude that the desorption and reaction processes account for $Rh_8(N_2O)^+$ depletion in roughly equal amounts. The total depletion in $Rh_8(N_2O)^+$ is less than the sum of enhancements in Rh_8^+ and Rh_8O^+. This is likely due to the fact that the $Rh_8(N_2O)^+$ is being produced at the same time as it depletes, by desorption of N_2O from clusters with multiple adsorbed N_2O molecules (*cf.* section 3.4.2). The true size of the $Rh_8(N_2O)^+$ depletion is thus partially masked.

Larger clusters

By the time we have reached the Rh_9^+ size regime, the clusters exhibit a markedly increased propensity to form complexes with several coadsorbed oxygen atoms and are thus not directly comparable to the clusters presented above. In addition, there is a marked decrease in cluster signal intensity, owing to the way the cluster source was optimized in this experimental run (see section 3.2). Clusters with $n \geq 9$ have therefore been left out of this study.

3.4.5 Summary

The sum of these results allows us to draw a number of general conclusions regarding the reactivity of rhodium (oxide) clusters with N_2O. First, it is important

	Cluster size n =				
m	4	5	6	7	8
0	−−	−−	=	=	=
1	++	++	+	+	+
2		++	−−	+	

Table 3.1 The extent of the N_2O reduction reaction (eq. (3.1)) for $Rh_nO_m(N_2O)^+$ clusters ($n = 4-8$). The icons indicate whether the reaction is dominant (> 80 %, ++), major (80 – 60 %, +), comparable to desorption (60 – 40 %, =), minor (40 – 20 %, −) or minimal (< 20 %, −−).

to note that for all the species examined here, there appears to be no meaningful difference in the behaviour of a cluster when it is pumped by one particular mode or another (*e.g.* N_2O bend or Rh–O stretch), *viz.* the reactivity exhibits no noticeable mode-specificity. This supports the interpretation that the IR-MPD process is thermal, *i.e.* that the source of the energy does not affect the way the cluster reacts.

Second, fragmentation processes, in which one or more transition metal atoms are ejected as a result of infra-red irradiation, do not appear to be a significant loss process for these rhodium clusters with the exception of the $n = 4$ clusters, where the possibility of fragmentation cannot be excluded.

Finally, consider the trends in branching ratio between desorption and reaction as a function of both cluster size and oxygen coverage. Table 3.1 summarizes the qualitative trends deduced in the preceding sections. In all cases the propensity of a $Rh_n(N_2O)^+$ cluster towards N_2O reduction is promoted by the presence of coadsorbed oxygen. The effect of additional coadsorbed oxygen atoms is less clear, suppressing the reactivity of $Rh_6O_2(N_2O)^+$ completely, yet having no suppressing effect for $n = 5, 7$.

In the next section, we present a computational investigation of this oxygen-induced effect, using the case of the Rh_5^+ cluster, which shows it very clearly.

3.5 Computational results

This section presents the structure and reaction pathways for $Rh_5O(N_2O)^+$, determined by computation using density functional theory.

3.5.1 Structure

The first step to understanding the anomalous reactivity of $Rh_5O(N_2O)^+$ lies in determining the geometric — and subsequently electronic — structure of the cluster. The starting points for these calculations were based on the structures of the larger Rh_n^+ clusters, for which spectroscopic evidence exists.[47,48] These showed a clear preponderance for close-packed structures in contrast to the plane-wave DFT predictions by the Kawazoe group.[106] A large number of possible arrangements of oxygen and N_2O on both trigonal bipyramidal (TBP) and square-based planar (SQP) Rh_5^+ clusters were explored, in several spin states ($2S+1 = 5, 7, 9$). Note that the nomenclature is based upon the initial structure, which some cases distored significantly over the course of the structural optimization. The 11-tet and triplet spin state were also tested using a number of trial structures, but were found to be significantly higher in energy than the comparable structures in spin states $2S+1 = 5-9$.

Spectroscopic evidence suggests that N_2O favours the atop or one atom binding mode through the terminal N atom.[166] This fact is reflected in our calculations, with all alternative binding modes being consistently higher on a number of trial systems. As a result, we restricted our structure search to only those systems with end-bound N_2O.

It has also been shown[196] that oxygen is preferentially bound in many-atom sites, and we have biased our structure search hence.

The low-lying structures and energies thus found are shown in figs. 3.11 and 3.12, relative to the energy of the putative global minimum structure found in our calculations (structure TBP7 from fig. 3.11). As the geometric structures of the clusters were found to be approximately independent of spin state, only the structures of the 7-tet state are shown in the diagrams. As the the relative energy

plots show, the trigonal bi-pyramidal (TBP) motif is significantly favoured over the square-base pyramidal (SQP) motif, with the lowest energy SQP structure being over 0.4 eV higher in energy than the TBP global minimum.

The calculations confirm the preference for oxygen to bind in multi-haptic sites, with the lowest energy structures (TBP 6 and 7) both containing oxygen in a three-atom site, more than 0.3 eV more stable than the lowest energy structure containg oxygen in a two-atom site. Structures with N_2O bound to a rhodium vertex that also binds oxygen are favoured over equivalent structures (see *e.g.* the difference between structures TBP3 and TBP7), which is likely due to the increased positive charge on rhodium atoms bound to oxygen. On the other hand neither of the two chemically distinct rhodium sites on the TBP motif ("axial" and "equatorial") are strongly favoured for N_2O binding. This can be seen by comparing *e.g.* structures TBP 6&7 or 4&5, with an energy difference of less than 0.1 eV, which is beyond the accuracy of DFT on these systems.

In almost all cases, the most favoured $Rh_5O(N_2O)^+$spin state was the septet ($2S + 1 = 7$). In contrast, the most stable $Rh_5(N_2O)^+$ structures are all found to have a spin multiplicity of $2S + 1 = 9$. Moreover the most stable states of the dioxide structures found as products of the pathways in section 3.5.2 are of lower spin still ($2S + 1 = 5$). The addition of oxygen has therefore shifted the preference of the cluster to lower spin.

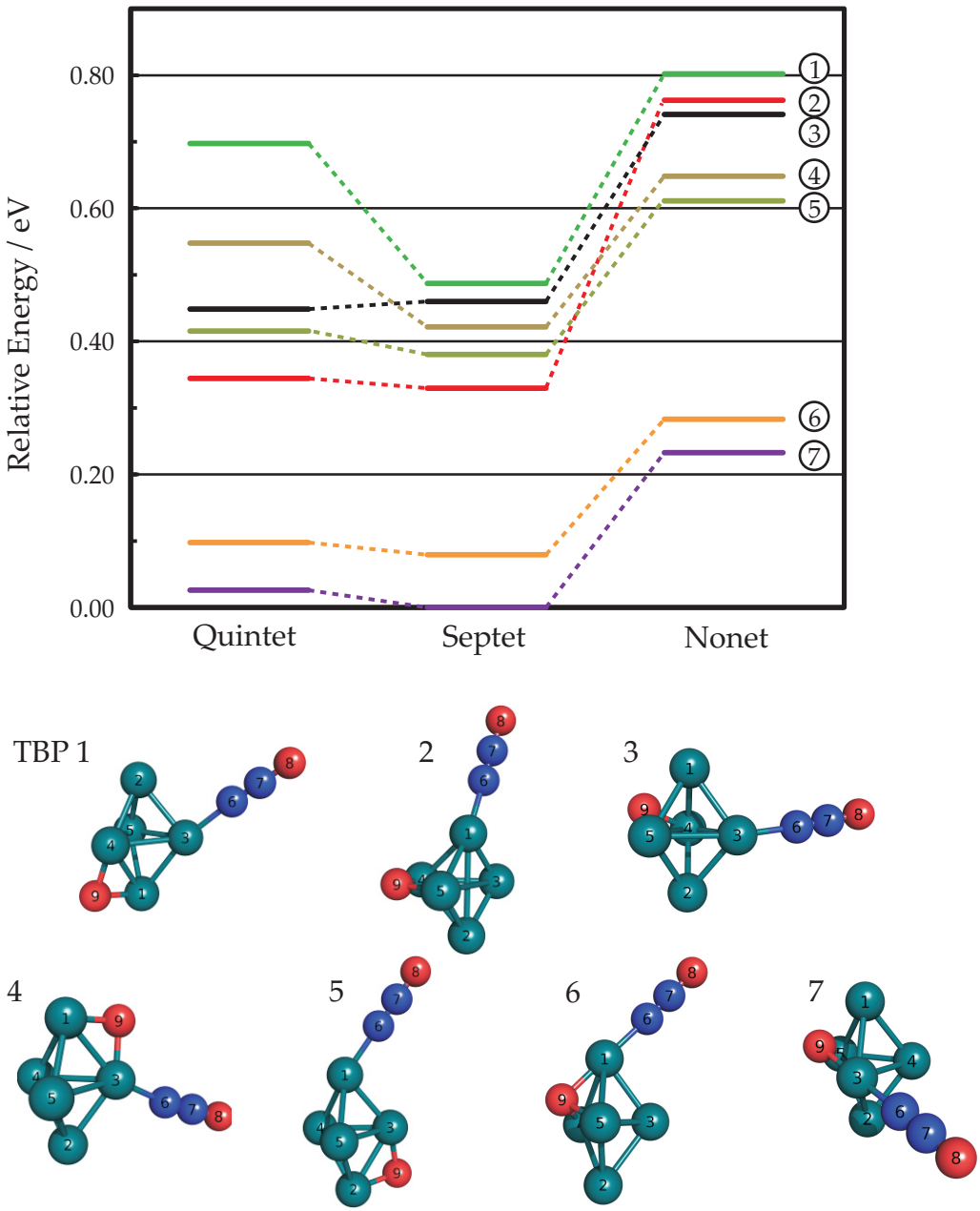

Figure 3.11 Plot showing the calculated energies of the seven lowest lying $Rh_5O(N_2O)^+$ structures based on trigonal bi-pyramidal (TBP) motifs, in three different spin states. Teal spheres indicate rhodium atoms, blue spheres nitrogen, and red ones oxygen. The solid lines indicate the relative energy of each structure, relative to the global minimum found in the calculations (structure 7, in the septet spin state). The dashed lines serve as guides to the eye, indicating the way the energy of a certain structure changes with spin state.

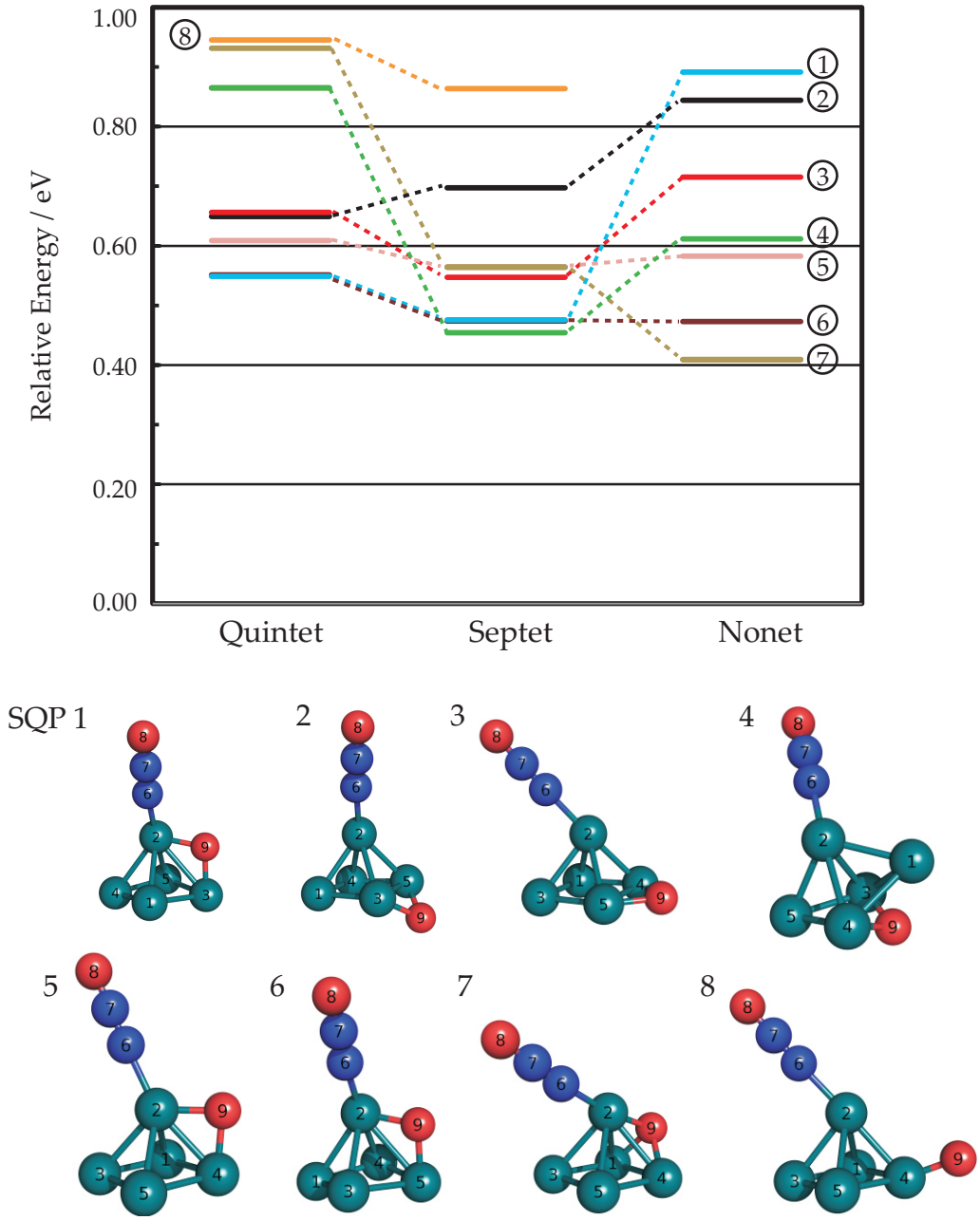

Figure 3.12 Plot showing the calculated energies of the eight lowest lying $Rh_5O(N_2O)^+$ structures based on square base pyramidal (SQP) motifs. The solid lines indicate the relative energy of each structure, relative to the global minimum found in the calculations, *i.e.* structure TBP7 from fig. 3.11. The dashed lines serve as guides to the eye, indicating the way the energy of a certain structure changes with spin state.

3.5.2 Reaction pathways

Having identified likely cluster structures, we can now consider the mechanism by which the cluster surface reaction proceeds. Previous work in this group has investigated the mechanism for reaction on the bare rhodium clusters Rh_n^+.[165] The lowest energy pathway for a variety of clusters was found to involvem at first, a transition state in which the N_2O molecule bends across the surface so as to form a Rh–NNO–Rh bridging intermediate. In a second step the N–O bond cleaves, whereupon the N_2 molecule quickly desorbs, leaving a rhodium oxide cluster.

Taking this work as basis, our calculations have examined the reaction mechanisms involved in the reduction of N_2O on $Rh_5O(N_2O)^+$. Using the lowest energy structures and spin states from fig. 3.11, we calculate intermediates and transition states connecting reactant with products, using the TRIM method detailed in section 2.6.2.

The key minima and transition states along the resultant pathways are shown as an overview in fig. 3.13. In each case, the hollow arrow marks the starting point, with the desorption step being to the left and the reaction pathway to the right. On the whole, the reaction pathway is very similar to that previously observed, with N_2O bending towards a free rhodium atom in the first transition state. Note, however, that the bridging intermediate was found to be only very weakly bound (< 0.1 eV) and in some cases not stable enough for calculations to converge. As the first transition state represents the highest barrier encountered on the reduction pathway in every case, the very weakly bound is likely not to be significant in determining the course of the reaction, so it has been omitted from the pathways.

The key factor determining the branching ratio between surface reaction and desorption is the barrier height for each process. The desorption process is a simple process without many geometric constraints and is thus entropically favoured. Moreover, it directly produces two gas phase molecules and is therefore irreversible. This is in contrast with the reaction pathway which requires a highly coordinated transition state, and which is reversible up to the second transition state. Hence, for reaction to compete efficiently with desorption, the barrier to reaction must be markedly lower than that for desorption. In the context of the

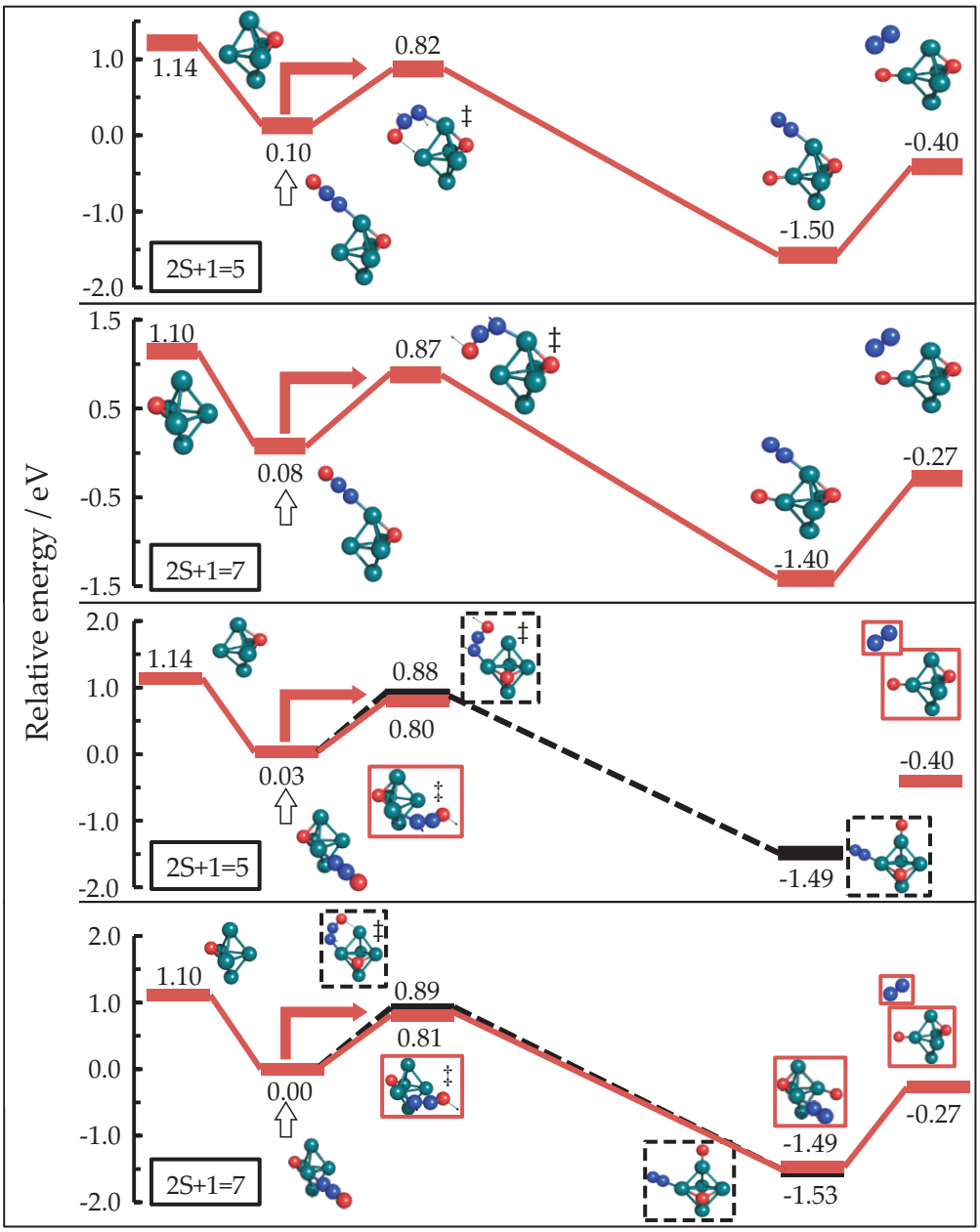

Figure 3.13 Key minima on the N_2O reduction pathways for the four lowest-energy $Rh_5ON_2O^+$ structures/ spin states. The hollow arrow marks the starting structure and the energies are all relative to the global minimum. Where two possible pathways stem from the same structure, the alternative path is shown with a black dotted lines. ‡ mark transition states, which have arrows showing the atomic displacements in the vibrational mode with negative eigenvalue.

	$2S+1$	Isomer[a]	desorption energy[b] / eV	reaction barrier[c] / eV	ΔE[d] / eV
$Rh_5(N_2O)^+$	9	D	0.67	0.70	0.03
	9	C	0.68	0.76	0.08
	9	B	0.73	0.73	0.00
	9	A	0.72	0.76	0.04
$Rh_5O(N_2O)^+$	5	TBP6	1.04	0.72	−0.32
	7	TBP6	1.02	0.79	−0.23
	5	TBP7	1.11	0.77	−0.34
	7	TBP7	1.10	0.81	−0.29

Table 3.2 Calculated N_2O desorption energies and surface reaction barriers for N_2O reduction on the four lowest energy Rh_5^+/Rh_5O^+ isomers. Data for $Rh_5(N_2O)^+$ taken from ref. [165]. [a] Labels for $Rh_5O(N_2O)^+$ refer to fig. 3.11. [b] $E[Rh_nO_m^+] + E[N_2O] - E[Rh_nO_m(N_2O)^+]$ [c] $E[TS] - E[Rh_nO_m(N_2O)^+]$ [d] Reaction barrier – Desorption energy.

IR-MPD experiment, this would mean that significantly fewer IR photons would have to be absorbed for reaction to proceed than for desorption to proceed.

As established above, the first transition state on the pathway represents the highest barrier to reaction. The barriers to reaction and desorption are thus easily extracted from fig. 3.13, and are shown in table 3.2. For every pathway, the barrier to reaction is noticeably lower (by about 0.2 – 0.3 eV), which translates to an appreciable number (4 – 5) of IR photons at the wavenumbers studied (505 – 685 cm^{-1}). The calculations therefore predict that reaction will take place to a significant extent, as borne out by the experimental results.

Comparison with $Rh_5(N_2O)^+$

Having predicted the reactivity of $Rh_5O(N_2O)^+$, we now compare it to the closely related case of $Rh_5(N_2O)^+$. Recall that while almost all of the $Rh_5O(N_2O)^+$ reacts, the opposite is true for $Rh_5(N_2O)^+$ (fig. 3.14). It is therefore natural to compare the reaction pathways for these two species in order to understand this difference. Figure 3.14 and table 3.2 contrast the pathways and the barriers involved in them. We note that in the case of $Rh_5(N_2O)^+$, the barrier to reaction is always at least

equal ($\Delta E \geq 0$) to the barrier for desorption. Therefore, the entropic effects noted above mean that desorption dominates over reaction. This is in contrast to the case for $Rh_5O(N_2O)^+$, examined above, where the difference in barriers means that reaction can effectively compete with desorption.

Comparison of the reaction barriers of $Rh_5(N_2O)^+$ and $Rh_5O(N_2O)^+$ indicates that the difference between the two species does not lie in the barrier to reaction as these are very similar in each case. On the other hand, the presence of the oxygen has a profound effect on the the barrier to desorption, which is about 0.4 eV larger for $Rh_5O(N_2O)^+$ than for $Rh_5(N_2O)^+$. The coadsorbed oxygen thus acts to stabilize the N_2O molecule on the surface of the cluster, and this means that the first channel to open upon successive absorption of photons is the reaction channel, which allows the reaction to proceed.

These results are consistent with those obtained by Yamada *et al.*[206] Studying neutral rhodium clusters Rh_n ($n = 10 - 28$), they found that the presence of some surface oxygen increased the rates of reaction with N_2O considerably. They also noted that while one (or in the case of larger clusters, two) oxygen atom boosted the reactivity, further oxygen reduced reactivity.

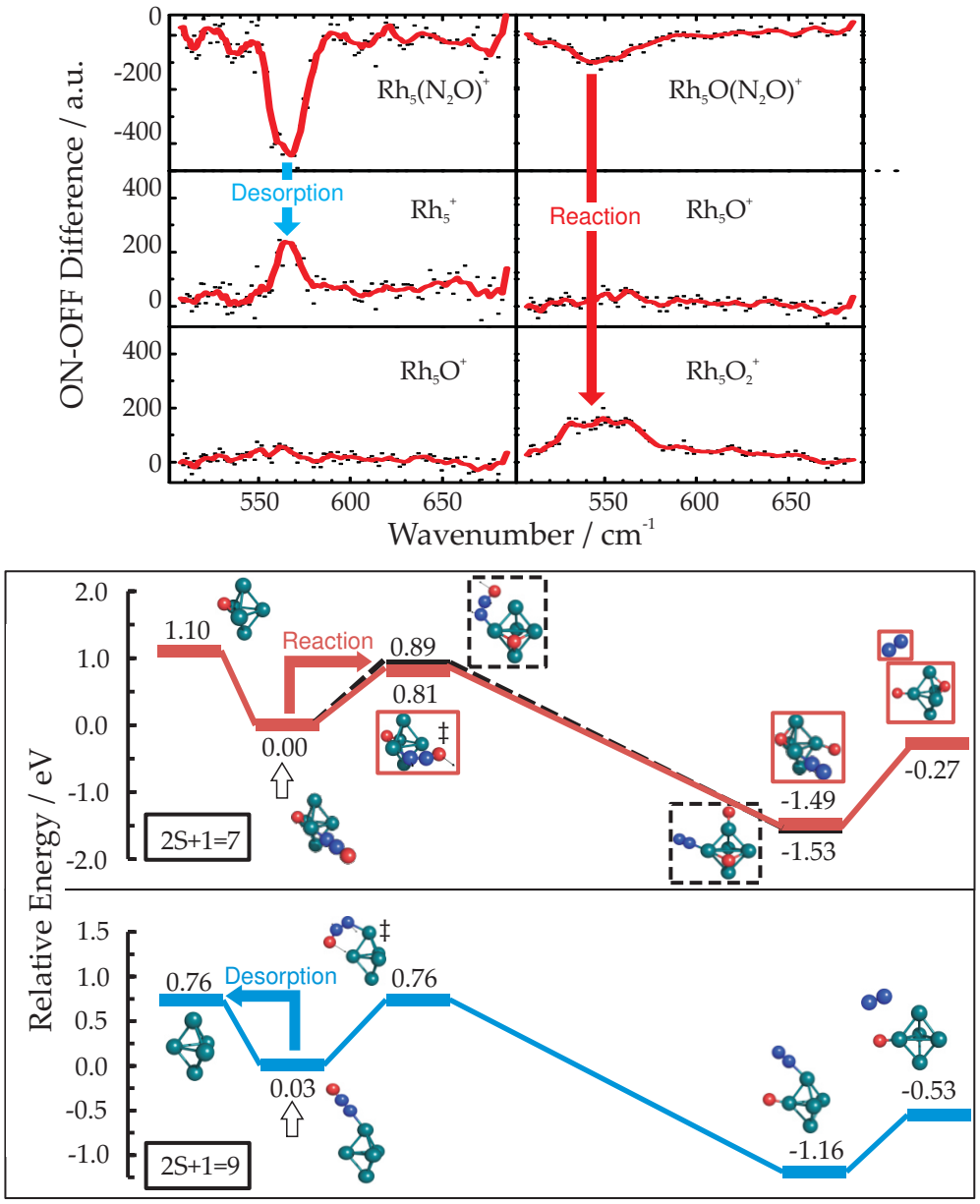

Figure 3.14 (Top) IR-MPD spectra of $Rh_5O(N_2O)^+$ and $Rh_5(N_2O)^+$ and the potential products of desorption and reaction. (Bottom) Calculated N_2O reduction pathways for (red) $Rh_5O(N_2O)^+$ and (blue) $Rh_5(N_2O)^+$ based on TBP motifs. The energies are relative to the global minimum structure for each species. ‡ mark transition states, while hollow arrows mark starting structures. The relative differences between desorption and reaction barriers in each case lead to different dominant processes, marked by the red and blue arrows.

3.6 Conclusion

IR-MPD has been successfully employed to study Rh_n^+ ($n = 4-8$) clusters decorated with N_2O. Using the loss of N_2O as a tag, a number of aspects of the N_2O band became evident. Adsorption on the cluster surface red-shifts the N_2O bend, and this red shift increases with increasing cluster size. The band position does not appear to be clearly converging to a limit (bulk) value, as previously observed for other clusters.[45] A similar red shift is observed upon the adsorption of multiple N_2O molecules. One possible explanation for this similarity might be that N_2O bend frequency is affected by the electron density on the cluster: an increase in cluster size means a lessening of the effect of the positive charge and an effective increase in electron density. Similarly, N_2O is known to act as a Lewis base (electron donor) on platinum surfaces,[203] and thus the presence of additional N_2O adsorbates can also be considered as an effective increase in electron density.

In addition, the reduction of N_2O on the surface of $Rh_nO_m^+$ ($n = 4-8$, $m = 0-2$) clusters has been successfully induced *via* the multiple absorption of infra-red photons, with no difference observed pumping either N_2O bend or Rh–O stretch, which is taken as evidence that the reaction is thermal. On the larger bare clusters ($n \geq 6$), the process proceeds in roughly equal proportion with the competing N_2O desorption process, while on the smaller bare clusters reaction was not observed.

Coadsorbed oxygen has a profound impact upon the infra-red triggered reactivity. In all cases, the presence of a single oxygen atom promotes the reactivity. This is most clearly observed for $n = 5$, where the presence of a single oxygen atom reverses the reactivity from being dominated by desorption on the bare cluster Rh_5^+, to being dominated by reaction on Rh_5O^+. Further addition of oxygen does not have such a uniform effect, and may thus merit further study.

The case of $Rh_5O(N_2O)^+$ was further investigated with calculations using DFT. A trigonal bipyramidal motif with axially adsorbed N_2O and oxygen bound in a hollow (three atom) site is the global minimum. Reaction profiles were hence calculated for $Rh_5O(N_2O)^+$ and compared with the previously obtained profiles for $Rh_5(N_2O)^+$. The difference between the barriers for desorption and reaction, which governs the branching ratio, is distinct in the two cases.

On the bare cluster the two barriers are very similar in energy, explaining how the entropically favoured desorption process dominates. On $Rh_5O(N_2O)^+$, the desorption barrier is raised appreciably (*ca.* 0.4 eV) with respect to the barrier on the bare cluster. In the context of the experiments, this means that significantly fewer (*ca.* 5 – 6) IR photons need to be absorbed to reach the top of the reaction barrier than to desorb N_2O. Therefore reaction effectively competes with desorption on the $Rh_5O(N_2O)^+$ cluster.

These results illustrate the potential for IR-MPD as a technique suitable for studying surface processes on size-selected clusters, and is readily extended to study even more complex reactions (as we will show in chapter 4). Comparison with results from DFT demonstrate that the technique is exquisitely sensitive to changes in the energy landscape topology, and can thus be combined with calculation to form a powerful probe.

CHAPTER 4

Bimolecular reactions on platinum clusters*

This chapter describes a significant development over the work on rhodium clusters (chapter 3), extending the IR-driven cluster surface chemistry approach to encompass bimolecular reactions. Specifically, we have investigated the analogue to the oxidation of carbon monoxide on extended platinum surfaces ($CO_{(ads)} + O_{(ads)} \longrightarrow CO_{2(g)}$) on the surface of small platinum cluster cations $Pt_nO_m^+$ ($n = 3-7$, $m = 2, 4$). These small cluster cations have been decorated with CO and subjected to the infrared beam of FELIX in the range $400 - 2100\,cm^{-1}$.

The clusters were first probed by rare gas tagged IR-MPD, and evidence of both dissociatively and molecularly adsorbed oxygen on the cluster surface was found. Analysis of the CO band of the decorated $Pt_nO_mCO^+$ clusters revealed a red shift in CO band position with increasing cluster sizes, in accordance with previous results[44] as well as a blue shift with increasing O_2 coverage and both

*The work presented in this chapter is the result of joint experimental runs with the Meijer group (FHI Berlin). The Berlin group focussed on the analysis of the spectroscopy and structure of the platinum clusters — see C. Kerpal et al. "Structures of Platinum Oxide Clusters in the Gas Phase". *The Journal of Physical Chemistry A*, **117**: 1233–1239, (2013). Our group concentrated on the reactivity of the platinum clusters, presented in this chapter and published in adapted form as A. C. Hermes et al. "Infrared driven CO oxidation reactions on isolated platinum cluster oxides, $Pt_nO_m^+$". *Faraday Discussions*, **157**: 213–225, (2012).

effects are interpreted in the context of a backbonding model.

In a separate experiment, the infrared FELIX beam was used to heat $Pt_nO_mCO^+$ clusters *via* the CO stretch around 2100 cm^{-1}. Clear evidence for the infrared driven bimolecular oxidation of CO was found on all cluster sizes in the form of CO_2 loss and formation of odd oxide clusters $Pt_nO_{m-1}CO^+$. The branching ratio of oxidation *vs.* desorption was found to be constant at approximately 40 % : 60 % across the range of clusters studied, contrasting the strong size fluctuations that have been observed in other work. Preliminary DFT calculations identified key stationary points on the $Pt_4O_2CO^+$ reaction pathway, finding a CO binding energy of 2.7 eV and a reaction barrier of 2.0 eV.

4.1 Introduction

4.1.1 Platinum clusters

Platinum is widely used as a catalyst in a range of industrial processes[208] — *inter alia* platinum catalysts are used in nitric acid synthesis, dehydrogenation and hydrogenation reactions as well as in the automobile three-way catalytic converter.[169]

Considering the importance of these processes, it comes as no surprise that many of the corresponding reactions have been studied using metal clusters as model systems. The work of Kaldor *et al.* demonstrated the ability of neutral platinum clusters $Pt_n (n = 1 - 25)$ to dehydrogenate hydrocarbons such as methane.[209] These reactions were investigated in more detail by Bondybey and coworkers,[95] who noted the production of carbenes $Pt_nCH_2^+$ as a result of dehydrogenation. The group of Schwarz has explored the gas-phase reactions of platinum with a variety of inorganic substrates *via* fourier-transform ion cyclotron resonance (FT-ICR), finding a multitude of size-specific effects with respect to several substrates.[210]

4.1.2 CO oxidation on platinum

This work explores what is one of the most well-known examples of platinum catalyzed reactivity and the process which takes places in the catalytic converter, namely the oxidation of CO which can be summarized as

$$CO_{(ads)} + O_{(ads)} \longrightarrow CO_{2(g)} . \tag{4.1}$$

This reaction is one of the most studied reactions of its type.[211] It is believed to proceed *via* the Langmuir-Hinshelwood mechanism,[212] following absorption of CO and dissociative absorption of O_2. Temperature programmed reaction (TPR) studies on Pt(111) show that the reaction proceeds *via* at least two distinct mechanisms. One mechanism, producing so-called α-CO_2, is a result of the reaction of CO with hot oxygen atoms produced by O_2 dissociation at *ca.* 160 K, and therefore requires adsorbed O_2 *molecules*. The β-CO_2 mechanism, observed most efficiently at 260 K, involves the reaction of CO with co-adsorbed O *adatoms*, which are a result of dissociatively adsorbed O_2, and is therefore highly sensitive to the local environment.[213] The ratio of α *vs.* β-CO_2 is very sensitive to the ratio of O to CO coverage.

For small deposited platinum clusters, reaction (4.1) was first investigated by Heiz *et al.*,[214] who deposited small platinum clusters ($n \leq 20$) on a MgO(100) film. Using TPR, they showed that platinum clusters with 5 or more platinum atoms successfully catalyze this reaction. The efficiency of CO_2 production was found to vary drastically with cluster size — in particular a step change in efficiency in going from Pt_8 to Pt_{15} was ascribed to a change in geometry from pseudo two- to three-dimensional structures.

The first investigation of this reaction on isolated gas-phase clusters was undertaken by Shi *et al.*[215], who were able to observe a full catalytic cycle involving the oxidation of CO on anionic Pt_n^- clusters ($n = 3 - 6$). Using guided ion beam techniques, the clusters were first oxidized by a N_2O/O_2 mixture and eventually reduced by reaction with CO. The authors noted that the efficiency of reaction increased with cluster size from $n = 3$ to $n = 6$. In a similar approach, Balaj and coworkers[216] studied the reactions of cationic platinum clusters $Pt_n^+ (n = 6 - 8)$

exposed to a CO/N_2O mixture in an ICR cell. The results indicate that the reaction proceeds efficiently on all clusters, but that the sequential absorption of CO rapidly leads to poisoning of the reaction.

In this work, we adopt a hybrid approach to study reactions on clusters. First, isolated platinum clusters are decorated with reactive precursors (CO and O_2) under thermal conditions (*ca.* 300 K). This permits the observation of intermediate species that are not usually observable under single collision conditions. The clusters are subsequently "heated" by pumping a vibrationally allowed transition (the CO stretch) using infrared radiation. In this way, the internal energy of the cluster is raised, triggering a variety of processes such as CO desorption and CO oxidation. By simultaneously monitoring all mass channels *via* mass spectrometry we are able to match depletions in one channel to enhancements in another channel, and thus obtain a clear picture of any reactive dynamics resulting in moiety loss from the clusters.

4.2 Experimental method

The data were collected using the setup described in section 2.3. An isotopically enriched ^{194}Pt foil (96.4 % enrichment, Oak Ridge National Laboratory) wrapped around a target rod served as a source of platinum, while the backing gas was helium (8 bar) seeded with 1 % argon. The two late mixing valves were used to seed O_2 (typical backing pressure 500 mbar) and CO (1.2 bar) into the cluster channel. The two valves were be tuned to produce a range of $Pt_nO_mCO^+$ clusters with different oxygen / CO coverage, as required.

All FELIX spectra were recorded at 5 cm^{-1} intervals and averaged over several scans to improve the signal to noise ratio. The spectra cover the range 400 – 2100 cm^{-1}, encompassing both metal oxides Pt–O modes as well as CO stretch modes. The reactivity studies focussed on the CO stretch region around 2100 cm^{-1}. The majority of the scans were performed at full FELIX power, to maximize our chances of triggering the reactions. However, the full power of FELIX leads to some saturation (power broadening) effects on the spectra, and so a few spectra were recorded with the attenuated (5 dB) beam, to obtain a better spectral resolution.

Using this setup, two distinct experiments are performed. First, IR-MPD spectra of the platinum complexes were recorded using argon as a messenger (*cf.* section 2.3.3). That is, we monitor the loss of Ar in the process

$$\mathrm{Pt}_n\mathrm{O}_m\mathrm{COAr}^+ \;+\; \mathrm{IR} \quad\longrightarrow\quad \mathrm{Pt}_n\mathrm{O}_m\mathrm{CO}^+ \;+\; \mathrm{Ar}\;. \tag{4.2}$$

Note that the Ar tagged clusters form readily even at the 300K temperature used in this experiment. In a second experiment we investigate the infrared induced reactivity of CO on the platinum cluster, more precisely the oxidation reaction

$$\mathrm{Pt}_n\mathrm{O}_m\mathrm{CO}^+ \;+\; \mathrm{IR} \quad\longrightarrow\quad \mathrm{Pt}_n\mathrm{O}^+_{m-1} \;+\; \mathrm{CO}_2\;, \tag{4.3}$$

versus CO desorption

$$\mathrm{Pt}_n\mathrm{O}_m\mathrm{CO}^+ \;+\; \mathrm{IR} \quad\longrightarrow\quad \mathrm{Pt}_n\mathrm{O}^+_{m} \;+\; \mathrm{CO}\;. \tag{4.4}$$

Loss of $\mathrm{Pt}_n\mathrm{O}_m\mathrm{CO}^+$ and corresponding enhancement in $\mathrm{Pt}_n\mathrm{O}^+_{m-1}$ serves as a signature for reaction (4.3), while enhancement in $\mathrm{Pt}_n\mathrm{O}^+_m$ indicates reaction (4.4). Our setup deliberately does not include a mass selection stage prior to extraction. This means that we are able to collect the spectra of all the species simultaneously.

However, as we saw in chapter 3, the multiple potential sources and products of each species mean that it can be difficult to directly correlate enhancements and depletions. To simplify this process, we use molecular oxygen (O_2) in the formation of our decorated platinum clusters $\mathrm{Pt}_n\mathrm{O}_m\mathrm{CO}^+$ and $\mathrm{Pt}_n\mathrm{O}^+_m$. As a result clusters with *even* numbers of oxygen ($m = 0, 2, \ldots$) are formed preferentially. The products of eq. (4.3), $\mathrm{Pt}_n\mathrm{O}^+_{m-1}$, will therefore be clusters with $(m-1)$ O atoms, *i.e.* an *odd* number of oxygen atoms. In contrast, the other major IR-induced process, CO desorption (eq. (4.4)), leaves the number of oxygen atoms adsorbed on the cluster unchanged. As the intensity of odd oxygen clusters formed in the source is very low, any enhancement in odd oxygen cluster signal is therefore a clear signature for the oxidation reaction (4.3).

4.2.1 Data processing

The data were processed in the same way as for the Rh experiments (*cf.* section 3.2.1): For each IR-MPD spectrum, a portion of the mass spectrum with no features (the first 500 points) was used as a background and subtracted, to minimize systematic error. Each IR-MPD spectrum shows the raw data (black dots •) and a three point adjacent average (red line —) used to compensate for the bandwidth of the FELIX beam. For comparison with calculated results, some of the IR-MPD spectra were converted to absorption cross-sections $\sigma(\nu)$ *via*

$$\sigma(\nu) = \ln \frac{I(\nu)}{I_0} \Big/ P(\nu)\,, \tag{4.5}$$

where $P(\nu)$ is the FELIX power at a wavelength ν, $I(\nu)$ the measured intensity at that wavelength and I_0 the intensity in the absence of FELIX. Note that eq. (4.5) defines the *depletion* crossection, that is, a depleted signal will give a negative crossection. See ref. [101] for details of this procedure.

4.3 Computational method

To accompany the experimental work, we performed calculations on $Pt_nO_2CO^+$ ($n = 3-5$) to determine structural minima as well as reaction pathways.

All the calculations were performed using Density Functional Theory as implemented in Turbomole (see section 2.6). In common with our previous findings[166] no single functional provided optimal performance for every single type of calculation. As discussed in section 3.3.1, the TPSSh[156,160] functional represents a good compromise for both structure search and the calculation of reaction profiles. Furthermore, the non hybrid version of the functional, TPSS, has previously been used in comparison with Pt_n spectra, yielding good agreement with the experimental data.[108] In the present work, the performance of TPSS was very similar to that of TPSSh, favouring the same low energy structures as well as putative global minima, with only small differences in energies. Hence, the computationally cheaper TPSS functional was employed throughout.

Triple-ζ valence basis sets def2-TZVP[199,200] were once again used for all atoms (*cf.* section 3.3.1), with def2-ecp effective core potentials substituting the core electrons of Pt. As work on small platinum clusters has found the effect of including spin orbit coupling (SOC) to be marginal,[108] SOC effects were not included in the present calculations.

As a starting point for the structure search we generated a wide range of $Pt_nO_2^+$ structures by using DFT-based basin hopping.[217] Basin hopping is a variant of Monte Carlo (MC) sampling[218] in which each new random structure is optimised prior to the MC step in the search routine. In this way, the PES is transformed into regions (basins) associated with each minimum, which do not have barriers between them. This increases the probability of inter-basin hopping, decreasing the probability of becoming trapped in a local minimum, allowing a larger number of configurations to be sampled. The lowest energy structures of $Pt_nO_2^+$ thus found were then decorated with CO in a variety of potential absorption sites, and the whole structure reoptimized. Normal mode analysis (see section 2.6.2) confirmed the identity of the minima found as well as yielding vibrational frequencies. A number of spin states were explored for each cluster size, with the doublet spin state ($2S + 1 = 2$) lying significantly lower than the other spin states. Therefore, all the calculations presented herein were performed in this spin state.

To facilitate comparison of experimental and computed spectra, the stick spectra produced by the calculation were convoluted with gaussian lineshapes ($18\,cm^{-1}$ full width at half maximum).

4.4 Experimental results

Before we delve into the details of the IR-MPD spectroscopy it is essential to understand what species are produced by our source and hence arrive at the detector. A typical time-of-flight mass spectrum is shown in fig. 4.1, illustrating the range and intensity of complexes produced. Figure 4.1b shows an expanded view of the section of the mass spectrum corresponding to Pt_4^+ based clusters. Aside from the dominant bare cluster peak Pt_4^+, the major species are complexes of Pt_4^+ with a number of coadsorbed O and CO. In particular, species with even

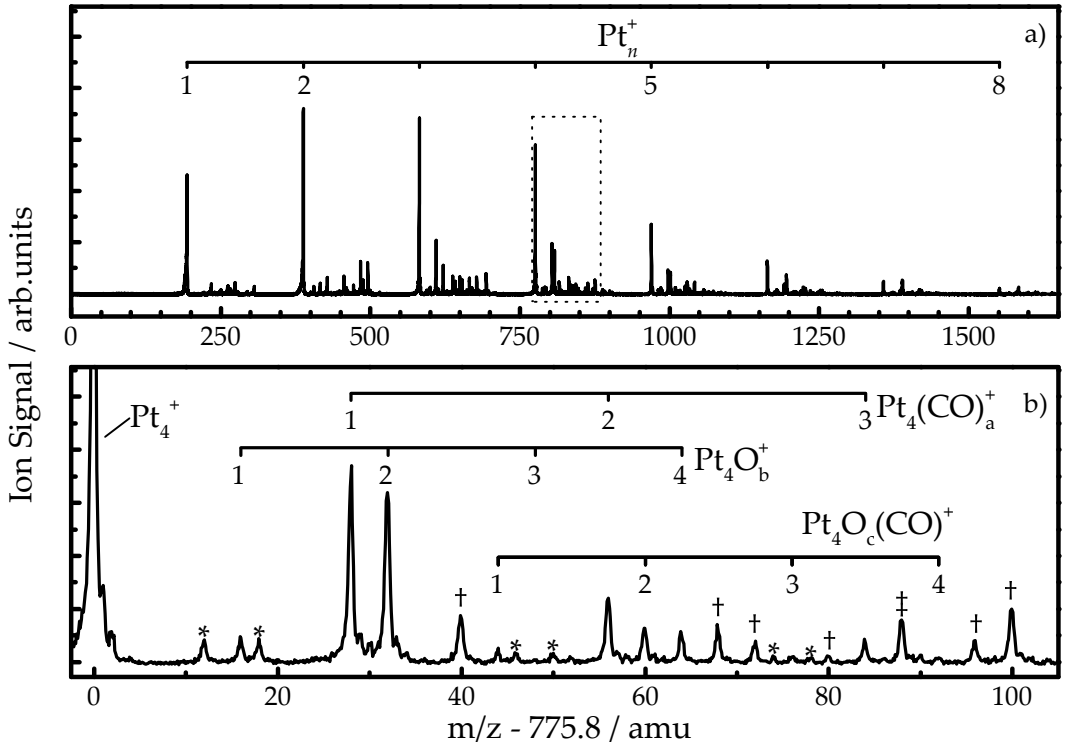

Figure 4.1 Mass spectra recorded in the absence of infrared irradiation. a) Full mass spectrum of the signficant species in the beam. b) Expanded section of the mass spectrum corresponding to Pt_4^+ clusters. (*) Minor Pt_4X^+ species (X = N, H_2O, *etc.*), (†) Ar-tagged species, (‡) $Pt_4O_2(CO)_2^+$.

numbers of oxygen ($b, c = 2$ or 4 in fig. 4.1) are noticeably more intense than their counterparts containing odd numbers of oxygen, reflecting the use of molecular oxygen O_2 as a source of oxygen. Although this might suggest that the O_2 is also molecularly bound on the surface, the mass spectrum itself cannot give any indication as to the nature of the adsorption. Ar-tagged versions of all the intense peaks are present in the mass spectrum at 40 amu above the mass of the original peak. It is worth noting that the clustering efficiency was significantly reduced in the absence of the seeding gas Ar, which suggests it may be involved in the clustering process itself. For example, Ar atoms coadsorbed upon the cluster surface may desorb during the adsorption of another species onto the cluster,

which helps to dissipate the binding energy of the other species

$$\mathrm{Pt}_n\mathrm{Ar}_l^+ \;+\; \mathrm{CO} \;\longrightarrow\; \mathrm{Pt}_n\mathrm{CO}^+\mathrm{Ar}_x \;+\; (l-x)\mathrm{Ar}\;. \tag{4.6}$$

4.4.1 IR-MPD spectroscopy

The spectroscopy of the oxide platinum clusters $\mathrm{Pt}_n\mathrm{O}_m^+$ (without coadsorbed CO) was performed alongside the work here presented, and analyzed by our collaborators in a separate publication,[207] so we will not present it here.

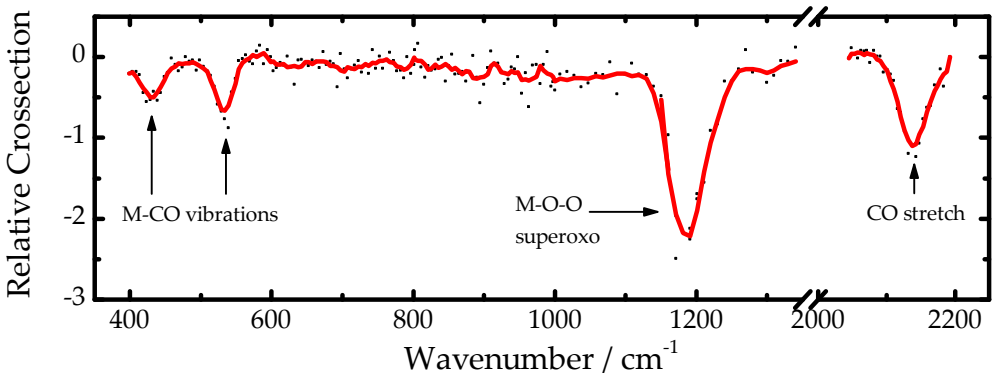

Figure 4.2 IR-MPD spectrum of $\mathrm{Pt}_2\mathrm{O}_2(\mathrm{CO})\mathrm{Ar}^+$.

Of the complexes that have both O_2 and CO coadsorbed, only $\mathrm{Pt}_4\mathrm{O}_2\mathrm{CO}^+$ and $\mathrm{Pt}_2\mathrm{O}_2\mathrm{CO}^+$ showed a clear signal across the range studied (400 – 2100 cm^{-1}). The spectrum of $\mathrm{Pt}_2\mathrm{O}_2\mathrm{CO}^+$, recorded *via* an Ar tag, is quite simple (fig. 4.2). It contains two smaller features at 425 cm^{-1} and 475 cm^{-1}, a broad, intense peak at 1190 cm^{-1} and a strong peak at 2140 cm^{-1}. By comparison with the bare oxide spectra[207] as well as data from extended surfaces[219,220] we can assign the two smaller peaks at 425 cm^{-1} and 475 cm^{-1} to M–CO vibrations, while the broad, intense feature at 1190 cm^{-1} is due to a a *superoxo* (*i.e.* M–O–O) stretch. The peak at 2140 cm^{-1} is a CO stretch.

The IR-MPD spectrum of $\mathrm{Pt}_4\mathrm{O}_2\mathrm{CO}^+$, also recorded *via* an Ar tag, is shown in Figure 4.3a across the regions containing metal oxygen modes (400 – 1050 cm^{-1}) as well as the CO vibrational fundamental (1900 – 2100 cm^{-1}).

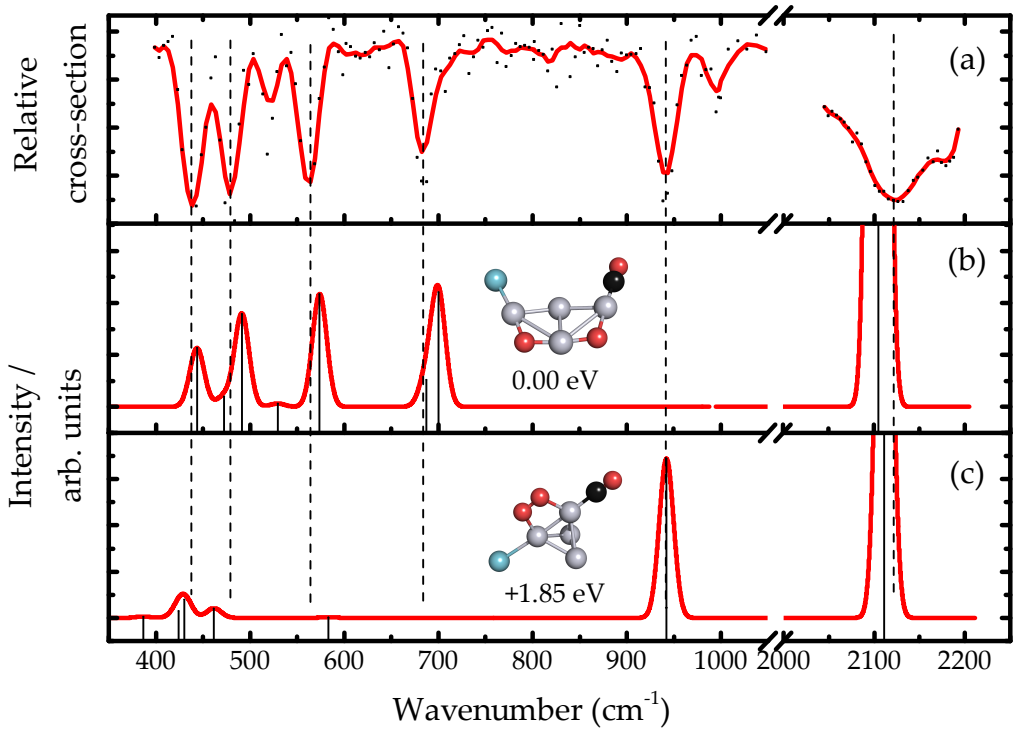

Figure 4.3 (a) Experimental IR-MPD spectrum of $Pt_4O_2(CO)Ar^+$. (b) Calculated spectrum of the lowest lying isomer found. (c) Calculated spectrum of a low-lying *peroxo* type structure, labelled with the energy relative to the (b) structure. Platinum atoms are white, oxygen red, argon dark turquoise and carbon black.

We can assign the features observed experimentally by considering the simulated spectra of the calculated $Pt_4O_2CO^+$ structures. The spectrum of the putative global minimum structure is shown in fig. 4.3b. This structure consists of a buckled two-dimensional Pt structure, with O_2 dissociatively adsorbed on the surface and CO bound atop (μ_1). The simulated spectrum captures most of the major features in the range 400 – 1050 cm^{-1} very well, and confirms their identity as Pt–O modes. The CO band at 2125 cm^{-1} is similarly well reproduced.

However, one strong feature that is experimentally observed at *ca.* 940 cm^{-1} is not accounted for by the spectrum of the global minimum. On the basis of our calculations, two possibilities present themselves.

The first is a structure with an atop bound oxygen atom. These structures have

calculated Pt–O features up to *ca.* 900 cm^{-1}, and typically lie > 1 eV above the putative global minimum. However, they also exhibit additional features in the range 400 – 600 cm^{-1} for which no evidence exists.[207]

The alternative explanation is a structure containing O_2 bound in a *peroxo* fashion. Oxygen bound in this fashion to extended platinum surfaces has been previously observed to exhibit vibrational frequencies up to 930 cm^{-1}.[219,220] Our calculations support this notion, with several peroxo-type isomers having bands at frequencies around 940 cm^{-1}. An example, chosen for its match to the experimental spectrum, is shown in fig. 4.3c. As we can see, the simulated spectrum matches the experimental feature quite well, and does not contain additional unexplained features at low energy. It should be noted that all of the peroxo type structures calculated have peroxo bands in the range 850 – 950 cm^{-1} and lie > 1.4 eV above the putative global minimum. Given the potential need to scale the calculated spectrum as well as potential spectral shifts caused by coadsorbed Ar atoms an assignment to a unique peroxo structure is therefore not feasible.

On extended surfaces, both the aformentioned alternatives are possible. Temperature programmed desorption experiments with isotopically labelled oxygen have found evidence of oxygen bound both dissociatively and moleculary, showing O_2 evolution between 150 – 200 K (molecularly absorbed) and > 700 K (dissociatively absorbed).

Irrespective of the exact assignment of the 940 cm^{-1} feature, it is clear that at least one additional isomeric form of $Pt_4O_2CO^+$ beyond the global minimum must be present in the cluster beam. Both possibilities involve structures lying significantly above the putative global minimum — it is therefore surprising to observe these but not some other low-lying isomeric forms. Nevertheless, it is possible that a portion of the $Pt_4O_2CO^+$ in the beam have become trapped in such a high energy structure — for example, after initial clustering with several Ar atoms, the structure can become trapped in a higher energy isomer if the Ar coadsorbates boil off without the possibility for structural rearrangement. This would suggest that the presence of Ar is a more significant perturbation of the structure than is often assumed. Indeed, recent studies of bare platinum structures using Ar as a messenger showed that the presence or absence of the Ar must be

accounted for in the calculations for a good match.[108]

While the CO vibrational fundamental is not a very sensitive probe of the geometry of the underlying metal framework, it is sensitive to changes in both cluster size and coadsorbates, and this will be discussed in the next section.

Variations in the CO band

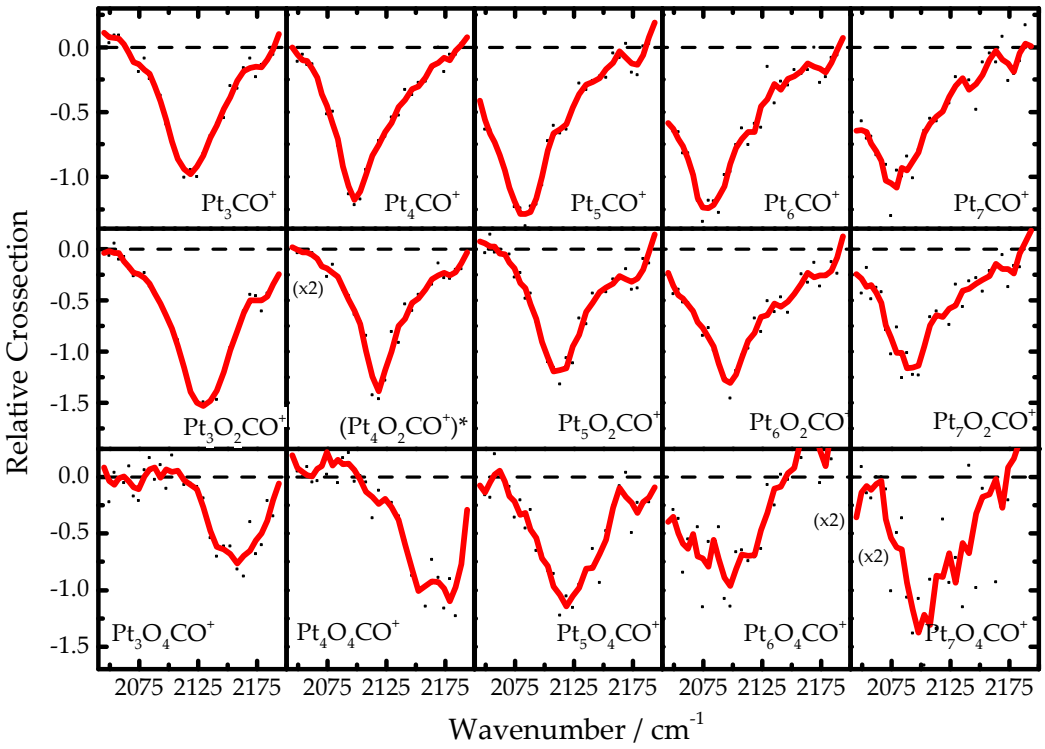

Figure 4.4 IR-MPD spectra of isolated $Pt_nO_mCO^+$ ($n = 3-7, m = 0, 2, 4$) clusters collected at full FELIX power. (*) The $Pt_4O_2CO^+$ is compensated for depletion from $Pt_4O_2COAr^+$ (see also section 4.4.2).

The CO band of $Pt_nO_mCO^+$ complexes can be studied without the need for a coadsorbed Ar messenger: the resonance of the CO band is sufficiently intense as to directly induce a depletion of the complex, either by desorption of CO or, as we will see later, oxidation of CO followed by desorption of the CO_2 formed.

The IR-MPD depletion spectra of $Pt_nO_mCO^+$ ($n = 3-7, m = 0, 2, 4$) obtained by CO-loss are shown in fig. 4.4 in the range $2050 - 2200\,cm^{-1}$. For all of the

complexes shown, the CO band lies in the range 2075 – 2175 cm^{-1}. Two trends are evident from the spectra: first, for otherwise identical species, there is a general shift in the position of the CO band, ν_{CO}, to lower frequency as the size n of the underlying cluster increases (*i.e.* across fig. 4.4). This matches the data previously obtained by Gruene *et al.* for the binding of CO on bare platinum clusters.[44] The trend can be explained in the context of a cluster back-bonding model,[221] where the decrease in positive charge density with increasing n leads to an increase of π-backdonation into an antibonding orbital of CO. The CO bond is thus weakened, which leads to a red shift in absorption frequency. The limit of this trend is represented by extended surfaces, and indeed the vibrational frequency of CO adsorbed on Pt(111) is measured to be $2095 \pm 10\,cm^{-1}$.[222,223]

The second phenomenon that is apparent is that there is a noticeable blue shift in CO band position with increasing O coverage (down fig. 4.4). This can also be understood in the simple model, if we consider the oxygen adatoms as locally fixing electron density and reducing the amount of π-backdonation to CO, strengthening the CO bond and blue-shifting its absorption frequency. A similar effect was observed for H-atoms co-adsorbed with CO on cobalt cluster cations.[224] The fact that this effect is most strongly observed on the smaller ($n = 3, 4$) clusters can also be explained with this interpretation, as the extent of electron fixing provided by a given number of oxygen atoms is greater on a smaller metal cluster.

All of the CO bands shown in fig. 4.4 are broad. This is, in part, due to saturation of the CO band by the full power of FELIX (up to 80 % signal depletion is observed at the peaks of the CO bands). We can mitigate this effect by reducing the power of the FELIX beam. Unfortunately, the reduced infrared intensity also means that that the signal to noise is reduced, and only the cluster sizes $n = 4 - 6$ showed a spectral signature clearly above the noise level. Their IR-MPD spectra, recorded with a beam attenuation of 5 dB, are shown in fig. 4.5. As we can see, the CO bands are indeed much narrower when the FELIX beam is attenuated, providing us with more tightly defined peak position. The variation of the peak positions follows that observed at full power (fig. 4.4).

The peak centres extracted from attenuated spectra (where possible) *via* fits of gaussian curves are shown, by way of summary, in table 4.1.

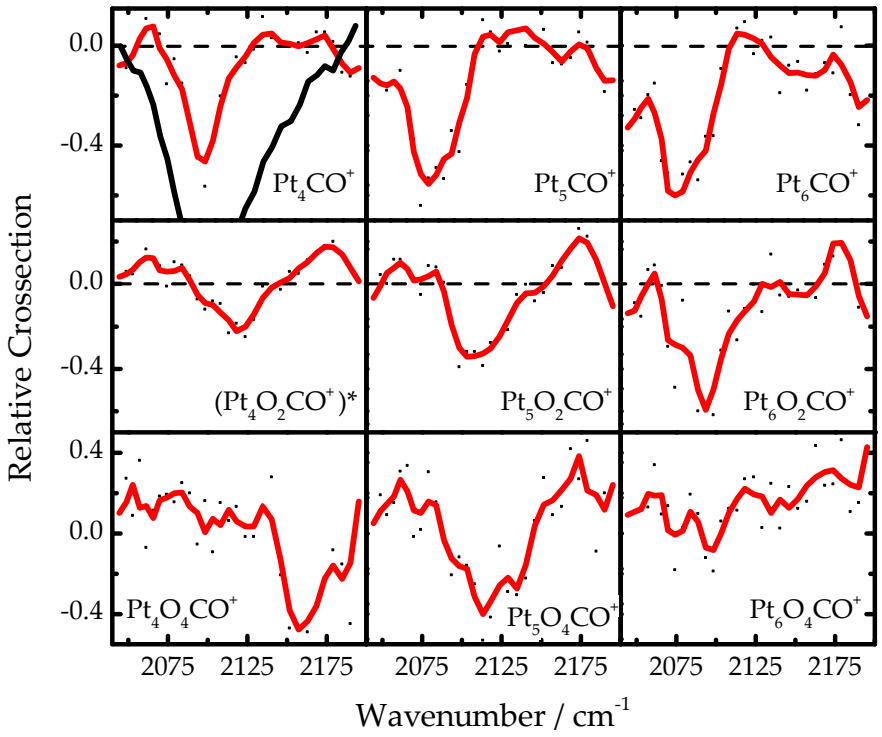

Figure 4.5 IR-MPD spectra of $Pt_nO_mCO^+$ ($n = 4-6, m = 0, 2, 4$) collected with the attenuated (5 dB) FELIX beam. On the Pt_4CO^+ spectrum, the full power spectrum(*cf.* fig. 4.4) is shown in black, for comparison. (*) The $Pt_4O_2CO^+$ is compensated for depletion from $Pt_4O_2COAr^+$ (see also section 4.4.2).

4.4.2 Infrared induced reactivity

Further to the spectroscopic characterisation described in the preceding sections, we also investigated the potential for surface processes on $Pt_nO_mCO^+$ clusters. The clusters were excited *via* the CO stretch using the intense IR beam of FELIX, leading to reaction processes on the cluster surface and/or CO desorption.

However, these clusters not only deplete as a result of these processes, but they are also produced by other parent species as a result of irradiation — and this enhancement may mask or distort the depletion signature we are interested in. Fortunately, this is relatively easy to correct for by summing an appropriate portion of the spectra of the parent species to the spectrum of the $Pt_nO_mCO^+$ in question. Over the size range studied ($n = 3-7$), only the species $Pt_nArO_mCO^+$,

n	m	Peak centre ν_{CO} / cm^{-1}	Band shift $\Delta\nu$/ cm^{-1}
3	0	2120 ± 5.0^a	0
3	2	2127 ± 8.0^a	7
3	4	2156 ± 8.0^a	36
4	0	2097 ± 2.5	0
4	2	2125 ± 2.5	28
4	4	2164 ± 5.0	67
5	0	2080 ± 2.5	0
5	2	2112 ± 5.0	32
5	4	2118 ± 5.0	37
6	0	2078 ± 5.0	0
6	2	2092 ± 5.0	14
6	4	2087 ± 10.0^a	9
7	0	2072 ± 8.0^a	0
7	2	2090 ± 5.0^a	18
7	4	2109 ± 10.0^a	37

[a] Full power spectrum used

Table 4.1 Centres of the CO stretch for $Pt_nO_mCO^+$ extracted from gaussian fits of the IR-MPD spectra. Where the signal to noise was acceptable ($n = 4 - 6$), the attenuated spectra where used, otherwise the full power spectra were used.

$Pt_nO_m(CO)_2^+$ and $Pt_nO_m(CO)_3^+$ have a significant impact on the $Pt_nO_mCO^+$ signal. We can assume that Ar loss from $Pt_nArO_mCO^+$ is the only loss process, while (as we will see later, *cf.* table 4.2) about 60 % of the depletion in $Pt_nO_m(CO)_2^+$ and $Pt_nO_m(CO)_3^+$ is from CO loss. The adjusted $Pt_nO_2CO^+$ spectrum is thus obtained by adding 100 % of the $Pt_nArO_mCO^+$ spectrum, and 60 % of the $Pt_nO_m(CO)_2^+$ and $Pt_nO_m(CO)_3^+$ spectra. This process is illustrated in fig. 4.6 for the case of $Pt_4O_2CO^+$. Henceforth, all the $Pt_nO_mCO^+$ spectra shown have been corrected using this method.

The IR-MPD spectrum of $Pt_4O_2CO^+$ is shown in fig. 4.7. The intense depletion in $Pt_4O_2CO^+$ signal around 2120 cm^{-1} is matched by enhancements in both Pt_4O^+

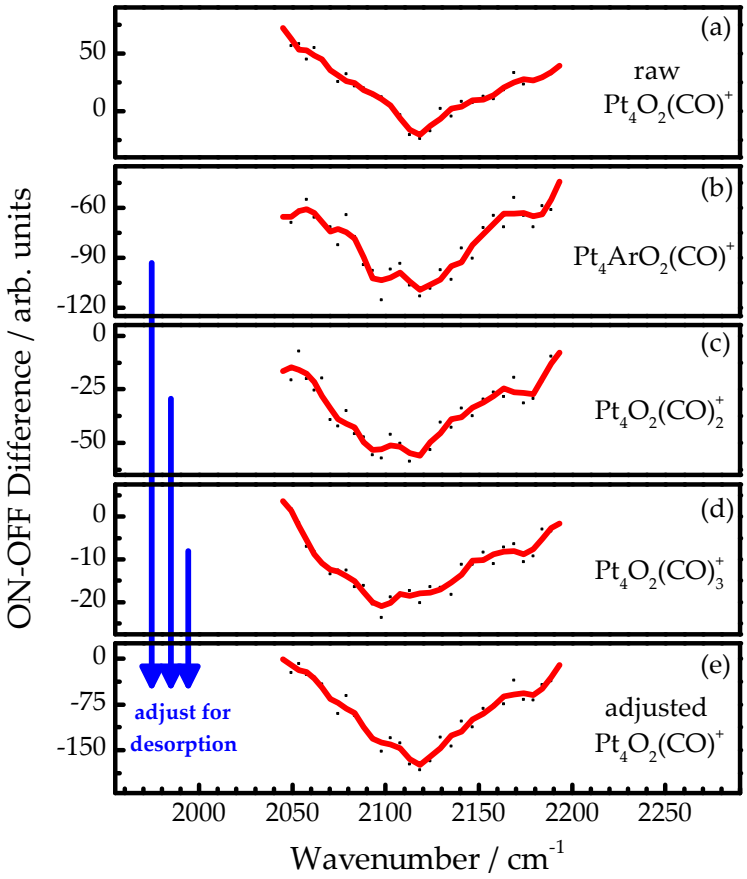

Figure 4.6 (a) IR-MPD spectrum of $Pt_4O_2CO^+$. (b)-(d) IR-MPD spectra of major species forming $Pt_4O_2CO^+$. (e) Adjusted IR-MPD spectrum of $Pt_4O_2CO^+$. The adjusted spectrum (e) is formed by coadding the signals of the species that form $Pt_4O_2CO^+$, which removes the effect of the enhancement that they cause from the $Pt_4O_2CO^+$ trace.

and $Pt_4O_2^+$ spectra. The largest enhancement observed is that of $Pt_4O_2^+$, which corresponds to the IR-induced loss of CO

$$Pt_4O_2CO^+ + IR\,(2120\,cm^{-1}) \longrightarrow Pt_4O_2^+ + CO\,. \tag{4.7}$$

However, this process does not fully account for the depletion in $Pt_4O_2CO^+$, and indeed, we also observe an enhancement in the Pt_4O^+ mass channel. In

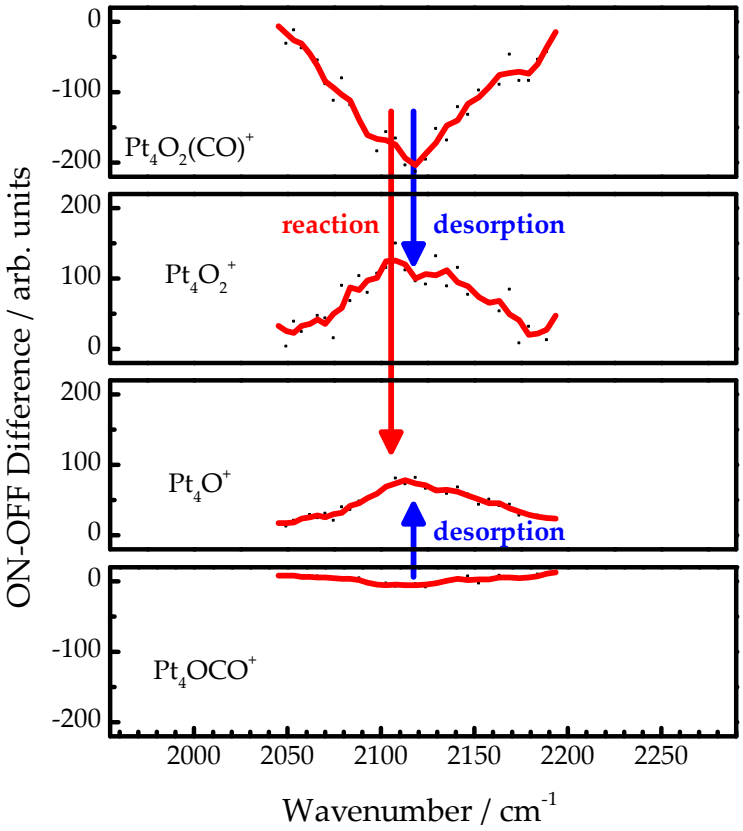

Figure 4.7 IR-MPD spectrum of $Pt_4O_2CO^+$ showing a strong signal depletion at 2120 cm^{-1}. Accompanying this depletion, enhancements are observed at the same spectral position in the Pt_4O^+ and $Pt_4O_2^+$ mass channels. The depletion in the Pt_4OCO^+ channel, whilst observed, is much too small to account for the increase in Pt_4O^+ by CO loss.

principle this enhancement could also be due to a CO desorption process, namely

$$Pt_4OCO^+ + IR\,(2120\,cm^{-1}) \longrightarrow Pt_4O^+ + CO\,. \tag{4.8}$$

However the signal of Pt_4OCO^+ is very weak (see the bottom of fig. 4.7) and thus cannot account for more than a small fraction of the Pt_4O^+ signal enhancement. In fact, the observed enhancement in Pt_4O^+ is larger than the total Pt_4OCO^+ signal (*cf.* fig. 4.1), on account of the fact that O_2 is used in the source to produce oxygen-decorated clusters.

The Pt_4O^+ enhancement can instead be understood as the result of the cluster

surface oxidation of CO

$$Pt_4O_2CO^+ + IR\,(2120\,cm^{-1}) \longrightarrow Pt_4O^+ + CO_2\,. \tag{4.9}$$

This is a key finding, indicating that infrared driven cluster chemistry goes beyond the unimolecular decomposition studied in chapter 3 and can be *e.g.* extended to two reactants (O_2 and CO in this case).

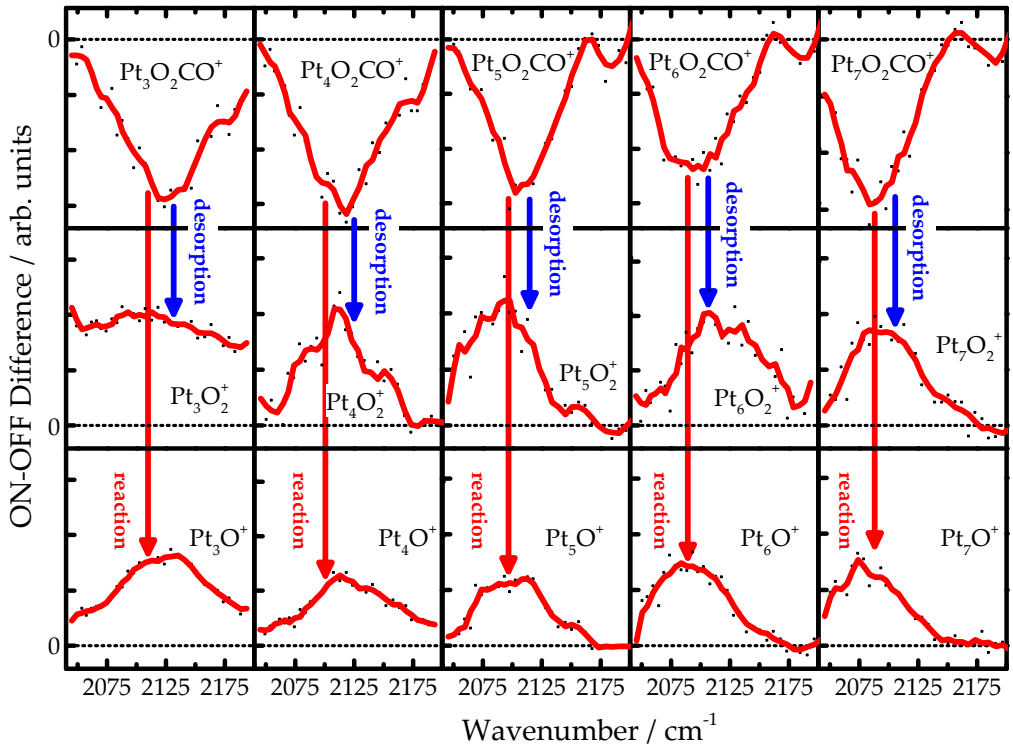

Figure 4.8 Infrared driven CO oxidation on $Pt_nO_2CO^+$ ($n = 3-7$) following excitation of the CO stretch around 2100 cm^{-1}. Both CO desorption to produce $Pt_nO_2^+$ and CO oxidation (yielding Pt_nO^+) represent important channels in the size range studied.

As we have seen in chapter 3, the reactivity of transition metal clusters can change quite drastically with size. It is therefore very interesting to see to what extent the oxidation process occurs on the other platinum cluster sizes. Figure 4.8 shows a summary plot of the IR-MPD spectra of $Pt_nO_2CO^+$ ($n = 3-7$) as well as their putative reaction / desorption products. The spectra show that, over the full

size range observed, the platinum clusters $Pt_nO_2CO^+$ behave in a very similar way with respect to oxidation / desorption: in each case there is a significant amount of CO desorption triggered by IR irradiation, as evidenced by clear enhancements in the $Pt_nO_2^+$ signal. On the other hand, the Pt_nO^+ spectra also exhibit significant enhancement features for all n, which shows us that the oxidation reaction is a major $Pt_nO_2CO^+$ depletion process over the entire range.

The integrated intensity of the enhancement features in the Pt_nO^+ and $Pt_nO_2^+$ spectra gives us a measure of the extent of reaction and desorption, respectively. Within experimental uncertainty, the sum of these intensities is equal to the signal depletion in $Pt_nO_2CO^+$ (for all n), indicating that there are no other major processes occurring as a result of IR irradiation. The ratio of the integrated intensities of Pt_nO^+ and $Pt_nO_2^+$ will therefore give us the branching ratio of CO oxidation *vs.* CO desorption. Table 4.2 shows the branching ratios as a function of underlying cluster size. As we can see, the branching ratio is constant, within uncertainty, for all the platinum cluster sizes studied.

n	Spectral range / cm^{-1}	% Reaction[a]	% Desorption[a]
3	2088 – 2169	43	(57)
4	2083 – 2153	38	62
5	2079 – 2134	40	60
6	2055 – 2134	46	54
7	2055 – 2123	38	62

[a] Estimated uncertainty = ±5 %

Table 4.2 Branching ratios for the CO oxidation reaction and CO desorption for $Pt_nO_2CO^+$ ($n = 3 – 7$).

At this point, it is worthwhile to undertake a comparison with previous studies on platinum clusters. Particularly relevant are the works of Shi *et al.*[215] and Balaj *et al.*;[216] who performed kinetic studies on isolated platinum clusters. Comparing these results with those obtained by IR-MPD is difficult, because collision based techniques are, by design, not sensitive to ineffective collisions (such as $Pt_n^+ + CO \longrightarrow Pt_n^+ + CO$).

Nevertheless, Shi *et al.* find that the reaction efficiency increases from $n = 3$ to $n = 6$ for the platinum cluster anions, reaching nearly unity at $n = 6$. For the cations, Balaj *et al.* note that the while $n = 6 - 8$ readily undergo the oxidation reaction, the $n = 5$ cluster efficiently attaches CO molecules, preventing (poisoning) the oxidation process.

As has been previously shown,[166] driving cluster surface reactions *via* IR-MPD is in general not mode selective. It might therefore be reasonable to expect to see the oxidation and desorption process to also occur when the $Pt_nO_2CO^+$ clusters are pumped *via* one of the oxide stretches shown in fig. 4.3. However, the observation of this process is hindered by a number of factors:

First, the absorption crossection of the Pt–O bands is markedly lower than the intense CO stretch band, resulting in fewer photons absorbed per laser shot. Indeed, the calculations carried out as part of this work find the oscillator strength of the CO band to be approximately 20 times greater than that of any Pt–O bands.

Second, the frequency of the Pt–O absorption bands is 3 – 5 times lower than that of the CO band, so that a significantly larger number of photons would have to be adsorbed to overcome any reaction barriers. For example, even accounting for the thermal energy of the cluster at 300 K, overcoming the 2 eV reaction barrier that we calculate (see section 4.5) would require *ca.* 8 quanta at 2100 cm^{-1} (CO stretch), while 36 or 23 would be required at 440 cm^{-1} and 680 cm^{-1} (Pt–O stretches).

Furthermore, the $Pt_nO_2CO^+$ spectra show strong enhancements due to Ar desorption from $Pt_nArO_2CO^+$ at precisely the wavelengths where we would expect to see a depletion caused by the oxidation reaction. There is no evidence of an enhancement in the Pt_4O^+ channel which might signify CO_2 loss. Finally the $Pt_4O_2^+$ is strongly perturbed by the fact that $Pt_4O_2^+$ and its Ar-tagged variant have strong absorptions of their own in the Pt–O spectral region.

4.5 Computational results

In addition to the experimental work above we have also performed preliminary calculations on the $Pt_4O_2CO^+$ cluster, in an attempt to to identify likely reac-

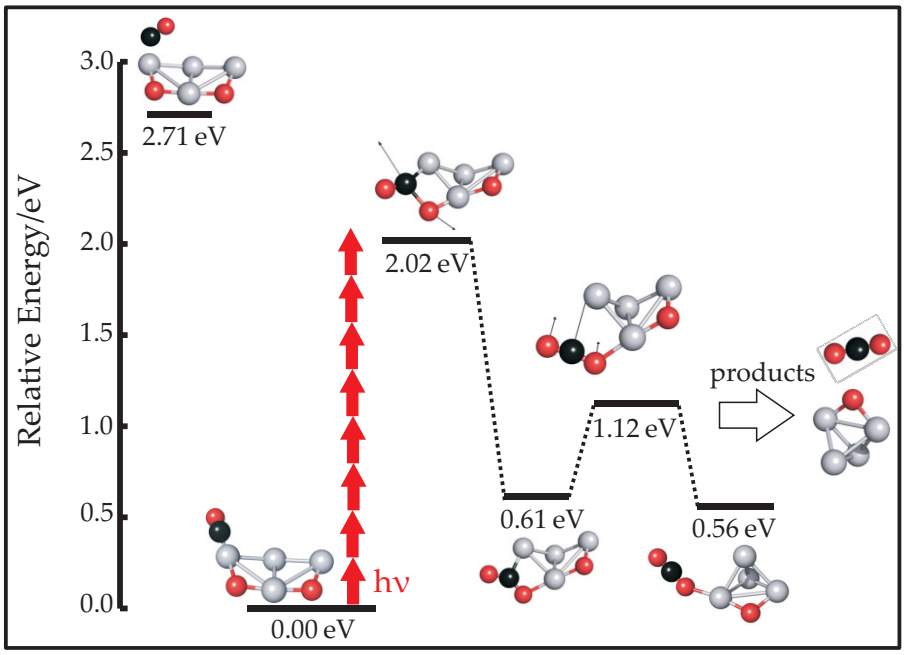

Figure 4.9 Key stationary points along the pathway of CO oxidation on $Pt_4O_2CO^+$ triggered by infrared multiple-photon excitation *via* the CO stretch. The structures shown are the result of eigenvector following, and do not necessarily represent the lowest energy structures. The arrows show the approximate energy of each IR photon.

tion pathways. The CO oxidation mechanism computed for reactions on metal surfaces[225] served as a starting point to identify the most important stationary points along the reaction profile.

The calculations proved to be quite a challenge: in contrast with rhodium, whose underlying metal framework is relatively unchanged throughout the reaction with N_2O (see section 3.5.2), the structure of the platinum clusters appears highly susceptible to the coadsorbates, with even a single coadsorbed oxygen atom triggering drastic changes in platinum cluster structure. Nevertheless, we were able to identify the key stationary points along the reaction pathway for $Pt_4O_2CO^+$, and these are shown in fig. 4.9.

The calculated CO binding energy is 2.71 eV, while the largest reaction barrier is 2.02 eV. Thus the reaction is favoured by 0.68 eV, which is more than the energy of one of the photons used in the IR-MPD process. Therefore, as photons are

sequentially absorbed by the cluster, the reactive channel will be open before the desorption channel. As we saw for the case of rhodium clusters (section 3.5.2), this is necessary for the reaction channel to effectively compete with the desorption channel — if the two processes are nearly isoenergetic, entropic factors will tend to favour the desorption process heavily.

Our value for the CO binding energy compares well with 2.3 – 2.7 eV determined by Grushow *et al.*[226] for the CID desorption of CO from anionic platinum clusters, as well as the binding energy of 2.6 eV computed by Xu *et al.*[227] for CO on neutral Pt_4. However, it is important to note that those values were obtained in the absence of coadsorbed oxygen, which, as we have shown in other contexts,[82] can have a large effect upon binding energies.

The activation barrier for CO oxidation has not been previously determined for isolated platinum clusters, but we can compare our data to the activation barrier for the process occurring on extended Pt(111) surfaces ($CO_{(ads)} + O_{(ads)} \longrightarrow CO_{2(g)}$). The barrier for CO oxidation on surfaces is strongly coverage-dependent,[212] but has been variously determined to be from about 1 eV by molecular beam scattering[228] to 1.7 eV by temperature programmed desorption.[229] On the other hand, DFT calculations on Pt(111) surfaces by Eichler *et al.*[225] determined a barrier of 0.74 eV. The reaction barrier in fig. 4.9 (2.02 eV) is markedly higher than all of those values. This discrepancy is perhaps not so surprising if we consider that reaction barriers, and indeed the geometries of the transition states, are highly dependent on the exchange-correlation functional used in the calculations.

4.6 Conclusion and outlook

Using IR-MPD, we have probed both the structure of small gas-phase platinum clusters decorated with oxygen and carbon monoxide, $Pt_nO_mCO^+$ ($n = 3 - 7$, $m = 0, 2, 4$), as well as their reactivity as a result of infrared radiation.

Ar-loss IR-MPD of $Pt_4O_2CO^+$, in combination with spectral simulation, demonstrated the presence of two isomeric forms of $Pt_4O_2CO^+$ in the molecular beam. One of these could be conclusively assigned to a boat shaped Pt_4 structure supporting dissociatively bound O_2 and atop bound CO, while the remaining spectral

features provide evidence for a higher lying isomeric form contain atop bound or peroxo oxygen.

The spectra of the CO bands of all the $Pt_nO_mCO^+$ clusters were recorded *via* CO-loss IR-MPD, and CO band positions extracted. These showed a good match to the CO band spectra previously obtained on bare clusters.[44] Two clear trends emerge: On the one hand, the CO band shifts towards lower frequency with increasing cluster size n, on the other increasing oxygen coverage m leads to a blue shift in peak position. Both trends are explained in the context of a simple backbonding model.

In a significant extension of previous work,[166] we demonstrated the possibility of driving a complex bimolecular reaction on a metal cluster surface *via* multiple infrared photon absorption. Alongside CO desorption, a major loss process of $Pt_nO_2CO^+$ was shown to be the infrared induced CO oxidation on the cluster surface. The reaction was observed over the whole size range studied, with a constant branching ratio of about 40 % CO oxidation to 60 % CO desorption. This is a strong contrast to the unimolecular decomposition observed on rhodium clusters (chapter 3), where the branching ratio was strongly affected by size, once again highlighting the diverse nature of transition metal clusters.

A series of preliminary calculations on the $Pt_4O_2CO^+$ cluster determined a complex reaction pathway for CO oxidation involving significant structural rearrangement, once again contrasting the rhodium work. The barrier to reaction was found to be 2.0 eV, markedly higher than the barriers that have been observed on extended Pt(111) surfaces. Our calculations also obtained a value of 2.7 eV for the binding energy of CO to the $Pt_4O_2^+$ cluster. This value is well within the range previously reported both experimentally and computationally.

The results presented in this chapter are a good illustration of the the advantages of the IR-MPD technique, which, with suitable computational support, allows us to probe both structure and reactivity in a single experimental setup. The technique allows us to trigger even complex bimolecular reactions on clusters in a thermal way, and its nature means that the data of a large range of clusters is collected simultaneously. This study also shows that it is possible, through careful choice of experimental conditions, to mitigate the complexity introduced by the

multiplex nature of the experiment. This allows clear deductions about the nature and relative proportion of the processes triggered even though these processes are occurring simultaneously.

While we are confident in our understanding of the data here presented, a number of supplementary experiments may reveal additional insights — for example the study of the anions of the same clusters, or the extension of the present study to larger clusters sizes. On the other hand, the vast number of reactions observed on extended surfaces of transition metals show that there is no shortage of interesting targets for IR-MPD study, no doubt each with their own fascinating story to tell.

CHAPTER 5

Velocity map imaging study of tantalum dimer dissociation

This chapter presents an investigation of the one-colour photodissociation of Ta_2 by photoionization spectroscopy in the range 18 000 – 23 800 cm^{-1} and VMI in the range 23 500 – 23 800 cm^{-1}. The one colour action spectrum of Ta^+ exhibits a very high spectral density of peaks, many of which cannot be assigned on the basis of the Ta emission spectrum and indicate a process producing Ta^+ as a result of irradiation. VMI confirms that Ta^+ is produced in a range of electronic states by fragmentation of Ta_2^+ in this spectral region. Analysis of product kinetic energies shows that fragmentation occurs at the two photon level out of cationic Ta_2^+, which itself is formed at the three photon level. Dissociation producing at least one atom in the electronic ground state is heavily favoured, with a majority of the observed channels producing either atomic ($Ta(^4F_{3/2})$) or cationic ($Ta^+(^5F_1)$) ground state.

The assignment of product channels allows us to place the dissociation energy of Ta_2^+, $D_0(Ta_2^+)$ at 5.094 – 5.090 eV, in good agreement with computational predictions performed in parallel with this work. The anisotropies observed in the VMI
the photodissociation process.

5.1 Introduction

5.1.1 Context

Homonuclear diatomics represent the smallest systems which permit the study of the fundamentals of homonuclear bonding, which is of critical importance in the understanding of larger clusters, as well as an understanding of the key interactions that play a role in heterogeneous catalysis.

The dimers of several transition metals have received a considerable amount of interest from both theoretical and experimental perspectives in the last few decades.[230] The electronic complexity of transition metals makes them very worthwhile targets for study. At the same time, a system comprised of only two atoms in sufficiently limited in scope as to remain amenable to high level *ab initio* calculations and spectroscopy.

The group 5B transition metal diatomics have attracted significant interest on account of their very high bond order (two σ and π bonds as well as a δ bond), and both V_2 and Nb_2 have been the subject of a number of successful experimental and computational studies.[231–235] As a result, the electronic ground states, spectroscopic constants and dissociation energies are relatively well determined.

In contrast, the other naturally occurring member of the group, tantalum, has been considerably less well researched. The only available data is summarized in the next two sections.

5.1.2 Previous experimentation

Remarkably few experimental results concerning the tantalum dimer have been reported. Early predictions based upon empirical rules were only able to place the dissociation energy broadly at 4 ± 1 eV.[230] Armentrout and coworkers have since measured the bond energy of the small cation clusters Ta_n^+ ($n = 2-4$) using guided ion beam mass spectrometry, yielding a dissociation energy $D_0(Ta_2^+) = 6.87$ eV.[236]

The following year, the ionization potentials of a large range of tantalum clusters Ta_n ($n = 3-64$) were determined using photoioniziation efficiency spectra.[237] The smaller clusters ($n < 20$) showed a strong size dependence, underscoring the

impact of the distinct electronic and geometric structure at each cluster size. The ionization potential of the tantalum dimer was also investigated, but its exact value could only be bracketed broadly to lie between 5.98 and 6.42 eV. Combining the measurement of the ionization potential and dissociation energy of Ta_2^+ yields an estimated dissociation energy for the neutral dimer $D_0(Ta_2) = 4.96 - 5.40$ eV.

Spectroscopically, Ta_2 was first studied by scattering depletion in an Argon matrix.[238] A series of weak absorptions were observed between 250 and 350 nm as well as in the region 550 – 700 nm, but no vibronic assignments could be made. Nonetheless, additional Raman spectroscopy of a band at 480 nm yielded $\omega_e = 300.20 \pm 0.12\,\mathrm{cm}^{-1}$. The only other known study is by Simard *et al.*, who reported initial findings *via* LIF spectroscopy which indicated a series of features in the range 534 – 640.9 nm with a lower state vibrational frequency of $280\,\mathrm{cm}^{-1}$.[239] Unfortunately, the full results hinted at in that work remain unpublished.

5.1.3 Previous computation

This scarcity of experimental results underscores the importance of computational study as both support and extension of the experimental data. In 2000, Heaven *et al.* first reported on density functional theory (DFT) calculations of the neutral tantalum dimer, finding a $^1\Sigma_g^+$ ground state.[240] However, their study was limited to singlet and doublet states only and later DFT calculations by Wu *et al.* predicted higher spin ground states ($^5\Sigma_g$ or $^3\Sigma_g$ for Ta_2, and $^4\Sigma_g$ or $^2\Delta_g$ for Ta_2^+).

On the other hand, the same study reported dissociation energies somewhat outside the range indicated by the experimental studies mentioned above: they predicted $D_0(Ta_2) = 2.877$ eV and $D_0(Ta_2^+) = 4.510$ eV. In the same year Fa *et al.* reported values more in line with the experimental results ($D_0(Ta_2) = 4.53$ eV).[241] The group of Jiang studied several 5*d* dimers, also finding the quintet states of Ta_2 to be lowest-lying, with a dissociation energy of $D_0(Ta_2) = 3.51$ eV.[242,243] More recently, Borin and coworkers applied multiconfiguration second-order perturbation theory (CASSCF//CASPT2) to study the electronic states of Ta_2, predicting a $^3\Sigma_g^-$ ground state with dissociation energy $D_0(Ta_2) = 4.63$ eV.[98]

Here we report on an experimental investigation into the photoinduced disso-

ciation of the tantalum dimer Ta_2, leading, amongst other things, to a much more precise determination of $D_0(Ta_2^+)$.

5.2 Experimental method

The experimental apparatus and the techniques employed for this work are those described in the earlier sections 2.4 and 2.5.

In this case, the ablation target was a 1 mm thick disc of high purity tantalum (99.9 %). As tantalum is nearly monoisotopic (↑Ta has a natural abundance of greater than 99.99 %), it is ideally suited for mass spectroscopic studies. The same target was used for all the studies here presented, on account of the relatively low rate of material used per laser shot. The molecular beam was formed by 5 – 6 bar of pure Helium for the action spectra, whereas 8 bar was used during imaging.

Photoionization and excitation were performed by the same laser in both types of experiment. In each case laser light was provided by the visible component of an optical parametric oscillator (Continuum Panther EX, typical energy 4 – 6 mJ) pumped by the second harmonic of a Nd:YAG laser (Continuum Surelite II-10). The OPO light, whose polarization vector was parallel with the image plane, crossed centrally between the repeller and extractor plates of the electrode stack, and was temporally synchronized to intersect the most dimer-rich portion of the molecular beam. For the a majority of the experiments, a 30 cm bi-convex focussing lens was employed to enhance the density of OPO photons.

Using this setup, we first collected a series of action spectra starting at the highest available photon energy (420 nm) until the photoionization efficiency was significantly diminished (620 nm). In a second step, the OPO laser was tuned to a series of features in the range 418 – 435 nm and velocity map images were recorded. Several species were investigated, but only the tantalum atom channel showed appreciable off-centre ion image intensity, characteristic evidence of a photodissociation process.

5.3 Experimental results

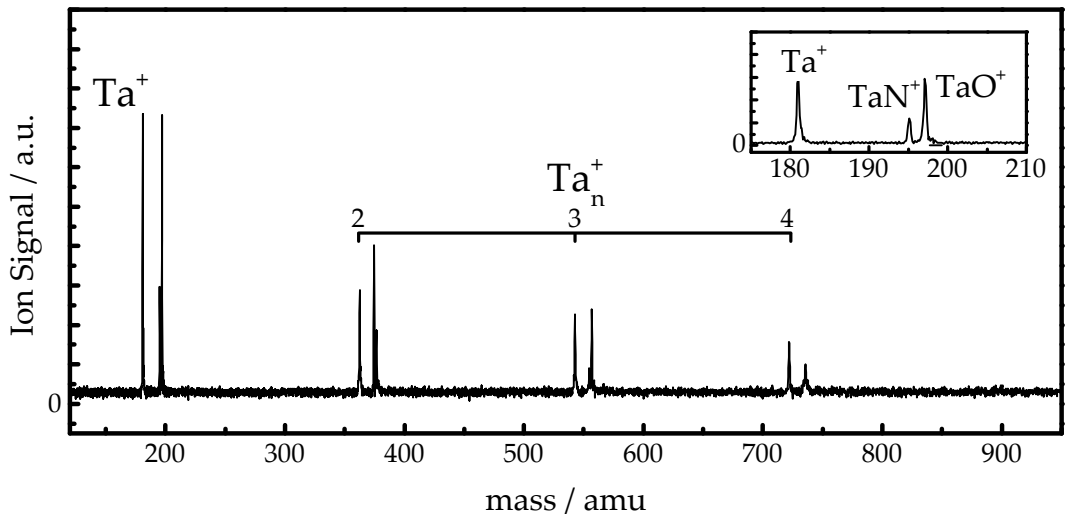

Figure 5.1 Typical time-of-flight mass spectrum of recorded at 23 399 cm^{-1}, showing the major species generated by the cluster source. (Inset) Magnification of the mass spectrum in the region of the tantalum atom and atom complexes, showing how the peak at *ca.* 200 amu splits into two components.

Thorough knowledge of the species present in the molecular beam empowers a good understanding of the processes leading to the observed spectra and images. Figure 5.1 shows the mass spectrum representative of the source conditions during the images and scans. The major species in the mass spectrum are the bare tantalum atom and clusters Ta_n^+ as well as their oxides and nitrides, Ta_nN^+ and Ta_nO^+.

Note that several species present in the beam have intensity comparable with or exceeding that of the tantalum atom Ta^+. Therefore, any processes involving the dissociation of such a species to produce Ta^+ will result in a significant change in the amount of Ta^+ that is detected — hence, these processes should be easily detected.

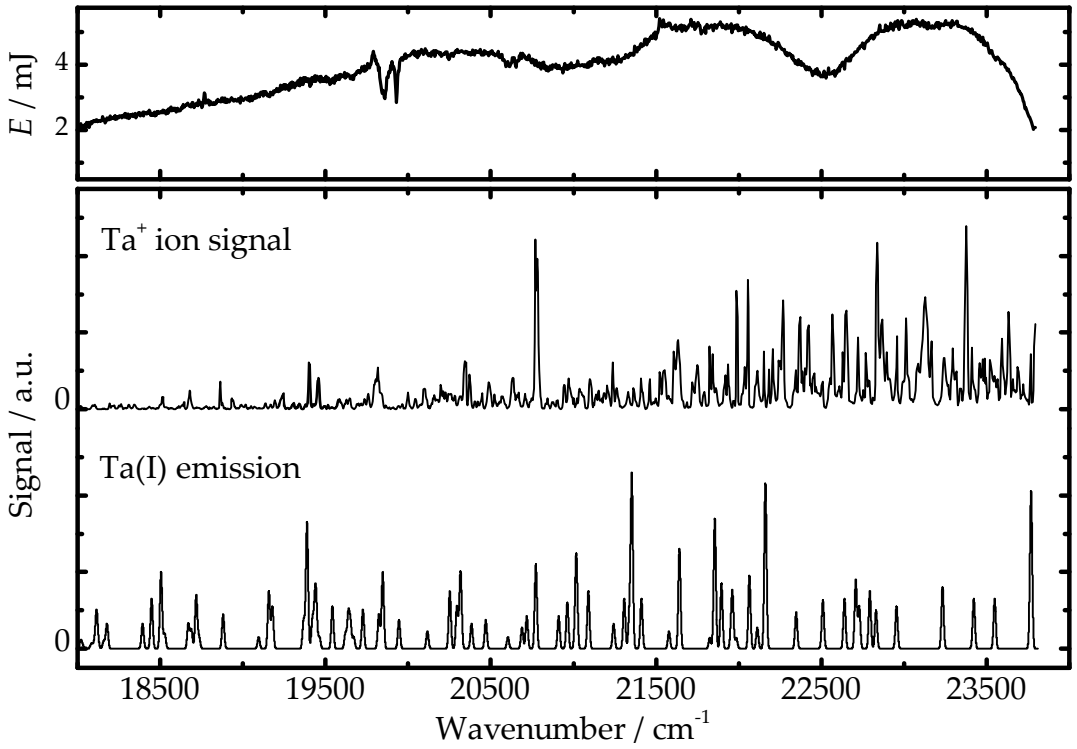

Figure 5.2 (Top) Variation of laser pulse energy E with wavenumber. (Centre) Ta^+ action spectrum. (Bottom) Ta emission spectrum generated from the known line spectrum[244,245] by convolution with a gaussian function to compare with the experimental spectrum.

5.3.1 Enhancement spectra

Any dissociation process involving a tantalum based species is likely to produce the tantalum atom at least as a minor product. It is therefore important to determine how the Ta^+ intensity varies as a function of OPO wavelength. Figure 5.2 shows this action spectrum of Ta^+ as well as the known[244,245] emission lines for Ta(I).

The spectrum is very rich in features across the entire observed range, but particularly so at the higher photon energies. A number of the enhancements in Ta^+ signal intensity match the known emission lines and we can therefore attribute these enhancements to resonant ionization of Ta *via* one of the many electronic states of the atom.

Nevertheless, despite a number of correspondences between the two spectra,

there are many features which are not explained by the known emission lines, especially in the range 23 000 – 23 800 cm^{-1}. These features may be a result of resonant ionization *via* transitions that are not active in emission spectroscopy, autoionization of Ta excited to states above the ionization threshold, or they may be indicative of a process which produces Ta^+, *i.e.* a fragmentation process.

To further explore the possibility of fragmentation, we consider the spectra of the other species in the mass spectrum. However, with the exception of TaO^+ and TaN^+, none of the species previously shown (see the mass spectrum fig. 5.1) exhibited any spectral features in their action spectra.

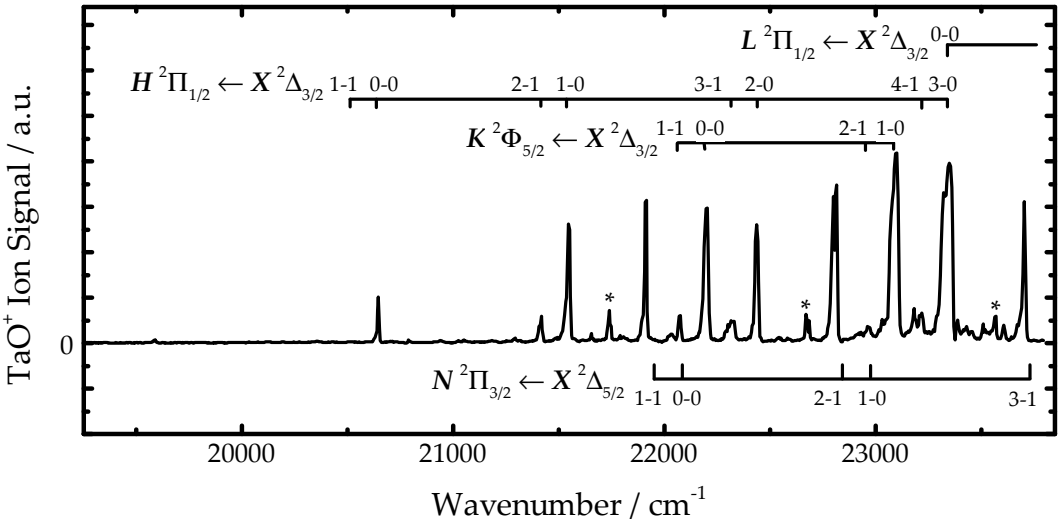

Figure 5.3 TaO^+ action spectrum, with line positions based on the work of Al-Khalili *et al.*[246] The electronic states are labelled as in that work, and using the convention $v' - v''$, where v' and v'' are the vibrational quantum numbers of the lower and upper states, respectively. (*) Unassigned peaks.

The TaO action spectrum is shown in fig. 5.3. The spectrum is much less dense than the Ta spectrum and thus more amenable to analysis. The majority of the peaks can be explained by resonant ionization *via* one of the vibronic states of TaO previously observed by Al-Khalili *et al.*[246] Most of the transitions observed are from the lower lying spin-orbit component of the ground state, X $^2\Delta_{3/2}$, which suggests that the amount of electronically excited TaO is quite limited.

A few features, marked in fig. 5.3, could not be assigned to TaO transitions.

These may be a result of unknown TaO electronic states, or perhaps a result of fragmentation from a larger species. Overall, while the TaO spectrum confirms our wavelength calibration, there is no direct evidence of TaO dissociation in the form of an intensity dip or a direct match with a Ta enhancement feature.

The spectrum of TaN showed only enhancement features, *i.e.* no evidence of TaN fragmentation. The enhancement features that were observed match those previously observed[247] and confirm our wavelength calibration, but offer no additional insight. We thus do not include it here.

In conclusion, while some evidence for fragmentation exists in the Ta spectrum, no clear pathway emerges from the spectroscopy. This question is addressed in the next section when we consider the velocity map images.

5.3.2 Velocity map images

As shown in section 5.3.1, there are several features in the Ta spectrum that do not match the emission spectrum, and that may arise as a result of several other processes. To investigate this possibility a large range of VMI images of the tantalum atom were recorded, focussing in particular on the high energy region 23 000 – 23 800 cm^{-1}. Of the images collected in this range, those below 23 500 cm^{-1} showed only a strong central spot, indicating that the signal does not arise from photodissociation in the ionization region of the chamber, but rather a photoionization or autoionization process.

In contrast, several off-centre features appear when images are collected on enhancement features in the range between 23 500 cm^{-1} and 23 800 cm^{-1} (see fig. 5.4). Besides intense central spots, several rings are visible above the background in each image. This indicates that at these wavelengths Ta atoms are produced with three distinct kinetic energies, which implies that they are the result of (at least) three distinct dissociation processes.

As noted, the most important datum that can be gleaned from these images is the off-centre kinetic energy of the Ta fragments. To obtain these, we employ the procedures described in section 2.5.2 to first recover the virtual slice through the ion distribution, and then generate a kinetic energy release (KER) spectrum.

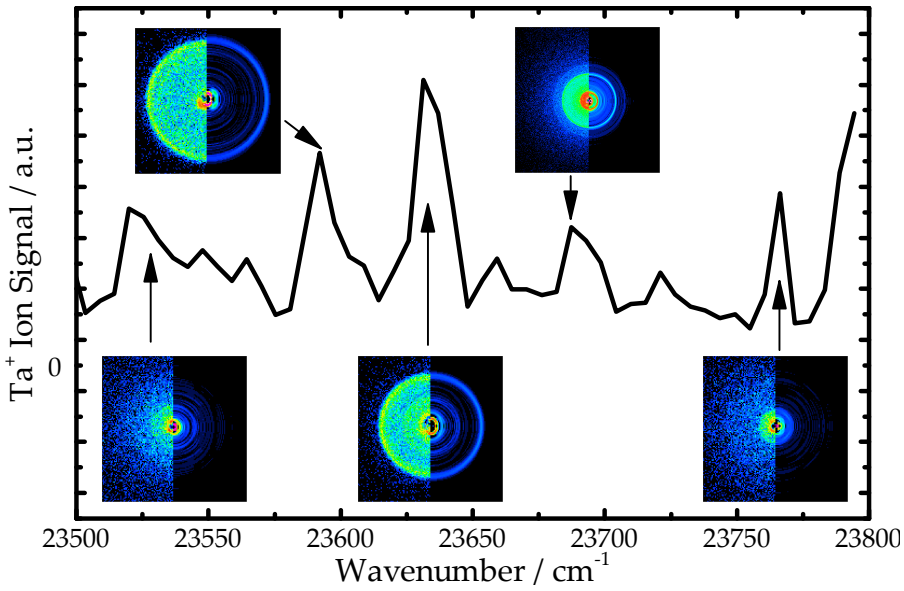

Figure 5.4 A portion of the Ta^+ action spectrum, showing some of the Ta^+ VMI images collected when the laser is tuned to various features in the action spectrum (the left halves of the images show the raw data, while the right halves show the result of onion-peeling as per section 2.5.2). The rings in the images indicate the occurrence of a fragmentation process that produces Ta^+.

Figure 5.5 shows the VMI image recorded at 23 687 cm^{-1}, exhibiting three rings, corresponding to Ta^+ produced with three distinct velocities. The KER spectrum corresponding to fig. 5.5 is shown in fig. 5.6. The three rings from the image manifest as three peaks in the KER spectrum.

In order to understand the process leading to these off-centre velocities it is best to consider the rings in all the images together. To this end, we generated all the KER spectra associated with the images collected, and subsequently fit the peaks in them using gaussian functions. In this way we obtain a plot of KER peak position versus wavelength (for an example, see fig. 5.7 on page 117). This plot can be used to deduce the exact dissociation process which is occurring, and this is the object of the next section.

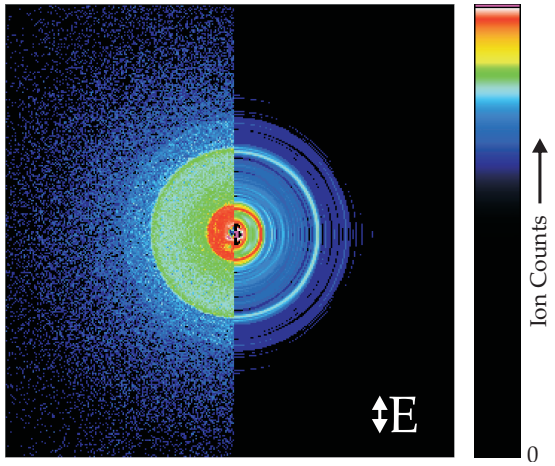

Figure 5.5 Velocity map image of Ta^+ fragments produced at 23 687 cm^{-1}. Three distinct rings indicate that Ta^+ fragments are produced with three distinct kinetic energies. The left half shows the raw image, while the right half shows the result of onion-peeling as per section 2.5.2. The image colour represents the intensity on a temperature scale ranging from white (high) to black (low).

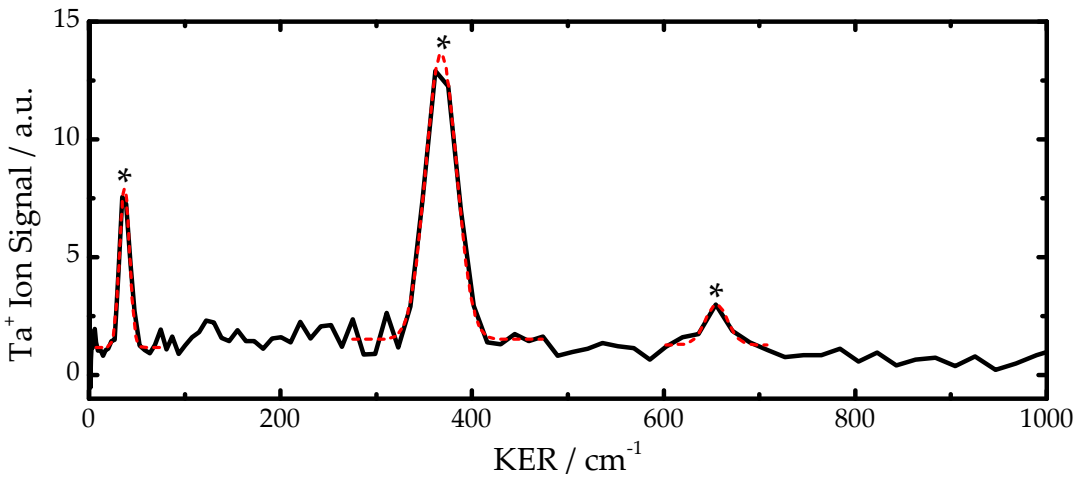

Figure 5.6 Kinetic energy release (KER) spectrum of Ta^+ at 23 687 cm^{-1}. Three peaks (marked with $*$) corresponding to different fragment product states, are evident. The gaussian line fits are shown with red dotted lines.

5.3.3 Photodissociation

Before considering the variation of Ta fragment kinetic energy with wavelength it is instructive to consider the process that leads to the off-centre Ta signal. By analogy with eq. (2.7) we can represent this as

$$\mathrm{TaX} + n \times h\nu \longrightarrow \mathrm{Ta} + \mathrm{X}\,. \tag{5.1}$$

The Ta fragment is subsequently photoionized, which, out of the tantalum ground state, requires three photons across the entire wavelength range studied.

In each case the first step is the dissociation step and thus determines the fragment velocities — the second, ionization step, does not affect the kinetic energy significantly as the recoil is minimal, with the electron carrying away energy in excess of the ionization energy in the form of electron kinetic energy (eKE). The energy that goes into the dissociation step must balance with that present after the dissociation. This leads to

$$n \times h\nu = \mathrm{TKER} + E(\mathrm{Ta}) + E(\mathrm{X}) + D_0(\mathrm{TaX}) \tag{5.2}$$

where $E(\mathrm{Ta})$ and $E(\mathrm{X})$ mark the internal energies of the Ta and X fragments, $D_0(\mathrm{TaX})$ the dissociation energy of TaX and TKER the *total* kinetic energy released, *i.e.* the sum of the KER of both fragments.

From conservation of linear momentum (see eq. (2.6)) TKER is related to KER by

$$\mathrm{TKER} = \mathrm{KER(Ta)} \times \left(1 + \frac{m_{\mathrm{Ta}}}{m_{\mathrm{X}}}\right) \tag{5.3}$$

where KER(Ta) is the KER of the observed tantalum fragment, m_{Ta} the mass of tantalum and m_{X} the mass of the unobserved cofragment. Using this substitution, eq. (5.2) becomes

$$n \times h\nu = \mathrm{KER(Ta)} \times \left(1 + \frac{m_{\mathrm{Ta}}}{m_{\mathrm{X}}}\right) + E(\mathrm{Ta}) + E(\mathrm{X}) + D_0(\mathrm{TaX})\,. \tag{5.4}$$

Consider how the KER changes as a function of wavelength for Ta atoms

that are the result of one particular dissociation channel, *i.e.* a dissociation that produces Ta and X in one particular set of electronic states. In such a case $E(\mathrm{Ta}) + E(\mathrm{X}) - D_0(\mathrm{TaX}) = c$ is constant, and we can rewrite eq. (5.4) as

$$\begin{aligned} n \times h\nu &= \mathrm{KER(Ta)} \times \left(1 + \frac{m_{\mathrm{Ta}}}{m_{\mathrm{X}}}\right) + c \\ \Leftrightarrow \mathrm{KER(Ta)} &= h\nu \times \left(\frac{n}{1 + m_{\mathrm{Ta}}/m_{\mathrm{X}}}\right) - c' , \end{aligned} \tag{5.5}$$

where $c' = c/(1 + m_{\mathrm{Ta}}/m_{\mathrm{X}})$. Note that this analysis is analogous for the case of a cation ($\mathrm{TaX^+}$) dissociation, substituting $E(\mathrm{Ta})$ for $E(\mathrm{Ta^+})$, *etc.*

A plot of KER (Ta) vs. photon energy $h\nu$ will hence yield a slope of $\frac{n}{1+m_{\mathrm{Ta}}/m_{\mathrm{X}}}$. In addition, we know that there are only a few candidates for the cofragment X and so, given the slope we can deduce an n for each of them. However, the number of photons n must clearly be integer and small for a real physical process, and this determines which choice of X is plausible.

Figure 5.7 shows such a plot of KER versus photon energy. Two sets of peak positions obtained from the recorded images (see section 5.3.2) are shown alongside the lines of best fit through them. Assuming that each set belongs to a single dissociation channel we can now apply the analysis above. The possible results for a number of cofragments are given in table 5.1.

Gradient	X	n
0.95 ± 0.08	$\mathrm{Ta_2}$	1.4 ± 0.1
	Ta	1.9 ± 0.2
	O	12 ± 1
	N	13 ± 1
	C	15 ± 1

Table 5.1 Table showing the number of photons n deduced from the slope of fig. 5.7 for different cofragments X.

The light cofragments C, N and O would all require unfeasibly large number (≥ 12) of photons to be involved in the dissociation. The sequential absorption of

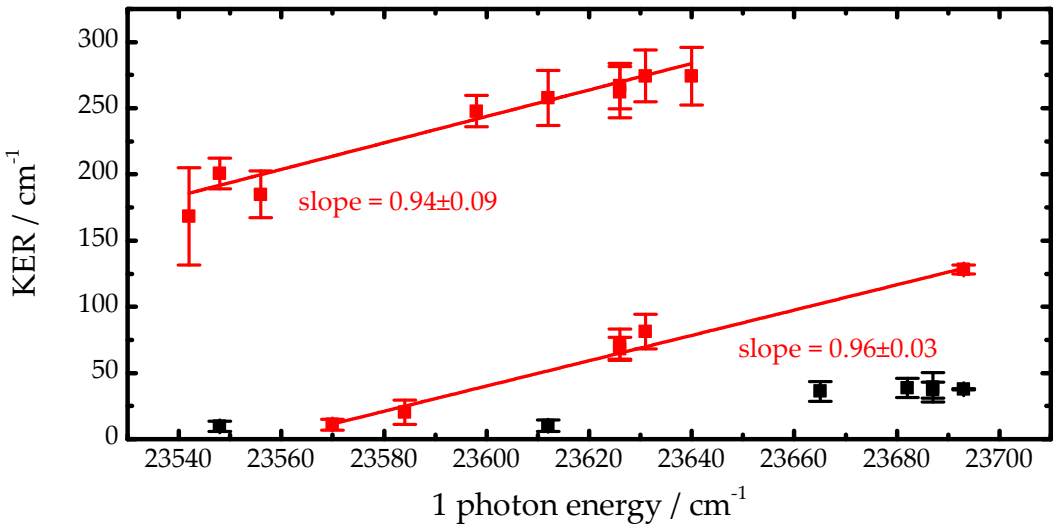

Figure 5.7 Plot of kinetic energy release (KER) versus excitation photon energy. The positions of the KER peaks, fitted with gaussian functions, are shown by the solid squares (■). The uncertainties show the half width at half maximum (HWHM) of the gaussian functions. Two sets of features are assigned to individual dissociation channels (■). Lines of best fit, labelled with their slope, are also shown in red (—).

so many photons is very unlikely given the relatively low photon fluence, and we can hence rule out C, N and O as cofragments.

The heaviest co-fragment shown, Ta_2, results in a value for n that is far from the bounding integer values 1 and 2, indicating that both one and two-photon dissociation of Ta_3 to produce Ta and Ta_2 are a poor fit for the data. This fact also allows us to rule out heavier cofragments: any cofragment heavier than Ta_2 would produce a value of n closer to one, *i.e.* would predict a one-photon dissociation. However, the energy of a single photon in the observed range (2.85 – 2.90 eV) is well below all of the known dissociation energies of larger clusters.[237] Finally, the sharpness of the rings suggests that the cofragment is not molecular, as this would be expected to exhibit rotational or vibrational structure around each ring.

This leaves Ta as a possible cofragment. This yields a value for n which is approximately equal to two, and thus a good fit for a two-photon process. In addition, two OPO photons are sufficient to overcome the dissociation energies for the tantalum dimer or dimer cation (see section 5.1). Overall we can conclude

that Ta is the only physically plausible cofragment.

The two processes which are consistent with this result are illustrated in fig. 5.8: Dissociation of Ta_2 followed by ionization of the ejected Ta or ionization of Ta_2 to Ta_2^+ followed by dissociation to produce Ta^+. The two possibilities are now examined in turn.

Photodissociation of Ta_2

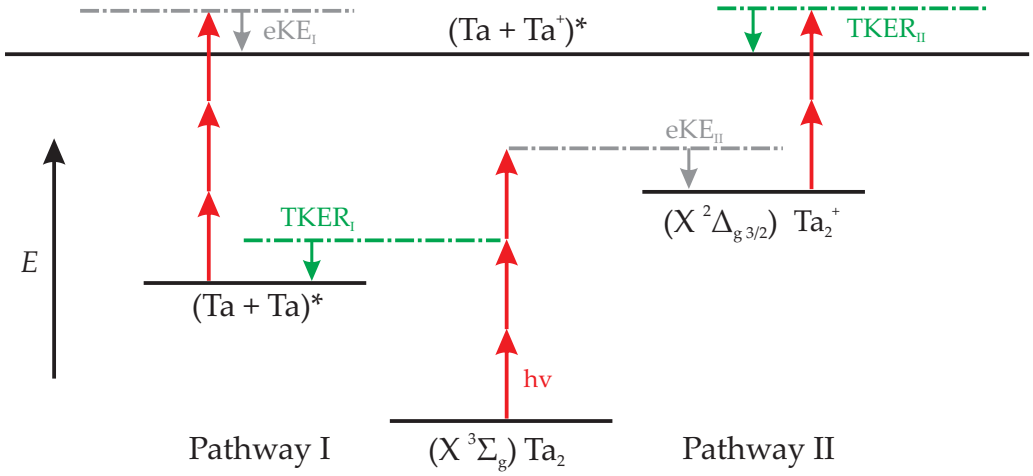

Figure 5.8 Schematic representation of the two dissociation pathways. (Left) Pathway I, neutral Ta_2 photodissociation followed by ionization. (Right) Pathway II, ionization of Ta_2 to Ta_2^+ followed by photodissociation. The asterisk (*) indicates Ta and Ta^+ produced in a range of electronic states, leading to a variety of photodissociation channels.

The two photon photodissociation of Ta_2, followed by Ta ionization, is illustrated on the left hand side of fig. 5.8. The TKER yielded by this process can be obtained by rearranging eq. (5.2) (with the substitution $n = 2$) to give

$$2 \times h\nu = \mathrm{TKER} + E(\mathrm{Ta}) + E'(\mathrm{Ta}) + D_0(\mathrm{Ta}_2)\,, \tag{5.6}$$

where we have written E and E' to distinguish between the energies of the two Ta atoms. While the discrete possible combinations for the internal energy $E_{\mathrm{int}} = E(\mathrm{Ta}) + E'(\mathrm{Ta})$ can be accurately determined from known atom energy levels;[244,245] the literature values for D_0 are quite widely scattered. Thus the direct prediction

of possible dissociation channels and associated TKER is difficult, as the error in predicted TKER would be substantial.

Fortunately, this difficulty can be circumvented: if one considers two distinct dissociation channels 1 and 2 into which dissociation occurs at some photon energy $h\nu$, the TKER for each dissociation is

$$2 \times h\nu = \mathrm{TKER}_1 + E_1(\mathrm{Ta}) + E_1'(\mathrm{Ta}) + D_0(\mathrm{Ta}_2) \tag{5.7}$$

and

$$2 \times h\nu = \mathrm{TKER}_2 + E_2(\mathrm{Ta}) + E_2'(\mathrm{Ta}) + D_0(\mathrm{Ta}_2)\,. \tag{5.8}$$

If we now take the difference between the TKERs we obtain

$$\mathrm{TKER}_1 - \mathrm{TKER}_2 = E_2(\mathrm{Ta}) + E_2'(\mathrm{Ta}) - E_1(\mathrm{Ta}) - E_1'(\mathrm{Ta}) \tag{5.9}$$

$$= E_{\mathrm{int},2} - E_{\mathrm{int},1} \tag{5.10}$$

which no longer depends on the dissociation energy D_0.

	Dissociation Products			Energy / cm^{-1}
D	$\mathrm{Ta}(^4\mathrm{F}_{5/2})$	+	$\mathrm{Ta}(^4\mathrm{F}_{5/2})$	4020.2
E	$\mathrm{Ta}(^4\mathrm{F}_{3/2})$	+	$\mathrm{Ta}(^4\mathrm{F}_{9/2})$	5621.0
F	$\mathrm{Ta}(^4\mathrm{F}_{5/2})$	+	$\mathrm{Ta}(^4\mathrm{F}_{7/2})$	5974.0
G	$\mathrm{Ta}(^4\mathrm{F}_{3/2})$	+	$\mathrm{Ta}(^4\mathrm{P}_{1/2})$	6049.4
H	$\mathrm{Ta}(^4\mathrm{F}_{3/2})$	+	$\mathrm{Ta}(^4\mathrm{P}_{3/2})$	6068.9
I	$\mathrm{Ta}(^4\mathrm{F}_{5/2})$	+	$\mathrm{Ta}(^4\mathrm{F}_{9/2})$	7631.1
J	$\mathrm{Ta}(^4\mathrm{F}_{7/2})$	+	$\mathrm{Ta}(^4\mathrm{F}_{7/2})$	7927.8
K	$\mathrm{Ta}(^4\mathrm{F}_{5/2})$	+	$\mathrm{Ta}(^4\mathrm{P}_{1/2})$	8059.5
L	$\mathrm{Ta}(^4\mathrm{F}_{5/2})$	+	$\mathrm{Ta}(^4\mathrm{P}_{3/2})$	8079.0

Table 5.2 Table showing the low-lying dissociation channels (Energy < 9000 cm^{-1}) for Ta_2. Channels below 4000 cm^{-1} are omitted as these would yield D_0 well outside the range previously observed. The energies are given relative to an energy zero corresponding to dissociation into two ground state $\mathrm{Ta}(^4\mathrm{F}_{3/2})$ atoms.

Table 5.2 shows a number of dissociation channels and the internal energy of the products. The dissociation channels responsible for our images can now be identified by fitting the differences in TKER to the differences in the internal energies shown in table 5.2. Having obtained a fit, eq. (5.6) can be used to work back to a value for D_0.

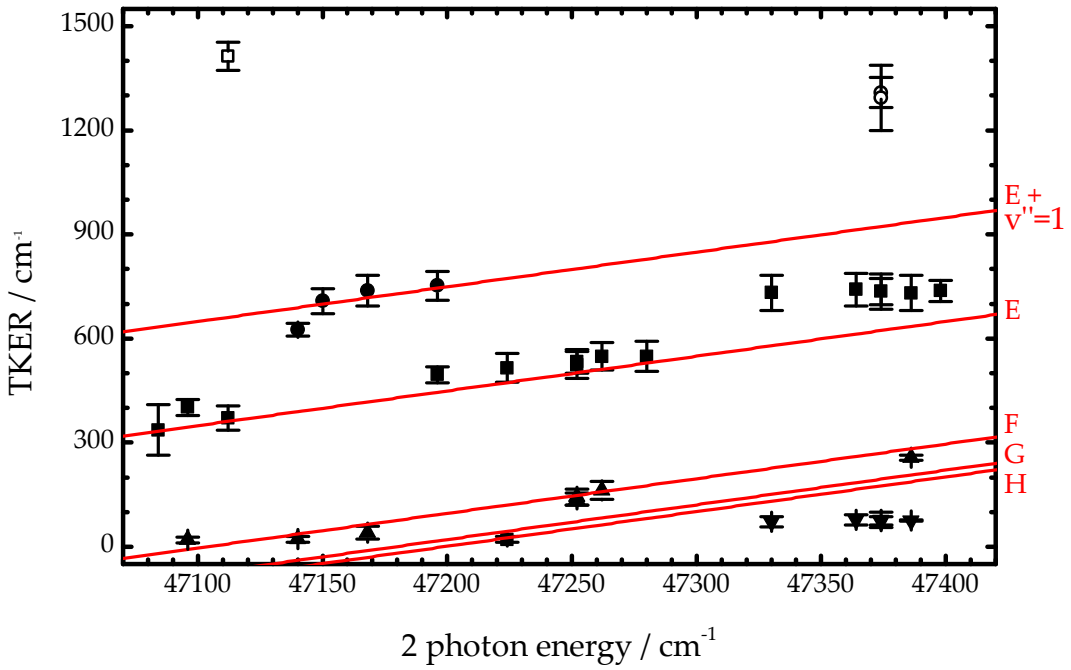

Figure 5.9 Total kinetic energy release (TKER) plotted as a function of photon energy. The solid and hollow shapes (▼, ▲, ■, ●, ○, ❑) indicate the peak positions, with points likely belonging to the same series given the same shape. The uncertainties show the half width at half-maximum of the peaks. The red lines (—) show the predicted TKER for the dissociation of Ta_2^+ *via* the pathways shown in table 5.2 and are labelled accordingly. $E + v'' = 1$ indicates the predicted TKER for vibrationally excited ($v'' = 1$) Ta_2 dissociating into channel E.

The result of this analysis is shown in fig. 5.9: the plot shows the fitted TKER peak positions of all the images with off-centre intensity *versus* the energy of two of the photons used. Plotted alongside are the TKER expected for each of the dissociation channels in table 5.2, with D_0 chosen by fitting the differences to give the best match to the dissociation channels. While this assignment captures most

of the peaks in the TKER range 0 – 1000 cm^{-1} a number of issues are apparent.

First, the high TKER peaks at photon energies of 47 112 cm^{-1} and 47 374 cm^{-1} as well as some low TKER features at around 47 000 cm^{-1} are not accounted for in this scheme. Second, the assignments requires the presence of vibrationally excited Ta_2 to explain the four peaks with TKER 625, 668, 738 and 752 cm^{-1} observed between 47 120 cm^{-1} and 47 195 cm^{-1}. However, we do not see evidence of any other TKER features that could be related to vibrationally excited Ta_2 even at those particular wavelengths. Finally, the value for D_0 associated with this best assignment is *ca.* 5.10 eV, contrasting the values for D_0 hitherto observed as well as our own calculations (see section 5.4).

In conclusion, while the two photon photodissociation of neutral Ta_2 cannot be excluded as a contributor to some of the features observed, it does not fully explain the TKER of all the Ta fragments observed.

Photodissociation of Ta_2^+

As alluded to earlier, the other pathway consistent with a Ta cofragment is the two photon photodissociation of Ta_2^+ shown on the right hand side of fig. 5.8. In the first step the Ta_2 species is ionized by three photons. As before, we assume that the off-axis velocity imparted to Ta_2 by ionization is minimal, with energy in excess of the ionization potential going into the electron kinetic energy (eKE).

Equating the energy input and output for the photodissociation process we can form the analogue to eq. (5.6)

$$2 \times h\nu = \mathrm{TKER} + E(\mathrm{Ta}) + E(\mathrm{Ta}^+) + D_0(\mathrm{Ta}_2^+)\,. \tag{5.11}$$

As was the case for Ta_2, the dissociation energy of Ta_2^+, *i.e.* $D_0(Ta_2^+)$, is poorly defined. We therefore employ the same method of differences described in the previous section, which does not require knowledge of D_0 to assign dissociation channels.

The dissociation channels of Ta_2^+ that have products with suitable energy separation are shown in table 5.3 — note how the large number of closely spaced electronic states of Ta^+ makes for more densely spaced dissociation channels.

		Dissociation Products			Energy / cm^{-1}
	I'	**$Ta(^4F_{3/2})$**	+	$Ta^+(^5F_4)$	4415.7
✓	J'	$Ta(^4F_{5/2})$	+	$Ta^+(^5F_3)$	4652.3
✓	K'	$Ta(^4F_{7/2})$	+	$Ta^+(^5F_2)$	4995.3
	L'	$Ta(^4F_{5/2})$	+	$Ta^+(^5F_2)$	5190.1
✓	M'	$Ta(^4F_{3/2})$	+	$Ta^+(^3P_1)$	5330.7
✓	N'	$Ta(^4F_{9/2})$	+	**$Ta^+(^5F_1)$**	5621.0
✓	O'	**$Ta(^4F_{3/2})$**	+	$Ta^+(^3P_2)$	5658.0
✓	P'	$Ta(^4P_{1/2})$	+	**$Ta^+(^5F_1)$**	6049.4
✓	Q'	$Ta(^4P_{3/2})$	+	**$Ta^+(^5F_1)$**	6068.9
✓	R'	$Ta(^4F_{5/2})$	+	$Ta^+(^3P_0)$	6134.9
✓	S'	**$Ta(^4F_{3/2})$**	+	$Ta^+(^5F_5)$	6186.7

Table 5.3 Table showing the low-lying dissociation channels (Energy < 7000 cm^{-1}) for Ta_2^+. Channels below 4000 cm^{-1} are omitted as these would yield D_0 well outside the range previously observed and inconsistent product channel assignments. Observed channels are marked with a ✓. Ground electronic states of the atom and cation are **in bold**. The energies are given relative to an energy zero corresponding to dissociation into ground state $Ta(^4F_{3/2})$ and $Ta^+(^5F_1)$.

Fitting the differences in these to the differences in observed TKER leads to a unique assignment. Figure 5.10 shows the best fits of dissociation channels to the TKER data, and we can hence deduce the origin of each data point. The close spacing between a few of the dissociation channels means that some assignments are ambiguous, *e.g.* in the case of channels N' and O'.

As we can see, the TKER lines of our predicted dissociation channels match the data quite well, with almost every data point matching the dissociation channel it is attributed to, within uncertainty. Note that the channels which appear over a wide range of wavelengths (M', N'/O', P'/Q', S') are all associated with the production of a ground state atom $Ta(^4F_{3/2})$ or cation $Ta^+(^5F_1)$.

In contrast to the assignment on the basis of neutral Ta_2 dissociation (see previous section), all the TKER peaks are assigned, including those at 47 112 cm^{-1} and 47 374 cm^{-1}. Additionally, we do not need to invoke vibrationally excited Ta_2^+ to explain our data. On the basis of these considerations we conclude that the process

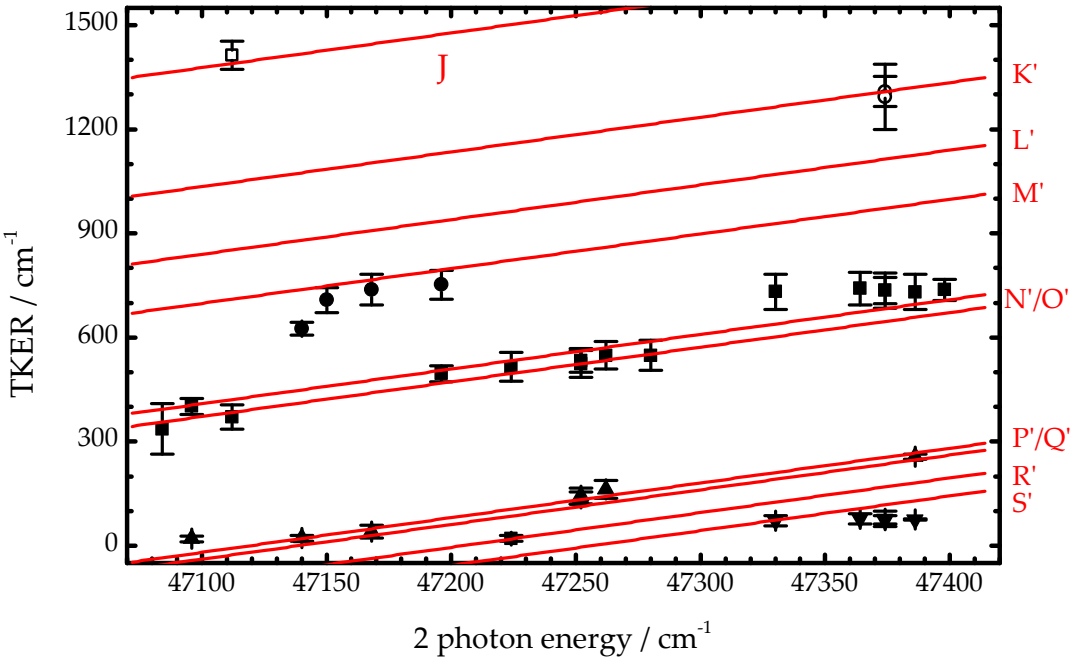

Figure 5.10 Total kinetic energy release (TKER) plotted as a function of photon energy. The solid and hollow shapes (▼, ▲, ■, ●, ○, ❑) indicate the peak positions, with points likely belonging to the same series given the same shape. The errors bars show the half width at half-maximum of the peaks. The red lines (—) show the predicted TKER for the dissociation of Ta_2^+ *via* the pathways shown in table 5.3.

we observe is indeed the ionization of Ta_2 followed by the photodissociation of Ta_2^+ at the two photon level.

Assuming that our assignment of data to particular dissociation channels is correct, we can derive a new value for the dissociation energy D_0: for each set of data belonging to a particular dissociation channel, the intercept of the line in fig. 5.10 will be equal to $E(\mathrm{Ta}) + E(\mathrm{Ta}^+) + D_0(\mathrm{Ta}_2^+)$ — and as we know the value of $E(\mathrm{Ta}) + E(\mathrm{Ta}^+)$ by assignment, the value of D_0 is easily obtained.

The D_0 determined in this way for the dissociation channels in fig. 5.10 are shown in table 5.4. We have limited ourselves to channels that were observed at several wavelengths. The assignments of N'/O' and P'/Q' are ambiguous, and so the associated D_0 values differ slightly. As a result, there is no single best estimate for D_0, but rather a number of possibilities depending on the exact

assignment. The bracketing values are $41\,076 \pm 6\,\mathrm{cm}^{-1}$ and $41\,055 \pm 6\,\mathrm{cm}^{-1}$, or, in eV, 5.0928(7) eV and 5.0902(7) eV, which may be summarised as 5.094 – 5.090 eV. Note that as the slope of the lines of fig. 5.10 is fixed, the calculated uncertainty may be lower than the true uncertainty.

Channel	$D_0(\mathrm{Ta}_2^+)$ / cm^{-1}
M'	$41\,162 \pm 20$
N'†	$41\,070 \pm 10$
O'†	$41\,033 \pm 10$
P'†	$41\,073 \pm 4$
Q'†	$41\,054 \pm 4$
Mean* (M',N',P')	$41\,076 \pm 6$
Mean* (M',O',Q')	$41\,055 \pm 6$

Table 5.4 Table showing the dissociation energies D_0 calculated for three sets of Ta_2^+ dissociation channels. The uncertainties shown account for both the standard error (1σ) of the fit as well as the OPO linewidth ($5\,\mathrm{cm}^{-1}$). (†) The D_0 shown for N'&O' and P'&Q' represent two possible assignments of *the same* datasets in each case. The two bounding mean values consistent with the data are shown. (*) Weighted mean $\bar{x}$ of individual measurements x_i — defined as $\bar{x} = \sum x_i w_i / \sum w_i$, weights $w_i = 1/\sigma_i^2$, where σ_i is the uncertainty in each measurement.

From this value for $D_0(\mathrm{Ta}_2^+)$, as well as the ionization energies $\mathrm{IE}(\mathrm{Ta}_2)$ and IE(Ta), we can determine the dissociation energy $D_0(\mathrm{Ta}_2)$ of the neutral dimer *via* a thermodynamic cycle

$$D_0(\mathrm{Ta}_2) = D_0(\mathrm{Ta}_2^+) + \mathrm{IE}(\mathrm{Ta}_2) - \mathrm{IE}(\mathrm{Ta})\,. \tag{5.12}$$

The ionization potential of Ta is well known(7.550 eV);[248] while the ionization potential of Ta_2 has been loosely bracketed as 5.98 – 6.42 eV.[237] Hence, eq. (5.12) yields a range of 3.52 – 4.80 eV for $D_0(\mathrm{Ta}_2)$.

5.3.4 Other considerations

In addition to the KER peak positions presented in the previous section we have also calculated the branching ratios of the associated dissociation channels (see section 2.5.3). Unfortunately, the number of images in which dissociation channels are present concurrently are rather small, so we are unable to obtain a statistically relevant number of points of comparison, which precludes a quantitative analysis. However, we can make a few qualitative comments, based on the presence or absence of certain channels across the observed range.

The channel N'/O' is the most consistent throughout the studied region. Both possible assignments (N' and O') correlate with the formation of a ground state atom (or ion). In contrast, channels R', J' and K', which produce electronically excited Ta and Ta^+, are only observed at single wavelengths, indicating that they are only local perturbations. It is worth noting that in the region where N'/O' is not observed, we *do* observe the channel M' which differs from O' only in the spin orbit excitation of the Ta^+ fragment ($Ta^+(^3P_2)$ in O' *vs.* $Ta^+(^3P_1)$ in M'). Given the above it is not surprising to find that the second most dominant channel (P'/Q') also involves the formation of ground state products. Channel S' is at the edge of detection capability, and it is therefore difficult to infer much about its relative importance.

In addition to considering the kinetic energy of our fragments, and the presence or absence of certain photodissociation channels, we can also learn something about the photodissociation process from the way the intensity in the observed rings changes as a function of polar angle, *i.e.* the anisotropy (see section 2.5.3). Using the method described in section 2.5.3 we have attempted to quantify the anisotropy by calculating the beta parameters β_2 and β_4.

The overall low count and relatively weak angular intensity variation mean that the second order beta parameter β_4 is not well defined, and thus we have limited our analysis to β_2 only. The result of this is plotted in fig. 5.11, using the assignment of data to dissociation channels that was introduced in section 5.3.3. The scatter in the data is rather large even within a single channel, and precludes a clear conclusion, but we note the following: Most of the β_2 are just slightly

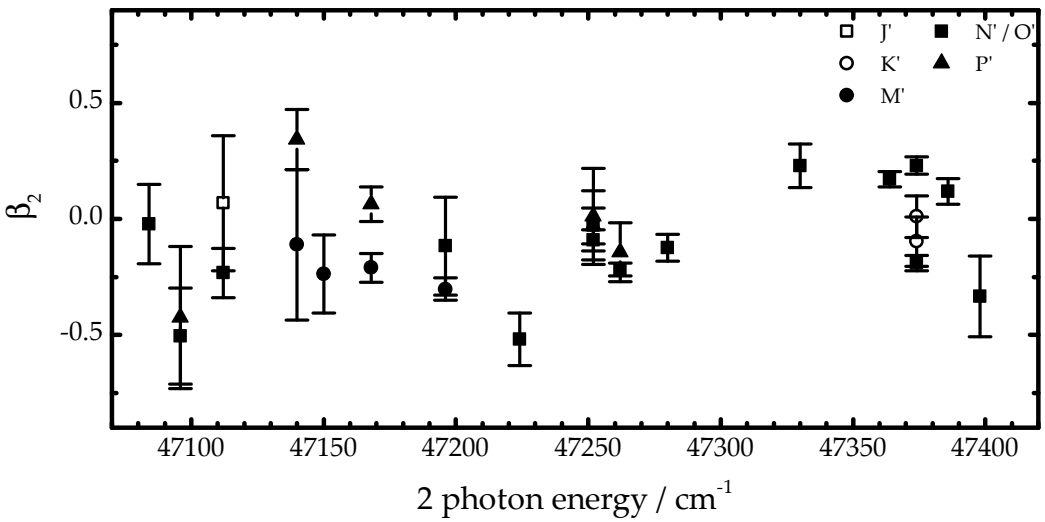

Figure 5.11 Observed β_2 anisotropy parameters, labelled according to dissociation channel. The uncertainties shown indicate the standard error (1σ) of the fit.

below zero, indicating images with weak vertical anisotropy. This suggests that the transitions to the intermediate (virtual) states in the photodissociation are perpendicular. Given that the calculated electronic ground state for Ta_2^+ is $^2\Delta_{g,3/2}$, this would mean that the intermediate states are of Φ or Π type.[145] The comparatively small anisotropy may be a result of some rotation in the intermediate states prior to photodissociation, or may arise due to electronic state mixing.

5.4 Discussion

No other detailed study of the photodissociation of the tantalum dimer exists. The only previous experiment that provides a comparable datum is that of Armentrout and coworkers.[236] In their guided ion beam study they determine the dissociation energy $D_0(Ta_2^+)$ to be 6.87 eV. This represents an appreciable discrepancy from our result of 5.094 – 5.090 eV. We note, however, that their results are described as "preliminary". The only known value for the dissociation energy of neutral Ta_2 (4.96 – 5.40 eV) is based on a combination of the result by Armentrout as well as the ionization potential of Collings[237]. It therefore presents the same discrepancy

with our result of 3.52 – 4.80 eV.

The comparison with computational results is mixed. The value reported for $D_0(Ta_2^+)$ by Wu (4.510 eV) is closer to our result, especially considering the level of theory employed, while the best value given by Jiang and coworkers (3.51 eV) shows some significant discrepancy. However, the authors of said study also report values of (5.54 eV) and (4.70 eV) with different functionals and basis sets. On the other hand, the dissociation energy of the neutral dimer, $D_0(Ta_2)$, calculated by Fa (4.53 eV) and Borin (4.63 eV) falls within the range of our result of 3.52 – 4.80 eV.

In addition, to accompany the experimental work presented herein, calculations were performed by our coworkers in Canada using a combination of density functional theory and high level spin-orbit multiconfigurational quasi-degenerate perturbation theory (SO-MCQDPT).[249] The details of this work shall be discussed elsewhere, but crucially for this work the calculated ground state of Ta_2^+ is found to be $^2\Delta_{g,3/2}$ with a dissociation energy $D_0(Ta_2^+) = 5.35$ eV and a bond length of $r_e = 2.16$ Å. On the other hand, the ground state of Ta_2 is found to be $^3\Sigma_{g,0}^-$ with a dissociation energy $D_0(Ta_2) = 4.35$ eV and a bond length of $r_e = 2.20$ Å. Both of the calculated values for the dissociation energy D_0 are in good agreement with the experimental results. Importantly for the analysis here presented, the similarities in calculated bond lengths and vibrational frequencies of Ta_2^+ and Ta_2 mean that the vertical ionization of Ta_2 $^3\Sigma_{g,0}^-$ ($v = 0$) should result predominantly in the formation of $^2\Delta_{g,3/2}$ ($v = 0$). This is a crucial finding in support of our analysis: if the Ta_2^+ parent species were formed in vibrationally excited states, the experimentally derived D_0 would only represent a lower bound on the true D_0, since Ta_2^+ in excited vibrational states would require less energy to dissociate and thus have a lower D_0.

5.5 Conclusion

The one colour photodissociation of tantalum dimer in the region 23 500 – 23 800 cm^{-1} has been successfully characterized using a combination of action spectroscopy and velocity map imaging.

Use of the velocity map images permits the analysis of the kinetic energy

distribution of the ejected Ta^+ fragments for the first time. We are able to assign every image to three photon ionization of Ta_2 followed by fragmentation of the cation Ta_2^+ at the two photon level. Several different dissociation channels are observed throughout the region, corresponding to different internal energies of the products Ta and Ta^+. The dissociation into the electronic ground state of at least one of the products is heavily favoured, with all but a few KER peaks correlating with a dissociation channel that produces the atomic ($Ta(^4F_{3/2})$) or cationic ($Ta^+(^5F_1)$) ground state.

The dissociation energy of Ta_2^+, $D_0(Ta_2^+)$ is measured to be in the range 5.094 – 5.090 eV, in good agreement with computational predictions. The dissociation energy of neutral Ta_2, $D_0(Ta_2)$ is hence calculated to lie in the range 3.52 – 4.80 eV. The anisotropies observed show weak evidence of a perpendicular transition being involved in the photodissociation process.

These results illustrate the power of velocity map imaging in combination with action spectroscopy for the study of small molecule and cluster dissociations, even in a case such as Ta_2^+, where comparatively little information is available beforehand. Nevertheless the main barrier to application of this technique to a wider range of transition metal dimers and clusters remains the limited knowledge of even basic information such as the dissociation energy or the internal energy structure of parent clusters. As more data is available, the effectiveness of study *via* VMI grows.

Chapter 6 shows the application of the technique to the photodissociation of the copper dimer.

CHAPTER 6

Imaging the photodissociation dynamics of the neutral copper dimer*

This chapter presents a study of the UV spectroscopy and photodissociation dynamics of Cu_2, using a combination of action spectroscopy and velocity map imaging. The enhancement spectra of Cu_2 and Cu have been recorded in the range 36 000 – 38 200 cm^{-1}, showing evidence of extensive Cu_2 photodissociation as a result of irradiation at wavelengths corresponding to the $H \leftarrow X$, $I \leftarrow X$ and $J \leftarrow X$ transitions as well as Okazaki's system 5. Resonant excitation *via* several vibrational components of the $J \leftarrow X\ ^1\Sigma_g^+$ system leads to fragmentation which is interpreted as a combination of direct dissociation of $Cu_2^+\ ^2\Pi$ ion state produced in the resonant photoionization process and the dissociation of doubly excited Cu_2 states above the dissociation threshold. Fitting the observed kinetic energy release spectra obtained from the velocity map images yields a value of $D_0(Cu_2^+\ X\ ^2\Sigma_g^+) = 1.71 \pm 0.05$ eV, from which a value of $D_0(Cu_2,\ X\ ^1\Sigma_g^+) = 1.88 \pm 0.05$ eV can be obtained *via* the known ionization energy. With the exception of the band assigned

*Published, in adapted form, as I. S. Parry et al. "Imaging the photodissociation dynamics of neutral metal clusters: copper dimer, Cu_2 and copper oxide, CuO". *Physical Chemistry Chemical Physics*, Advance Article, (2013).

$H \leftarrow X$ (0-0), photolysis leads to kinetic energy releases consistent with the same kind of dissociation pathways as observed for $J \leftarrow X$. Finally, the production of Cu_2^+ with non-zero kinetic energy release is interpreted as evidence of photolysis of Cu_3 to produce Cu and Cu_2, and from this a Cu_3 dissociation energy of 0.61 ± 0.03 eV is derived.

6.1 Introduction

Coinage metals have long been favoured targets for the study of metal and metal-containing clusters, on account of their closed *d*-shell ground states and open *d*-shell excited states. This has led to their use as benchmark systems for both experimental[56,250] and computational[251–254] approaches.

Small copper complexes are among the best-known and most studied transition metal complexes, and compounds containing such complexes have important applications in a variety of synthetic applications such as the functionalization of alkanes[11] or selective oxidation reactions.[12] The copper dimer is thought to be an important part of the metalloenzyme that catalyses the biological oxidation of methane;[255] and has been studied extensively in order to understand its electronic structure and bonding.

6.1.1 Previous work on Cu_2

Much of the early work on Cu_2 has been reviewed by Morse,[230] and key results reported therein will be highlighted in the following paragraphs (a detailed discussion of these results may be found in the review itself).

The first accurate determinations of the Cu_2 binding energy stem from third law determinations using Knudsen cell effusion spectrometry[256,257] of which the value recorded by Hilpert[258] (1.925 ± 0.029 eV) is the most precise. Rohlfing *et al.* used their data from dispersed fluorescence of Cu_2 to obtain, *via* a Birge-Sponer extrapolation, a dissociation energy of 2.061 ± 0.025 eV. On the basis of these results, the aforementioned review by Morse adopted a value of 2.01 ± 0.08 eV. More recently, two separate collision induced dissociation studies by Ingólfsson[259]

and Krückeberg[121] investigated the the dissociation energy of the cationic copper clusters, measuring the dissociation energy of Cu_2^+ as 1.64 ± 0.14 eV and 1.57 ± 0.08 eV, respectively. Coupled with the well known ionization potentials of Cu[260] and Cu_2,[261] this would imply $D_0(Cu_2)$ of 1.81 ± 0.14 eV and 1.74 ± 0.08 eV respecively.

The spectroscopy of Cu_2 has been probed using a wide range of techniques including direct absorption,[262] fluorescence,[24,263,264] photoionization,[261,265–268] and Fourier transform emission.[269]

The $X\,^1\Sigma_g^+$ ground state of Cu_2 is well established as a result of detailed studies of, in particular, the $A\,^3\Sigma_u \leftarrow X\,^1\Sigma_g^+$ and $B\,^1\Sigma_u \leftarrow X\,^1\Sigma_g^+$ band systems.[270–272]

Computational investigations of Cu_2 have progressed over several decades, of which the early *ab initio* calculations by Miyoshi and coworkers[273] are particularly noteworthy (for a more complete overview see the works cited in ref. [274]). The recent developments have been reviewed by Lecoultre *et al.* in their TD-DFT study.[250]

Here, we apply our VMI techniques toin combination with electronic spectroscopy to Cu_n (n=2,3) in order to unravel the fragmentation dynamics and deduce parent molecule dissociation energies.

6.2 Experimental procedure

The experimental apparatus and the techniques employed for this work are those described in the earlier sections 2.4 and 2.5.

The target consisted of a 1 mm thick disc of copper. The copper clusters are expanded in a gas mixture consisting of helium (8 bar) with a small admixture of N_2O (5 – 10 %), which, although introduced primarily to generate oxides for other studies, was also found to improve the clustering of copper. A single UV laser was used to trigger photoexcitation / photofragmentation as well as photoionization. The UV light was provided by the frequency doubled output of a Sirah Panther EX dye laser (Coumarin 153, typically 0.5 – 1 mJ/pulse), focussed into the cluster beam by a 30 cm bi-convex lens. The UV light was aligned to cross centrally between the repeller and extractor plates of the electrode stack, and was

temporally synchronized to intersect the most dimer-rich portion of the molecular beam. All experiments used UV with vertical polarization, *i.e.* with polarization vector lying in the image plane. The scans and images were performed on the ^{63}Cu isotope of the monomer and the ^{63}Cu^{63}Cu isotopologue of the dimer.

In a first step, a series of coarse grained (0.05 nm/step) action spectra were collected in the range 36 000 – 38 200 cm^{-1} and enhancement features identified. Three regions corresponding to the fundamental, first overtone and first hotband of the $J \leftarrow X$ transition (see section 6.3.1) were subsequently scanned at higher resolution (0.0075 nm/step). Velocity map images of ^{63}Cu were collected by tuning the UV laser to each of the peaks identified in the action spectrum of ^{63}Cu.

6.3 Results and discussion

Over the whole wavelength range investigated, the only copper species that were observed in the mass spectrum were the isotopologues of the monomer Cu and dimer Cu_2. It is important to note that this does not, in itself, exclude the possibility of other species (*e.g.* CuO) being present in cluster beam. If such species are not efficiently ionized in this UV range, then they will not appear in the mass spectrum. However, if these species fragment to form Cu or Cu_2 as a result of irradiation, then their signature may still appear in the action spectra or velocity map images.

6.3.1 UV spectroscopy

Figures 6.1 and 6.2 show the one-colour UV action spectra of the copper monomer and dimer. The range of the spectrum encompasses the photosystems previously observed by Smalley ("III-V", designated $H \leftarrow X$, $I \leftarrow X$ and $J \leftarrow X$ by Morse,[230] whose nomenclature we will use) as well as Okazaki's system 5.[262] Of these, only the $J \leftarrow X$ band system has been studied in greater detail using laser-induced fluorescence, though the state symmetry could not be determined owing to severe perturbations in the rotational envelope.[263] The major enhancement features in

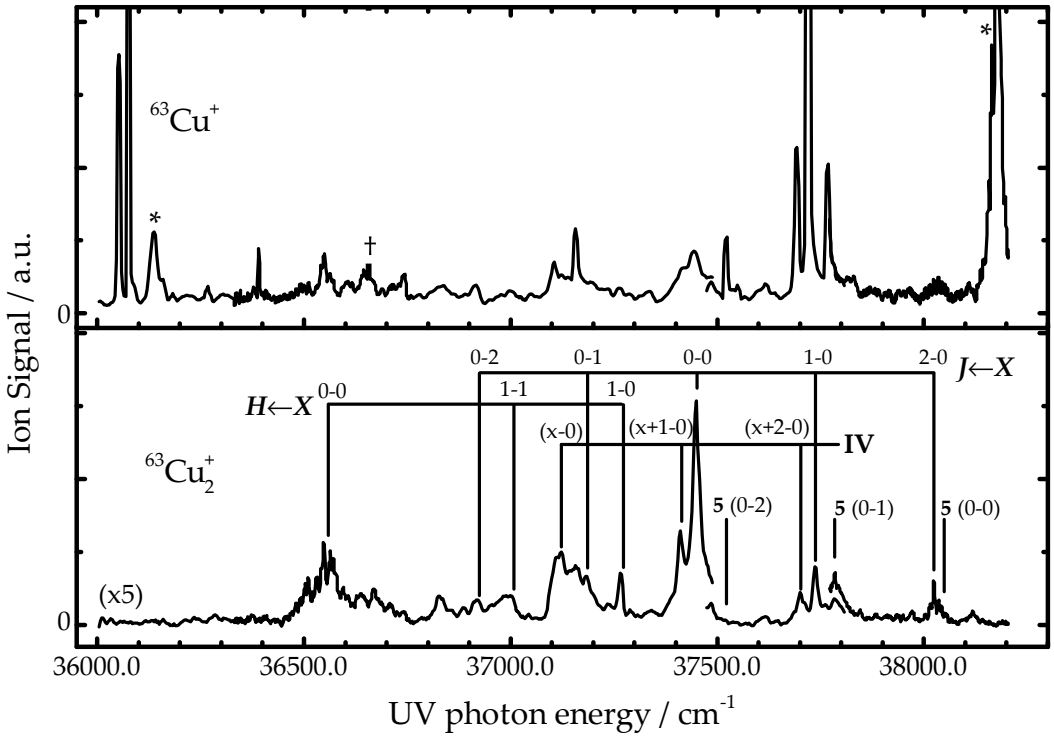

Figure 6.1 One colour action spectra of ^{63}Cu(top) and $^{63}Cu_2$(bottom). The labels above the ^{63}Cu spectrum show the assignments of ^{63}Cu features to autoionization of doubly excited ^{63}Cu states, while (*) marks features corresponding to resonant ionization *via* an excited atomic state (see ref. [245]). The assignments of Cu_2 features to the known band systems are indicated on the Cu_2 spectrum. (†) Artefact removed for clarity.

the Cu_2 spectrum may be assigned to two photon ionization (R2PI) *via* one of the aforementioned Cu_2 band systems. All of the band systems expected in this range on the basis of prior work are observed in the Cu_2 spectrum, and the relatively weak intensity of hot bands indicates that only a small portion of the clusters in the beam are in the first or second vibrationally excited state.

The smooth rotational envelope of the $J \leftarrow X$ (0-0) band differs markedly from that observed by Page *et al.*[263], whose study showed strong perturbations in the rotational envelope of the (0-0) band, attributed to some other (unseen) state. This difference is also observed, to a lesser degree, in the rotational structure of the (1-0) band. One explanation for this difference would be that the perturbation

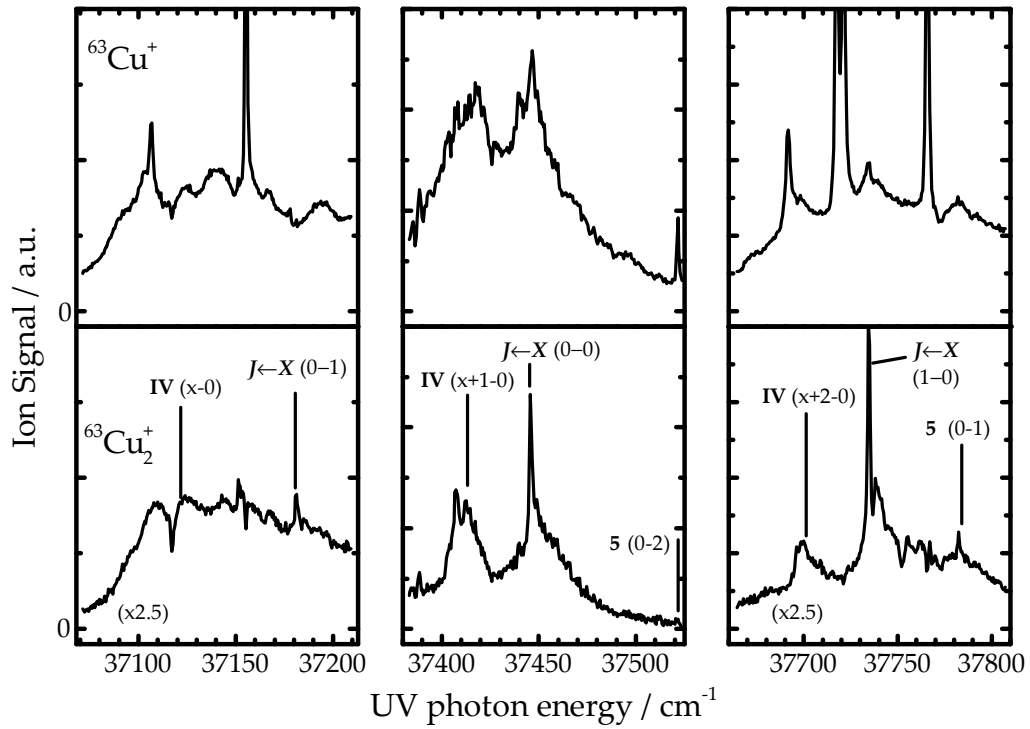

Figure 6.2 High resolution one colour action spectra of ^{63}Cu (top) and $^{63}Cu_2$ (bottom) in the regions of the spectrum containing the $J \leftarrow X$ (0-0),(1-0) and (0-1) bands. The labels above the ^{63}Cu spectra show the assignements of ^{63}Cu features to autoionization of doubly excited ^{63}Cu states.[245] The assignments of Cu_2 features to the known band systems are indicated on the Cu_2 spectra.

by the unseen state offers a non-fluorescent energy loss pathway, reducing the fluorescence quantum yield of certain rotational states. This would not affect the resonant ionization *via* those states, explaining why the rotational structure envelope in our study is smooth.

Two of the enhancement features (indicated by *) in the Cu spectrum can be assigned to R2PI *via* an excited atomic state, while several others can be ascribed to the autoionization of excited Cu states prepared by two-photon absorption. In addition, a large portion of the enhancements in the Cu spectrum directly correlate with the aforementioned enhancements in the Cu_2 channel, strongly indicating that these Cu enhancements are due to some form of resonant photofragmentation

of Cu_2.

Two of the Cu enhancements (at 36 390 cm^{-1} and 37 107 cm^{-1}) are not explained by the above processes. Their presence may indicate that Cu is produced by the fragmentation of a species other than Cu_2. However, as indicated earlier, no other copper containing species were observed in the mass spectrum across the spectral range. Therefore, if these Cu signals are a result of fragmentation of another species, these other species are not efficiently ionized by the UV in this range — their identity cannot be determined on the basis of the UV spectrum alone.

In next section, we present in investigation of the likely fragmentation mechanism(s) by one-colour VMI recorded at all of the Cu enhancements observed in the one-colour spectrum. This will allow a better understanding of the Cu_2 photofragmentation mechanism(s) as well as providing clues to the identity of the unknown Cu containing species.

6.3.2 Photodissociation pathways of Cu_2

The UV spectra provide very strong evidence that a process involving the resonant excitation of Cu_2 is responsible for a large portion of the Cu^+ produced in the UV region studied. The two main possibilities are the resonant photoionization of Cu_2, followed by fragmentation of the Cu_2^+ produced, and resonant photofragmentation of the neutral Cu_2, followed by photoionization of the atoms produced. In the next sections, these pathways are discussed in turn and subsequently compared to experimental results.

Photodissociation of the cationic dimer Cu_2^+

As seen in the UV spectra figs. 6.1 and 6.2, Cu_2^+ is readily produced by resonant photoionization. The photoionization *via* the J(v=0) state was studied in detail by Sappey and coworkers by photoelectron spectroscopy.[261] They identified the ionic ground state $X\ ^2\Sigma_g^+$ as well as a pair of $^2\Pi$ states at $9219 \pm 11\ cm^{-1}$ ($^2\Pi_{3/2}$) and $10\,127 \pm 16\ cm^{-1}$ ($^2\Pi_{1/2}$). Ionization to the $^2\Pi$ proceeds *via* direct photoionization out of the neutral ground state, with a branching ratio of 3 : 1 in favour of the

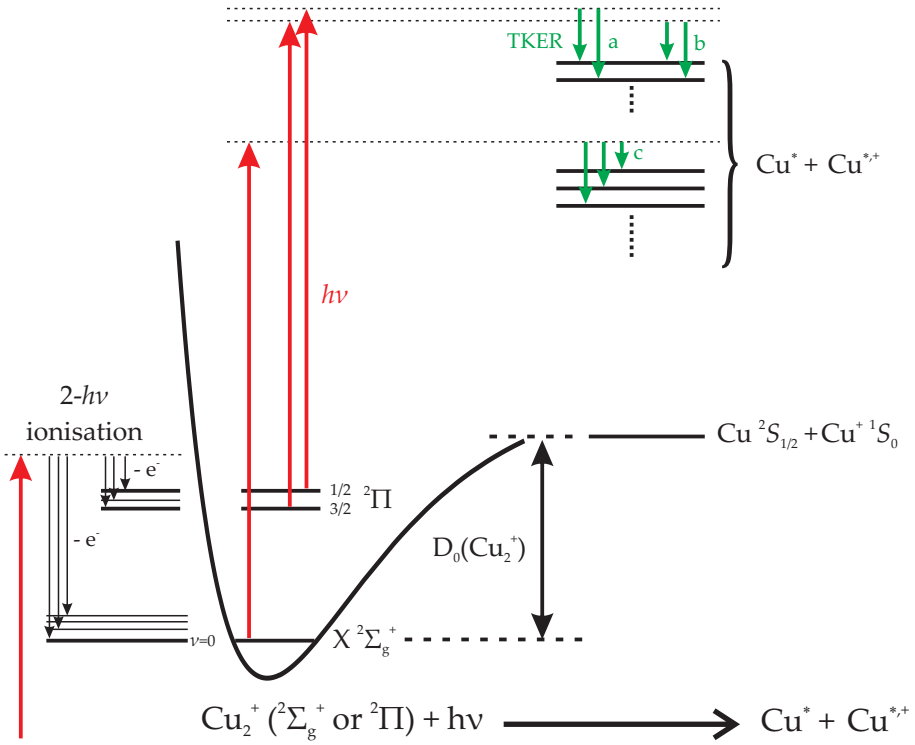

Figure 6.3 Illustration of Cu_2^+ photofragmentation, showing the schematic $X\,^2\Sigma_g^+$ ground state potential energy surface. One photon excitation out of the X and $^2\Pi$ ion states accesses different Cu and $Cu^{+,*}$ states and leads to different TKER (a-c).

$^2\Pi_{3/2}$ state. In contrast, the photoelectron spectrum corresponding to ionization to the $X\,^2\Sigma_g^+$ state showed a long vibrational progression up to $v^+ = 49$ (where v^+ is the vibrational quantum number of the ionic state). This is ascribed to a process involving the two-photon excitation of a neutral Cu_2 molecule to a doubly excited Cu_2^{**} state upon which dissociation and autoionization compete. This leads to a portion of the ionized Cu_2 molecules being significantly elongated prior to ionization, which in turn means a large number of vibrational quantum states of the ion can be accessed.

Following photoionization, the fragmentation of the Cu_2^+ ion results in the formation of Cu and Cu^+:

$$Cu_2^+ + n \times h\nu \longrightarrow Cu^{+,*} + Cu^* \,. \tag{6.1}$$

The photon energy $h\nu$ corresponds to an electronic transition of the Cu_2 species, while $Cu^{+,*}$ and Cu^* denote copper atom and cation formed in some electronic state (which may not be the ground state). As before (see eq. (2.7) and section 5.3.3) we can find the total kinetic energy released (TKER) (see fig. 6.3) for n-photon fragmentation out of the Cu_2 ground state as

$$\mathrm{TKER} = n \times h\nu - E(\mathrm{Cu}^*) - E(\mathrm{Cu}^{+,*}) - D_0(\mathrm{Cu}_2^+)\,, \tag{6.2}$$

where $E(Cu^*)$ and $E(Cu^{+,*})$ denote the internal energies of the fragments and $D_0(Cu_2^+)$ the dissociation energy of Cu_2^+. The dissociation energy will depend on the initial state of Cu_2^+, with excited electronic states of Cu_2^+ requiring less energy to fragment, yielding more energetic fragments than those formed from the ground state (*cf.* fig. 6.3).

As there is no evidence of higher-lying excited electronic states of Cu_2^+ that could be accessed by resonant ionization in the photon energy range studied ($36\,000 - 38\,200\,\mathrm{cm}^{-1}$) we can set aside the possibility of multiphoton fragmentation, as such a process would require the preparation of a multiply excited Cu_2^+ species. This in turn would require the sequential absorption of photons, which is unlikely given the lack of a bound intermediate state. The fragmentation channels that can be accessed from the one-photon fragmentation are presented in table 6.1.

Cu_2^+ state	Channel	Cu product	Cu^+ product	Rel. Energy/cm^{-1}
$X\ ^2\Sigma_g^+$	1	$3d^{10}4s\ ^2S_{1/2}$	$3d^{10}\ ^1S_0$	0
	2	$3d^{10}4s\ ^2S_{1/2}$	$3d^9 4s\ ^3D_3$	21929
	3	$3d^{10}4s\ ^2S_{1/2}$	$3d^9 4s\ ^3D_2$	22847
	4	$3d^9 4s^2\ ^2D_{5/2}$	$3d^{10}\ ^1S_0$	11503
	5	$3d^9 4s^2\ ^2D_{3/2}$	$3d^{10}\ ^1S_0$	13245
$^2\Pi_{3/2}$	6a	$3d^{10}4s\ ^2S_{1/2}$	$3d^9 4s\ ^3D_3$	12710
	7a	$3d^{10}4s\ ^2S_{1/2}$	$3d^9 4s\ ^3D_2$	13628
	8a	$3d^{10}4s\ ^2S_{1/2}$	$3d^9 4s\ ^3D_1$	14779
	9a	$3d^{10}4s\ ^2S_{1/2}$	$3d^9 4s\ ^1D_2$	17046
	10a	$3d^9 4s^2\ ^2D_{5/2}$	$3d^9 4s\ ^3D_3$	23912
	11a	$3d^{10}4p\ ^2P_{1/2}$	$3d^{10}\ ^1S_0$	21316
	12a	$3d^{10}4p\ ^2P_{3/2}$	$3d^{10}\ ^1S_0$	21565
$^2\Pi_{1/2}$	6b	$3d^{10}4s\ ^2S_{1/2}$	$3d^9 4s\ ^3D_3$	11802
	7b	$3d^{10}4s\ ^2S_{1/2}$	$3d^9 4s\ ^3D_2$	12720
	8b	$3d^{10}4s\ ^2S_{1/2}$	$3d^9 4s\ ^3D_1$	13871
	9b	$3d^{10}4s\ ^2S_{1/2}$	$3d^9 4s\ ^1D_2$	16137
	10b	$3d^9 4s^2\ ^2D_{5/2}$	$3d^9 4s\ ^3D_3$	23004
	11b	$3d^{10}4p\ ^2P_{1/2}$	$3d^{10}\ ^1S_0$	20408
	12b	$3d^{10}4p\ ^2P_{3/2}$	$3d^{10}\ ^1S_0$	20657

Table 6.1 Table showing the accessible dissociation channels following one-photon fragmentation of $Cu_2^+\ ^2\Sigma_g^+$ and $^2\Pi$ into Cu* and $Cu^{+,*}$ (see eq. (6.1)).

Photodissociation of the neutral dimer Cu_2

Another pathway to forming Cu^+ is the resonant photodissociation of Cu_2 at the one or two photon level, followed by ionization of one of the Cu fragments produced. As the ionization step does not significantly affect the recoil of the Cu fragment, the key step in this pathway is the initial fragmentation step

$$Cu_2 + n \times h\nu \longrightarrow Cu^{*,1} + Cu^{*,2}\,, \tag{6.3}$$

with

$$\mathrm{TKER} = n \times h\nu - E(\mathrm{Cu}^{*,1}) - E(\mathrm{Cu}^{*,2}) - D_0(\mathrm{Cu}_2)\,, \tag{6.4}$$

where $\mathrm{Cu}^{*,1}$ and $\mathrm{Cu}^{*,2}$ are atomic fragments produced in some particular electronic state. The process is illustrated in fig. 6.4 assuming a reasonable $D_0(\mathrm{Cu}_2)$. At the one photon level, the photon energy is only sufficient to produce a copper atom in the electronic ground state ($^2S_{1/2}$) as well as a copper atom in the ground state or one of the first two excited states ($^2D_{5/2}$ and $^2D_{5/2}$). The corresponding channels are shown in table 6.2

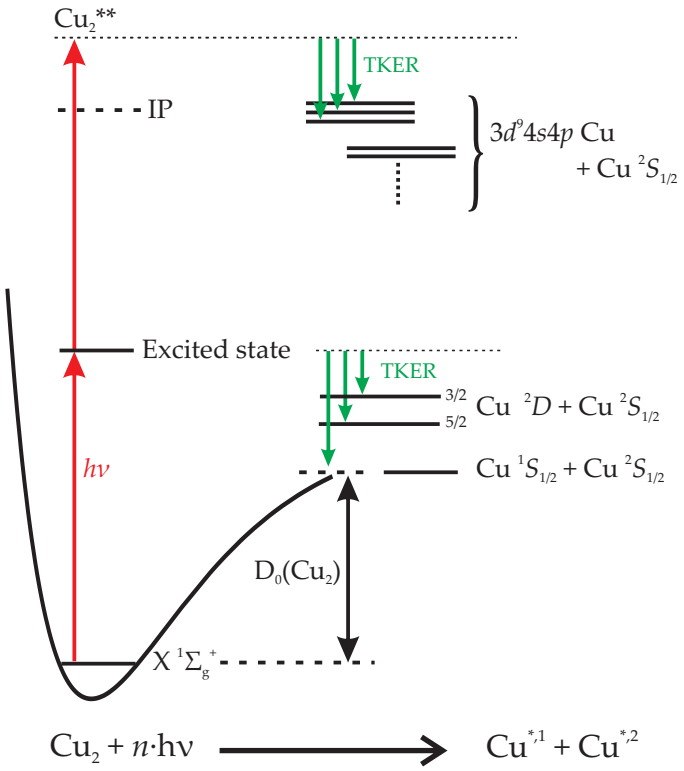

Figure 6.4 Illustration of the resonant photofragmentation of neutral Cu_2, showing the schematic potential energy curve for the $\mathrm{X}\,^1\Sigma_g^+$ ground state. Resonant excitation at the one photon level followed by Cu_2 fragmentation accesses the atomic ground state ($^2S_{1/2}$) as well as the the first two excited states ($^2D_{5/2}$ and $^2D_{5/2}$). Two photon excitation to a doubly excited Cu_2^{**} followed by fragmentation can access a large number of high-lying Cu $3d^9 4s4p$ states.

	$Cu^{*,1}$ product	$Cu^{*,2}$ product	Rel. Energy/cm^{-1}
A	$3d^{10}4s\ ^2S_{1/2}$	$3d^{10}4s\ ^2S_{1/2}$	0
B	$3d^{10}4s\ ^2S_{1/2}$	$3d^9 4s^2\ ^2D_{5/2}$	11203
C	$3d^{10}4s\ ^2S_{1/2}$	$3d^9 4s^2\ ^2D_{3/2}$	13245

Table 6.2 Accessible channels following one-photon dissociation of $Cu_2\ ^1\Sigma_g^+$ into atomic fragments $Cu^{*,1}$ and $Cu^{*,2}$ (see eq. (6.3)).

As discussed earlier, the evidence from photoelectron spectroscopy suggests that Cu_2 can absorb resonant radiation to form a doubly excited Cu_2^{**} state above the ionization threshold.[261] The high internal energy of such a species means that its photodissociation results in significantly more energetic product states. As a result, a large number of dissociation channels corresponding to combinations of the many high-lying Cu states[245,275] are, in principle, accessible. However, in the aforementioned photoelectron study, Sappey *et al.* reported that the spectra exhibited features corresponding to atoms in $3d^9 4s4p$ electronic configurations lying 6.6 – 8.1 eV above ground state Cu, and this was attributed to dissociation from Cu_2^{**} states.[261] A number of closely spaced dissociation channels consistent with this results are available at the two photon level, taking the general form

$$Cu_2 + 2 \times h\nu \longrightarrow Cu\ 3d^9 4s4p + Cu\ ^1S_{1/2}\,. \tag{6.5}$$

6.3.3 Velocity map imaging of Cu

The $J \leftarrow X$ system

The VMI images of $^{63}Cu^+$ recorded at wavelengths corresponding to Cu_2 $J \leftarrow X$ transitions are shown in fig. 6.5, while the extracted TKER spectra are shown in fig. 6.6. Both spectra exhibit a broad unresolved feature at TKER < 5000 cm^{-1} as well as an intense feature at 6000 – 9000 cm^{-1} which resolves into two peaks in the case of $J \leftarrow X$ (0-0). The spacing of the two intense peaks approximately matches the spin-orbit splitting of the $^2\Pi$ levels of Cu_2^+ (909 cm^{-1}). On this basis,

we assign the two peaks to channel 9a/b (see table 6.1)

$$Cu_2^+ \, ^2\Pi + h\nu \longrightarrow Cu^+ \, ^2S_{1/2} + Cu \, ^1D_2 \, . \tag{6.6}$$

The TKER of a fragmentation process such as (6.6) depends not only on the internal energies of starting materials and products, but also on the dissociation energy of the initial species — in this case, Cu_2^+ (*cf.* eq. (6.2)). Sappey *et al.* used their measured Cu_2 ionization energy of 7.899 ± 0.007 eV in combination with a value of $D_0(Cu_2) = 2.01 \pm 0.08$ eV to obtain a dissociation energy $D_0(Cu_2^+ \; X \; ^2\Sigma_g^+) = 1.84 \pm 0.08$ eV. Collision induced dissociation (CID) studies by Ingólfsson and coworkers yielded a value of 1.64 ± 0.14 eV;[259] while Krückeberg *et al.* report a value of 1.57 ± 0.08 eV.[121] If we assume that the assignment of the double feature to eq. (6.6) is correct, the best fit to the VMI data is obtained with a value of $D_0(Cu_2^+ \; X \; ^2\Sigma_g^+) = 1.71 \pm 0.05$ eV, which agrees relatively well with the results from CID. The plots of fig. 6.6 include simulations from a range of vibrational components of the $^2\Pi$ level of Cu_2^+ ($v = 0 - 4$), which account for the width of the features. In contrast to the findings of Sappey *et al.* we observe approximately 50 % more fragmentation products arising from the $^2\Pi_{1/2}$ spin orbit component than from the $^2\Pi_{3/2}$ component. One explanation for this discrepancy could be that the photodissociation crossection out of the $^2\Pi_{1/2}$ state is much larger than that out of the $^2\Pi_{3/2}$ state, so that even though less $Cu_2^+ \; ^2\Pi_{1/2}$ is produced, more of it photodissociates to give the TKER signature. An additional contribution to the observed peak width may be due to $^{63}Cu^+$ ions formed by dissociation of the Cu_2^+ isotopologue $^{63}Cu^{65}Cu^+$, whose intensity in the mass spectrum is comparable to that of $^{63}Cu_2$: $^{63}Cu^+$ ions recoiling from ^{65}Cu will have a slightly different recoil velocity than $^{63}Cu^+$ ions recoiling from ^{63}Cu, leading to a slightly different TKER (1.5 %). At a TKER of $8000 \, cm^{-1}$ this may account for an additional width of up to $120 \, cm^{-1}$.

Having obtained a value for $D_0(Cu_2^+)$, we can use the ionization energies of Cu

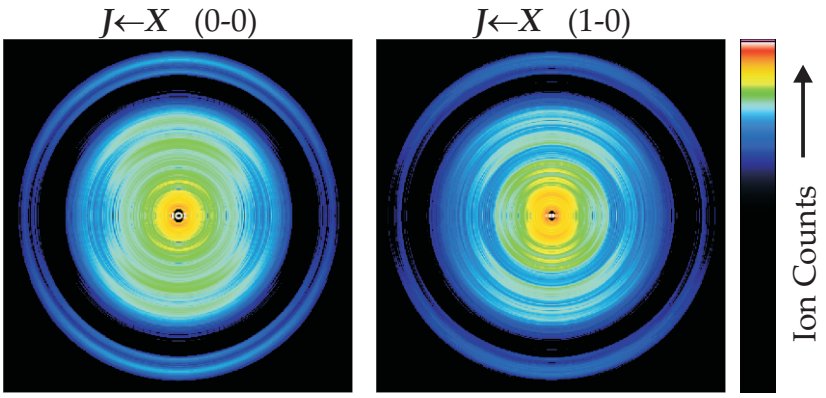

Figure 6.5 VMI images of $^{63}Cu^+$ recorded at the band heads of $J \leftarrow X$ (1-0) (37 734 cm^{-1}) and (0-0) (37 446 cm^{-1}).

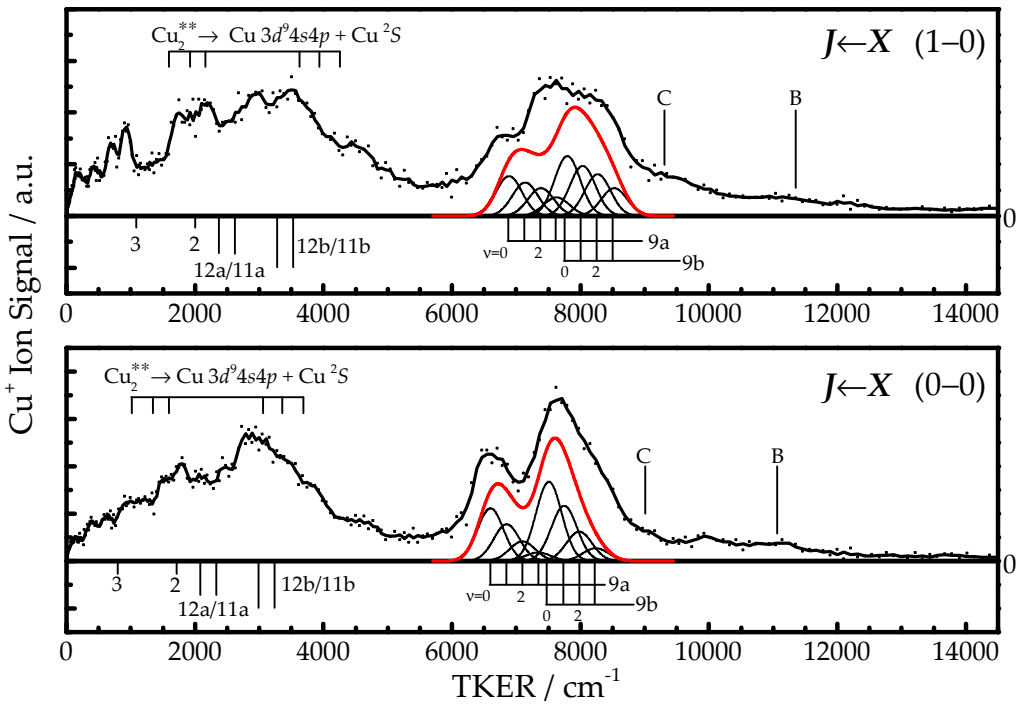

Figure 6.6 TKER spectra of $^{63}Cu^+$ recorded at the band heads of $J \leftarrow X$ (1-0) (37 734 cm^{-1}) and (0-0) (37 446 cm^{-1}). On each spectrum, dissociation channels of neutral Cu_2 are indicated by lines on the top portion, whereas dissociation channels of cationic Cu_2^+ are indicated below (the numbering schemes refer to tables 6.1 and 6.2). For channels 9a/b we show a simulation of the expected peak shape including a range of vibrational levels observed in the PES spectrum[261] ($v = 0 - 4$).

and Cu_2 to determine the dissociation energy of the neutral dimer

$$D_0(Cu_2) = D_0(Cu_2^+) + IE(Cu_2) - IE(Cu)\,, \tag{6.7}$$

where $IE(Cu_2)$ and IE(Cu) represent the ionization energies. The values of $IE(Cu_2)$ (7.899 eV)[261] and IE(Cu) (7.726 eV)[260] are well known from photoelectron and laser microwave studies. Thus, using our value from above, eq. (6.7) gives us $D_0(Cu_2\ X\ ^1\Sigma_g^+) = 1.88 \pm 0.05\,\text{eV}$.

We cannot rule out a contribution to the TKER spectrum arising from photodissociation of the Cu_2 J state (*cf.* eq. (6.3)). However, there are only two possible dissociation channels (B&C in table 6.2) that yield TKER in the range observed — they are marked on fig. 6.6 assuming the value for $D_0(Cu_2)$ determined above.

The broad feature in the range 0 – 5000 cm^{-1} is likely the result of several overlapping channels. We assign the main contribution to this peak as dissociation of doubly excited Cu_2^{**} on the neutral potential energy surface (see eq. (6.5)). Cu $3d^9 4s4p$ terms ^2S, ^2P and ^2D yield TKER in the range 1000 – 3700 cm^{-1}, consistent with the broad feature observed (see fig. 6.6). Other, lower-lying Cu terms would result in fragments with kinetic energies outside the observed range. One further possibility would be the photofragmentation of $Cu_2^+\ ^2\Pi$ into different atomic channels than those mentioned above — this would produce fragments with TKER well inside the broad envelope in all three spectra (channels 11a/b and 12a/b). Finally, we cannot exclude an additional contribution to the broad feature arising from channel 2 (dissociation out of $Cu_2^+\ X\ ^2\Sigma_g^+$).

The $J \leftarrow X$ (1-0) TKER spectrum shows an additional double peak at $700 < \text{TKER}/\text{cm}^{-1} < 900$. Channel 3 matches the TKER of this channel quite closely, but we do not observe a similar feature correlating with channel 3 in the (0-0) spectrum. The double peak would also fit consistently with photodissociation out of Cu_2^{**} to produce Cu $3d^9 4s4p$ and an *excited state* cofragment Cu $^2D_{3/2}$.

Other Cu_2 photosystems

Considerably less is known about the other photosystems observed in this study ($H \leftarrow X$, $I \leftarrow X$, Okazaki's system 5). In particular, there is no information on

the electronic states of Cu_2 that form system 5, or the vibrational states of I involved in the $I \leftarrow X$ transition, and even the assignment of system $H \leftarrow X$ is considered tentative[230] as it invokes a $\Delta G_{1/2}$ that is more than twice as large as that of comparable photosystems.[266] Without this knowledge, it is challenging to predict the dissociation channels (and their associated TKER) that would be expected following irradiation *via* each of these photosystems. Nevertheless, we can gain some insight by making the simplistic assumption that the photosystems in question access the same dissociation channels as those observed for the $J \leftarrow X$ system. Such an assumption requires that the same Cu_2^+ states ($^2\Pi_{3/2}$ and $X\ ^2\Sigma_g^+$) are populated through these photosystems and is predicated on the idea that the dissociation energies out of these photosystems are not too dissimilar.

Figure 6.7 shows the positions of the TKER peaks observed at each wavelength, as well as lines showing the expected TKER for the dissociation channels discussed earlier. The TKER spectra of Cu^+ recorded at wavelengths corresponding to photosystems 5 as well as the $I \leftarrow X$ and $H \leftarrow X$ (1-0) transitions contain peaks between 6000 cm^{-1} and 8000 cm^{-1} which are consistent with photodissociation through channel 9b (see table 6.1). No peaks consistent with photodissociation out of the $\Omega = 3/2$ spin-orbit component of the $^2\Pi$ state (channel 9a) are observed, in contrast with the case for $J \leftarrow X$. This suggests that photoionization through these photosystems populates the $^2\Pi_{1/2}$ less than photoionization through $J \leftarrow X$ (0-0) (where the branching ratio is around 3:1 in favour of $^2\Pi_{3/2}$).[261]

Similar to the case of $J \leftarrow X$ described in the previous section, several possible pathways are consistent with the peaks observed at low TKER ($< 3500\ cm^{-1}$). As we can see, both the TKER predicted from photodissociation *via* doubly excited Cu_2^{**} as well as that predicted from one-photon dissociation of the Cu_2^+ cation (channels 2,3,10 – 12) match the data.

The $H \leftarrow X$ (0-0) fundamental (36 559 cm^{-1}) produces fragments with markedly different TKER (see fig. 6.8). Both the number and the positions of the peaks are clearly distinct from those observed at other wavelengths, and cannot be fully explained on the basis of the dissociation channels discussed so far. This suggests that a fundamentally different process than the ones considered so far is responsible for the Cu^+ fragments recorded at that wavelength. The strong

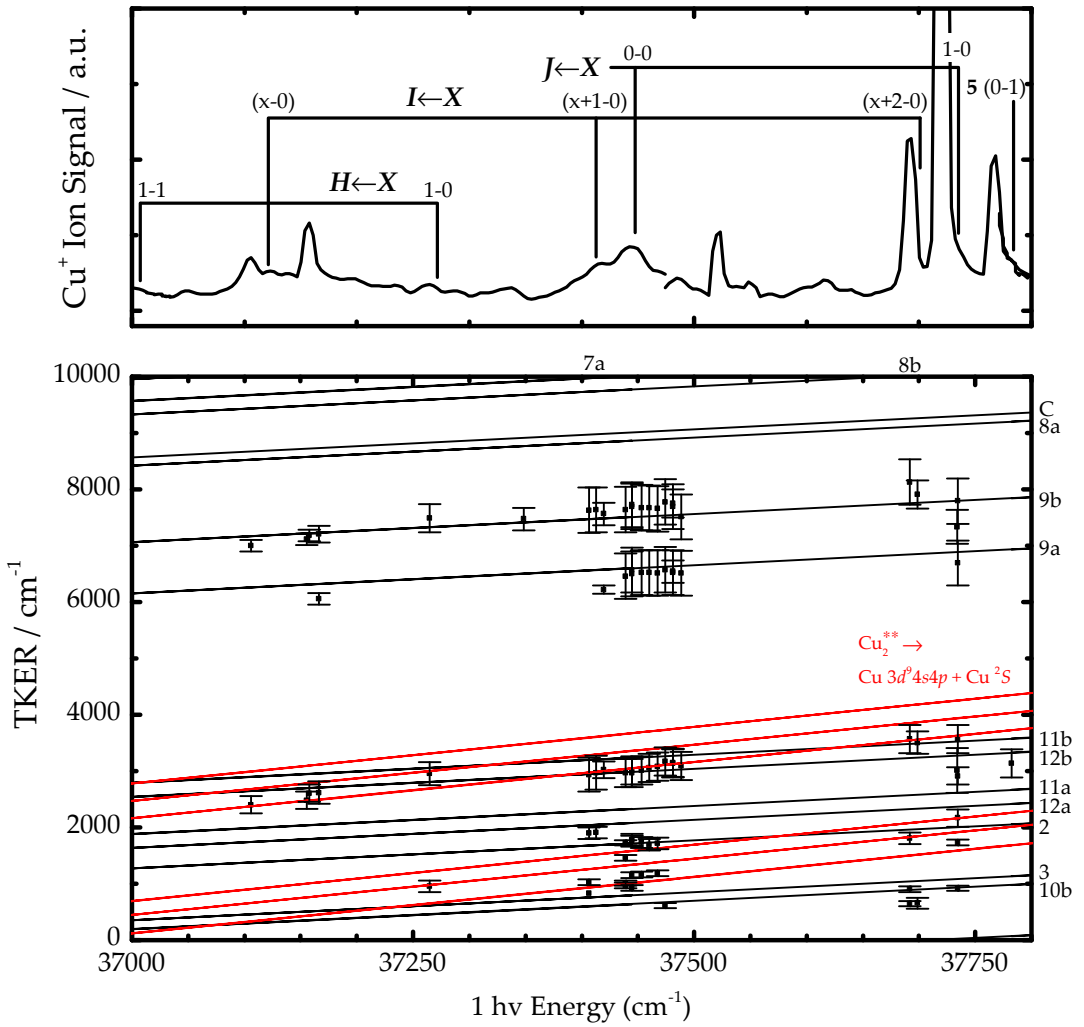

Figure 6.7 (Top) One colour action spectrum of ^{63}Cu. The labels show the positions of Cu_2 resonances (*cf.* fig. 6.1). (*) Features corresponding to resonant ionization *via* an excited atomic state (see [245]), (†) artefact removed for clarity. (Bottom) Total kinetic energy release (TKER) of $^{63}Cu^+$ plotted as a function of photon energy. The squares (■) indicate the positions of the features in the TKER spectra obtained from gaussian fits. The solid black lines show the predicted TKER for the dissociations channels of tables 6.1 and 6.2, while the red lines indicate the dissociation out of doubly excited Cu_2^{**} (see text).

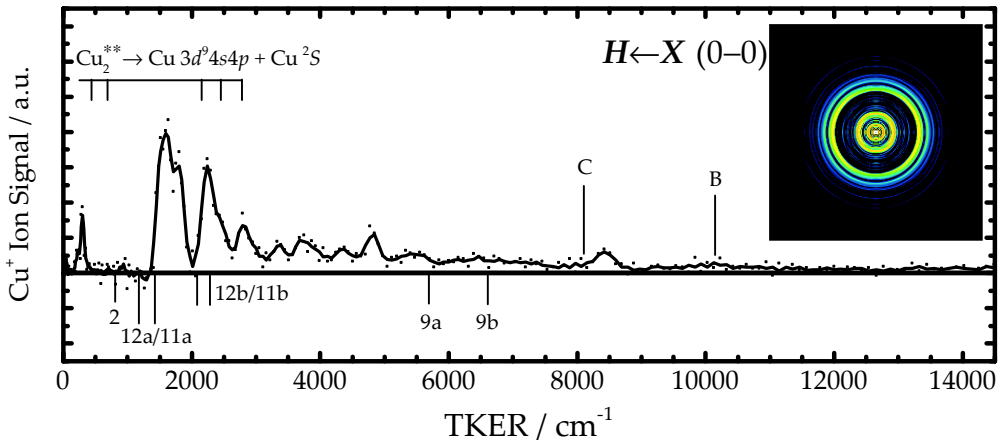

Figure 6.8 TKER spectrum of $^{63}Cu^+$ recorded at the $H \leftarrow X$ (0-0) band head (36 536 cm^{-1}). The dissociation channels are marked on the spectrum as per fig. 6.6. The inset shows the VMI image corresponding to the TKER spectrum.

contrast between the TKER recorded through the (0-0) and (1-0) transitions is surprising, as we would expect dissociations proceeding *via* the same electronic system to produce similar TKER, albeit it with potentially different branching ratios. One possible explanation for this would be that the two resonances assigned as (1-0) and (0-0) may not belong to the same electronic band system. This explanation would not be unexpected in the context of the numerous problems that have been highlighted with the assignment of the resonances to the $H \leftarrow X$ system.[230]

In conclusion, the comparison of TKER with predicted dissociation channels indicates that, at wavenumbers corresponding to $H \leftarrow X$, $I \leftarrow X$ and Okazaki's system 5, Cu^+ is produced both by photodissociation of Cu_2^+ (at the one photon level) as well as as by photodissociation (and subsequent ionization) of doubly excited Cu_2^{**}.

6.3.4 Photodissociation of larger species

A majority of the VMI images recorded by gating on Cu_2^+ contained only an intense central spot, resulting from ionization of Cu_2 $X\,^1\Sigma_g^+$ species within the cluster beam possessing zero kinetic energy. However, images recorded *via* the (0-0) and

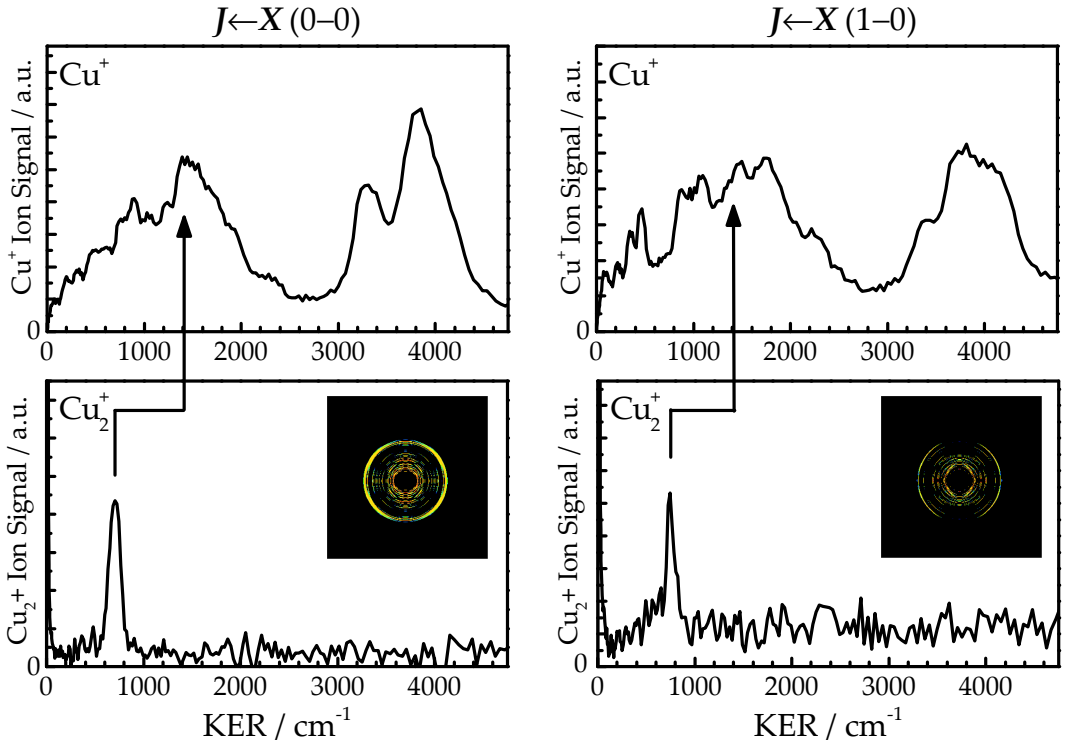

Figure 6.9 KER spectra of $^{63}Cu^+$ (top) and $^{63}Cu_2^+$ (bottom) recorded at 37 446 cm^{-1} and 37 734 cm^{-1}, corresponding to $J \leftarrow X$ (0-0) and $J \leftarrow X$ (1-0). The ring observed in the VMI of Cu_2^+ (see inset) indicates that a larger species dissociates to produce Cu_2^+. In the image, the central spot due to Cu_2 X ($v = 0$) has been removed for clarity. The arrow indicates the Cu KER commensurate with the peak in the Cu_2 distribution, corresponding to trimer dissociation.

(1-0) vibrational components of the $J \leftarrow X$ transition show clear ring features at 705 ± 75 cm^{-1} and 744 ± 75 cm^{-1}, respectively, in addition to an intense central spot (due to R2PI *via* the J ($v = 0$) state). This indicates that a larger species Cu_2R must be fragmenting to produce Cu_2 $X\,^1\Sigma_g^+$ ($v = 0$) with non-zero kinetic energy

$$Cu_2R + h\nu \longrightarrow Cu_2\, X\,^1\Sigma_g^+(v = 0) + R\,. \tag{6.8}$$

The fragments are then ionized by further absorption of photons, which does not alter their off-axis kinetic energy release (KER).

The bottom part of fig. 6.9 shows the images and KER spectra recorded in the

Cu_2^+ channel. The ring features observed therein are not present when the laser is off resonance and detection / ionization of Cu_2 is markedly less efficient. The most likely candidate for the cofragment R is Cu, meaning that the ring features are a result of photodissociation of the copper trimer Cu_3. Conservation of momentum means that the cofragment Cu would be expected to have a KER twice the size of the Cu_2 KER; this is indicated by arrows on fig. 6.9. The corresponding region of the Cu^+ KER spectrum is, as previously discussed, congested

Nevertheless, we proceed with the assumption that the Cu_2^+ KER ring features are a result of neutral trimer dissociation, previously observed by photodepletion[57] and inert gas-tagging.[276,277] The Cu_3 dissociation energy has been previously estimated as $0.75 \pm 0.23\,\mathrm{eV}$[259] ($0.73 \pm 0.20\,\mathrm{eV}$)[121] by collision induced dissociation, and $1.08 \pm 0.19\,\mathrm{eV}$ by third law determination *via* temperature dependent mass spectrometry.[230] Excitation at $37\,446\,\mathrm{cm}^{-1}$ or $37\,734\,\mathrm{cm}^{-1}$ takes us well above the dissociation energy with one photon, but is still below the ionization energy of $5.80 \pm 0.04\,\mathrm{eV}$.[52] In view of the fact that we are resonantly ionizing only the Cu_2 produced in the $X\,^1\Sigma_g^+(v = 0)$ state, the photon energy that is not portioned into KER or dissociation energy must go into the atomic cofragment. At the one photon level, the remaining energy is only sufficient to access the ^2S, ^2P and ^2D states of the Cu atom. Of these, only the ^2P state yields a TKER consistent with the observed TKER of $2115 \pm 225\,\mathrm{cm}^{-1}$(0-0) and $2175 \pm 225\,\mathrm{cm}^{-1}$. Taken together, these imply a Cu_3 dissociation energy of $0.61 \pm 0.03\,\mathrm{eV}$.

6.4 Conclusion

The dynamics of Cu_2 photofragmentation in the ultraviolet ($36\,000$ – $38\,200\,\mathrm{cm}^{-1}$) region of the spectrum have been studied by spectroscopy and velocity map imaging. The spectral evidence clearly demonstrates that Cu_2 undergoes extensive fragmentation as a result of resonant excitation through a variety of photosystems.

Excitation *via* $J \leftarrow X\,^1\Sigma_g^+$ leads to fragments which can be tentatively assigned to two processes: firstly, direct dissociation of the Cu_2^+ Π ion state produced in the resonant photoionization process and secondly, dissociation of doubly excited Cu_2^{**} on the neutral potential energy surface. The fit of the kinetic energies

predicted from known thresholds to the experimentally observed kinetic energy release spectra, obtained from the velocity map images, yields new values for the dissociation energy of Cu_2^+, $D_0(Cu_2^+\ X\ ^2\Sigma_g^+) = 1.71 \pm 0.05$ eV, from which a value of $D_0(Cu_2,\ X\ ^2\Sigma_g^+) = 1.88 \pm 0.05$ eV can be obtained *via* the known ionization energy. With the the exception of the band assigned $H \leftarrow X$ (0-0), photolysis through the other observed band systems ($H \leftarrow X$ (1-0), $I \leftarrow X$ and Okazaki's system 5) leads to kinetic energy releases consistent with the same kind of dissociation pathways as observed for $J \leftarrow X$. Ring features in the velocity map images of Cu_2^+ recorded on resonance with $J \leftarrow X$ ($v = 0$) transitions provide evidence for the photolysis of Cu_3 into Cu^* and Cu_2 X, and yield a Cu_3 dissociation energy of 0.60 ± 0.03 eV.

A full understanding of the velocity map images obtained at transitions corresponding to band systems $H \leftarrow X$, $I \leftarrow X$ and Okazaki's system 5 is hampered by the relative lack of clear information on these states. In this context, high-resolution spectroscopic studies of these systems would be very beneficial. Of particular interest would be a better understanding of the problematic $H \leftarrow X$ system, whose components exhibit markedly differing velocity map images, which could not be fully explained on the basis of the current assignment. Another promising avenue of investigation, which is currently being explored in this group, would be the introduction of a second laser: this may open the possibility of spectrally tagging some of the product states, or, alternatively, may be used to induce a dissociation process prior to UV photoexcitation / photoioniziation.

CHAPTER 7

Conclusions and outlook

This dissertation has presented the experimental investigation of transition metal clusters ranging from the very smallest (dimers) to medium size (3 – 8 atoms). A diverse range of techniques have been deployed to cover this range, from VMI and photoionization for dimers to IR-MPD studies on medium sizes.

VMI of the tantalum dimer Chapter 5 presents an investigation of the one-colour Ta_2 photodissociation *via* photoionization spectroscopy in the range 18 000 – 24 000 cm^{-1} and VMI in the range 23 500 – 24 000 cm^{-1}. The one colour spectrum of Ta exhibits a very high density of peaks, many of which cannot be assigned to the known Ta emission spectrum.[244,245] The most likely source of these additional peaks is a fragmentation process that yields Ta as one of its products.

Using VMI we confirm that Ta is produced in a range of electronic states by fragmentation of the tantalum dimer in this spectral region. The kinetic energies of the products allow us to deduce that the Ta_2 is first ionized to Ta_2^+ (likely at the three photon level) before dissociation with an additional two photons takes place. Dissociation into the electronic ground state of at least one of the products is heavily favoured, with a majority of the observed channels producing either atomic ($Ta(^4F_{3/2})$) or cationic ($Ta^+(^5F_1)$) ground state.

The anisotropies observed in the images indicate a perpendicular transition that is perturbed by rotation of intermediate states or electronic mixing. We infer

that the intermediate state in the Ta_2^+ photodissociation is of Σ or Π type. The assignement of product channels allows us to place the dissociation energy of Ta_2^+, $D_0(Ta_2^+)$, at 5.0928(7) – 5.0902(7) eV, in good agreement with computational predictions performed in parallel with this work. As data on Ta_2 are scarce, many possible avenues for further investigation exist. In particular, a dedicated study of the Ta_2 spectrum, *e.g. via* LIF, may reveal the identity of the putative Σ or Π intermediate state of Ta_2^+ that we observed.

Cu_2 photodissociation dynamics In chapter 6 the electronic spectroscopy and photodissociation dynamics of the copper dimer Cu_2 are investigated using a combination of UV action spectroscopy and velocity map imaging. Spectroscopic analysis of Cu_2 and Cu spectra allows for the identification of Cu_2 photofragmentation as a result of resonant excitation through one of the Cu_2 band systems, yielding Cu fragments with appreciable kinetic energy.

UV excitation of the $J \leftarrow X\ ^1\Sigma_g^+$ band leads to photofragmentation *via* two processes: firstly, direct dissociation of the Cu_2^+ Π ion state produced in the resonant photoionization process and secondly, dissociation of doubly excited Cu_2^{**} on the neutral potential energy surface. The kinetic energies of the Cu fragments yield new values for the dissociation energy of Cu_2^+, $D_0(Cu_2^+\ X\ ^2\Sigma_g^+) = 1.71 \pm 0.05$ eV, from which a value of $D_0(Cu_2,\ X\ ^2\Sigma_g^+) = 1.88 \pm 0.05$ eV can be obtained *via* the known ionization energy.

With the the exception of the band assigned $H \leftarrow X$ (0-0), photolysis through the other observed band systems ($H \leftarrow X$ (1-0), $I \leftarrow X$ and Okazaki's system 5) leads to kinetic energy releases consistent with the same kind of dissociation pathways as observed for $J \leftarrow X$. Ring features in the velocity map images of Cu_2^+ recorded on resonance with $J \leftarrow X$ ($v = 0$) transitions provide evidence for the photolysis of Cu_3 into Cu^* and Cu_2 X, and yield a Cu_3 dissociation energy of 0.61 ± 0.03 eV.

Further work on the $H \leftarrow X$, $I \leftarrow X$ and 5 band systems with the aim of identifying the symmetry of the states involved, would greatly benefit the understanding of the dissociation dynamics of Cu_2 in this spectral range. The $H \leftarrow X$ system in particular deserves renewed attention, in view of the markedly different TKER spectra observed following excitations of different vibrational components as-

signed to the $H \leftarrow X$ system. A natural extension of the experiment herein would be the inclusion of a second (pump or probe) laser in the setup, which would permit spectral tagging of some of the product states. This work is currently underway in our group, and is showing some promise.[112]

Reactivity of N_2O on small Rh clusters Small cationic rhodium clusters and their oxides are investigated in chapter 3 by IR-MPD in the spectral region corresponding to the N_2O bend 505 – 685 cm^{-1}, and computationally using density functional theory. The N_2O band shifts towards the red with increasing cluster size, similar to what has been observed on extended surfaces.[203,204] The presence of additional N_2O adsorbates also shifts the N_2O band position towards lower frequencies, suggesting that the two trends share a common origin. One possible explanation is that the N_2O bend frequency is affected by the electron density on the cluster: an increase in cluster size means a lessening of the effect of the positive charge and an effective increase in electron density. Similarly, N_2O is known to act as a Lewis base (electron donor) on platinum surfaces,[203] and thus the presence of additional N_2O adsorbates can also be considered as an effective increase in electron density.

Both N_2O desorption and the unimolecular dissociation of N_2O can be effectively triggered by IR-MPD *via* either N_2O bend or Rh–O modes, confirming that the IR-MPD process is thermal. The proportions of desorption *vs.* dissociation of N_2O vary as a function of cluster size and oxygen coverage, with an increased proportion of dissociation correlating with an increased oxygen coverage. The most extreme example of this is observed at $n = 5$, with the $Rh_5(N_2O)^+$ cluster supporting desorption almost exclusively, while the $Rh_5O(N_2O)^+$ cluster supports the dissociation reaction almost exclusively. The calculated reaction profile for $Rh_5(N_2O)^+$ shows that barriers to both reaction and desorption are very similar in energy, explaining how the entropically favoured desorption process dominates. The coadsorption of oxygen raises the desorption barrier appreciably, while the reaction barrier is unaffected — this means that reaction can effectively compete with desorption. This behaviour is a contrast to that typically observed on surfaces,[278] where oxygen deactivates the dissociation reaction. However, the

origin of this effect on surfaces is believed to be site blocking by oxygen in combination with a stabilization of molecular N_2O by lateral interactions. In our case, site blocking has a much reduced impact, as the adsorption of one or two oxygen atoms on a Rh_n cluster cannot effectively block all the sites available. On the other hand, as the case of $Rh_5(N_2O)^+$ shows, the stabilization of N_2O on the cluster by the cooperative binding of oxygen is key in allowing the dissociation channel to effectively compete with the desorption channel. Therefore, it is not so surprising that the overall effect of oxygen is to boost the reactivity.

A potential future development of this work would be to probe the anions of the clusters studied, or to investigate the effect of using a different chromophore to drive the same reaction. For example, the CO stretch of a CO molecule adsorbed together with N_2O would provide an alternative means of pumping the reaction (this would require isotopically enriched ^{13}CO, as it would otherwise be impossible to distinguish CO and N_2 loss). Alternatively, one could use a different source of energy than infrared radiation. Indeed, work is underway in this group[279] to probe the reactions of N_2O on rhodium clusters using collision induced dissociation with Ar and CO, which should provide more information on the effects reported here.

Bimolecular reactions on Pt clusters A natural extension of the work on rhodium clusters is the study of a bimolecular process, *i.e.* one in which two moieties on the cluster surface react together. Chapter 4 discusses an example of this in the form of an IR-MPD investigation of platinum clusters decorated with oxygen and carbon monoxide, with the aim to study the oxidation of carbon monoxide in analogue to the reaction on surfaces.[211] In an improvement over the rhodium work, the use of molecular O_2 as a source of oxygen means that the occurrence of odd oxygen species unambiguously confirm that the infrared driven reactivity proceeds.

In a first step, the structure of the decorated clusters was probed by Ar-messenger tagging. In the spectrum of $Pt_4O_2CO^+$ evidence for multiple isomeric forms is observed, one of which can be assigned to the calculated global minimum structure containing dissociatively adsorbed O_2. The remaining isomer could not

be uniquely assigned, but must consist of either a structure with an atop bound oxygen or with *peroxo* bound O_2. Both possibilities involve structures that are calculated to lie significantly (> 1 eV) above the global minimum. One explanation for this is that the clusters become kinetically trapped in these forms after the initial Ar coadsorbates boil off.

The vibrational frequency of the CO molecule on platinum clusters is affected by both the size of the underlying cluster as well as the presence or absence of coadsorbed oxygen. While increasing cluster size tends to red shift the CO stretch, increasing oxygen coverage has the opposite effect. Both trends can be explained in terms of the electron density available for π-backbonding between the metal cluster and CO (an effect which weakens the C–O bond itself): increasing cluster size decreases the portion of positive charge on the platinum atom bonded to CO, while oxygen reduces the electron density available for backbonding by fixing it locally. Where overlap exists, these results agree with recent data.[44]

We have shown that CO oxidation $CO_{(ads)} + O_{(ads)} \longrightarrow CO_{2(g)}$ can be efficiently driven on the surface of small platinum clusters by multiple photon absorption using the CO stretch as a chromophore. In bringing together two distinct moieties, this reaction represents a a noticeable step up in complexity from the unimolecular N_2O dissociation noted in chapter 3. This is an important finding which suggests that IR-MPD may be used to probe a wide range of systems.

In striking contrast to the dissociation of N_2O on rhodium clusters, the branching ratio of reaction *vs.* desorption remains at a constant 60 : 40 across the size range observed. In light of the results for rhodium, we expect that this corresponds to a barrier for reaction significantly below the CO desorption barrier for all cluster sizes as the oxidation reaction would otherwise be unable to effectively compete with desorption. Preliminary calculations on $Pt_4O_2CO^+$ identify a series of transition states along the reaction pathway, and find a reaction barrier significantly below the barrier for CO desorption, in agreement with experimental observation. However, the calculated reaction barriers lie significantly above the values determined on extended surfaces.

Aside from a continuation of the computational work to extend to additional cluster sizes and/or isomers, several avenues of future work appear fruitful. IR-

MPD of the far-infrared region of the spectrum containing the metal-metal modes of platinum clusters, which are characteristic of the metal-metal framework, would provide additional insights into the isomer structure and may help resolve the ambiguities discussed above. An investigation of the reaction using collisional activation *via* a rare gas atom would offer a better determination of the energetic barriers involved. This may also provide information on the presence of multiple isomers, as was the case in previous work on the reaction of rhodium and N_2O.[87]

Concluding remarks Some have called clusters the *third dimension* of the periodic table. While such statements may seem grandiose, this thesis once again highlights the fact that the size of system, even when it is measured in atoms, is of fundamental importance for its properties. The challenge of understanding these phenomena calls for the use of diverse techniques combining both experimental and computational work, as shown in this thesis. In the years to come, further development of such approaches will no doubt yield fascinating new insights into the realm below.

Bibliography

[1] P. Armentrout. "Reactions and Thermochemistry of Small Transition Metal Cluster Ions". *Annual Review of Physical Chemistry*, **52**: 423–461, (2001). (see pp. 1, 48).

[2] M. B. Knickelbein. "Reactions of Transition Metal Clusters with Small Molecules". *Annual Review of Physical Chemistry*, **50**: 79–115, (1999). (see p. 1).

[3] R. A. O'Hair and G. N. Khairallah. "Gas Phase Ion Chemistry of Transition Metal Clusters: Production, Reactivity, and Catalysis". *Journal of Cluster Science*, **15**: 331–363, (2004). (see p. 1).

[4] M. L. Anderson, M. S. Ford, P. J. Derrick, T. Drewello, D. P. Woodruff, and S. R. Mackenzie. "Nitric Oxide Decomposition on Small Rhodium Clusters, $Rh_n^{\pm}$". *The Journal of Physical Chemistry A*, **110**: 10992–11000, (2006). (see pp. 1, 49).

[5] R. L. Johnston. *Atomic and molecular clusters*. London: Taylor & Francis, (2002). (see p. 1).

[6] A. Terasaki. "Physical and Chemical Properties of Metal Clusters in the Gas Phase and on Solid Surfaces". In: *Progress in Experimental and Theoretical Studies of Clusters*. Ed. by T. Kondow and F. Mafuné. Vol. 13. Advanced Series in Physical Chemistry. Singapore: World Scientific, (2003). Chap. 3, pp. 121–153. (see p. 1).

[7] D. J. Harding, C. Kerpal, G. Meijer, and A. Fielicke. "Activated Methane on Small Cationic Platinum Clusters". *Angewandte Chemie International Edition*, **51**: 817–819, (2012). (see pp. 1, 11, 24).

[8] G. Somorjai. *Chemistry in Two Dimensions*. The George Fisher Baker non-resident lectureship in chemistry at Cornell University. Ithaca: Cornell University Press, (1981). (see p. 1).

[9] H. Over, Y. D. Kim, A. P. Seitsonen, S. Wendt, E. Lundgren, M. Schmid, P. Varga, A. Morgante, and G. Ertl. "Atomic-Scale Structure and Catalytic Reactivity of the RuO_2(110) Surface". *Science*, **287**: 1474–1476, (2000). (see p. 2).

[10] C. J. Cramer and D. G. Truhlar. "Density functional theory for transition metals and transition metal chemistry". *Physical Chemistry Chemical Physics*, **11**: 10757–10816, (2009). (see pp. 2, 14, 42, 53).

[11] A. M. Kirillov, M. V. Kirillova, and A. J. Pombeiro. "Multicopper complexes and coordination polymers for mild oxidative functionalization of alkanes". *Coordination Chemistry Reviews*, **256**: 2741–2759, (2012). (see pp. 2, 130).

[12] R. F. Brissos, S. García, A. Presa, and P. Gamez. "Bio-related copper-mediated oxidative processes". *Comments on Inorganic Chemistry*, **32**: 219–245, (2011). (see pp. 2, 130).

[13] O. Echt, K. Sattler, and E. Recknagel. "Magic Numbers for Sphere Packings: Experimental Verification in Free Xenon Clusters". *Physical Review Letters*, **47**: 1121–1124, (1981). (see pp. 2, 4).

[14] E. Robbins, R. Leckenby, and P. Willis. "The ionization potentials of clustered sodium atoms". *Advances in Physics*, **16**: 739–744, (1967). (see p. 2).

[15] D. R. Preuss, S. A. Pace, and J. L. Gole. "The supersonic expansion of pure copper vapor". *The Journal of Chemical Physics*, **71**: 3553–3560, (1979). (see p. 2).

[16] T. G. Dietz, M. A. Duncan, D. E. Powers, and R. E. Smalley. "Laser production of supersonic metal cluster beams". *The Journal of Chemical Physics*, **74**: 6511–6512, (1981). (see p. 2).

[17] V. E. Bondybey and J. H. English. "Laser induced fluorescence of metal clusters produced by laser vaporization: Gas phase spectrum of Pb_2". *The Journal of Chemical Physics*, **74**: 6978–6979, (1981). (see pp. 2, 4).

[18] M. A. Duncan. "Invited Review Article: Laser vaporization cluster sources". *Review of Scientific Instruments*, **83**: 041101, (2012). (see p. 2).

[19] I. Katakuse, T. Ichihara, Y. Fujita, T. Matsuo, T. Sakurai, and H. Matsuda. "Mass distributions of copper, silver and gold clusters and electronic shell structure". *International Journal of Mass Spectrometry and Ion Processes*, **67**: 229–236, (1985). (see p. 3).

[20] H. Haberland, M. Mall, M. Moseler, Y. Qiang, T. Reiners, and Y. Thurner. "Filling of micron-sized contact holes with copper by energetic cluster impact". *Journal of Vacuum Science & Technology A: Vacuum, Surfaces, and Films*, **12**: 2925–2930, (1994). (see p. 3).

[21] H. Haberland, M. Karrais, M. Mall, and Y. Thurner. "Thin films from energetic cluster impact: A feasibility study". *Journal of Vacuum Science & Technology A: Vacuum, Surfaces, and Films*, **10**: 3266–3271, (1992). (see p. 3).

[22] C.-Y. Cha, G. Ganteför, and W. Eberhardt. "New experimental setup for photoelectron spectroscopy on cluster anions". *Review of Scientific Instruments*, **63**: 5661–5666, (1992). (see p. 3).

[23] X. Liu, M. Atwater, J. Wang, and Q. Huo. "Extinction coefficient of gold nanoparticles with different sizes and different capping ligands". *Colloids and Surfaces B: Biointerfaces*, **58**: 3–7, (2007). (see p. 3).

[24] E. A. Rohlfing and J. J. Valentini. "UV laser excited fluorescence spectroscopy of the jet-cooled copper dimer". *The Journal of Chemical Physics*, **84**: 6560–6566, (1986). (see pp. 4, 131).

[25] W. D. Knight, K. Clemenger, W. A. de Heer, W. A. Saunders, M. Y. Chou, and M. L. Cohen. "Electronic Shell Structure and Abundances of Sodium Clusters". *Physical Review Letters*, **52**: 2141–2143, (1984). (see pp. 4, 5).

[26] W. de Heer, W. Knight, M. Chou, and M. Cohen. "Electronic Shell Structure and Metal-Clusters". *Solid State Physics - Advances in Research and Applications*, **40**: 93–181, (1987). (see p. 4).

[27] W. Ekardt. "Work function of small metal particles: Self-consistent spherical jellium-background model". *Physical Review B*, **29**: 1558–1564, (1984). (see p. 4).

[28] P. Hohenberg and W. Kohn. "Inhomogeneous Electron Gas". *Physical Review B*, **136**: B864–B871, (1964). (see pp. 4, 42).

[29] W. Kohn and L. J. Sham. "Self-Consistent Equations Including Exchange and Correlation Effects". *Physical Review*, **140**: A1133–A1138, (1965). (see pp. 4, 42).

[30] O. Echt, O. Kandler, T. Leisner, W. Miehle, and E. Recknagel. "Magic numbers in mass spectra of large van der Waals clusters". *Journal of the Chemical Society, Faraday Transactions*, **86**: 2411–2415, (1990). (see p. 4).

[31] A. L. Mackay. "A dense non-crystallographic packing of equal spheres". *Acta Crystallographica*, **15**: 916–918, (1962). (see p. 5).

[32] L. L. Boyer and J. Q. Broughton. "Statics and dynamics of icosahedrally twinned and single-crystal fcc clusters". *Physical Review B*, **42**: 11461–11468, (1990). (see p. 5).

[33] E. K. Parks, B. J. Winter, T. D. Klots, and S. J. Riley. "The structure of nickel clusters". *The Journal of Chemical Physics*, **94**: 1882–1902, (1991). (see p. 5).

[34] S. J. Riley. "The atomic structure of transition metal clusters". *Journal of Non-Crystalline Solids*, **205-207, Part 2**: 781–787, (1996). (see p. 5).

[35] S. Gilb, P. Weis, F. Furche, R. Ahlrichs, and M. M. Kappes. "Structures of small gold cluster cations (Au_n^+, $n < 14$): Ion mobility measurements versus density functional calculations". *The Journal of Chemical Physics*, **116**: 4094–4101, (2002). (see pp. 6, 14).

[36] D. Schooss, P. Weis, O. Hampe, and M. M. Kappes. "Determining the size-dependent structure of ligand-free gold-cluster ions". *Philosophical Transactions of the Royal Society A: Mathematical, Physical and Engineering Sciences*, **368**: 1211–1243, (2010). (see p. 6).

[37] F. Furche, R. Ahlrichs, P. Weis, C. Jacob, S. Gilb, T. Bierweiler, and M. M. Kappes. "The structures of small gold cluster anions as determined by a combination of ion mobility measurements and density functional calculations". *The Journal of Chemical Physics*, **117**: 6982–6990, (2002). (see p. 6).

[38] M. F. Jarrold and J. E. Bower. "Mobilities of metal cluster ions: Aluminum and the electronic shell model". *The Journal of Chemical Physics*, **98**: 2399–2407, (1993). (see p. 6).

[39] R. R. Hudgins, M. Imai, M. F. Jarrold, and P. Dugourd. "High-resolution ion mobility measurements for silicon cluster anions and cations". *The Journal of Chemical Physics*, **111**: 7865–7870, (1999). (see p. 6).

[40] M. Maier-Borst, D. B. Cameron, M. Rokni, and J. H. Parks. "Electron diffraction of trapped cluster ions". *Physical Review A*, **59**: R3162–R3165, (1999). (see p. 6).

[41] M. P. Johansson, A. Lechtken, D. Schooss, M. M. Kappes, and F. Furche. "2D-3D transition of gold cluster anions resolved". *Physical Review A*, **77**: 053202, (2008). (see p. 6).

[42] A. Lechtken, D. Schooss, J. R. Stairs, M. N. Blom, F. Furche, N. Morgner, O. Kostko, B. von Issendorff, and M. M. Kappes. "Au_{34}^-: A Chiral Gold Cluster?" *Angewandte Chemie International Edition*, **46**: 2944–2948, (2007). (see p. 6).

[43] D. Schooss, M. N. Blom, J. H. Parks, B. v. Issendorff, H. Haberland, and M. M. Kappes. "The Structures of Ag_{55}^+ and Ag_{55}^-: Trapped Ion Electron Diffraction and Density Functional Theory". *Nano Letters*, **5**: 1972–1977, (2005). (see pp. 6, 14).

[44] P. Gruene, A. Fielicke, G. Meijer, and D. M. Rayner. "The adsorption of CO on group 10 (Ni, Pd, Pt) transition-metal clusters". *Physical Chemistry Chemical Physics*, **10**: 6144–6149, (2008). (see pp. 7, 81, 93, 103, 154).

[45] A. Fielicke, G. von Helden, G. Meijer, D. B. Pedersen, B. Simard, and D. M. Rayner. "Size and Charge Effects on the Binding of CO to Small Isolated Rhodium Clusters". *The Journal of Physical Chemistry B*, **108**: 14591–14598, (2004). (see pp. 7, 56, 79).

[46] A. Fielicke, C. Ratsch, G. von Helden, and G. Meijer. "Isomer selective infrared spectroscopy of neutral metal clusters". *The Journal of Chemical Physics*, **122**: 091105, (2005). (see p. 7).

[47] D. J. Harding, T. R. Walsh, S. M. Hamilton, W. S. Hopkins, S. R. Mackenzie, P. Gruene, M. Haertelt, G. Meijer, and A. Fielicke. "Communications: The structure of Rh_8^+ in the gas phase". *The Journal of Chemical Physics*, **132**: 011101, (2010). (see pp. 7, 15, 49, 70).

[48] D. J. Harding, P. Gruene, M. Haertelt, G. Meijer, A. Fielicke, S. M. Hamilton, W. S. Hopkins, S. R. Mackenzie, S. P. Neville, and T. R. Walsh. "Probing the structures of gas-phase rhodium cluster cations by far-infrared spectroscopy". *The Journal of Chemical Physics*, **133**: 214304, (2010). (see pp. 7, 15, 49, 53, 70).

[49] W. J. C. Menezes and M. B. Knickelbein. "Photodissociation spectroscopy of Nb_nAr_m complexes". *The Journal of Chemical Physics*, **98**: 1856–1866, (1993). (see p. 7).

[50] M. B. Knickelbein, S. Yang, and S. J. Riley. "Near-threshold photoionization of nickel clusters: Ionization potentials for Ni_3 to Ni_{90}". *The Journal of Chemical Physics*, **93**: 94–104, (1990). (see p. 8).

[51] M. M. Kappes, M. Schär, U. Röthlisberger, C. Yeretzian, and E. Schumacher. "Sodium cluster ionisation potentials revisited: Higher-resolution measurements for Na_x ($x < 23$) and their relation to bonding models". *Chemical Physics Letters*, **143**: 251–258, (1988). (see p. 8).

[52] M. B. Knickelbein. "Electronic shell structure in the ionization potentials of copper clusters". *Chemical Physics Letters*, **192**: 129–134, (1992). (see pp. 8, 148).

[53] S. Yang and M. B. Knickelbein. "Photoionization studies of transition metal clusters: Ionization potentials for Fe_n and Co_n". *The Journal of Chemical Physics*, **93**: 1533–1539, (1990). (see p. 8).

[54] M. B. Knickelbein and S. Yang. "Photoionization studies of niobium clusters: Ionization potentials for Nb_2-Nb_{76}". *The Journal of Chemical Physics*, **93**: 5760–5767, (1990). (see p. 8).

[55] M. D. Morse, G. P. Hansen, P. R. R. Langridge-Smith, L.-S. Zheng, M. E. Geusic, D. L. Michalopoulos, and R. E. Smalley. "Spectroscopic studies of the jet-cooled nickel dimer". *The Journal of Chemical Physics*, **80**: 5400–5405, (1984). (see p. 9).

[56] G. A. Bishea and M. D. Morse. "Spectroscopic studies of jet-cooled AgAu and Au_2". *The Journal of Chemical Physics*, **95**: 5646–5659, (1991). (see pp. 9, 130).

[57] M. D. Morse, J. B. Hopkins, P. R. R. Langridge-Smith, and R. E. Smalley. "Spectroscopic studies of the jet-cooled copper trimer". *The Journal of Chemical Physics*, **79**: 5316–5328, (1983). (see pp. 9, 148).

[58] D.-S. Yang et al. "Vibrational and geometric structures of Nb_3C_2 and $Nb_3C_2^+$ from pulsed field ionization-zero electron kinetic energy photoelectron spectra and density functional calculations". *The Journal of Chemical Physics*, **105**: 10663–10671, (1996). (see p. 9).

[59] D.-S. Yang and P. A. Hackett. "ZEKE spectroscopy of free transition metal clusters". *Journal of Electron Spectroscopy and Related Phenomena*, **106**: 153–169, (2000). (see p. 9).

[60] M. S. Ford and S. R. Mackenzie. "Preparing transition-metal clusters in known structural forms: The mass-analyzed threshold ionization spectrum of V_3". *The Journal of Chemical Physics*, **123**: 084308, (2005). (see p. 9).

[61] S. M. Casey and D. G. Leopold. "Negative ion photoelectron spectroscopy of chromium dimer". *The Journal of Physical Chemistry*, **97**: 816–830, (1993). (see p. 9).

[62] Y. D. Kim and G. Ganteför. "Non-dissociative adsorption of diatomic molecules on nanoclusters at room temperature". *Chemical Physics Letters*, **382**: 644–649, (2003). (see p. 9).

[63] J. Conceicao, R. T. Laaksonen, L.-S. Wang, T. Guo, P. Nordlander, and R. E. Smalley. "Photoelectron spectroscopy of transition-metal clusters: Correlation of valence electronic structure to reactivity". *Physical Review B*, **51**: 4668–4671, (1995). (see p. 9).

[64] M. B. Knickelbein. "Electric dipole polarizabilities of Ni_{12-58}". *The Journal of Chemical Physics*, **115**: 5957–5964, (2001). (see p. 9).

[65] M. B. Knickelbein. "Electric dipole polarizabilities of Nb_{2-27}". *The Journal of Chemical Physics*, **118**: 6230–6233, (2003). (see p. 9).

[66] R. Moro, X. Xu, S. Yin, and W. A. de Heer. "Ferroelectricity in Free Niobium Clusters". *Science*, **300**: 1265–1269, (2003). (see p. 9).

[67] M. K. Beyer and M. B. Knickelbein. "Electric deflection studies of rhodium clusters". *The Journal of Chemical Physics*, **126**: 104301, (2007). (see pp. 10, 49).

[68] D. C. Douglass, A. J. Cox, J. P. Bucher, and L. A. Bloomfield. "Magnetic properties of free cobalt and gadolinium clusters". *Physical Review B*, **47**: 12874–12889, (1993). (see p. 10).

[69] A. J. Cox, J. G. Louderback, and L. A. Bloomfield. "Experimental observation of magnetism in rhodium clusters". *Physical Review Letters*, **71**: 923–926, (1993). (see pp. 10, 14).

[70] A. J. Cox, J. G. Louderback, S. E. Apsel, and L. A. Bloomfield. "Magnetism in 4*d*-transition metal clusters". *Physical Review B*, **49**: 12295–12298, (1994). (see pp. 10, 48).

[71] J. Louderback, A. Cox, L. Lising, D. Douglass, and L. Bloomfield. "Magnetic properties of nickel clusters". *Zeitschrift für Physik D Atoms, Molecules and Clusters*, **26**: 301–303, (1993). (see p. 10).

[72] M. B. Comisarow and A. G. Marshall. "Fourier transform ion cyclotron resonance spectroscopy". *Chemical Physics Letters*, **25**: 282–283, (1974). (see p. 10).

[73] A. G. Marshall, C. L. Hendrickson, and G. S. Jackson. "Fourier transform ion cyclotron resonance mass spectrometry: A primer". *Mass Spectrometry Reviews*, **17**: 1–35, (1998). (see p. 10).

[74] M. E. Geusic, M. D. Morse, and R. E. Smalley. "Hydrogen chemisorption on transition metal clusters". *The Journal of Chemical Physics*, **82**: 590–591, (1985). (see p. 11).

[75] M. D. Morse, M. E. Geusic, J. R. Heath, and R. E. Smalley. "Surface reactions of metal clusters. II. Reactivity surveys with D_2, N_2, and CO". *The Journal of Chemical Physics*, **83**: 2293–2304, (1985). (see p. 11).

[76] D. N. Shin, Y. Matsuda, and E. R. Bernstein. "On the iron oxide neutral cluster distribution in the gas phase. I. Detection through 193 nm multiphoton ionization". *The Journal of Chemical Physics*, **120**: 4150–4156, (2004). (see p. 11).

[77] S.-G. He, Y. Xie, F. Dong, and E. R. Bernstein. "Reaction of niobium and tantalum neutral clusters with low pressure, unsaturated hydrocarbons in a pickup cell: From dehydrogenation to Met-Car formation". *The Journal of Chemical Physics*, **125**: 164306, 164306, (2006). (see p. 11).

[78] L. Holmgren, M. Andersson, and A. Rosén. "CO reactivity of small transition-metal clusters: Ni_n and Nb_n". *Surface Science*, **331-333, Part A**: 231–236, (1995). (see p. 11).

[79] M. Ichihashi, T. Hanmura, R. T. Yadav, and T. Kondow. "Adsorption and Reaction of Methanol Molecule on Nickel Cluster Ions, Ni_n^+ ($n = 3 - 11$)". *The Journal of Physical Chemistry A*, **104**: 11885–11890, (2000). (see p. 11).

[80] R. H. Schultz, K. C. Crellin, and P. B. Armentrout. "Sequential bond energies of iron carbonyl $Fe(CO)_x^+$ ($x = 1 - 5$): systematic effects on collision-induced dissociation measurements". *Journal of the American Chemical Society*, **113**: 8590–8601, (1991). (see p. 11).

[81] S. M. Hamilton, W. S. Hopkins, D. J. Harding, T. R. Walsh, P. Gruene, M. Haertelt, A. Fielicke, G. Meijer, and S. R. Mackenzie. "Infrared Induced Reactivity on the Surface of Isolated Size-Selected Clusters: Dissociation of N_2O on Rhodium Clusters". *Journal of the American Chemical Society*, **132**: 1448–1449, (2010). (see pp. 11, 51, 53).

[82] A. C. Hermes, S. M. Hamilton, W. S. Hopkins, D. J. Harding, C. Kerpal, G. Meijer, A. Fielicke, and S. R. Mackenzie. "Effects of Coadsorbed Oxygen on the Infrared Driven Decomposition of N_2O on Isolated Rh_5^+ Clusters". *Journal of Physical Chemistry Letters*, **2**: 3053–3057, (2011). (see pp. 11, 16, 47, 48, 102).

[83] A. C. Hermes, S. M. Hamilton, G. A. Cooper, C. Kerpal, D. J. Harding, G. Meijer, A. Fielicke, and S. R. Mackenzie. "Infrared driven CO oxidation reactions on isolated platinum cluster oxides, $Pt_nO_m^+$". *Faraday Discussions*, **157**: 213–225, (2012). (see pp. 11, 16, 81).

[84] M. Haruta, N. Yamada, T. Kobayashi, and S. Iijima. "Gold catalysts prepared by coprecipitation for low-temperature oxidation of hydrogen and of carbon monoxide". *Journal of Catalysis*, **115**: 301–309, (1989). (see p. 11).

[85] J. M. Alford, F. D. Weiss, R. T. Laaksonen, and R. E. Smalley. "Dissociative chemisorption of molecular hydrogen on niobium cluster ions. A supersonic cluster beam FT-ICR experiment". *The Journal of Physical Chemistry*, **90**: 4480–4482, (1986). (see p. 12).

[86] J. L. Elkind, F. D. Weiss, J. M. Alford, R. T. Laaksonen, and R. E. Smalley. "Fourier transform ion cyclotron resonance studies of H_2 chemisorption on niobium cluster cations". *The Journal of Chemical Physics*, **88**: 5215–5224, (1988). (see pp. 12, 13).

[87] D. Harding, M. S. Ford, T. R. Walsh, and S. R. Mackenzie. "Dramatic size effects and evidence of structural isomers in the reactions of rhodium clusters, $Rh_n^{\pm}$, with nitrous oxide". *Physical Chemistry Chemical Physics*, **9**: 2130–2136, (2007). (see pp. 12, 51, 155).

[88] G. Kummerlöwe, I. Balteanu, Z. Sun, O. P. Balaj, V. E. Bondybey, and M. K. Beyer. "Activation of methane and methane-d4 by ionic platinum clusters". *International Journal of Mass Spectrometry*, **254**: 183–188, (2006). (see p. 12).

[89] Å. M. L. Øiestad and E. Uggerud. "Gas phase reactivity of small cationic cobalt clusters towards methanol". *Chemical Physics*, **262**: 169–177, (2000). (see p. 12).

[90] G. Albert, C. Berg, M. Beyer, U. Achatz, S. Joos, G. Niedner-Schatteburg, and V. E. Bondybey. "Methane activation by rhodium cluster argon complexes". *Chemical Physics Letters*, **268**: 235–241, (1997). (see p. 13).

[91] V. E. Bondybey and M. K. Beyer. "Temperature Effects in Transition Metal Ion and Cluster Ion Reactions". *The Journal of Physical Chemistry A*, **105**: 951–960, (2001). (see p. 13).

[92] S. A. Mitchell, D. M. Rayner, T. Bartlett, and P. A. Hackett. "Reaction of tungsten clusters with molecular nitrogen". *The Journal of Chemical Physics*, **104**: 4012–4018, (1996). (see p. 13).

[93] T. H. Lee and K. M. Ervin. "Reactions of Copper Group Cluster Anions with Oxygen and Carbon Monoxide". *The Journal of Physical Chemistry*, **98**: 10023–10031, (1994). (see p. 13).

[94] D. Cox, R. Brickman, K. Creegan, and A. Kaldor. "Gold clusters: reactions and deuterium uptake". *Zeitschrift für Physik D Atoms, Molecules and Clusters*, **19**: 353–355, (1991). (see p. 13).

[95] U. Achatz, C. Berg, S. Joos, B. S. Fox, M. K. Beyer, G. Niedner-Schatteburg, and V. E. Bondybey. "Methane activation by platinum cluster ions in the gas phase: effects of cluster charge on the Pt_4 tetramer". *Chemical Physics Letters*, **320**: 53–58, (2000). (see pp. 13, 82).

[96] I. Balteanu, U. Achatz, O. P. Balaj, B. S. Fox, M. K. Beyer, and V. E. Bondybey. "The effect of charge upon CO-adsorption by ionic group 5 and group 9 transition metal clusters". *International Journal of Mass Spectrometry*, **229**: 61–65, (2003). (see p. 13).

[97] B. J. Winter, E. K. Parks, and S. J. Riley. "Copper clusters: The interplay between electronic and geometrical structure". *The Journal of Chemical Physics*, **94**: 8618–8621, (1991). (see p. 13).

[98] A. C. Borin and J. P. Gobbo. "Electronic structure and chemical bonding in the ground and low-lying electronic states of Ta_2". *International Journal of Quantum Chemistry*, **111**: 1306–1315, (2011). (see pp. 14, 107).

[99] E. R. Davidson, ed. *Computational Transition Metal Chemistry*. Vol. 100. Washington, DC: American Chemical Society, (2000). (see p. 14).

[100] A. Fielicke, A. Kirilyuk, C. Ratsch, J. Behler, M. Scheffler, G. von Helden, and G. Meijer. "Structure Determination of Isolated Metal Clusters via Far-Infrared Spectroscopy". *Physical Review Letters*, **93**: 023401, (2004). (see pp. 14, 21).

[101] A. Fielicke, G. von Helden, and G. Meijer. "Far-Infrared spectroscopy of isolated transition metal clusters". *The European Physical Journal D - Atomic, Molecular, Optical and Plasma Physics*, **34**: 83–88, (2005). (see pp. 14, 86).

[102] H.-J. Zhai and L.-S. Wang. "Probing the electronic structure of early transition metal oxide clusters: Molecular models towards mechanistic insights into oxide surfaces and catalysis". *Chemical Physics Letters*, **500**: 185–195, (2010). (see p. 14).

[103] B. V. Reddy, S. N. Khanna, and B. I. Dunlap. "Giant magnetic moments in 4*d* clusters". *Physical Review Letters*, **70**: 3323–3326, (1993). (see pp. 14, 48).

[104] B. V. Reddy, S. K. Nayak, S. N. Khanna, B. K. Rao, and P. Jena. "Electronic structure and magnetism of Rh_n ($n = 2 - 13$) clusters". *Physical Review B*, **59**: 5214–5222, (1999). (see pp. 15, 49).

[105] T. Futschek, M. Marsman, and J. Hafner. "Structural and magnetic isomers of small Pd and Rh clusters: an ab initio density functional study". *Journal of Physics: Condensed Matter*, **17**: 5927, (2005). (see pp. 15, 49).

[106] Y.-C. Bae, H. Osanai, V. Kumar, and Y. Kawazoe. "Nonicosahedral growth and magnetic behavior of rhodium clusters". *Physical Review B*, **70**: 195413, (2004). (see pp. 15, 49, 70).

[107] V. Kumar and Y. Kawazoe. "Magnetism in clusters of non-magnetic elements: Pd, Rh, and Ru". *The European Physical Journal D - Atomic, Molecular, Optical and Plasma Physics*, **24**: 81–84, (2003). (see p. 15).

[108] D. J. Harding, C. Kerpal, D. M. Rayner, and A. Fielicke. "Communication: The structures of small cationic gas-phase platinum clusters". *The Journal of Chemical Physics*, **136**: 211103, (2012). (see pp. 15, 86, 87, 92).

[109] A. N. Gloess, H. Schneider, J. M. Weber, and M. M. Kappes. "Electronically excited states and visible region photodissociation spectroscopy of $Au_m^+ \cdot Ar_n$ clusters ($m = 7 - 9$): Molecular dimensionality transition?" *The Journal of Chemical Physics*, **128**: 114312, 114312, (2008). (see p. 15).

[110] M. Harb, F. Rabilloud, and D. Simon. "Optical response of silver nanoclusters complexed with aromatic thiol molecules: a time-dependent density functional study". *Journal of Physics B: Atomic, Molecular and Optical Physics*, **44**: 035101, (2011). (see p. 15).

[111] D. Harding, S. R. Mackenzie, and T. R. Walsh. "Structural Isomers and Reactivity for Rh_6 and Rh_6^+". *The Journal of Physical Chemistry B*, **110**: 18272–18277, (2006). (see p. 15).

[112] I. S. Parry, A. C. Hermes, A. Kartouzian, and S. R. Mackenzie. "Imaging the photodissociation dynamics of neutral metal clusters: copper dimer, Cu_2 and copper oxide, CuO". *Physical Chemistry Chemical Physics*, Advance Article, (2013). (see pp. 17, 129, 152).

[113] C. Berg, T. Schindler, G. Niedner-Schatteburg, and V. E. Bondybey. "Reactions of simple hydrocarbons with Nb_n^+: Chemisorption and physisorption on ionized niobium clusters". *The Journal of Chemical Physics*, **102**: 4870–4884, (1995). (see p. 18).

[114] S. Maruyama, L. R. Anderson, and R. E. Smalley. "Direct injection supersonic cluster beam source for FT-ICR studies of clusters". *Review of Scientific Instruments*, **61**: 3686–3693, (1990). (see p. 18).

[115] W. C. Wiley and I. H. McLaren. "Time-of-Flight Mass Spectrometer with Improved Resolution". *Review of Scientific Instruments*, **26**: 1150–1157, (1955). (see p. 20).

[116] T. S. Zwier. "The spectroscopy of solvation in hydrogen-bonded aromatic clusters". *Annual Review of Physical Chemistry*, **47**: 205–241, (1996). (see p. 21).

[117] M. Putter, G. von Helden, and G. Meijer. "Mass selective infrared spectroscopy using a free electron laser". *Chemical Physics Letters*, **258**: 118–122, (1996). (see p. 21).

[118] G. von Helden, D. van Heijnsbergen, and G. Meijer. "Resonant Ionization Using IR Light: A New Tool To Study the Spectroscopy and Dynamics of Gas-Phase Molecules and Clusters". *The Journal of Physical Chemistry A*, **107**: 1671–1688, (2003). (see pp. 21, 27).

[119] J. L. Lyman, B. E. Newnam, J. W. Early, and A. F. G. van der Meer. "Infrared Free-Electron-Laser Photolysis of $CFCl_3$ and CF_2Cl_2". *The Journal of Physical Chemistry A*, **101**: 49–54, (1997). (see p. 21).

[120] V. N. Bagratashvili, V. S. Letokhov, A. A. Makarov, and E. A. Ryabov. *Multiple Photon Infrared Laser Photophysics and Photochemistry*. Harwood Academic Publishers, (1985). (see p. 21).

[121] S. Krückeberg, L. Schweikhard, J. Ziegler, G. Dietrich, K. Lützenkirchen, and C. Walther. "Decay pathways and dissociation energies of copper clusters, Cu_n^+ ($2 \leq n \leq 25$), Cu_n^{2+} ($15 \leq n \leq 25$)". *The Journal of Chemical Physics*, **114**: 2955–2962, (2001). (see pp. 23, 131, 141, 148).

[122] M. Okumura, L. I. Yeh, J. D. Myers, and Y. T. Lee. "Infrared spectra of the cluster ions $H_7O_3^+ \cdot H_2$ and $H_9O_4^+ \cdot H_2$". *The Journal of Chemical Physics*, **85**: 2328–2329, (1986). (see p. 23).

[123] M. Okumura, L. I. Yeh, J. D. Myers, and Y. T. Lee. "Infrared spectra of the solvated hydronium ion: Vibrational predissociation spectroscopy of mass-selected $H_3O^+ \cdot (H_2O)_n \cdot (H_2)_m$". *The Journal of Physical Chemistry*, **94**: 3416–3427, (1990). (see p. 23).

[124] C. Ratsch, A. Fielicke, A. Kirilyuk, J. Behler, G. von Helden, G. Meijer, and M. Scheffler. "Structure determination of small vanadium clusters by density-functional theory in comparison with experimental far-infrared spectra". *The Journal of Chemical Physics*, **122**: 124302, 124302, (2005). (see p. 24).

[125] D. Oepts, A. F. G. van der Meer, and P. van Amersfoort. "The Free-Electron-Laser user facility FELIX". *Infrared Physics & Technology*, **36**: 297–308, (1995). (see p. 26).

[126] M. N. R. Ashfold and J. D. Howe. "Multiphoton Spectroscopy of Molecular Species". *Annual Review of Physical Chemistry*, **45**: 57–82, (1994). (see p. 29).

[127] A. M. Wodtke and Y. T. Lee. "Photodissociation of acetylene at 193.3 nm". *The Journal of Physical Chemistry*, **89**: 4744–4751, (1985). (see p. 32).

[128] J. Segall, R. Lavi, Y. Wen, and C. Wittig. "Acetylene carbon-hydrogen bond dissociation energy using 193.3-nm photolysis and sub-Doppler resolution hydrogen-atom spectroscopy: 127.0 ± 1.5 kcal/mol". *The Journal of Physical Chemistry*, **93**: 7287–7289, (1989). (see p. 32).

[129] M. N. R. Ashfold, N. H. Nahler, A. J. Orr-Ewing, O. P. J. Vieuxmaire, R. L. Toomes, T. N. Kitsopoulos, I. A. Garcia, D. A. Chestakov, S.-M. Wu, and D. H. Parker. "Imaging the dynamics of gas phase reactions". *Phys. Chem. Chem. Phys.* **8**: 26–53, (2006). (see p. 32).

[130] D. W. Chandler and P. L. Houston. "Two-dimensional imaging of state-selected photodissociation products detected by multiphoton ionization". *The Journal of Chemical Physics*, **87**: 1445–1447, (1987). (see p. 32).

[131] A. T. J. B. Eppink and D. H. Parker. "Velocity map imaging of ions and electrons using electrostatic lenses: Application in photoelectron and photofragment ion imaging of molecular oxygen". *Review of Scientific Instruments*, **68**: 3477–3484, (1997). (see pp. 32, 33).

[132] A. Eppink, S.-M. Wu, and B. Whitaker. In: *Imaging in molecular dynamics: technology and applications*. B. J. Whitaker, ed. Chap. 3. Cambridge: Cambridge University Press, (2003). (see pp. 32, 34).

[133] C. R. Gebhardt, T. P. Rakitzis, P. C. Samartzis, V. Ladopoulos, and T. N. Kitsopoulos. "Slice imaging: A new approach to ion imaging and velocity mapping". *Review of Scientific Instruments*, **72**: 3848–3853, (2001). (see p. 33).

[134] K. Tonokura and T. Suzuki. "Slicing photofragment spatial distribution by laser sheet ionization". *Chemical Physics Letters*, **224**: 1–6, (1994). (see p. 33).

[135] D. Townsend, M. P. Minitti, and A. G. Suits. "Direct current slice imaging". *Review of Scientific Instruments*, **74**: 2530–2539, (2003). (see p. 33).

[136] A. J. R. Heck and D. W. Chandler. "Imaging Techniques for the Study of Chemical Reaction Dynamics". *Annual Review of Physical Chemistry*, **46**: 335–372, (1995). (see p. 34).

[137] T. P. Rakitzis. "Direct measurement of photofragment alignment from unnormalized Abel-invertible images". *Chemical Physics Letters*, **342**: 121–126, (2001). (see p. 34).

[138] V. Dribinski, A. Ossadtchi, V. A. Mandelshtam, and H. Reisler. "Reconstruction of Abel-transformable images: The Gaussian basis-set expansion Abel transform method". *Review of Scientific Instruments*, **73**: 2634–2642, (2002). (see p. 34).

[139] G. A. Garcia, L. Nahon, and I. Powis. "Two-dimensional charged particle image inversion using a polar basis function expansion". *Review of Scientific Instruments*, **75**: 4989–4996, (2004). (see p. 34).

[140] C. Bordas, F. Paulig, H. Helm, and D. L. Huestis. "Photoelectron imaging spectrometry: Principle and inversion method". *Review of Scientific Instruments*, **67**: 2257–2268, (1996). (see p. 34).

[141] K. Zhao, T. Colvin, W. T. H. III, and G. Zhang. "Deconvolving two-dimensional images of three-dimensional momentum trajectories". *Review of Scientific Instruments*, **73**: 3044–3050, (2002). (see p. 34).

[142] G. M. Roberts, J. L. Nixon, J. Lecointre, E. Wrede, and J. R. R. Verlet. "Toward real-time charged-particle image reconstruction using polar onion-peeling". *Review of Scientific Instruments*, **80**: 053104, 053104, (2009). (see pp. 34–36).

[143] K. L. Reid. "Photoelectron Angular Distributions". *Annual Review of Physical Chemistry*, **54**: 397–424, (2003). (see pp. 35, 40).

[144] R. N. Zare. *Angular Momentum*. New York: Wiley, (1988). (see pp. 35, 40).

[145] R. N. Dixon. "Recoil anisotropy following multiphoton dissociation via near-resonant intermediate states". *The Journal of Chemical Physics*, **122**: 194302, 194302, (2005). (see pp. 40, 126).

[146] E. Wrede, S. Laubach, S. Schulenburg, A. Brown, E. R. Wouters, A. J. Orr-Ewing, and M. N. R. Ashfold. "Continuum state spectroscopy: A high resolution ion imaging study of IBr photolysis in the wavelength range 440 – 685 nm". *The Journal of Chemical Physics*, **114**: 2629–2646, (2001). (see p. 40).

[147] D. A. Dahl. "Simion for the personal computer in reflection". *International Journal of Mass Spectrometry*, **200**: 3–25, (2000). (see p. 40).

[148] W. S. Hopkins, S. M. Hamilton, P. D. McNaughter, and S. R. Mackenzie. "VUV photodissociation dynamics of diatomic gold, Au_2: A velocity map imaging study at 157 nm". *Chemical Physics Letters*, **483**: 10–15, (2009). (see p. 41).

[149] M. Reid and S. P. K. Koehler. "Validation of velocity map imaging conditions over larger areas". *Review of Scientific Instruments*, **84**: 044101, 044101, (2013). (see p. 41).

[150] J. P. Perdew, A. Ruzsinszky, L. A. Constantin, J. Sun, and G. I. Csonka. "Some Fundamental Issues in Ground-State Density Functional Theory: A Guide for the Perplexed". *Journal of Chemical Theory and Computation*, **5**: 902–908, (2009). (see p. 43).

[151] J. P. Perdew and K. Schmidt. *Density Functional Theory and Its Applications to Materials*. Melville, NY: American Institute of Physics, (2001). (see p. 43).

[152] F. Jensen. In: *Introduction to Computational Chemistry*. Chap. 12. Wiley, (2007). (see pp. 43, 45).

[153] J. P. Perdew, K. Burke, and M. Ernzerhof. "Generalized Gradient Approximation Made Simple". *Physical Review Letters*, **77**: 3865–3868, (1996). (see pp. 43, 44, 53).

[154] C. Lee, W. Yang, and R. G. Parr. "Development of the Colle-Salvetti correlation-energy formula into a functional of the electron density". *Physical Review B*, **37**: 785–789, (1988). (see p. 43).

[155] B. Miehlich, A. Savin, H. Stoll, and H. Preuss. "Results obtained with the correlation energy density functionals of Becke and Lee, Yang and Parr". *Chemical Physics Letters*, **157**: 200–206, (1989). (see p. 43).

[156] J. Tao, J. P. Perdew, V. N. Staroverov, and G. E. Scuseria. "Climbing the Density Functional Ladder: Nonempirical Meta-Generalized Gradient Approximation Designed for Molecules and Solids". *Physical Review Letters*, **91**: 146401, (2003). (see pp. 44, 54, 86).

[157] A. D. Boese and N. C. Handy. "New exchange-correlation density functionals: The role of the kinetic-energy density". *The Journal of Chemical Physics*, **116**: 9559–9569, (2002). (see p. 44).

[158] P. J. Stephens, F. J. Devlin, C. F. Chabalowski, and M. J. Frisch. "Ab Initio Calculation of Vibrational Absorption and Circular Dichroism Spectra Using Density Functional Force Fields". *The Journal of Physical Chemistry*, **98**: 11623–11627, (1994). (see pp. 44, 53).

[159] J. P. Perdew, M. Ernzerhof, and K. Burke. "Rationale for mixing exact exchange with density functional approximations". *The Journal of Chemical Physics*, **105**: 9982–9985, (1996). (see pp. 44, 53).

[160] V. N. Staroverov, G. E. Scuseria, J. Tao, and J. P. Perdew. "Comparative assessment of a new nonempirical density functional: Molecules and hydrogen-bonded complexes". *The Journal of Chemical Physics*, **119**: 12129–12137, (2003). (see pp. 44, 54, 86).

[161] Turbomole *V6.3 2011, a development of University of Karlsruhe and Forschungszentrum Karlsruhe GmbH, 1989-2007, TURBOMOLE GmbH, since 2007; available from* `http://www.turbomole.com` (see pp. 44, 54).

[162] M. Häser and R. Ahlrichs. "Improvements on the direct SCF method". *Journal of Computational Chemistry*, **10**: 104–111, (1989). (see p. 45).

[163] M. von Arnim and R. Ahlrichs. "Geometry optimization in generalized natural internal coordinates". *The Journal of Chemical Physics*, **111**: 9183–9190, (1999). (see p. 45).

[164] P. Csàszàr and P. Pulay. "Geometry optimization by direct inversion in the iterative subspace". *Journal of Molecular Structure*, **114**: 31–34, (1984). (see p. 45).

[165] S. M. Hamilton. *Spectroscopy and Dynamics of Metal Clusters*. PhD thesis. United Kingdom: University of Oxford, 2010. (see pp. 45, 55, 74, 76).

[166] S. M. Hamilton, W. S. Hopkins, D. J. Harding, T. R. Walsh, M. Haertelt, C. Kerpal, P. Gruene, G. Meijer, A. Fielicke, and S. R. Mackenzie. "Infrared-Induced Reactivity of N_2O on Small Gas-Phase Rhodium Clusters". *The Journal of Physical Chemistry A*, **115**: 2489–2497, (2011). (see pp. 45, 51, 59, 70, 86, 100, 103).

[167] P. Deglmann, F. Furche, and R. Ahlrichs. "An efficient implementation of second analytical derivatives for density functional methods". *Chemical Physics Letters*, **362**: 511–518, (2002). (see p. 45).

[168] T. Helgaker. "Transition-state optimizations by trust-region image minimization". *Chemical Physics Letters*, **182**: 503–510, (1991). (see p. 46).

[169] H. Gandhi, G. Graham, and R. McCabe. "Automotive exhaust catalysis". *Journal of Catalysis*, **216**: 433–442, (2003). (see pp. 48, 82).

[170] M. Shelef and G. W. Graham. "Why Rhodium in Automotive Three-Way Catalysts?" *Catalysis Reviews*, **36**: 433–457, (1994). (see p. 48).

[171] M. Shelef and R. McCabe. "Twenty-five years after introduction of automotive catalysts: what next?" *Catalysis Today*, **62**: 35–50, (2000). (see p. 48).

[172] D. A. Hickman and L. D. Schmidt. "Production of Syngas by Direct Catalytic Oxidation of Methane". *Science*, **259**: 343–346, (1993). (see p. 48).

[173] P. D. Vernon, M. L. Green, A. K. Cheetham, and A. T. Ashcroft. "Partial oxidation of methane to synthesis gas". *Catalysis Letters*, **6**: 181–186, (1990). (see p. 48).

[174] J. Wei and E. Iglesia. "Structural requirements and reaction pathways in methane activation and chemical conversion catalyzed by rhodium". *Journal of Catalysis*, **225**: 116–127, (2004). (see p. 48).

[175] V. Zhdanov and B. Kasemo. "Mechanism and kinetics of the NO-CO reaction on Rh". *Surface Science Reports*, **29**: 31–90, (1997). (see pp. 48, 50).

[176] L. A. DeLouise and N. Winograd. "Adsorption and desorption of no from Rh{111} and Rh{331} surfaces". *Surface Science*, **159**: 199–213, (1985). (see p. 48).

[177] M. R. Zakin, D. M. Cox, and A. Kaldor. "Gas-phase rhodium cluster chemistry: Influence of adsorbate electronic structure on reaction rate". *The Journal of Chemical Physics*, **89**: 1201–1202, (1988). (see p. 48).

[178] V. Bertin, R. Lopez-Rendón, G. del Angel, E. Poulain, R. Avilés, and V. Uc-Rosas. "Comparative theoretical study of small Rh_n nanoparticles ($2 \leq n \leq 8$) using DFT methods". *International Journal of Quantum Chemistry*, **110**: 1152–1164, (2010). (see p. 49).

[179] C. Adlhart and E. Uggerud. "C–H activation of alkanes on Rh_n^+ ($n = 1 - 30$) clusters: Size effects on dehydrogenation". *The Journal of Chemical Physics*, **123**: 214709, (2005). (see p. 49).

[180] C. Adlhart and E. Uggerud. "Mechanisms of catalytic dehydrogenation of alkanes by rhodium clusters Rh_n^+ probed by isotope labelling". *International Journal of Mass Spectrometry*, **249 - 250**: 191–198, (2006). (see p. 49).

[181] C. Berg, M. Beyer, U. Achatz, S. Joos, G. Niedner-Schatteburg, and V. E. Bondybey. "Effect of charge upon metal cluster chemistry: Reactions of Nb_n and Rh_n anions and cations with benzene". *The Journal of Chemical Physics*, **108**: 5398–5403, (1998). (see p. 49).

[182] I. Balteanu, O. P. Balaj, B. S. Fox-Beyer, P. Rodrigues, M. T. Barros, A. M. C. Moutinho, M. L. Costa, M. K. Beyer, and V. E. Bondybey. "Size- and Charge-State-Dependent Reactivity of Azidoacetonitrile with Anionic and Cationic Rhodium Clusters $Rh_n^{\pm}$". *Organometallics*, **23**: 1978–1985, (2004). (see p. 49).

[183] M. S. Ford, M. L. Anderson, M. P. Barrow, D. P. Woodruff, T. Drewello, P. J. Derrick, and S. R. Mackenzie. "Reactions of nitric oxide on Rh_6^+ clusters: abundant chemistry and evidence of structural isomers". *Physical Chemistry Chemical Physics*, **7**: 975–980, (2005). (see p. 49).

[184] H. Wang, H. Haouari, R. Craig, Y. Liu, J. R. Lombardi, and D. M. Lindsay. "Spectroscopy of mass-selected rhodium dimers in argon matrices". *The Journal of Chemical Physics*, **106**: 2101–2104, (1997). (see p. 49).

[185] J. D. Langenberg and M. D. Morse. "The bond energy of Rh_2". *The Journal of Chemical Physics*, **108**: 2331–2335, (1998). (see p. 49).

[186] R. V. Zee, Y. Hamrick, S. Li, and W. W. Jr. "ESR of Co, Rh, Ir trimers and diatomic ions". *Chemical Physics Letters*, **195**: 214–220, (1992). (see p. 49).

[187] F. Barker and R. Gasser. "The reaction of nitrous oxide with rhodium". *Surface Science*, **39**: 136–142, (1973). (see p. 50).

[188] K. Imamura, H. Horino, I. Rzeźnicka, I. Kobal, A. Kokalj, Y. Ohno, B. E. Nieuwenhuys, A. Hiratsuka, and T. Matsushima. "Multi-directional N_2 desorption in N_2O decomposition on Rh(110)". *Surface Science*, **566 - 568**: 1076–1081, (2004). (see p. 50).

[189] K. Imamura and T. Matsushima. "N_2 Desorption in the Isothermal Decomposition of N_2O on Rh(110) at Low Temperatures". *Catalysis Letters*, **97**: 197–202, (2004). (see p. 50).

[190] Y. Li and M. Bowker. "The adsorption and decomposition of nitrous oxide on Rh(110) and Rh(111)". *Surface Science*, **348**: 67–76, (1996). (see p. 50).

[191] S. Wehner, M. T. Paffett, and F. Zaera. "Molecular Beam Studies of the Kinetics of the Thermal Conversion of N_2O on Rh(111) Single-Crystal Surfaces". *The Journal of Physical Chemistry B*, **108**: 18683–18692, (2004). (see p. 50).

[192] S. Liu, H. Horino, A. Kokalj, I. Rzeźnicka, K. Imamura, Y. Ma, I. Kobal, Y. Ohno, A. Hiratsuka, and T. Matsushima. "N_2 Desorption in the Decomposition of Adsorbed N_2O on Rh(110)". *The Journal of Physical Chemistry B*, **108**: 3828–3834, (2004). (see p. 50).

[193] A. Kokalj and T. Matsushima. "A density-functional theory study of the interaction of N_2O with Rh(110)". *The Journal of Chemical Physics*, **122**: 034708, (2005). (see p. 50).

[194] J. Ricart, F. Ample, A. Clotet, D. Curulla, J. H. Niemantsverdriet, J. Paul, and J. Pérez-Ramírez. "Structure and catalytic processes of N-containing species on Rh(111) from first principles". *Journal of Catalysis*, **232**: 179–185, (2005). (see p. 50).

[195] J.-F. Paul, J. Pérez-Ramírez, F. Ample, and J. M. Ricart. "Theoretical Studies of N_2O Adsorption and Reactivity to N_2 and NO on Rh(111)". *The Journal of Physical Chemistry B*, **108**: 17921–17927, (2004). (see p. 50).

[196] D. Harding. Private communication (see pp. 52, 58, 70).

[197] F. Furche and J. P. Perdew. "The performance of semilocal and hybrid density functionals in 3*d* transition-metal chemistry". *The Journal of Chemical Physics*, **124**: 044103, (2006). (see p. 53).

[198] S. F. Sousa, P. A. Fernandes, and M. J. Ramos. "General Performance of Density Functionals". *The Journal of Physical Chemistry A*, **111**: 10439–10452, (2007). (see p. 53).

[199] F. Weigend and R. Ahlrichs. "Balanced basis sets of split valence, triple zeta valence and quadruple zeta valence quality for H to Rn: Design and assessment of accuracy". *Physical Chemistry Chemical Physics*, **7**: 3297–3305, (2005). (see pp. 54, 87).

[200] F. Weigend. "Accurate Coulomb-fitting basis sets for H to Rn". *Physical Chemistry Chemical Physics*, **8**: 1057–1065, (2006). (see pp. 54, 87).

[201] M. Sierka, A. Hogekamp, and R. Ahlrichs. "Fast evaluation of the Coulomb potential for electron densities using multipole accelerated resolution of identity approximation". *The Journal of Chemical Physics*, **118**: 9136–9148, (2003). (see p. 54).

[202] L. Rothman et al. "The HITRAN 2008 molecular spectroscopic database". *Journal of Quantitative Spectroscopy and Radiative Transfer*, **110**: 533–572, (2009). (see p. 56).

[203] N. R. Avery. "An EELS study of N_2O adsorption on Pt(111)". *Surface Science*, **131**: 501–510, (1983). (see pp. 56, 79, 152).

[204] T. E. Madey, N. R. Avery, A. B. Anton, B. H. Toby, and W. H. Weinberg. "The adsorption and decomposition of N_2O on Ru(001)". *Journal of Vacuum Science & Technology A: Vacuum, Surfaces, and Films*, **1**: 1220–1221, (1983). (see pp. 56, 152).

[205] D. Harding, S. Mackenzie, and T. Walsh. "Density functional theory calculations of vibrational spectra of rhodium oxide clusters". *Chemical Physics Letters*, **469**: 31–34, (2009). (see p. 58).

[206] A. Yamada, K. Miyajima, and F. Mafune. "Catalytic reactions on neutral Rh oxide clusters more efficient than on neutral Rh clusters". *Physical Chemistry Chemical Physics*, **14**: 4188–4195, (2012). (see p. 77).

[207] C. Kerpal, D. J. Harding, A. C. Hermes, G. Meijer, S. R. Mackenzie, and A. Fielicke. "Structures of Platinum Oxide Clusters in the Gas Phase". *The Journal of Physical Chemistry A*, **117**: 1233–1239, (2013). (see pp. 81, 89, 91).

[208] J. M. Thomas. "Turning Points in Catalysis". *Angewandte Chemie International Edition in English*, **33**: 913–937, (1994). (see p. 82).

[209] A. Kaldor and D. Cox. "Recent Advances in the Chemistry of Transition-metal Clusters". *Pure and Applied Chemistry*, **62**: 79–88, (1990). (see p. 82).

[210] K. Koszinowski, D. Schröder, and H. Schwarz. "Reactivity of Small Cationic Platinum Clusters". *The Journal of Physical Chemistry A*, **107**: 4999–5006, (2003). (see p. 82).

[211] G. Ertl. "Reactions at Surfaces: From Atoms to Complexity (Nobel Lecture)". *Angewandte Chemie International Edition*, **47**: 3524–3535, (2008). (see pp. 83, 153).

[212] J. Wintterlin, S. Völkening, T. V. W. Janssens, T. Zambelli, and G. Ertl. "Atomic and Macroscopic Reaction Rates of a Surface-Catalyzed Reaction". *Science*, **278**: 1931–1934, (1997). (see pp. 83, 102).

[213] T. Matsushima. "The mechanism of the CO_2 formation on Pt(111) and polycrystalline surfaces at low temperatures". *Surface Science*, **127**: 403–423, (1983). (see p. 83).

[214] U. Heiz, A. Sanchez, S. Abbet, and W.-D. Schneider. "Catalytic Oxidation of Carbon Monoxide on Monodispersed Platinum Clusters: Each Atom Counts". *Journal of the American Chemical Society*, **121**: 3214–3217, (1999). (see p. 83).

[215] Y. Shi and K. M. Ervin. "Catalytic oxidation of carbon monoxide by platinum cluster anions". *The Journal of Chemical Physics*, **108**: 1757–1760, (1998). (see pp. 83, 99).

[216] O. P. Balaj, I. Balteanu, T. T. J. Rossteuscher, M. K. Beyer, and V. E. Bondybey. "Catalytic Oxidation of CO with N_2O on Gas-Phase Platinum Clusters". *Angewandte Chemie International Edition*, **43**: 6519–6522, (2004). (see pp. 83, 99).

[217] D. J. Wales and J. P. K. Doye. "Global Optimization by Basin-Hopping and the Lowest Energy Structures of Lennard-Jones Clusters Containing up to 110 Atoms". *The Journal of Physical Chemistry A*, **101**: 5111–5116, (1997). (see p. 87).

[218] N. Metropolis, A. W. Rosenbluth, M. N. Rosenbluth, A. H. Teller, and E. Teller. "Equation of State Calculations by Fast Computing Machines". *The Journal of Chemical Physics*, **21**: 1087–1092, (1953). (see p. 87).

[219] J. Schmidt, C. Stuhlmann, and H. Ibach. "Oxygen adsorption on the Pt(110)(1×2) surface studied with EELS". *Surface Science*, **284**: 121–128, (1993). (see pp. 89, 91).

[220] H. Steininger, S. Lehwald, and H. Ibach. "Adsorption of oxygen on Pt(111)". *Surface Science*, **123**: 1–17, (1982). (see pp. 89, 91).

[221] A. Fielicke, G. von Helden, G. Meijer, D. B. Pedersen, B. Simard, and D. M. Rayner. "Size and charge effects on the binding of CO to late transition metal clusters". *The Journal of Chemical Physics*, **124**: 194305, (2006). (see p. 93).

[222] J. Yoshinobu and M. Kawai. "Initial adsorption sites of CO on Pt(111) and Ni(100) at low temperature". *Surface Science*, **363**: 105–111, (1996). (see p. 93).

[223] J. Nekrylova and I. Harrison. "Site resolved adsorption dynamics of CO on Pt(111)". *Chemical Physics*, **205**: 37–46, (1996). (see p. 93).

[224] I. Swart, A. Fielicke, D. M. Rayner, G. Meijer, B. M. Weckhuysen, and F. M. F. de Groot. "Controlling the Bonding of CO on Cobalt Clusters by Coadsorption of H_2". *Angewandte Chemie International Edition*, **46**: 5317–5320, (2007). (see p. 93).

[225] A. Eichler. "CO oxidation on transition metal surfaces: reaction rates from first principles". *Surface Science*, **498**: 314–320, (2002). (see pp. 101, 102).

[226] A. Grushow and K. M. Ervin. "Ligand and metal binding energies in platinum carbonyl cluster anions: Collision-induced dissociation of Pt_m^- and Pt_mCO^-". *The Journal of Chemical Physics*, **106**: 9580–9593, (1997). (see p. 102).

[227] Y. Xu, R. B. Getman, W. A. Shelton, and W. F. Schneider. "A first-principles investigation of the effect of Pt cluster size on CO and NO oxidation intermediates and energetics". *Physical Chemistry Chemical Physics*, **10**: 6009–6018, (2008). (see p. 102).

[228] C. T. Campbell, G. Ertl, H. Kuipers, and J. Segner. "A molecular beam study of the catalytic oxidation of CO on a Pt(111) surface". *The Journal of Chemical Physics*, **73**: 5862–5873, (1980). (see p. 102).

[229] J. L. Gland and E. B. Kollin. "Carbon monoxide oxidation on the Pt(111) surface: Temperature programmed reaction of coadsorbed atomic oxygen and carbon monoxide". *The Journal of Chemical Physics*, **78**: 963–974, (1983). (see p. 102).

[230] M. D. Morse. "Clusters of transition-metal atoms". *Chemical Reviews*, **86**: 1049–1109, (1986). (see pp. 106, 130, 132, 144, 146, 148).

[231] A. M. James, P. Kowalczyk, E. Langlois, M. D. Campbell, A. Ogawa, and B. Simard. "Resonant two photon ionization spectroscopy of the molecules V_2, VNb, and Nb_2". *The Journal of Chemical Physics*, **101**: 4485–4495, (1994). (see p. 106).

[232] K. Balasubramanian and X. L. Zhu. "Spectroscopic constants and potential energy curves of Nb_2 and Nb_2^+". *The Journal of Chemical Physics*, **114**: 10375–10388, (2001). (see p. 106).

[233] T. A. O'Brien, K. Albert, and M. C. Zerner. "The electronic structure and spectroscopy of V_2". *The Journal of Chemical Physics*, **112**: 3192–3200, (2000). (see p. 106).

[234] P. R. R. Langridge-Smith, M. D. Morse, G. P. Hansen, R. E. Smalley, and A. J. Merer. "The bond length and electronic structure of V_2". *The Journal of Chemical Physics*, **80**: 593–600, (1984). (see p. 106).

[235] W. S. Hopkins, S. M. Hamilton, and S. R. Mackenzie. "The electronic spectrum of vanadium monoxide across the visible: New bands and new insight". *The Journal of Chemical Physics*, **130**: 144308, (2009). (see p. 106).

[236] P. B. Armentrout, D. A. Hales, and L. Lian. In: *Advances in Metal and Semiconductor Clusters*. M. A. Duncan, ed. Vol. 2, pp. 1–55. JAI Press Inc, (1994). (see pp. 106, 126).

[237] B. Collings, D. Rayner, and P. Hackett. "Ionization potentials of tantalum clusters with three to 64 atoms". *International Journal of Mass Spectrometry and Ion Processes*, **125**: 207–214, (1993). (see pp. 106, 117, 124, 126).

[238] Z. Hu, B. Shen, J. R. Lombardi, and D. M. Lindsay. "Spectroscopy of mass-selected tantalum dimers in argon matrices". *The Journal of Chemical Physics*, **96**: 8757–8760, (1992). (see p. 107).

[239] B. Simard, A. M. James, P. Kowalczyk, R. Fournier, and P. A. Hackett. "High-resolution spectroscopy of small transition metal molecules: recent experimental and theoretical progress on group 5 diatomics". *SPIE proceedings*, **2124**: 376–387, (1994). (see p. 107).

[240] M. W. Heaven, G. M. Stewart, M. A. Buntine, and G. F. Metha. "Neutral Tantalum Carbide Clusters: A Multiphoton Ionization and Density Functional Theory Study". *The Journal of Physical Chemistry A*, **104**: 3308–3316, (2000). (see p. 107).

[241] W. Fa, C. Luo, and J. Dong. "Coexistence of ferroelectricity and ferromagnetism in tantalum clusters". *The Journal of Chemical Physics*, **125**: 114305, (2006). (see p. 107).

[242] J. Du, X. Sun, and G. Jiang. "A theoretical study on Ta_n^+ cluster cations: Structural assignments, stability, and electronic properties". *The Journal of Chemical Physics*, **136**: 094311, 094311, (2012). (see p. 107).

[243] X. Sun, J. Du, P. Zhang, and G. Jiang. "A Systemic DFT Study on Several 5*d*-Electron Element Dimers: Hf_2, Ta_2, Re_2, W_2, and Hg_2". *Journal of Cluster Science*, **21**: 619–636, (2010). (see p. 107).

[244] W. F. Meggers, C. H. Corliss, and B. F. Scribner. *Tables of Spectral-Line Intensities, Part I - Arranged by Elements*. Monograph 145. National Bureau of Standards (US), (1975). (see pp. 110, 118, 150).

[245] A. Kramida, Y. Ralchenko, J. Reader, and NIST ASD Team. *NIST Atomic Spectra Database (version 5.0)*. National Institute of Standards and Technology. 2012. URL: http://physics.nist.gov/asd (see pp. 110, 118, 133, 134, 140, 145, 150).

[246] A. Al-Khalili, U. Hällsten, and O. Launila. "Spectroscopy of TaO". *Journal of Molecular Spectroscopy*, **198**: 230–238, (1999). (see p. 111).

[247] R. Ram, J. Liévin, and P. Bernath. "Emission Spectroscopy and Ab Initio Calculations for TaN". *Journal of Molecular Spectroscopy*, **215**: 275–284, (2002). (see p. 112).

[248] B. Simard, P. Kowalczyk, and A. M. James. "First ionization potential of tantalum by mass-selected double-resonance field-ionization spectroscopy". *Physical Review A*, **50**: 846–849, (1994). (see p. 124).

[249] W. S. Hopkins and T. Zheng. Private communication (see p. 127).

[250] S. Lecoultre, A. Rydlo, J. Buttet, C. Félix, S. Gilb, and W. Harbich. "Ultraviolet-visible absorption of small silver clusters in neon: Ag_n ($n = 1 - 9$)". *The Journal of Chemical Physics*, **134**: 184504, (2011). (see pp. 130, 131).

[251] X. Wang, X. Wan, H. Zhou, S. Takami, M. Kubo, and A. Miyamoto. "Electronic structures and spectroscopic properties of dimers Cu_2, Ag_2, and Au_2calculated by density functional theory". *Journal of Molecular Structure: THEOCHEM*, **579**: 221–227, (2002). (see p. 130).

[252] P. Joyes and M. Leleyter. "Ab initio study of Cu_2 and Cu_2^+". *Journal of Physics B: Atomic and Molecular Physics*, **6**: 150, (1973). (see p. 130).

[253] J. C. Idrobo, W. Walkosz, S. F. Yip, S. Öğüt, J. Wang, and J. Jellinek. "Static polarizabilities and optical absorption spectra of gold clusters (Au_n, $n = 2 - 14$ and 20) from first principles". *Physical Review B*, **76**: 205422, (2007). (see p. 130).

[254] R. Hatz, M. Korpinen, V. Hänninen, and L. Halonen. "Characterization of the Dispersion Interactions and an ab Initio Study of van der Waals Potential Energy Parameters for Coinage Metal Clusters". *The Journal of Physical Chemistry A*, **116**: 11685–11693, (2012). (see p. 130).

[255] R. Lieberman and A. Rosenzweig. "Crystal structure of a membrane-bound metalloenzyme that catalyses the biological oxidation of methane". *Nature*, **434**: 177–182, (2005). (see p. 130).

[256] J. Drowart and R. E. Honig. "A Mass Spectrometric Method for the Determination of Dissociation Energies of Diatomic Molecules". *The Journal of Physical Chemistry*, **61**: 980–985, (1957). (see p. 130).

[257] P. Schissel. "Dissociation Energies of Cu_2, Ag_2, and Au_2". *The Journal of Chemical Physics*, **26**: 1276–1280, (1957). (see p. 130).

[258] K. Hilpert and K. Gingerich. "Atomization enthalpies of the molecules Cu_3, Ag_3 and Au_3". *Berichte der Bunsen Gesellschaft für Physikalische Chemie*, **84**: 739–745, (1980). (see p. 130).

[259] O. Ingólfsson, U. Busolt, and K.-i. Sugawara. "Energy-resolved collision-induced dissociation of Cu_n^+ (n = 2-9): Stability and fragmentation pathways". *The Journal of Chemical Physics*, **112**: 4613–4620, (2000). (see pp. 130, 141, 148).

[260] K. B. MacAdam, S. F. Dyubko, V. A. Efremov, V. G. Gerasimov, and A. S. Kutsenko. "Laser-microwave spectroscopy of Cu I atoms in S, P, D, F and G Rydberg states". *Journal of Physics B: Atomic, Molecular and Optical Physics*, **42**: 165009, (2009). (see pp. 131, 143).

[261] A. D. Sappey, J. E. Harrington, and J. C. Weisshaar. "Resonant two-photon ionization-photoelectron spectroscopy of Cu_2: Autoionization dynamics and Cu_2^+ vibronic states". *The Journal of Chemical Physics*, **91**: 3854–3868, (1989). (see pp. 131, 135, 140, 142–144).

[262] T. Okazaki and Y. Ando. "New optical absorption spectra of Cu_2 molecules produced by the gas evaporation technique". *Molecular Physics*, **98**: 447–452, (2000). (see pp. 131, 132).

[263] R. H. Page and C. S. Gudeman. "Rotationally resolved dicopper (Cu_2) laser-induced fluorescence spectra". *The Journal of Chemical Physics*, **94**: 39–51, (1991). (see pp. 131–133).

[264] J. L. Gole, J. H. English, and V. E. Bondybey. "Laser spectroscopy of cooled metal clusters: copper dimer". *The Journal of Physical Chemistry*, **86**: 2560–2563, (1982). (see p. 131).

[265] D. E. Powers, S. G. Hansen, M. E. Geusic, A. C. Puiu, J. B. Hopkins, T. G. Dietz, M. A. Duncan, P. R. R. Langridge-Smith, and R. E. Smalley. "Supersonic metal cluster beams: laser photoionization studies of copper cluster (Cu_2)". *The Journal of Physical Chemistry*, **86**: 2556–2560, (1982). (see p. 131).

[266] D. E. Powers, S. G. Hansen, M. E. Geusic, D. L. Michalopoulos, and R. E. Smalley. "Supersonic copper clusters". *The Journal of Chemical Physics*, **78**: 2866–2881, (1983). (see pp. 131, 144).

[267] A. D. Sappey, J. E. Harrington, and J. C. Weisshaar. "Cu_2^+ vibronic states at 0 – 1.4 eV from multiphoton ionization-photoelectron spectroscopy". *The Journal of Chemical Physics*, **88**: 5243–5245, (1988). (see p. 131).

[268] M. Doverstål, B. Lindgren, U. Sassenberg, and H. Yu. "The A-X system of the copper dimer studied by resonant two-photon ionization spectroscopy". *Chemical Physics Letters*, **192**: 283–288, (1992). (see p. 131).

[269] R. Ram, C. Jarman, and P. Bernath. "Fourier transform emission spectroscopy of the copper dimer". *Journal of Molecular Spectroscopy*, **156**: 468–486, (1992). (see p. 131).

[270] J. Ruamps. "Spectre d'emission des molecules Cu_2, Ag_2 et Au_2". *Comptes Rendus Hebdomadaires des Seances de l'Academie des Sciences*, **238**: 1489–1491, (1954). (see p. 131).

[271] N. Aslund, R. Barrow, W. Richards, and D. Travis. "Rotational analysis of bands of the B-X system of Cu_2 and of A-X system of Bi_2". *Arkiv for Fysik*, **30**: 171–, (1965). (see p. 131).

[272] J. G. McCaffrey, R. R. Bennett, M. D. Morse, and W. H. Breckenridge. "Laser excitation spectroscopy of the A and B states of jet-cooled copper dimer: Evidence for large electronic isotope shifts". *The Journal of Chemical Physics*, **91**: 92–103, (1989). (see p. 131).

[273] E. Miyoshi, H. Tatewaki, and T. Nakamura. "Electronic structure of small copper clusters. II. Localized *d* hole in excited states and ionized states of Cu_2 and Cu_3". *The Journal of Chemical Physics*, **78**: 815–826, (1983). (see p. 131).

[274] M. Witko and H.-O. Beckmann. "Ab initio MRD CI calculations for ground and excited states of Cu_2 molecule". *Molecular Physics*, **47**: 945–957, (1982). (see p. 131).

[275] A. G. Shenstone. "The First Spectrum of Copper (Cu I)". *Philosophical Transactions of the Royal Society of London. Series A, Mathematical and Physical Sciences*, **241**: 297–322, (1948). (see p. 140).

[276] M. B. Knickelbein. "Photodissociation spectroscopy of Cu_3, Cu_3Ar, and Cu_3Kr". *The Journal of Chemical Physics*, **100**: 4729–4737, (1994). (see p. 148).

[277] M. B. Knickelbein. "The copper trimer and its argon van der Waals complex: An anomalous shift in the $\tilde{A} \leftarrow \tilde{X}$ photodissociation spectrum". *The Journal of Chemical Physics*, **100**: 2388–2390, (1994). (see p. 148).

[278] A. Zeigarnik. "Adsorption and Reactions of N_2O on Transition Metal Surfaces". *Kinetics and Catalysis*, **44**: 233–246, (2003). (see p. 152).

[279] I. S. Parry, A. Kartouzian, S. M. Hamilton, O. P. Balaj, M. K. Beyer, and S. R. Mackenzie. "Collisional Activation of N_2O Decomposition and CO Oxidation Reactions on Isolated Rhodium Clusters". *The Journal of Physical Chemistry A*, **117**: 8855–8863, (2013). (see p. 153).

Production notes

This thesis was typeset using LaTeX2ϵ as implemented in pdfTeX using `biblatex/biber` for bibliography. The fonts are from the `kpfonts` package based on Zapf's Palatino as designed by URW.

No animals were hurt during the creation of this thesis.